FLOW CHARACTERISTICS
OF LEAD-BISMUTH TWO-PHASE FLOW

Gen Ariyoshi

FLOW CHARACTERISTICS OF LEAD-BISMUTH TWO-PHASE FLOW

Doctoral thesis

by

Gen Ariyoshi

for the degree of

Doctor of Energy Science

Kyoto University

2018

Outline of doctoral thesis

Acknowledgement

I would like to express my deep gratitude to many people to who have been helping my study and have supported me in a lot occasions.

Special thanks are extended to Professor Yasushi Saito, Department of fundamental energy science, Kyoto University for giving me interesting research subject and guidance.
I would like to express my appreciation to Professor Tsuyoshi Misawa, Department of fundamental energy science, Kyoto University for suggestion his opinion for this thesis.
Special thanks are extended to Professor Takehiko Yokomine, Department of Nuclear Engineering, Kyoto University for his suggestion for this thesis
Special thanks are extended to Professor Kei Ito, Department of fundamental energy science, Kyoto University for interest, for his suggestion.
Special thanks are extended to Professor Daisuke. Ito, Department of fundamental energy science, Kyoto University for interest, for his suggestion.

LIST OF FIGURES

LIST OF TABLES

Chapter 1

Introduction

1.1 Background

1.1.1 *Details of partitioning and transmutation technology development in Japan*

In Japan, the fundamental arrangement to deal with sizable High Level radioactive Wastes (HLWs) which come from large amount of fuels spent in the conventional Light Water Reactor (LWR) had been decided by the Japanese government. The first step of the HLWs processing is theri solidification, and the second step is the storage of the solidified HLWs in the period from 30 to 50 years to cool down their temperature. After that, as the final step, the HLWs are stored by utilizing deep geological disposal. However, the selection of candidate sites has been unsuccessful. In addition, it is well recognized by Japanese society that there exist serious difficulties in terms of management and disposal methods of such HLWs after the accident of Fukushima Daiichi Nuclear Power Plant. In this context, the Japanese government had newly rearranged the Basic Energy Plan on April 2014 and determined that the technology development of appropriate methods should be tackled to handle and dispose the HLWs and to reduce the amount and the radiotoxicity of the HLWs as a Japanese policy.

The HLWs include Minor Actinides (MAs) and Fission Products (FPs) , some of which have quite long half-life longer than several thousand years or millions of years. So, in the case of the geological disposal method, it must be necessary to ensure the confinement ability for preventing from the leakage of such MAs and FPs into environment where people are living and to manage them over such long period. However, it would be extremely difficult for human beings at present technological limitation and with poor public acceptance. The Partitioning and Transmutation (P&T) is the technology for relieving such burden, because the P&T is also technology to separate MAs and FPs corresponding to their purpose of use and to transmute these MAs and FPs to stable nuclides having shorter half-life and lighter radiotoxicity. Therefore, it could be achieved to reduce long-term risk of potential radiotoxicity of the HLWs and to increase practical disposal capacity of geological disposal site by the realization of the P&T technology in near future.

In 1988, the expert committee for radioactive wastes disposal in Atomic Energy Commission of Japan (JAEC) established the project of Option Making of Extra Gain from Actinides and fission products (OMEGA project) in order to promote research activities for P&T technology. And then various Researches and Developments (R&Ds) in terms of P&T were conducted based on the OMEGA project. In 2000, future policies for R&Ds of P&T were

summarized in the report entitled ‘Present situation of R&Ds and future policy in terms of P&T technology for long-lived radioactive nuclides’ by the expert committee for nuclear energy back end policy. Based on this report, R&Ds for P&T with ‘concept of utilizing power generating fast reactor’ and also with ‘hierarchical concept’ have been conducted in parallel so far. In the ‘concept of utilizing power generating fast reactor’, MAs and FPs could be utilized with normal nuclear fuel in the fast reactors, in which the transmutation of them would be accomplished. On the other hand, in the ‘hierarchical concept’, MAs and FPs are worked as a part of nuclear fuel in the small dedicated system for nuclear transmutation, which is prepared in addition to conventional nuclear fuel cycle [1-1], as indicated in **Figure 1-1**. In this ‘hierarchical concept’, Accelerator-Driven System (ADS) is positioned as the important dedicated system for nuclear transmutation.

In this context, R&Ds for realizing both of fast reactor and ADS have been conducted in Japan. Especially, regarding the ADS development, new research facilities called as ‘ADS Target Test Facility (TEF-T)’ and ‘Transmutation Physics Experimental Facility (TEF-P)’ shall be constructed in the Japan Proton Accelerator Research Complex (J-PARC) center to obtain valuable data in terms of sub-critical reactor physics, nuclear fuel fabrication, thermal hydraulics, structural materials and etc. [1-2, 1-3].

1.1.2 *Lead cooled Fast Reactor (LFR) and Accelerator-Driven System (ADS)*

As mentioned above, MAs and FPs must be separated and utilized to fabricate nuclear fuels,which should be exposed to neutrons in order to perform P&T. As for the options for irradiation using neutrons, there is a way to use fission reactor. Fast reactors are, of course, one of the fission reactors and have advantages to carry out nuclear transmutation for the MAs and FPs since high energy neutrons are required for the transmutation. The neutron spectrum in those fast reactors’ cores is close to the fission neutron spectrum, since the neutrons are not thermalized by light water as in a conventional LWRs. The fast reactor coolant is appropriately chosen in order to provide an effective heat transfer, without a significant thermalization of the neutron spectrum. In order to achieve this goal, liquid metals (Na or Pb, Pb-Bi) or gas can be (or have been) used. Those fast reactors can be classified as critical and sub-critical reactor i.e. ADS. Generation IV International Forum (GIF) has proposed Lead/Lead-Bismuth Eutectic (LBE) cooled Fast Reactor (LFR) as one of the next generation reactor. In addition, in the 7th Framework Program (FP7) of EURATOM and other countries including Japan, R&Ds of ADS is promoted.

LBE is the promising candidate for the primary coolant of the LFR and the ADS. The advantage of such liquid metal used as a coolant for the LFR and the ADS attributes to its physical, chemical and thermodynamic properties such as high boiling temperature, low melting

temperature, high thermal conductivity and chemical stability. Especially due to its high boiling temperature (1670℃), it is allowable to have a low pressure in the primary loop even when the outlet coolant temperature is equal to 400-500℃. This simplifies the reactor design and enhances its reliability [1-4 - 1-6]. The LFR consists of critical fuel assembly containing MAs and FPs, pump for coolant circulation and Steam Generator (SG) [1-7], as shown in **Figure 1-2**. On the other hand, as denoted in **Figure 1-3**, the ADS is composed of the high-current proton accelerator, the nuclear spallation target, the subcritical fuel assembly that contains MAs and FPs, the electro-magnetic pump and the SG [1-8]. One of the fast-developing areas of the nuclear engineering is associated with using high-current proton accelerators for realization of the ADS [1-9, 1-10]. The expediency of using heavy metals as a target material for proton beam is caused by a high neutron yield in spallation reactions between these materials. This necessity to apply a liquid metal target is associated also with the heat removal problem at a high energy release density. Hence, lead and LBE seem to be the best materials for liquid metal targets because of its high thermal conductivity [1-11, 1-12]. On the **Table 1-1** and **Table1-2**, the relevant characteristics of the LBE are summarized. In the present design of the ADS, the primary heat exchanger, SG, is going to be installed in main reactor pool so that the SG can touch directly to the primary coolant; lead or LBE. In addition, the coolant in the SG is basically chosen to be water. Nowadays, international design and investigation of LFRs and ADSs are in progress in many countries, for example BREST-OD-300, SVBR-100, ALFRED (LFRs), MYRRHA, EFIT and XADS (ADSs) [1-2, 1-3, 1-13], where details of these reactors will be described in following section and specifications of these reactors are summarized in the **Table 1-3** and **Table 1-4**.

1.1.3 *International trend of project for development of LFRs and ADSs*

An important step forward for Heavy Liquid Metal (HLM) nuclear systems has been observed for example in the Russian Federation, Europe, and in the framework of the GIF. In Russia, the small modular lead-bismuth-cooled SVBR is presently in the licensing stage. Europe has defined its Strategic Research and Innovation Agenda (SRIA), where both LFRs and lead-bismuth-cooled experimental reactors are being considered. Moreover, the irradiation of the MEGAPIE HLM neutron spallation target, shown in **Figure 1-4** was successfully completed and post irradiation examination (PIE) activities have begun. In the following section, details of international trend for LFRs and ADSs are introduced [1-14].

HLM such as lead (Pb) or LBE were proposed and investigated as coolants for fast reactors as early as the 1950s (e.g. in the United States). Sodium became the preferred choice in the 1960s, due to a higher power density achievable with this coolant, which resulted in lower doubling times, an important objective at that time (IAEA, 2002). However, LBE was chosen as

the coolant for a number of alpha-class submarine reactors in the former Soviet Union, which led to very extensive research and development on coolant technology and materials, with particular emphasis on the chemistry control of the liquid metal to avoid plugging due to slag formation and to enhance corrosion resistance of the steels specifically developed for such services.

More recently, there has been renewed interest in Russia in lead and LBE coolants for fast reactors. The lead-cooled BREST (Russian acronym for Pb-cooled fast reactor) concept developed since the early 1990s is the most widely known, with the LBE-cooled SVBR (Russian acronym for lead-bismuth fast reactor) concept competing for attention. Their features and the associated technologies inspired several projects in the emerging field of ADS, and in particular lead cooling was associated, in the mid-1990s, with the proposal for an energy amplifier project together with LBE as a spallation target coolant and material. Subsequent development of ADS in Europe, Japan, Korea, and the United States, has adopted a heavy liquid metal (most often LBE) as the coolant for the subcritical core and as coolant and material for the spallation target which provides the external neutron source.

Research in the field of LBE technology at SCK•CEN (Belgium) since 1997 has been related to the Multi-Purpose Hybrid Research Reactor for High-Tech Applications (MYRRHA) project and is aimed at the development of a research reactor driven by an accelerator, where LBE is used as a spallation target and coolant. Moreover, the European Programme that is defined within the Sustainable Nuclear Energy Technology Platform (SNETP) has launched the industrial initiative ESNII (2010), where, along with the MYRRHA system, a lead-cooled fast reactor system is also considered. The developments of both systems are supported through European Commission (EC), including EURATOM, funded projects in the fields of design, safety, technology and materials.

Liquid metals have been studied since the early development of fission energy as reactor core coolants for fast reactors, fusion energy blanket applications and, more recently, for both ADS proposed for high-level radioactive waste transmutation and for generation IV fast reactors. Moreover, HLM are being proposed as target materials for high-power neutron spallation sources.

ADS is the nuclear fission reactor with a subcritical core (i.e. $k_{\text{eff}} < 1$). Therefore, to operate the ADS, an external neutron source is needed for stable neutron economy in the core. One possible external neutron source is produced by a proton accelerator impinging on a spallation target (a heavy liquid metal is often considered). The protons hitting the heavy liquid metal generate neutrons which sustain the chain reaction in the subcritical core [1-8], as shown in **Figure 1-3**.

Neutron spallation targets are also being developed to provide a neutron source for

other applications. For example, the MEGAPIE spallation neutron target (a schematic view of the MEGAPIE target is shown in **Figure 1-4**), which has been successfully tested at the SINQ facility of the Paul Scherrer Institute in Switzerland, has been designed and constructed in the framework of ADS development. The objective was to demonstrate the operability of such a liquid metal target while providing a neutron source for the typical applications at SINQ. Material investigation with neutrons has been achieved with a high degree of success.

At the Korea Atomic Energy Research Institute (KAERI) and Seoul National University (SNU) in Korea, both ADS and LBE-cooled fast reactors (LFR) systems have been considered to explore proliferation-resistant and safe transmutation technology. KAERI's ADS, the Hybrid Power Extraction Reactor (HYPER) was designed to transmute TRU and some fission products such as 129I and 99Tc. HYPER uses Pb-Bi as both the coolant and target material. At SNU, a Pb-Bi-cooled transmutation reactor, the Proliferation-Resistant, Environment-Friendly, Accident-Tolerant, Continual and Economical Reactor (PEACER) was studied.

In Japan, both ADS and LFR systems using LBE were studied. At the Japan Atomic Energy Agency (JAEA), an ADS with the thermal power of 800 MW was designed, where 250 kg of minor actinides and some long-lived fission products (LLFP) can be transmuted annually. R&D has been conducted on ADS using LBE as a spallation target and a coolant, and research using J-PARC was planned as well. At present, Japan is revising its overall R&D program. The LFR systems using LBE as a coolant have been studied both at Tokyo Institute of Technology (TIT) and the Japan Nuclear Cycle Development Institute (JNC) separately. One of the LFR systems studied at TIT is designated as the Pb-Bi-cooled direct contact water fast reactor (PBWFR).

1.2 Conventional research activities of Lead-Bismuth Eutectic (LBE)

1.2.1 *Corrosion characteristics*

Generally, the LBE or lead have disadvantage of chemical reaction with dissolved contamination elements such as oxygen and iron, which leads to strong corrosion characteristics to the structural material, as well as the adequate advantages for ADS. Hence the control of the oxygen concentration in the LBE/lead and the development of appropriate structural materials which have possibility to perform efficient corrosion protection by itself are also one of the critical issues to realize the ADS [1-15]. Then investigations for development of measurement technics for the oxygen concentration and of appropriate structural material for the ADS are in progress. In present proposal of ADS design, T91 steel or AISI316L are promising candidates as the structural materials for the ADS so far. Such structural materials themselves normally could

endure the serious corrosion attack from the LBE/lead due to formation of adamant oxide layer on the surface of the materials. From this point of view, Martinelli et al. [1-16] proposed oxidation mechanism of structural material (T91) and modeled corrosion mechanism of such material as a first step in order to build a global corrosion model allowing making long term corrosion predictions.

1.2.2 *Oxygen concentration*

The development of heavy liquid metal chemistry control and monitoring is one of the issues that is critical for nuclear systems using LBE/lead either as a spallation target or as a coolant from the contamination control point of view as well as from the corrosion point of view.

Corrosion rates at temperatures below 450°C are rather low and satisfactory operation in this temperature range can be achieved using many materials, including stainless steels and alloy steels. However, low temperature operation comes at a sacrifice of thermal efficiency, which will have a direct effect on the economics of plant operation for any power producing system. Thus, for applications where economic power generation is the goal, reduced temperature operation is not an acceptable solution. This is especially true for fast reactor systems where capital cost is generally considered higher than that for current light water reactor systems. In the case of ADS and other non-critical systems, however, operation at a temperature for which corrosion becomes acceptable is an option. Low temperature operation does not, however, eliminate the production of spallation and activation products or other contaminants, such as the oxygen or the corrosion products. The design of a solid electrolyte type oxygen sensor was improved to provide better response in a high temperature lead-bismuth coolant system by JAEA. The excellent performance of the sensor with shorter stabilization time is achieved by reducing the gas volume in the reference compartment of the oxygen sensor.

1.2.3 *Thermal hydraulics*

In the present design of the ADS, the primary heat exchanger, SG, is going to be installed in main reactor pool so that the SG can touch directly to the primary coolant; lead or LBE. In addition, the coolant in the SG is basically chosen to be water. Then in the piping rupture accident of SG (PRASG), high pressurized water can be injected into primary lead or LBE coolant due to the pressure difference between such heavy liquid metals (~ 6 bar, 480℃) and water (~ 147 bar, 335℃) [1-17]. Once the high pressurized water can touch with the low pressurized primary hot liquid metals, it could be vaporized immediately. Then liquid metal-steam two-phase flow could be formed in the reactor pool. That might become a threat to the reactor safety.

According to Wang et al. [1-17] and Pesetti et al. [1-18], there are three possible

phenomena which might lead to bad situation for the reactors and should be concerned when the PRASG happens. The first one is the steam transmission in the reactor pool. The steam bubbles may be dragged into the reactor core and could affect to the reactivity of the core. The second one is the propagation of the pressure waves and cover gas pressurization, which could compromise the structural integrity of surrounding components. The third one is sloshing of primary lead or LBE coolant with mechanical impact of them on structures, which could be caused by vaporization of the water. Therefore, studies in relation to the PRASG have been considerably important for liquid metal cooled reactors' safety and have been previously conducted by many researchers internationally, who have been trying to make experimental and/or numerical approach to the problems.

Regarding the experimental studies on the PRASG, following researches were conducted. Nakamura et al. [1-19] observed molten LBE drop injected into U-shaped stainless steel vessel containing water, which the apparatus was developed by JAEA, by using high-frame-rate neutron radiography and Particle Image Velocimetry (PIV) technique in order to clarify interaction behavior between the heavy liquid metal and water. Results obtained from the neutron radiography showed rapid solidification of the molten LBE drops after the completion of injection of them and sustainable boiling at the surface of the solidified LBE drops. Also fragmentation of the molten LBE in the water was observed at the beginning of the molten LBE injection. Also Sibamoto et al. [1-20] carried out high-frame-rate neutron radiography and PIV measurements to understand the behavior of interaction between the molten LBE and the water and the flow characteristics inside of the molten LBE dropped and accumulated in the water. Their work provided the information of the renewal process of porous crust being formed at the interface between the meted LBE and the water. In the framework of EUROTRANS project, an experimental program LIFUS 5 is in progress at ENEA in order to evaluate the physical effects and possible consequences related to the interaction of liquid lead alloy with water in the EFIT reactor [1-21]. The first experiment that simulate PRASG has already been performed under following conditions: liquid metal temperature 340℃ water temperature 235℃ ,water sub-cooling 50 K and water injection pressure 70 bar. In the experiment, pressure evolution due to violent vaporization caused by the interaction between the liquid metal and the water was measured and assessed.

As for the previous investigations that take numerical approach, Wang et al. [1-17] numerically investigated the evolution of steam bubble transmission in the ADS reactor pool by using SIMMER-III code. Castelliti et al. [1-22] also carried out numerical simulation with several choked flow model, which could happen in the accident condition, for estimating mass flow rate of water injected from postulated location of tube break in the SG to primary liquid metal pool. Analysis using SIMMER-III, which postulates failure of five up to 91 tubes of SG

for EFIT reactor was also conducted by FZK [1-17]. Also Gu et al. of Chinese Academy of Science (CAS) carried out same kind of simulation for PRASG in CLEAR reactor by using NTC code [1-23]. The analyses conducted by both of groups are in relation to vapor transmission in the reactor pools. From analytical results performed by FZK, it was found that no vapor is dragged into the EFIT reactor core. On the other hand, analysis executed by CAS showed different results that some of the vapors were dragged into the CLEAR reactor core by LBE. From the examples of series of previous investigation, those studies have mostly tried to clarify the characteristics of pressure evolution, fragmentation behavior, vapor transmission, physics of thermal and hydraulic interactions between liquid metal and water. In addition to that, it can be found that it depends on configuration of reactor internals whether the vapors can be dragged into reactor core by primary coolant or not.

As mentioned above, understanding such three harmful phenomena which could happen in the PRASG and have a possibility to become a threat to the reactor safety are considerable important for realizing the ADS. Then some research activities are conducted in terms of PRASG. From above examples, however, it is found that most of such research activities do not cover the research enough regarding basic characteristics of HLM gas-liquid two-phase flow.

1.2.4 *Difference of LBE gas-liquid two-phase flow in comparison with ordinary two-phase flow*

As explained above, existence of appropriate oxygen concentration in the LBE or lead coolant is required in order to form adamant oxidation film on the surface of structural materials, for instance T91 and AISI 316L, where the oxidation film can protect the structural materials from strong corrosion characteristics of the LBE. However phenomena affecting the interactions between such a molten LBE and solid substrates vary for different liquid metals: lead or LBE. Their relevance depends on the characteristics of the structural materials as well as on the operating conditions of the system. The situations that are composed of the molten LBE and the solid metallic material can exist also in the ADS system. The knowledge of the interactions between the solid metallic material, such as T91 and AISI 316L, and the molten LBE and/or lead is quite important since it can help for choosing a suitable structural material for the ADS. To determine the wetting behavior of the LBE and/or lead on those candidates of structural materials, the study of the interactions was conducted by measurements of the contact angle as a function of temperature. Giuranno et al. [1-24] performed such contact angle measurements for molten Bi, lead and LBE in the temperature range from 623 to 773 K to investigate surface properties and wetting characteristics of these metals. Then their results provided results in terms of large contact angles from 120 to 150 degrees between those molten metals and the AISI 316L covered by the adamant oxidation film: showing poor wetting to the AISI 316L in their

temperature range, as shown in **Figure 1-5** and **1-6**. Therefore, it can be said that those molten LBE and/or lead have difficulties to achieve good wetting to the structural material.

In such situation having poor wetting to the solid wall, there is a possibility to form different two-phase flow characteristics. There is a number of investigations which give such consideration associated with different flow behavior. For example, Irons and Guthrie [1-25] investigated mechanism of bubble formation in stagnant molten indium-gallium system equipping horizontal nozzle having poor wettability characteristics to the molten metal by utilizing X-ray. Their experimental results indicated that bubbles that were injected into the molten indium and gallium show tendency of compression of themselves and attachment to the injection nozzle at low gas flow rate condition. In intermediate gas flowrate condition, the gas bubbles can easily show the tendency of attachment to the upper section of injection nozzle. In higher gas flowrate condition, the attached gas bubbles to the nozzle start to move back along the nozzle. Gnyloskurenko and Nakamura [1-26] and Gnyloskurenko et al. [1-27] researched wettability effect of gas injection nozzle on bubble formation in liquid aluminum by using X-ray. They supplied the data in terms of dependence of bubble volume on contact angles between the bubbles and the gas injection nozzle installed in the systems of air-water and argon-aluminum systems. From the results, it can be concluded that the volume of gas bubbles increase with increasing the contact angles. Thus it also can be concluded that the surface having poor wetting characteristic denotes tendency of capturing the gas bubbles, gas phase, on its surface.

In such poor wettability condition between the solid surface, i.e. channel wall, and fluids, i.e. gas and liquid phase, following interesting phenomena were observed in terms of air-water system. Iguchi and Terauchi [1-28 - 1-30] observed flow patterns of air-water two-phase flow flowing in each channel having good wetting surface and poor wetting surface respectively. From their observation results, it was found that, in poor wettability condition of channel wall, bubble behaviors of the attaching to and detaching from the channel wall happen in the air-water system. In addition, small spherical or ellipsoidal and slug bubbles showed deformation of its shapes to ring shape, film shape and etc. corresponding to wall wettability conditions. These behaviors in air-water two-phase flow have never observed in good wall wettability condition. Also, Fukushi and Iguchi [1-31, 1-32], Takamasa et al. [1-33], Hazuku et al. [1-34] and Uematsu et al. [1-35] observed similar characteristics of bubbles in air-water system in the case of poor wall wettability condition.

It can be anticipated that such strange flow behavior might be observed also in the LBE or lead gas-liquid two-phase flow since there is a poor wettability condition at the interface between the LBE/lead and the structural materials for the ADS, as explained above.

In addition, the gas/liquid density ratio of the LBE two-phase flow is 10 times larger than that of the ordinary air-water two-phase flow. Hence, it can be considered that there might

be larger effect of bubble expansion on axial development of LBE two-phase flow in comparison with air-water two-phase flow. In the previous research, LBE-nitrogen two-phase flow was visualized by utilizing neutron radiography to obtain two-dimensional void distribution and liquid velocity field [1-36]. However, in case of using neutron radiography technique, development characteristics of LBE gas-liquid two-phase flow along flow direction cannot be obtained due to restriction of size of experimental apparatus. Therefore there are quite few data available in terms of such topic.

Especially, basic data regarding local flow characteristics of LBE gas-liquid two-phase flow hardly exist at present regardless of the wall wettability conditions. Hence, it should be important to measure and construct database of the LBE gas-liquid two-phase flow because the data obtained will give important knowledge as the reference for design of the ADS and for validation of severe accident analysis code for the ADS.

1.3 Purpose of this study and the organization of this thesis

As explained before, there are different flow characteristics along flow direction between LBE two-phase flow and ordinary air-water two-phase flow because of density ratio between each phase. Such characteristics have not been clarified enough so far. Therefore, purpose of this study is to make clear the development characteristics of LBE two-phase flow along flow direction, which means local void fraction, local liquid velocity. And they can be affected by interfacial drag force and wall wettability too. Therefore in this study, measurement of fundamental characteristics of the LBE gas-liquid two-phase flow in vertical pipe was conducted as a first step. In order to obtain the fundamental characteristics such as radial distribution of local void fraction, local liquid velocity profile and turbulent intensity profile etc., development of measurement techniques, the electrical conductivity probe and the electro-magnetic probe, for the LBE were conducted as a second step. After that, the fundamental characteristics in the LBE gas-liquid two-phase flow are measured. Then the obtained experimental results are analyzed with one dimensional analytical models.

This thesis is composed of 6 chapters, summaries for each chapter are denoted below.

In chapter 2, measurement techniques for the LBE two-phase flow is introduced. Measurement principle for differential pressure gauge, electrical conductivity probe and electro-magnetic probe are described. Also, signal processing for each measurement techniques will be explained. Moreover, detail explanation about experiment performed with use of LBE test loop is given. And then, experimental results measured along flow direction are described.

In chapter 3, the objective is to analyze void fraction, gas velocity and liquid velocity using one-dimensional two-fluid model in terms of flow direction. From the comparison between experimental results and numerical results, validity of the conventional model is discussed.

In chapter 4, the objective is to investigate wall wettability effect on the LBE bubble column and to analyze experimental results in terms of phase distribution and local liquid velocity profile using force balance and momentum transfer balance using existing turbulence model. To achieve these objectives, development of LBE bubble column facility is performed as a first step. After completing the development, experiments and the one-dimensional analysis are carried out. Then validity of the experimental model is discussed.

In chapter 5, the objectives are to analyze radial profiles of local liquid velocity using force balance and momentum transfer balance using existing turbulence model that takes into account single phase turbulent flow and bubble induced turbulence. Validity of the conventional model is discussed from comparison between experimental results and analyzed results.

In chapter 6, conclusions are summarized.

References for Chapter 1

[1-1] Kenebel U J, Abderrahim A H, Cinotti L, Mansani L, Delage F, Fazio C, Giot M, Giraud B, Gonzalez E, Granget G, Monti S, Mueller C A. European research programme for the transmutation of high-level nuclear waste in an accelerator-driven system: EUROTRANS. ninth International Exchange Meeting on Actinides and Fission Products Partitioning and Transmutation (IEM9), 2006, At Nimes, France. (Figure 1-1)

[1-2] Bruyn DD, Abderrahim HA, Baeten P, Leysen P. The MYRRHA ADS Project in Belgium Enters the Front End Engineering Phase. Physics Procedia. 2015 Jun; 66: 75-84.

[1-3] Liu P, Chen X, Rineiski A, Maschek W. Transient analyses of the 400MWth-class EFIT accelerator driven transmuter with the multi-physics code: SIMMER-III. Nucl. Eng. and Des. 2010 Oct; 240: 3481-3494.

[1-4] Handbook on lead-bismuth eutectic alloy and lead properties, materials compatibility, thermal-hydraulics and technologies 2015 edition. Nuclear Energy Agency Organisation for Economic Co-operation and Development. 2015, No. 7268.

[1-5] Gromov BF, Belomitcev YuS, Yefimov EI, Leonchuk MP, Martinov PN, Orlov YuI, Pankratov DV, Pashkin YuG, Toshinsky GI, Chekunov VV, Shmatko BA, Stepanov VS. Use of lead-bismuth coolant in nuclear reactors and accelerator-driven systems. Nucl. Eng. and Des. 1997 Oct; 173: 207-217.

[1-6] Abderrahim HA, Kupschus P, Malambu E, Benoit Ph, Tichelen KV, Arien B, Vermeersch F, D'hondt P, Jongen Y, Ternier S, Vandeplassche D. MYRRHA: A multipurpose accelerator driven system for research & development. Nucl. Instrum. Meth. A. 2001 May; 463: 487-494.

[1-7] Hejzlar P, Buongiorno J, MacDonald E P. and Todreas E N. Design Strategy and Constraints for Medium Power Lead-alloy cooled Actinide Burners, Nuclear Technology; 2004 Vol. 147, 3, pp. 321-343. (Figure 1-2)

[1-8] ETWG (2001), A European Roadmap for Developing Accelerator Driven Systems (ADS) for Nuclear Incineration, Italian National Agency for New Technologies (ENEA), Rome, ISBN 88-8286-008-6. (Figure1-3)

[1-9] Mukaiyama T, Takizuka T, Mizimoto M, Ikeda Y, Ogawa T, Hasegawa A, Tkada H, Takano H. Review of research and development of accelerator-driven system in Japan for transmutation of long-lived nuclides. Prog. Nucl. Energ. 2001 Mar; 38: 107-134.

[1-10] Sasa T, Oigawa H. Studies on Accelerator-Driven System in JAEA. Plasma and Fusion Research. 2014 May; 9: 4401113-1- 4401113-5.

[1-11] Coccoluto G, Gaggini P, Labanti V, Tarantino M, Ambrosini W, Forgione N, Napoli A, Orioro F. Heavy liquid metal natural circulation in a one-dimensional loop. Nucl. Eng. and Des. 2011 May; 241: 1301-1309.

[1-12] Abanades A, Pena A. Steady-state natural circulation analysis with computational fluid dynamic codes of a liquid metal-cooled accelerator driven system. Nucl. Eng. and Des. 2009 Feb; 239: 418-424.

[1-13] Suzuki T, Chen X, Rineiski A, Maschek W. Transient analyses for accelerator driven system PDS-XADS using the extended SIMMER-III Code. Nucl. Eng. and Des. 2005 Dec; 235: 2594-2611.

[1-14] FZK (2003), Proceedings. of the 4th MEGAPIE Technical Review Meeting, C. Fazio, J.U. Knebel and F. Gröschel (eds.), Paris, 18-19 March 2003, FZKA 6876, Forschungszentrum Karlsruhe, Karlsruhe

[1-15] Weisenburger A, Mansani L, Schumacher G, Muller G. Oxygen for protective oxide scale formation on pins and structural material surfaces in lead-alloy cooled reactors. Nucl. Eng. and Des. 2014 Jul; 273: 584-594.

[1-16] Martinelli L, Courouau JL, Fanny BC. Oxidation of steels in liquid lead bismuth: Oxygen control to achieve efficient corrosion protection. Nucl. Eng. and Des. 2011 May; 241: 1288-1294.

[1-17] Wang S, Flad M, Maschek W, Agostini P, Pellini D, Bandini G, Suzuki T, Morita K. Evaluation of a steam generator tube rupture accident in an accelerator driven system with lead cooling. Progress in Nuclear Energy. 2007 Dec; 50: 363-369.

[1-18] Pesetti A, Nevo AD, Forgione N. Experimental investigation and SIMMER-III code modelling of LBE-water interaction in LIFUS5/Mod2 facility. Nucl. Eng. and Des. 2015 Aug; 15: 119-126.

[1-19] Nakamura H, Sibamoto Y, Anoda Y, Kukita Y, Mishima K, Hibiki T. Visualization of simulated molten-fuel behavior in a pressure vessel lower head using high frame-rate neutron radiography. Nucl. Technol. 1999 Feb; 125: 213-224.

[1-20] Sibamoto Y, Nakamura H, Anoda Y. Neutron radiography flow visualization of liquid metal injected into an empty vessel and a vessel containing saturated water. Nucl. Technol. 2001 Jan; 133: 119-132.

[1-21] Wang G. A review of research progress in heat exchanger tube rupture accident of heavy liquid metal cooled reactors. Annals of Nuclear Energy. 2017 Nov; 109: 1-8.

[1-22] Castelliti D, Van den Eynde G, Lomonaco G. MYRRHA primary heat exchanger tube rupture: phenomenology and evolution. Proc. 17th NURETH; 2017 Sep.

[1-23] Gu Z, Wang G, Bai Y, Song Y, Zhao Z. Preliminary investigation on the primary heat exchanger lower head rupture accident of forced circulation LBE-cooled fast reactor.

Annals of Nuclear Energy. 2015 Jul; 81: 84-90.

[1-24] Giuranno D, Gnecco F, Ricci E, Novakovic R. Surface tension and wetting behaviour of molten Bi-Pb alloys. Intermetallics. 2003 Oct; 11: 1313-1317.

[1-25] Irons A G, Guthrie I L R. Bubbling behavior in molten metals. Canadian Metallurgical Quarterly. 1981; 19: 381-387.

[1-26] Gnyloskurenko V S, Nakamura T. Wettability effect on bubble formation at nozzles in liquid aluminum. Materials transactions 2003 Sep; 44: 2298-2302.

[1-27] Gnyloskurenko S, Byakova A, Nakamura T, Raychenko O. Influence of wettability on bubble formation in liquid. Journal of material science 2005; 40: 2437-2441.

[1-28] Iguchi M, Terauchi Y. Boundaries among bubbly and slug flow regimes in air-water two-phase flows in vertical pipe of poor wettability. Int. J. Multiphase Flow 2001 27 729-735.

[1-29] Iguchi M and Terauchi Y. Rising behavior of air-water two-phase flows in vertical pipe of poor wettability. ISIJ International 2000 Feb; 40: 567-571.

[1-30] Terauchi Y, Iguchi M, Kosaka H, Yokoya S, Hara S. [Wettability Effect on the Flow Pattern of Air-water Two-phase Flows in a Vertical Circular Pipe]. Tetsu-To-Hagane. 1999 Jun; 85: 7-13 [in Japanese].

[1-31] Fukushi K, Iguchi M. Wettability effect on a single bubble rising in stagnant water contained in a vertical circular pipe. ISIJ International 2006 Feb; 46: 647-651.

[1-32] Fukushi K, Iguchi M. [The effect of wettability on the flow pattern and rising gas velocity of gas-liquid teo-phase flow in vertical pipe]. Tetsu-To-Hagane. 2005 Jan; 91: 29-34 [in Japanese].

[1-33] Takamasa T, Hazuku T, Hibiki T. Experimental study of gas-liquid two-phase flow affected by wall surface wettability. Int. J. Heat Fluid Fl. 2008 Dec; 29: 1593-1602.

[1-34] Hazuku T, Tamura N, Abe K, Fukuhara Y, Takamasa T, Hibiki T. Effect of surface wettability on flow characteristics in vertical upward gas-liquid two-phase flow. Transactions of the Japan Society of Mechanical Engineers, Series (B). 2007 73; Jul: ,78-85.

[1-35] Uematsu J, Abe K, Hazuku T, Takamasa T, Hibiki T. Effect of wall wettability on flow characteristics of gas-liquid two-phase flow. Proc. 15th ICONE; 2007 Apr 22-26; ICONE15-10315.

[1-36] Kudoh H, Zhao D, Sugiyama K, Narabayashi T, Ohshima H, Kurihara A. Void fraction distributions of inert gas jets across a single cylinder with non-wetting surface in liquid sodium. J. Nucl. Sci.Technol. 2012 Nov; 49: 1175-1185.

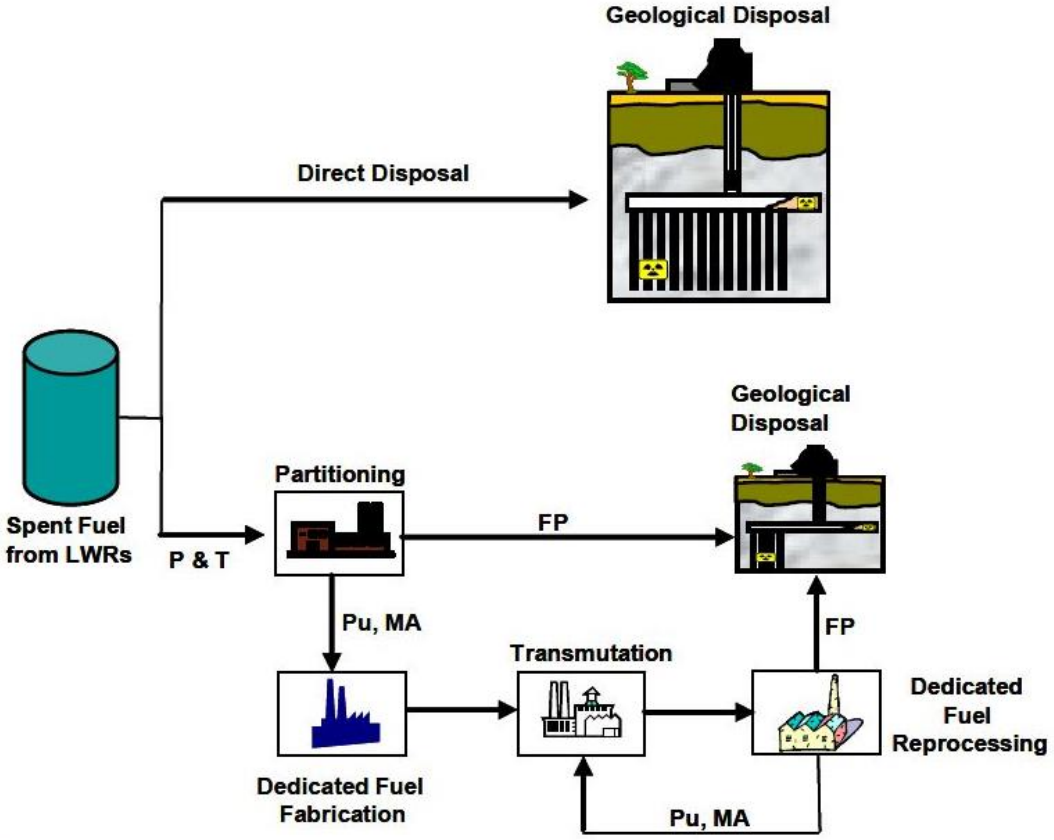

Figure 1-1 Direct disposal vs. transmutation [1-1].

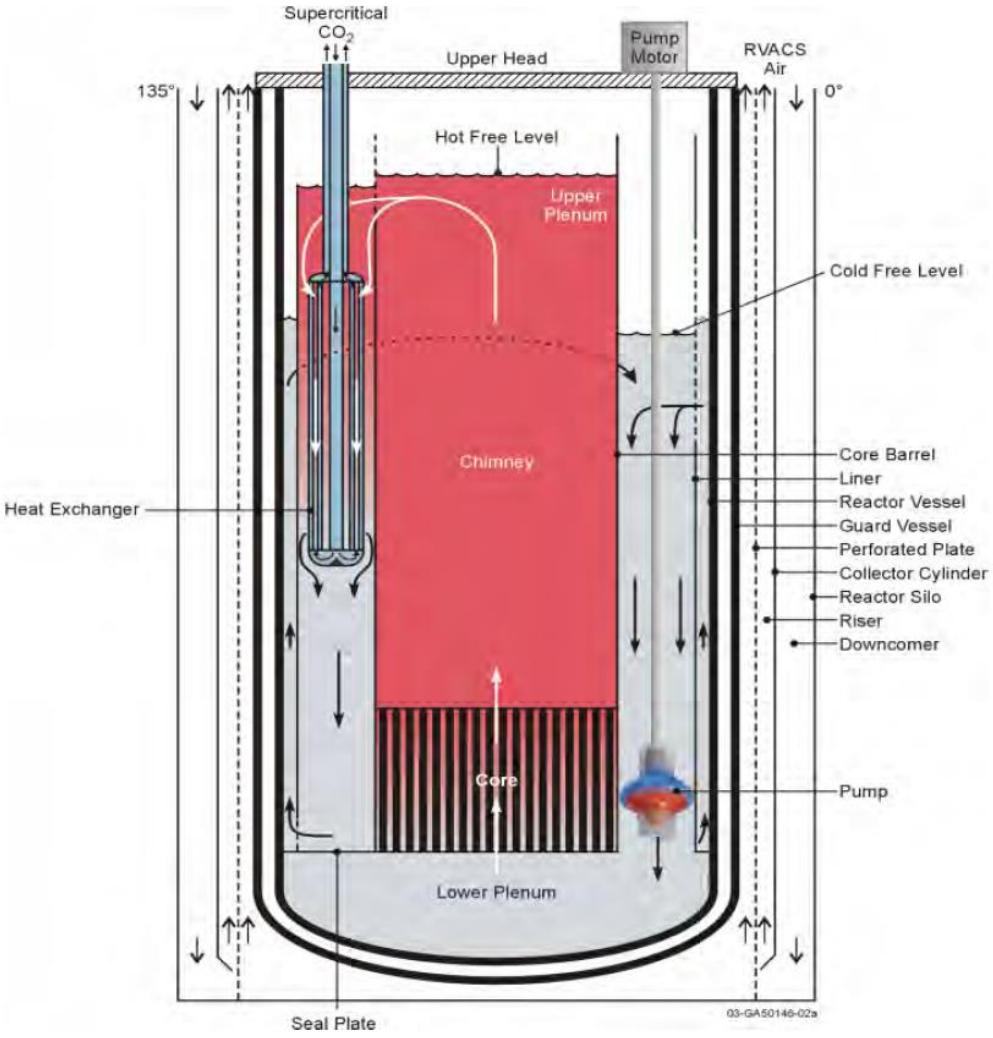

Figure 1-2 Schematic diagram of LFR [1-7].

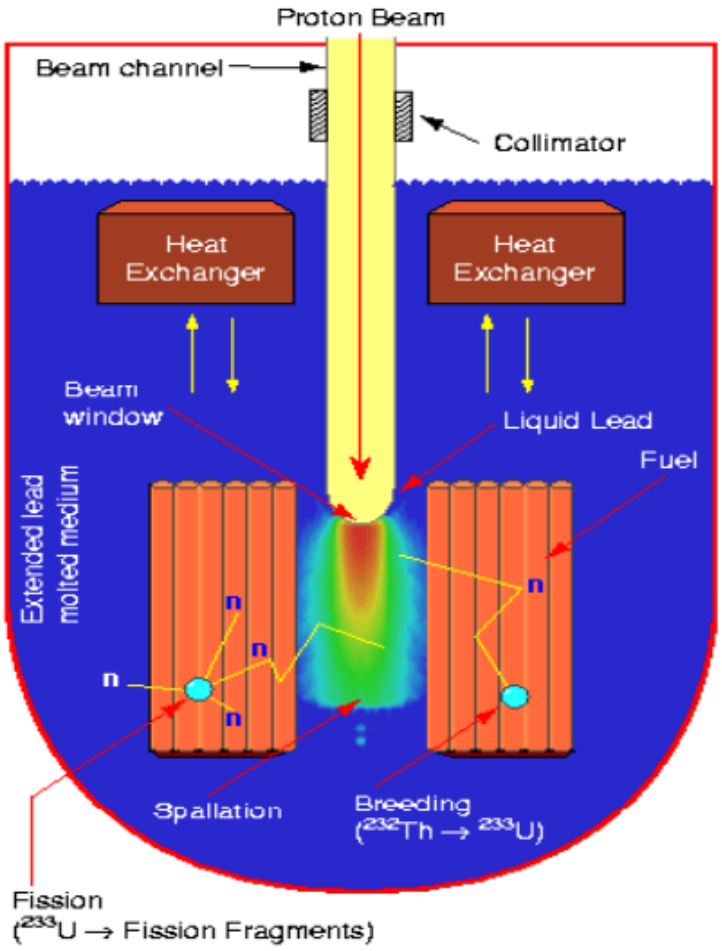

Figure 1-3 Schematic diagram of ADS [1-8].

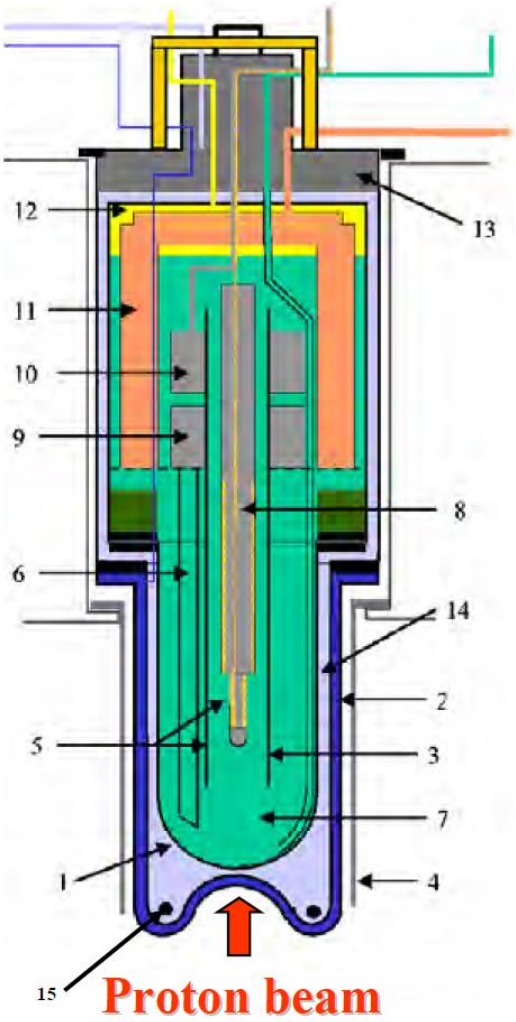

Figure 1-4 Schematic view of MEGAPIE spallation target [1-14].

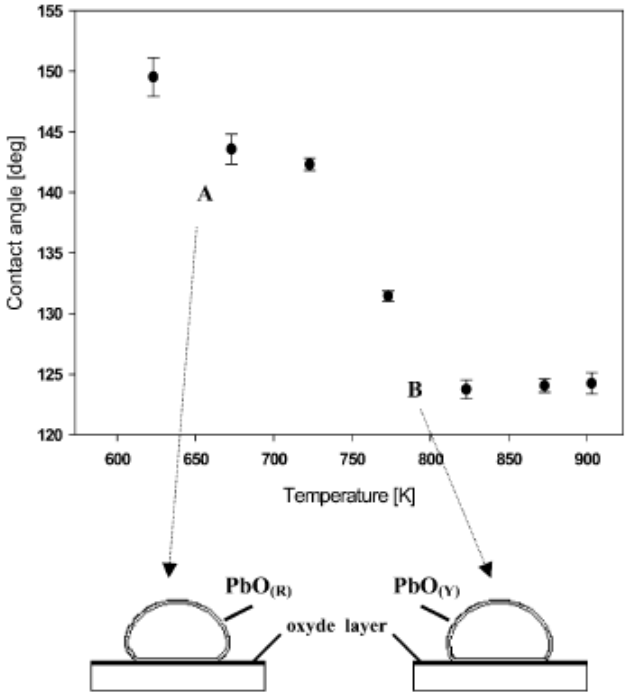

(a)

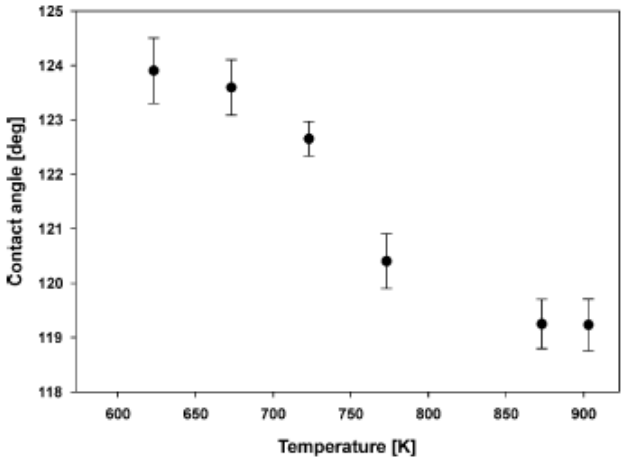

(b)

Figure 1-5 Contact angles of (a)Pb and (b)LBE on AISI 316L steel as a function of temperature measured by Giuranno et al. (2003) [1-24].

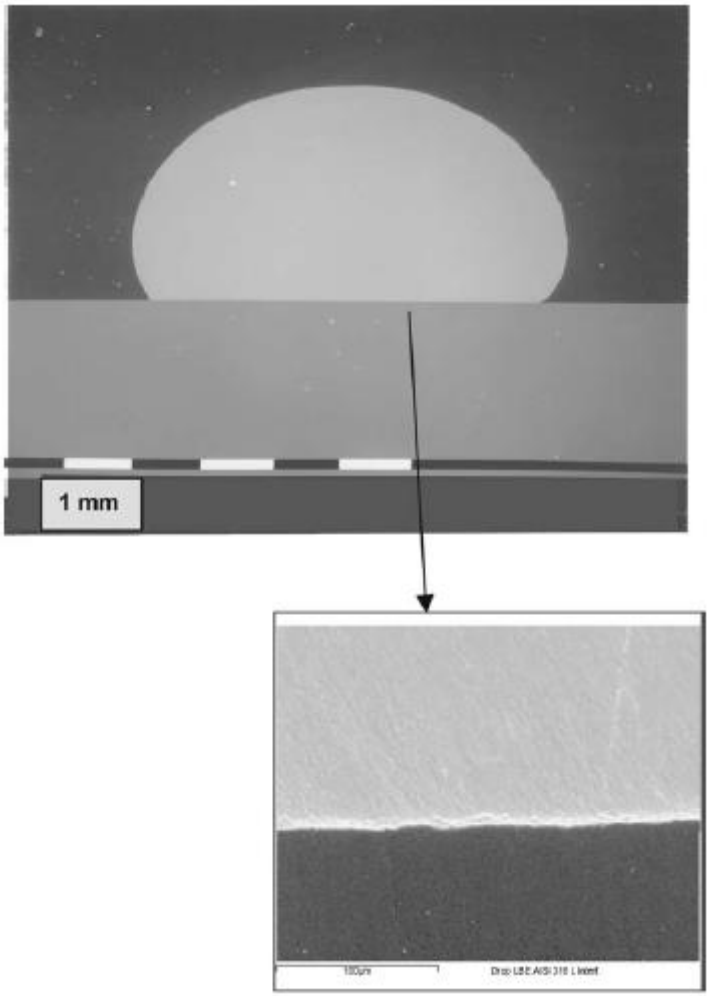

Figure 1-6 SEM Image of a cross section of the LBE drop on the AISI 316L substrate after contact angle measurements provided by Giuranno et al. (2003) [1-24].

Table1-1 Basic characteristics of reactor coolants.

Coolant	Atomic mass (g/mol)	Relative moderating power	Neutron absorption cross-section (1 MeV) (mbarn)	Neutron scattering cross-sections (barn)	Melting point (°C)	Boiling point (°C)	Chemical reactivity (with air and water)
Pb	207	1	6.001	6.4	327	1 737	Inert
LBE	208	0.82	1.492	6.9	125	1 670	Inert
Na	23	1.80	0.230	3.2	98	883	Highly reactive
H_2O	18	421	0.1056	3.5	0	100	Inert
D_2O	20	49	0.0002115	2.6	0	100	Inert
He	2	0.27	0.007953	3.7	–	-269	Inert

Table1-2 Some relevant properties of possible liquid metal target candidate materials.

Coolant	Composition (at %)	Density at 20°C (g/cm³)	Density liquid (g/cm³)	Linear coefficient of thermal expansion 10^{-5}/K (solid)	Linear coefficient of thermal expansion 10^{-5}/K (400°C)	Volume change upon solidification (%)	Specific heat (J/gK)	Thermal neutron absorption (barn)
Pb	Elem.	11.35	10.7	2.91	4	3.32	0.14	0.17
Bi	Elem.	9.75	10.07	1.75	–	-3.35	0.15	0.004
Pb-Mg eutectic	Pb 97.5% Mg 2.5%		10.6	–	–	0	0.15	0.17
Pb-Bi eutectic	Pb 45% Bi 55%	10.5	10.5			0	0.15	0.11
Hg	Elem.		13.55		6.1		0.12	389

Table 1-3 Characteristics of LFRs.

Countries	Russia	Russia	Italy (EURATOM)
Reactor name	BREST-OD-300	SVBR-100	ALFRED
Reactor type	LFR	LFR	LFR
Coolant	Molten lead	Moten LBE	Molten lead
Reactor inner pressure	-	-	< 0.1[MPa]
Operation temperature	540 [℃]	490 [℃]	480 [℃] (at Outlet)
Thermal power	700 [MWt]	280 [MWt]	300 [MWt]
Electrical output	300 [MWe]	101 [MWe]	125 [MWe]
Design life	30 [years]	60 [years]	40 [years]
Fuel	PuN-UN	UO_2	UO_2-PuO_2
Concentration degree of fuel	~ 13.5 [%]	16.5 [%]	less than 30 [%]
Operation cycle	1 [year]	7-8 [years]	1 [year]
Total neutron flux in first 6experimental positions	-	-	-
Fast neutron flux in first 6experimental positions	-	-	-
Current situation of design	Detailed design	Design will be completed in 2014	Conceptual design stage
Features	Demonstration reactor of LFR having higher inhert safety	Closed cycle of nuclear fuel	Miniture demonstration reactor for ELFR

Countries	Italy (EURATOM)	USA
Reactor name	ELFR	G4M
Reactor type	LFR	LFR
Coolant	Molten lead	Moten LBE
Reactor inner pressure	< 0.1[MPa]	-
Operation temperature	480 [℃] (at Outlet)	500 [℃]
Thermal power	1500 [MWt]	70 [MWt]
Electrical output	600 [MWe]	25 [MWe]
Design life	60 [years]	5 - 15 [years] (nominal 10 years)
Fuel	UO_2-PuO_2	Uranium nitride
Concentration degree of fuel	-	19.75 [%]
Operation cycle	30 [months]	10 [years]
Total neutron flux in first 6experimental positions	-	-
Fast neutron flux in first 6experimental positions	-	-
Current situation of design	Conceptual design stage	Conceptual design stage
Features	First prototype reactor	-

Table 1-4 Characteristics of ADSs.

Countries	Belgium	Japan	Europe (EURATOM/EUROTRANS)
Reactor name	MYRRHA	JAEA-ADS	EFIT
Reactor type	ADS/LFR	ADS	ADS
Coolant	Molten LBE	Moten LBE	Molten lead
Reactor inner pressure	Atmospheric pressure	Atmospheric pressure	Atmospheric pressure
Operation temperature	270 - 350 [℃]	300(inlet) - 407(outlet) [℃]	400(inlet) - 480(outlet) [℃]
Thermal power	50 - 110 [MWt]	800 [MWt]	384 [MWt]
Electrical output	0 [MWe]	270 [MWe]	154 [MWe]
Design life	-	60 [years]	-
Fuel	MOX	MA+Pu+ZrN	CERCER/CERMET
Fuel composition	Maximum enrichment 35 [%]	60 [%](MA), 40 [%](Pu)	MA/Pu=1.2
Operation cycle	-	600 [days]	1 [year]
Total neutron flux in first 6experimental positions	∼2-3 × 10^15 n/(cm^2*s)	-	-
Fast neutron flux in first 6experimental positions	∼4 × 10^14 n/(cm^2*s) for E > 0.75 [MeV]	-	-
Current situation of design	Detailed design stage	Conceptual design stage and elemental technology development stage	Conceptual design stage and elemental technology development stage
Features	Sub-critical and critical research reactor	-	-

Countries	China	China
Reactor name	CADS-DEMO	CLEAR I
Reactor type	ADS	ADS
Coolant	Molten LBE	Moten LBE
Reactor inner pressure	Atmospheric pressure	0.05 [Mpa]
Operation temperature	-	390 [℃]
Thermal power	800 [MWt]	10 [MWt]
Electrical output	-	-
Design life	-	30 [years] (nominal 10 years)
Fuel	-	UO_2
Fuel composition	-	19.75 [%]
Operation cycle	-	10 [years]
Total neutron flux in first 6experimental positions	-	-
Fast neutron flux in first 6experimental positions	-	-
Current situation of design	Conceptual design stage	Preliminary and fundamental design stage
Features	-	Research reactor

Table 1-5 Thermal hydraulics facilities.

Thermal hydraulics facilities							
Association/Country	Name of facility	Type of facility	Objectives	OCS - O_2 probe	T_{max}	Flow rate	Other information
FZK/Germany	THEADES	Loop	Single effect, beam window, window less, fuel elements, heat transfer	H_2/H_2O - yes	450 ℃	100 m^3/h	Hight of the test sections 3.4 m
ENEA/Italy	CIRCE	Pool	Thermal-hydraulics, component development, large-scale exp. And liquid metal chemistry in pool config.	OCS yes - no O_2 probe	450 ℃		8540 *l* of LBE
ENEA/Italy	CHEOPE I	Loop	Thermal-hydraulics, cooling pin	-	500 ℃	-	900 *l* of LBE
ENEA/Italy	HELENA	Loop	Thermal-hydraulics investigations and qualification of components and instrumentation.	-	500 ℃	35 kg/s at 3.5 bar	
ENEA/Italy	LIFUS 5	Static	Interaction HLM with water and simulate LOCA.	No	500 ℃	-	Facility relevant for safety-related experiments.
SCK-CEN/Belgium	COMPLOT	Loop	Investigations on hydraulics and hydrodynamics of MYRRHA components at full-scale: fuel assembly, spallation target, control rod and safety rod.	H_2/H_2O - yes	450 ℃	1.24-36 m^3/h	
SCK-CEN/Belgium	E-SCAPE	Loop/Pool	Investigations on liquid-metal pool thermal hydraulics.	No	350 ℃	0.8-40 m^3/h	Tests on integral system behaviour: flow distribution, decay heat removal. Tests on separate thermal-hydraulic phenomena: mixing and stratification, free surface oscillation.
KIT/Sweden	TALL	Loop	Thermal-hydraulics and heat transfer measurements	No OCS - yes sensor	550 ℃	2.5 m^3/h	Hight of the test section 6.8 m
LANL/USA	DELTA	Loop	Corrosion tests in flowing LBE, corrosion/precipitation and system kinetics models, oxygen sensors and control systems, thermal-hydraulics experiments, components testing, data acquisition and control systems.	Yes	550 ℃	2-5 m/s	
UW/USA	Wisconsin Tantalus facility	Loop	Multi-phase flow, heat transfer and flow stability/oscillations of steam/water injection into Pb/LBE.	-	550 ℃	1-10 g/sec	
JAEA/Japan	JLBL-2	Loop	Flow studies in horizontal LBE terget	No	< 450 ℃	50 *l* /min	Proof test of target - I
JAEA/Japan	JLBL-3	Loop	Thermal fluid test loop	Yes	450 ℃	500 *l* /min	Collaboration with MES
CRIEPI/Japan	Pb-Bi thermal hydraulics	Loop	Heat transfer characteristics of Pb-Bi, gas lift pump performance in Pb-Bi/gas two-phase flow	No	300 ℃	6 m^3/h	
TIT/Japan	LBE-H_2O Direct Contact	Appar.	Operation technique of steam gas lift pump type LBE-cooled fast reactor, thermal-hydraulics of LBE-water direct contact boiling flow.		460 ℃	33.8 kg/h	
KAERI/Korea	KPAL-1	Loop	OCS, corrosion, thermal hydraulics.	Yes OCS Yes sensor	550 ℃	3.6 m^3/h	
SNU/Korea	HELIOS	Loop	OCS, materials and thermal-hydraulics (natural circulation capabilities in PEACER-300).	Yes OCS	450 ℃	200 cm/s	HELIOS was designed by thermo-hydraulics scaling of PEACER-300.

Table 1-6 Material testing facilities.

Material testing facilities							
Association/Country	Name of facility	Type of facility	Objectives	OCS - O_2 probe	T_{max}	Flow rate	Other information
KIT/Germany	COSTA	Static	Corrosion mechanism investigation in controlled conditions.	H_2/H_2O – in the gas phase	1000 ℃	-	200 specimens at 5 different T and 10 different O_2 activities in one run.
KIT/Germany	CORRIDA	Loop	Corrosionrate in controlled atmosphere	H_2/H_2O – yes	550 ℃	2 - 4 m/s	Modelling of corrosion precipitation behaviour.
KIT/Germany	TELEMAT	Loop	High temperature corrsion in Pb.	H_2/H_2O – yes	700 ℃	2 m/s	Modelling of corrosion precipitation at high temperature.
ENEA/Italy	LECOR	Loop	Corrosion at low oxygen content, physicochemistry, component testing.	H_2/O_2 – yes	500 ℃	4.5 m^3/h	Three test sections
SCK-CEN/Belgium	CRAFT	Loop	Corrosion rate in controlled atmosphere.	Ar/H_2 yes	550 ℃	2 -5 m/s	Investigations on the mechanisms and the kinetics of material/LBE interactions, modelling of corrosion/precipitation behaviour in LBE, investigations on the applicability of gas-liquid based OCS in large LBE loops, long-term testing of oxygen sensors in LBE as part of the OCS.
JAEA/Japan	JLBS	Static	Compatibility of materials	OCS partially	600 ℃	-	
JAEA/Japan	JLBL-1	Loop	Corrosion studies and development of flow measurement techniques.	H_2/H_2O	450 ℃	18 *l* /min	Two test sections
TIT/Japan	LBE Corrosion	Loop	Material corrosion in flowing LBE, oxygen control technique, oxygen sensor, electromagnetic flow meter, ultrasonic flow meter.	PbO Yes sensor	550 ℃	0.36 m^3/h	

Table 1-7 Oxygen concentration and oxygen sensor testing facilities.

Oxygen concentration and oygen sensor testing facilities							
Association/Country	Name of facility	Type of facility	Objectives	OCS - O_2 probe	T_{max}	Flow rate	Other information
KIT/Germany	KOCOS	Loop	OCS development	H_2/H_2O - yes	550℃	-	Diffusion coefficient measurement of oxygen in LBE.
CEA/France	SOLDIF	Static	Solubilities, diffusivities, oxide layer characterisation.	? - yes	500℃	-	-
SCK-CEN/Belgium	MEXICO	Loop	Investigations on the applicability of solid (PbO) OCS in large LBE loops, long-term testing of oxygen sensors in LBE as part of the OCS, oxygen mass transfer modelling and monitoring, particle filter testing, cold trap testing.	PbO - yes	500℃	1.8 *l*/s	-
SCK-CEN/Belgium	HELIOS-3	Static	Investigations on the optimisation of LBE oxygen reduction, investigations on the feasibility of gas recycling, investigations on calamity recovery, component testing.	H_2/H_2O - yes	450℃	-	-
SCK-CEN/Belgium	Liliputter	Loop	Investigations on filtration, investigations on mass transfer of impurities, component testing.	No - yes	450℃	0.5 *l*/s	-

Chapter 2
Experimental methods and measurement techniques for LBE two-phase flow

2.1 Introduction

LBE is not transparent to visible light. So, measurement techniques which do not utilize the visible light must be effective to obtain two-phase flow characteristics and turbulent characteristics of LBE two-phase flow. Saito et al. performed simultaneous measurement using high-frame-rate neutron radiography and electrical conductivity probe (EC probe) to get local void fraction profile in LBE-nitrogen two-phase flow [1]. Then, they could obtain good agreement of measured void fraction profile between the high-frame-rate neutron radiography and EC probe methods. Therefore, in this study, EC probe was used to get local void fraction and bubble frequency of LBE two-phase flow. In respect to local liquid velocity and turbulent intensity, they can be measured by using electro-magnetic probe which can work on the basis of Faraday's law. In this chapter, detailed explanations of these measurement techniques are given.

To get two-phase flow characteristics such as local void fraction and bubble frequency and turbulent characteristics; local liquid velocity and turbulent intensity, in LBE two-phase flow, LBE test loop named as Heavy Liquid Metal Single and Two-phase flow Instrumentation for Accelerator-driven system (HESTIA) was utilized. In this chapter, details of experimental apparatus and methods are described too. Then experimental results are discussed.

2.2 Experimental apparatus

In the experiments, the LBE test loop named as HEavy liquid metal Single and Two-phase flow Instrumentation for Accelerator-driven system (HESTIA) was utilized for measurement of local flow structure in the LBE two-phase flow, where the HESTIA is installed in the heat transport laboratory at Institute for Integrated Radiation and Nuclear Science, Kyoto University. The schematic diagram of HESTIA is illustrated in **Figure 2-1**. HESTIA is composed of three parts; main loop, cold trap and nitrogen closed loop. Main loop of HESTIA consists of a test section, a gas-liquid separator, a down-comer, an Electro-Magnetic pump (EM pump) (LSP-20H-6R3, Sukegawa Electric. Co. Ltd.), a drain tank, a calibration tank and a gas injection system. In addition to main loop, HESTIA equips two other loops, which means cold trap and nitrogen closed loop.

Following section, detailed explanations are provided in terms of each part of HESTIA.

Main loop of HESTIA

Test section and gas-injection system

The test section was a vertical round stainless steel (Type 304) pipe and it has an inner diameter of 50 mm and a length of 2,000 mm. The stainless steel pipe is commercially available without any special surface treatment, which has a passivation film on its surface, showing poor wettability to the LBE. The test section has three measurement locations along the axial direction (z/D=3.2, 17.6 and 32.4) as shown in **Figure 2-2**. The test section also has four holes along the axial direction (z/D=1.16, 12.3, 23.5 and 34.7) in order to measure differential pressure between each sections that are formed by each holes. The gas injection system is installed at bottom of the test section and composed of mixing chamber having larger inner diameter of 155.2 mm and smaller inner diameter of 106.3 mm, as shown in **Figure 2-3**, and gas injection nozzles. The gas injector equipping 101 gas injection nozzles is used for experiments carried out in the higher superficial gas velocity region. The gas injector having 9 nozzles is also utilized for experiments conducted in the lower superficial gas velocity region. The outer and inner diameters of the nozzle are 0.95 mm and 0.75 mm, respectively. Photographs of the gas injectors are shown in **Figure 2-4**. The gas flow rate is controlled by a mass flow controller. Three intrusive probes are installed in the test section to investigate the axial development of flow structure in the LBE single-phase and two-phase flow as shown in **Figure 2-1**. In addition these probes are traversed in the radial direction by using one-dimensional traversing stages so that a portion of the length 50 mm from the tip of the probes can be inserted, as expressed in **Figure 2-5**. The working fluids in the test loop were kept at a constant temperature of 200 °C and the heating power was controlled by temperature controller units. The flow rate, differential pressure, temperature and liquid level were monitored by a data acquisition unit connected to a PC.

Gas-liquid separator and down-comer

The gas liquid separator is made by stainless steel circular pipe too, which has 155.2 mm of inner diameter and connected to both the test section and the down-comer. The LBE-nitrogen two-phase flow flowing in the test section is separated into gas and liquid phases respectively after reaching to the gas-liquid separator. The nitrogen gas is exhausted to intake pipe of nitrogen closed loop, which explanation of the nitrogen closed loop will be provided later section, then only the LBE can flow back to the test section via down-comer.

There might be quite small particles of LBE oxide on the free surface of the LBE and they have opportunities to enter the exhaust pipe for the nitrogen gas due to exhausted nitrogen.

Thus, as denoted in **Figure 2-6**, mesh filter was installed in order to prevent plugging of nitrogen exhaust pipe due to the accumulation of small particle of LBE oxide.

In addition to the mesh filter, larger mesh filter was installed in the down-comer to remove the LBE oxide from the molten LBE, where picture of the larger mesh-filter is denoted in **Figure 2-7**. At the bottom of the filter, it has a stainless steel demister which has efficiency from 99% to 100% to remove particles having more than 3 μm of diameter at the condition of flowrate from 1 to 6 m/s.

Electro-magnetic pump

To make forced convection flow of the LBE, EM pump (LSP-20H-6R3) manufactured by Sukegawa Electric. Co. Ltd. was utilized. Rated flow rate of the EM pump is 20 *l*/min and maximum temperature and pressure that the EM pump can work are 300℃ and 0.5 MPa.

Electro-magnetic flow meter, vortex flow meter and calibration tank

In the measurement of LBE two-phase flow, the flow rate of the LBE was measured by an electro-magnetic flow meter (EM flow meter). Calibration of the EM flow meter was carried out prior to each experiment by using a calibration tank for the flow meter. The calibration tank is a stainless steel cylindrical vessel equipped with 10 liquid level sensors. However, the EM flow meter was unstable in the long term operation caused by the temperature drift and the electrical conductance change between the LBE and the electrodes. Therefore, a vortex flow meter (PROWIRL F, Endress+Hauser Co. Ltd.) was utilized for this experiment. The vortex flow meter would be scarcely affected by the wettability to the working fluid. Calibration of the vortex flow meter was also carried out by the same procedure for the EM flow meter. The calibration results are shown in **Figure 2-8**. The results show good linearity and indicate that the calibration error was less than ±13%.

Drain tank

Drain tank is the tank to store the LBE, which equips 10 liquid level sensors. To prevent oxidation reaction of the LBE and to pressurize the drain tank for introducing the LBE into the test section, argon-hydrogen gas is injected, as shown in **Figure 2-9**.

Sub loop 1 of HESTIA

Cold trap

To remove LBE oxide, cold trap was installed to lower plenum between outlet of down-comer and inlet of EM pump, as shown in **Figure 2-10**. Near the inlet of the cold trap, it has heat exchanger using water to cool down the temperature of LBE and to precipitate LBE oxide in the

flowing LBE. The precipitated LBE oxide was removed by stainless steel mesh filter installed in the cold trap. Operation temperature of cold trap was kept at 150 °C by using temperature controller units. In the cold trap operation mode, temperature difference of LBE flowing in main loop and cold trap is kept about 40 °C.

Sub loop 2 of HESTIA

Nitrogen closed loop

To improve purity of nitrogen gas, nitrogen closed loop was constructed as shown in **Figure 2-11**. The nitrogen closed loop is composed of test section of HESTIA, intake pipe, filter made by molecular sieve, pressurizing compressor, vacuum pump, pressure vessel for nitrogen gas, gas suppling pipe connected to nitrogen gas injector and gas suppling pipe for controlling system pressure in HESTIA, which is connected to gas-liquid separator. Nitrogen gas injected into test section is sucked by pressurizing compressor via intake pipe after separating gas and liquid phase in the gas-liquid separator of HESTIA. Sucked nitrogen gas flows into molecular sieve filter. At the same time, water included in nitrogen gas is removed by molecular sieve. Then oxygen concentration in the nitrogen gas is decreased. After pass through the filter, the nitrogen gas is accumulated into pressure vessel by pressurizing compressor. Then the accumulated nitrogen gas is supplied again to test section, where flowrate of the nitrogen gas is controlled by mass flow controller. In case of happening of flow rate difference between nitrogen gas supplied again to the test section and nitrogen gas sucked by the pressurizing compressor, there is change of system pressure due to such flow rate difference. So, the accumulated nitrogen gas is also supplied to gas liquid separator of HESTIA to control the flowrate balance and system pressure in HESTIA. The flow rate and the system pressure is controlled by pressure reducing valve. Vacuum pump is used to exhaust air from the pressure vessel and HESTIA before accumulating nitrogen gas into the pressure vessel and the HESTIA.

2.3 Measurement techniques for LBE two-phase flow

2.3.1 *Electrical Conductivity probe (EC probe)*

Visible light cannot penetrate through the liquid metal. This nature is one of the technical difficulties to measure liquid metal flows. So, measurement technique using the visible light cannot be applied to measurement of the liquid metal flows.

In order to obtain two-phase flow characteristics such as local void fraction, bubble frequency and interfacial area concentration etc. EC probe is applied in previous study. EC probe can detect difference of electrical conductivity between gas and liquid phase. As mentioned above, good agreement of local void fraction profile in LBE two-phase flow simultaneously measured by using high-frame-rate neutron radiography and EC probe was

shown by Saito et al. [2-1]. And also, in that study, it was shown that effect of bubble-probe interaction on measurement of local void fraction in LBE two-phase flow was not distinct in case of using EC probe that equips acupuncture needle sensors. Local void fraction and bubble frequency can be measured by EC probe that equips only one acupuncture needle sensor, i.e. single sensor probe. Hence, in this study, single sensor probe was used to obtain local void fraction and bubble frequency.

Schematic information of a single-sensor probe is shown in **Figure 2-1**. The probe mainly consists of an acupuncture needle sensor, an Al_2O_3 insulating tube, a Teflon coated electrode wire and a stainless steel guide tube. Stainless steel acupuncture needles with the maximum diameter of 0.12 mm are coated with epoxy resin varnish in order to make insulating film except their tip whose diameter is less than 1 μm. The insulated needle was inserted into a 7-bored insulating tube made of Al_2O_3 [2-1, 2-2] and this needle is connected to Teflon coated electrode wires. Then the sensor head is inserted into stainless steel pipe and is fixed at inlet of the pipe by using epoxy resin glue.

Measurement system is shown in **Figure 2-2**. Since, the only tip of the needle can be exposed to the LBE two-phase flow, the needle tip and stainless steel cover pipe can work as point electrode and ground electrode, respectively. Here, voltage between signal line and ground, V_2, can be calculated as following equation when resistance between the point electrode and ground is assumed as $R_{EC\ probe}$. When the point electrode and ground are covered by LBE, $R_{EC\ probe}$ can be ideally considered as 0 Ω. So, V_2 equals to 0. On the other hand, V_2 equals to V_1 when gas bubble touch to and cover the point electrode because $R_{EC\ probe}$ can be considered as infinity.

$$V_2 = \frac{R_{EC\ probe}}{R_{Pull\ up} + R_{EC\ probe}} V_1 \tag{2-1}$$

$$V_2 = 0 \qquad \text{(Liquid phase)} \tag{2-2}$$

$$V_2 = V_1 \qquad \text{(Gas phase)} \tag{2-3}$$

Therefore, as shown in **Figure 2-3**, output signal becomes like a square wave. In case of using LBE as a working fluid, output signal becomes almost square wave because LBE has high electrical conductivity. The output signal is acquired by an A/D converter (ADM-688PCI, Micro Science Co. Ltd.) at a sampling frequency of 10 kHz and then processed on a PC. The detailed specifications of the A/D converter are summarized on **Table 2-1**.

2.2.2 *Obtained physical quantities from EC probe and signal processing*

The time-averaged local void fraction can be easily calculated by dividing the sum of the time fraction of gas phase by the total measurement time as indicated in Equation (2-4).

$$\alpha = \frac{1}{T_{total}} \int_0^{T_{total}} \Delta t_{bubble} \tag{2-4}$$

To estimate time fraction of gas phase, constant threshold value have to be applied to signal processing for separating gas and liquid phase signals as indicated in **Figure 2-4**. In the previous studies that conducted experiments using EC probe, 10 % to 50 % values of difference between maximum and minimum voltages were used as threshold value [??]. However, unfortunately, there are no rigid criteria to determine such threshold value. So, in this study, effect of threshold value on estimated time-averaged local void fraction was evaluated. The evaluated result is shown in **Figure 2-5**. Here, percentage value shown in **Figure 2-5** means rate of changes of estimated void fraction when the threshold value is changed from 10 % to 50 % values of difference between maximum and minimum voltage. From this figure, it is found that effect of threshold value on time-averaged local void fraction is only -0.66 % change and this value is small enough. Therefore, 10 % value of difference between maximum and minimum voltage was selected as threshold value to separate gas and liquid phase and to estimate time-averaged local void fraction.

Using signal processing result of gas-liquid separating, number of bubbles can be counted. Then number of bubbles which hit to needle sensor tip during one second, bubble frequency, can be calculated using following equation.

$$f_b = \frac{N_{bubble}}{T_{total}} \tag{2-5}$$

And also, average time of a bubble passing through the needle sensor tip, average bubble residence time, can be calculated by dividing the time-averaged local void fraction by the bubble frequency, as indicated Equation (2-6).

$$t_b = \frac{\alpha}{f_b} \tag{2-6}$$

2.3.3 *Electro-Magnetic probe (EM probe)*

As for measurement technique to obtain local liquid velocity without visible light, Ultrasonic Velocity Profiling (UVP) technique, hot-wire anemometer and Electro-Magnetic probe (EM probe) were utilized as existing measurement technique in previous studies. However, UVP cannot be applied to two-phase flow in condition of void fraction larger than 2~3% because of scattering of ultrasonic due to bubbles. In respect to hot-wire anemometer, it would be difficult to measure the velocity near 0 m/s and inversed flow. On the other hand, in previous research, EM probe had been reported as appropriate technique for velocity measurement in liquid metal. EM probe can measure the velocity near 0 m/s and inversed flow. Furthermore, EM probe can be applied to two-phase flow in condition of void fraction larger than 2~3%. Therefore, in this study, EM probe was selected to obtain liquid velocity of LBE flow.

The local liquid velocity fluctuations in the LBE two-phase flow was measured by using an EM probe. The measurement principle of the EM probe is based on Faraday's law. When a conductive fluid passes across the magnetic field, electrical voltage is induced in a direction normal to the magnetic field and the fluid motion. The local liquid velocity fluctuations can be estimated from the induced voltage. Ricou and Vives (1982) [2-4] measured liquid velocity in several molten metals such as mercury, lead, aluminum alloy, and so on. Also Von Weissenfluh (1984) [2-5] measured liquid velocity in liquid sodium.

The schematic of the EM probe used in this study is shown in **Figure 2-6**. It consists of a permanent magnet, two Teflon coated electrode wires and a stainless steel jacket [2-6]. The cylindrical-shaped magnet is 2 mm in diameter and 9 mm in length. The stainless steel jacket is a circular pipe with 3.18 mm in outer diameter and 270 mm in length. The diameter of the electrode wire is 0.127 mm. To apply the EM probe to high temperature conditions, a samarium-cobalt (SmCo) magnet was selected, which has a high Curie point of 800 °C. The physical properties of the magnet are listed in **Table 2-2**. On bottom surface of the SmCo magnet, a conical stud is putted to minimize influence of intrusive probe into LBE two-phase flow.

The measurement system consists of the EM probe, a low-noise pre-amplifier (CA-461F2, NF Co.Ltd.), a DC amplifier (AM30AZ, Unipulse Co. Ltd.), A/D converters and a PC, as shown in **Figure 2-7**. The output signal is amplified by the low-noise pre-amplifier and the DC amplifier, and then digitized by an A/D converter (ADM-688PCI, Micro Science Co. Ltd.) at a sampling frequency of 10 kHz.

2.3.4 *Calibration techniques for EM probe*

Calibration of the EM probe was carried out by using a rotating test apparatus as shown in **Figure 2-8 (a)**. The apparatus consists of a rotating container, a rotating system, an

electrical heater and measurement system. The diameter of the container is 300 mm. A small pipe which has the diameter of 102 mm is installed at the central part of the container to reduce the volume of LBE.

The container was filled with LBE and rotated at a constant rotating speed. The EM probe was installed in the rotating test apparatus so that the tip location of the EM probe was 130 mm away from the center of the container and 2 mm above from its bottom. The tip location was determined by taking into account the scale of the Ekman layer formed on the bottom of the rotating container, i.e. there are no serious differences of rotating speeds between the container and the LBE. Therefore, circumferential velocity of the LBE can be estimated by assuming a rigid body rotation of the LBE in the container. An example of the calibration results is shown in **Figure 2-8 (b)**. The result indicates that measured induced voltages are proportional to the circumferential velocity of the rotating LBE. However, the induced voltages are of the order of 10^{-6} V. Therefore it would be important to suppress the electrical noise to the signal pass between the signal source and the pre-amplifier. Hence, the EM probe and the pre-amplifier were combined directly, as indicated in **Figure 2-9**. With this combination, electrical wirings can be shorter and the pre-amplifier can be covered by a copper shielding case resulting in good S/N ratio.

2.3.5 *Obtained physical quantities from EM probe and signal processing*

Typical output signal of velocity fluctuations in the LBE two-phase flow measured by the EM probe is shown in **Figure 2-19**. As shown in this figure, there exist some overshoot or undershoot points in the time series. These points indicate the instances for bubbles passing across the probe. Therefore, these points should be removed by a signal processing to get time averaged data. The scheme of present signal processing is shown in **Figures 2-20, 19 and 2-22**.

1) To extract the liquid velocity information in the signal, frequency distribution in terms of measured signal was used to decide first threshold value as shown in **Figure 2-19 (a)**. It can be found that there are large values on both sides of horizontal axis. These values indicate voltage level of gas phase signals in the time series. On the other hand, distribution located at center area of the **Figure 2-19(a)** indicate mainly liquid phase signal. To make first threshold value, dispersion σ of this frequency distribution excepting large peak on the both side of horizontal axis was calculated. And then, the value of 3σ was utilized as the first threshold value.
2) The time derivative of the first extracted signal was used for finding change points of 90% of its value. Such changing points of the time derivative for the first extracted signal were chosen as second threshold values to adjust the precise interval between gas and liquid

phases (**Figure 2-15(b)**).

3) After the second step, signal corresponding to the liquid phase can be extracted from the original signal (**Figure 2-23**). Finally, the time averaged liquid velocity, turbulence intensity, void fraction, bubble frequency and bubble residence time can be obtained.

As mentioned in section 2.2.2 , there are no rigid criteria to determine such threshold value. So, in this study, superficial liquid velocities calculated by liquid velocity and void fraction profile were compared with superficial liquid velocity measured by vortex flow meter to confirm validity of signal processing. The comparison is shown in **Figure 2-26**. It is found that the superficial liquid velocity measured by EM probe show agreement with the superficial liquid velocity measured by vortex flow meter less than 10%.

2.4 Experimental results

2.4.1 *Radial distribution of local liquid velocity distributions*

Before showing experimental results for LBE two-phase flow, radial distributions of local liquid velocity measured in LBE single-phase flow are explained. **Figures 2-27** denotes such velocity distribution measured at each axial position, where dotted lines in each figure indicate theoretical velocity distribution for turbulent boundary layer i.e. 1/7 law.

$$U(r) = U_{\max}\left(1-\frac{r}{R}\right)^{1/7} \tag{2-7}$$

where $U_{\max}$ is the measured velocity at the pipe center. Of course, it is found that local liquid velocities increase corresponding to increase of superficial liquid velocity from 0.075 to 0.15 m/s. And it can be seen that these liquid velocity distributions show good agreement with 1/7 law, excepting the case of z/D=3.2. It can be considered that the cause of disagreement between experimental result and 1/7 law at z/D=3.2 is undeveloped flow generated by the structure of mixing section for two-phase flow measurement.

Next, radial distributions of liquid velocity and turbulence intensity measured in LBE two-phase flow, corresponding to experimental conditions of superficial gas velocity j_g=0.05 to 0.15 m/s and superficial liquid velocity j_l=0.1 and 0.2 m/s, are shown in **Figure 2-29, 2-30 2-31** and **2-32**. It is found that the liquid velocity shows wall-peak distribution and changes into core-peak distribution. This tendency could be measured at z/D=17.6 and 32.4. However, at z/D=3.2, measured liquid velocity distribution shows only wall-peak distribution because of

influence of gas-liquid mixing section.

2.4.2 *Radial distribution of time averaged local void fraction and bubble frequency*

Radial distributions of time averaged local void fraction and bubble frequency which means number of bubbles measured by EC probe in a one second are shown in **Figures 2-33** to **2-38**, respectively, where these distributions also indicate behavior of such distribution toward flow direction. As for void fraction distribution, it is found that the local void fraction shows increase as measurement location is higher along the flow direction regardless of experimental conditions. It can be consider that such increase of void fraction is caused by difference of pressure corresponding to measurement location along the flow direction. Regarding shapes of these radial distributions, it can be found that the shape of distribution shows change from flat distribution to core-peak distribution, excepting the case 0.05 m/s of superficial gas velocity j_g. In the case of 0.05 m/s of j_g, the shape of distribution shows change from wall-peak distribution to core-peak distribution.

As for bubble frequency distribution, it is also found that the local bubble frequency shows increase as measurement location is higher along the flow direction regardless of experimental conditions. Regarding shapes of these radial distributions, it can be found that the shape of distribution shows change from flat distribution to core-peak distribution, excepting the case 0.05 m/s of superficial gas velocity j_g. In the case of 0.05 m/s of j_g, the shape of distribution shows change from wall-peak distribution to core-peak distribution. This tendency is similar to void fraction distributions.

In the following sections, axial profiles of cross sectional averaged void fraction are focused for analyzing behavior of void fraction distributions toward the flow direction.

2.5 Conclusion

Due to physical characteristics of LBE two-phase flow, it is considered that prediction of flow characteristics of LBE two-phase flow using existing two-phase flow analytical model might be difficult because two-phase flow characteristics and turbulent characteristics are not clarified enough, so far. The cause of this situation is lacking of experimental data such as local void fraction, liquid velocity and etc. And also, measurement technique which can be applied to LBE two-phase flow is not developed completely. Therefore, in this study, measurement techniques such as EC and EM probe were developed. And also, signal processing method was established. Then local liquid velocity, turbulent intensity, void fraction, bubble frequency and bubble residence time in LBE two-phase flow were measured by utilizing HESTIA. As results, following conclusions were obtained.

From the comparison of superficial liquid velocity measured by EM probe and vortex flow meter, it was found that the superficial liquid velocity measured by EM probe shows good agreement with that measured by vortex flow meter. Hence it can be said that the signal processing method and estimated liquid velocity and etc. are correct in this experimental condition.

Radial profile of void fraction changes from wall-peak to core-peak along the flow direction. Axial development of the liquid velocity field shows similar tendency to the void fraction profiles.

References for Chapter 2

[2-1] Saito Y, Mishima K. Bubble measurements in liquid-metal two-phase flow by using a four-sensor probe, Multiphase Science and Technology 2012; 24: 279-297.

[2-2] Saito Y, Asai Y, Ito D, Mishima K. Two-Phase Flow Characteristics in a Liquid-Metal Two-Phase Flow, Proc. 8th Int. Conf. Multiphase Flow ICMF 2013, CD-ROM, Paper No. ICMF2013-822.

[2-3] Saito Y, Mishima K, Tobita Y, Suzuki T, Matsubayashi M. Measurements of liquid-metal two-phase flow by using neutron radiography and electrical conductivity probe. Experimental Thermal and Fluid Science 2005; 29: 323-330.

[2-4] Ricou, R. and Vives, C., Local Velocity and Mass Transfer Measurements in Molten Metals Using an Incorporated Magnet Probe, Int. J. Heat Mass Transfer, Vol. 25(10), 1579-1588 (1982).

[2-5] Wessenfluh T. Probes for local velocity and temperature measurements in liquid metal flow, Int.J.Heat.Mass.Transfer 1985; 28: 1563-1574.

[2-6] Iguchi M, Tokunaga H, Tatemichi H. Bubble and Liquid Flow Characteristics in a Wood's Metal Bath Stirred by Bottom Helium Gas Injection. Metallurgical and Materials Transactions B 1997; 28B: 1053-1061.

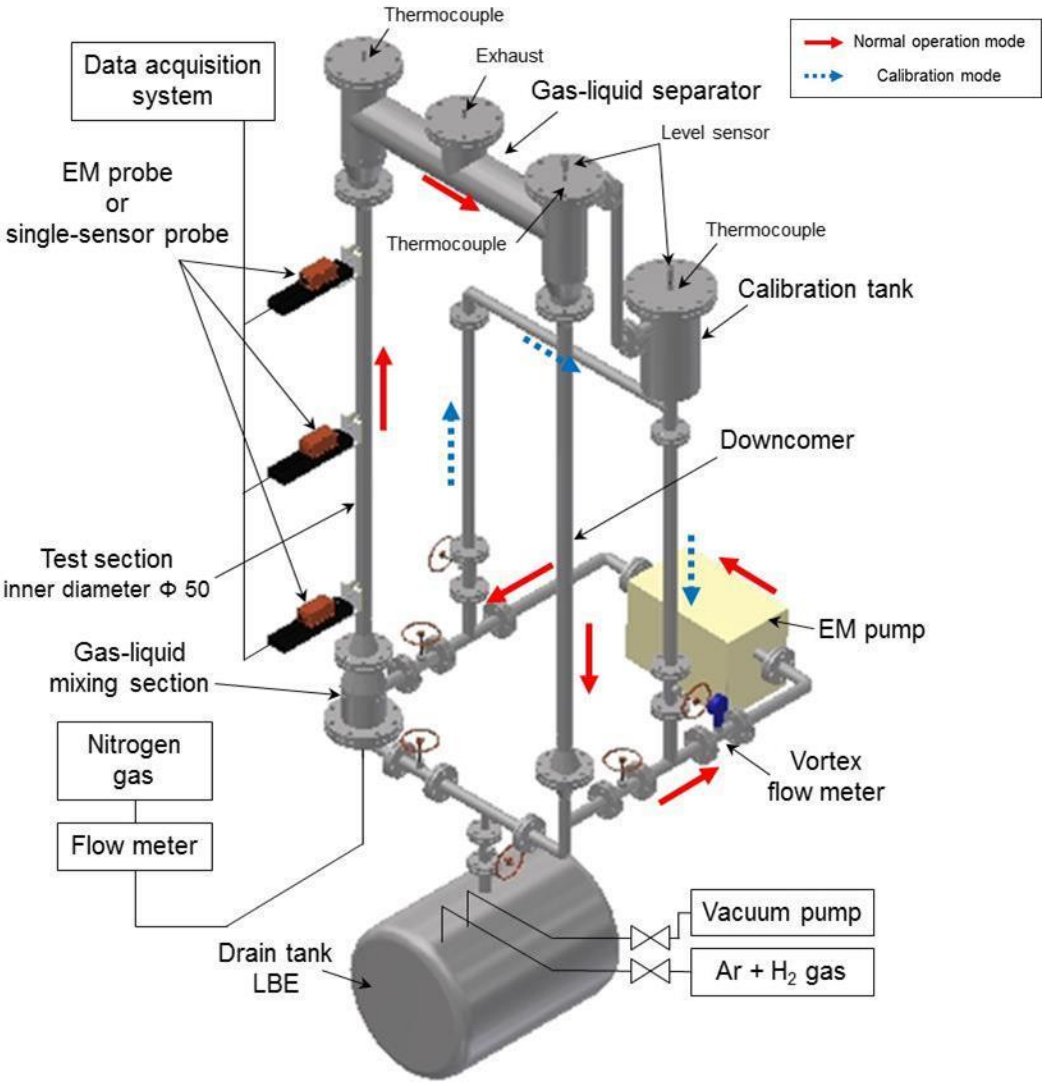

Figure 2-1. Schematic of HESTIA.

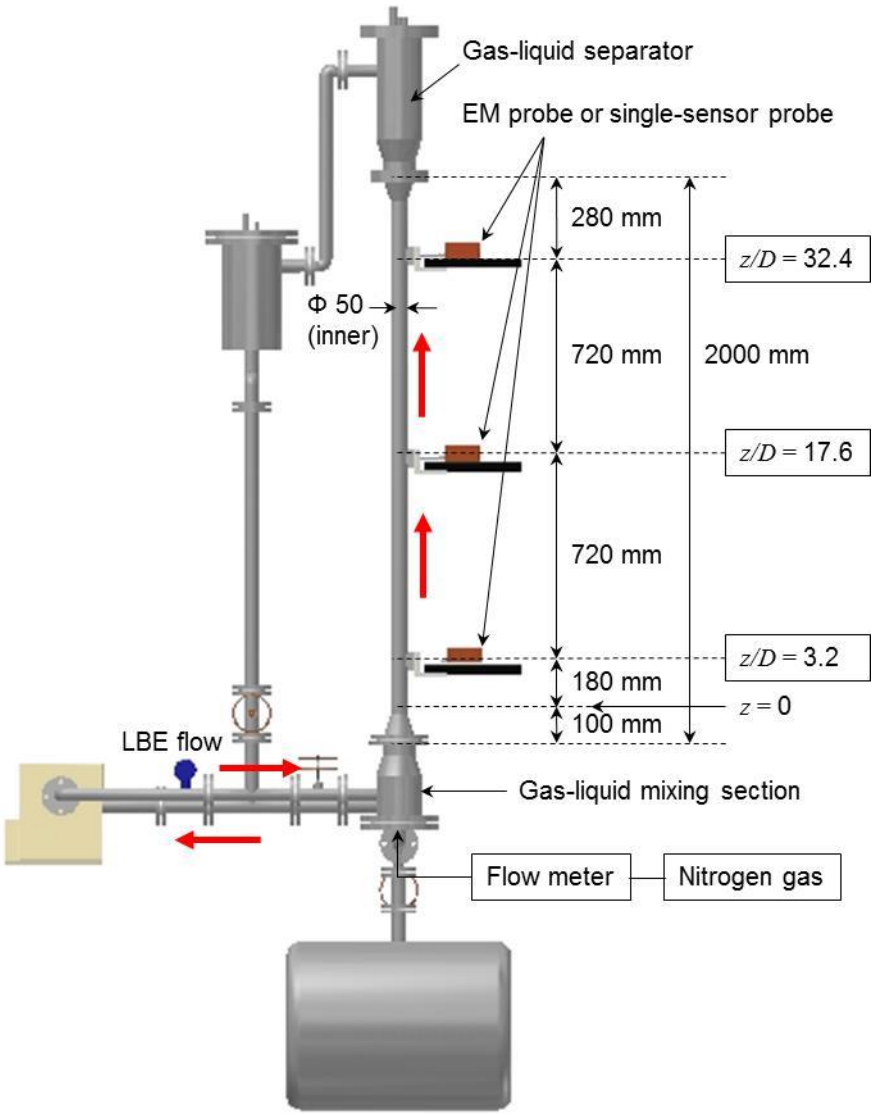

Figure 2-2. Details of test section of HESTIA.

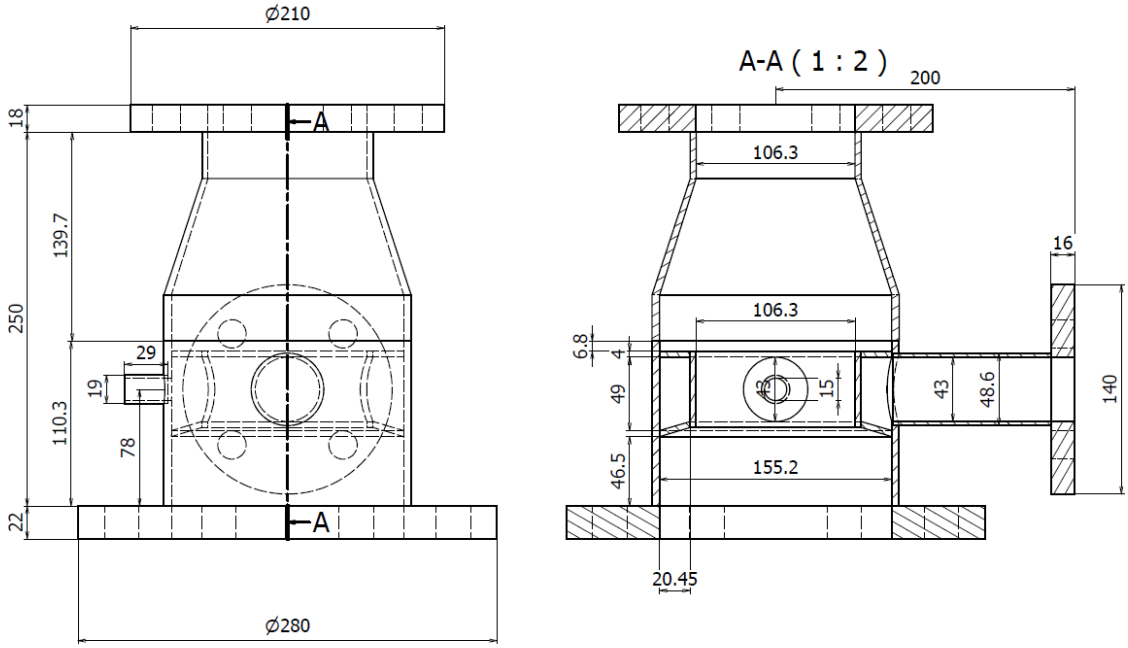

Figure 2-3. Schematic diagram of mixing chamber.

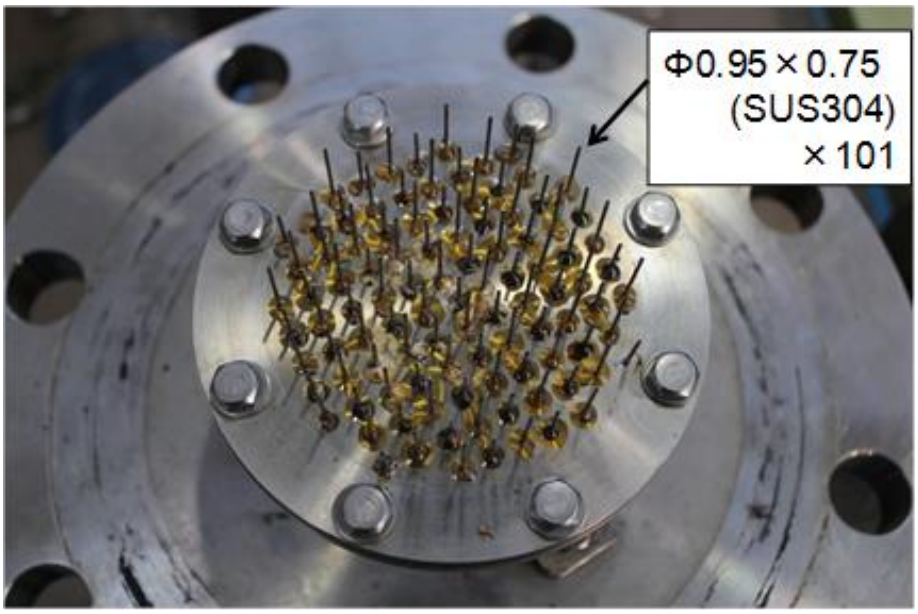

(a)

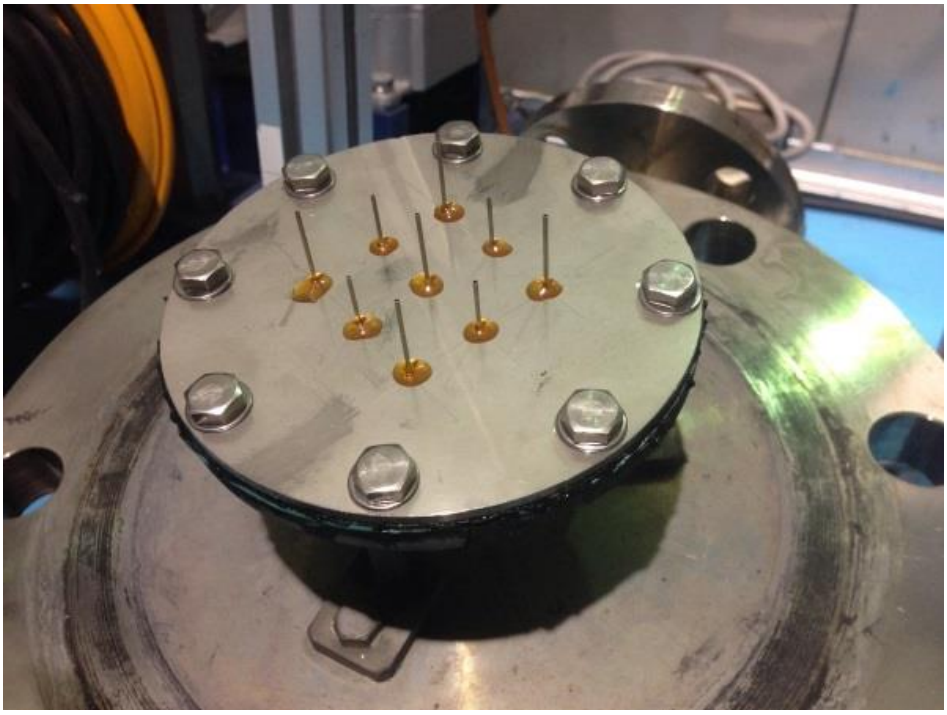

(b)

Figure 2-4. Gas injection nozzles installed in the mixing section of HESTIA, (a) 101 nozzles for higher superficial gas velocities region, (b) 9 nozzles for lower superficial gas velocities region

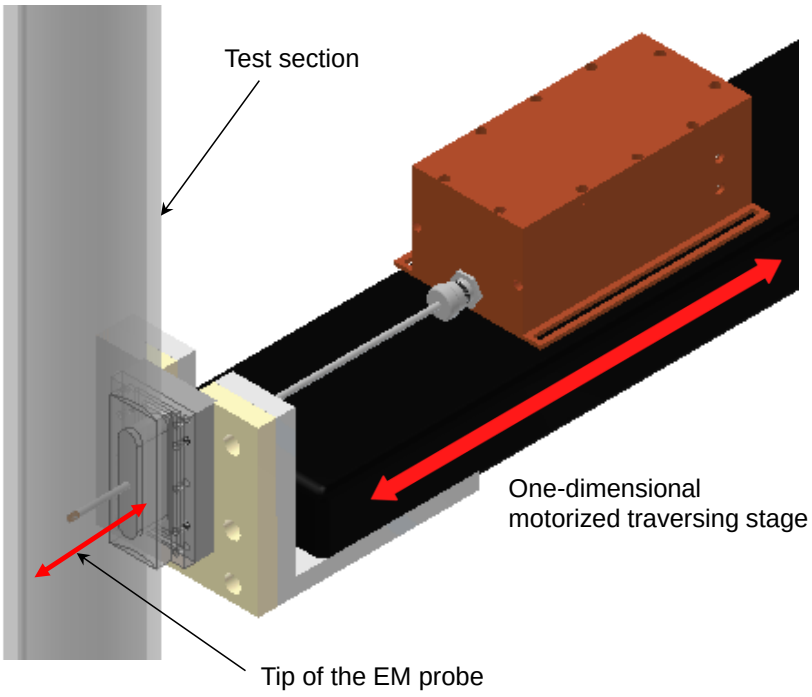

Figure 2-5 Schematic diagram of way to traverse probe.

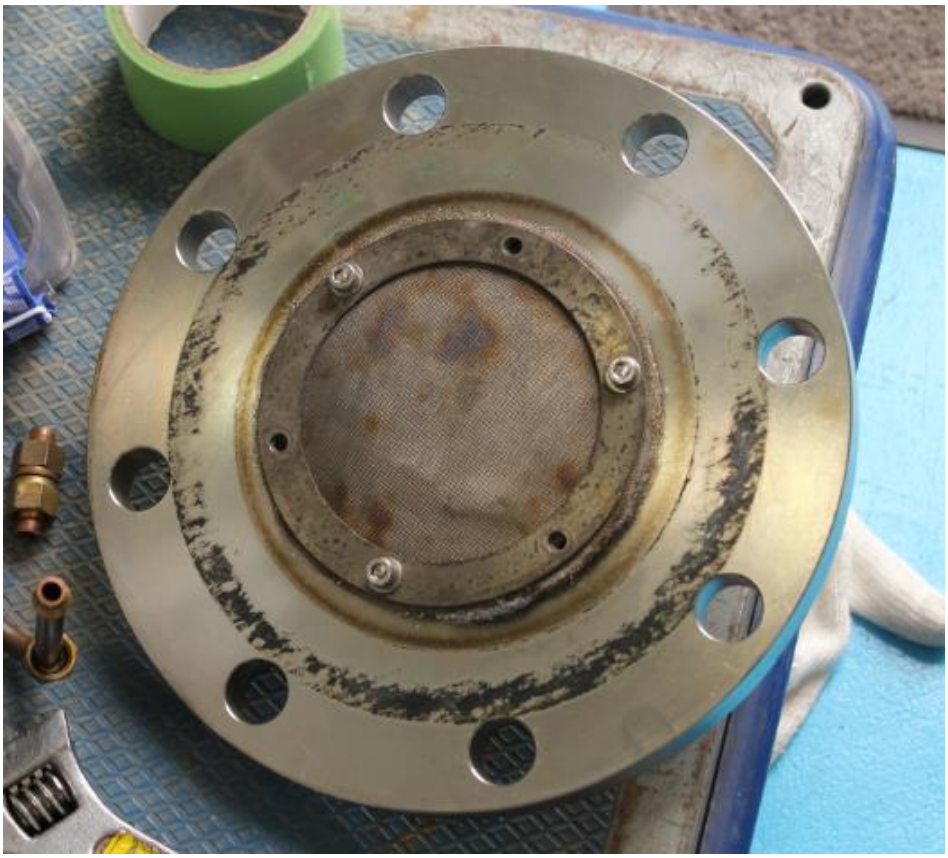

Figure 2-6. Mesh filter for preventing pipe plugging by quite small oxide particle of the LBE.

Figure 2-7. Mesh filter installed in the down-comer for removing the LBE oxide from the molten LBE.

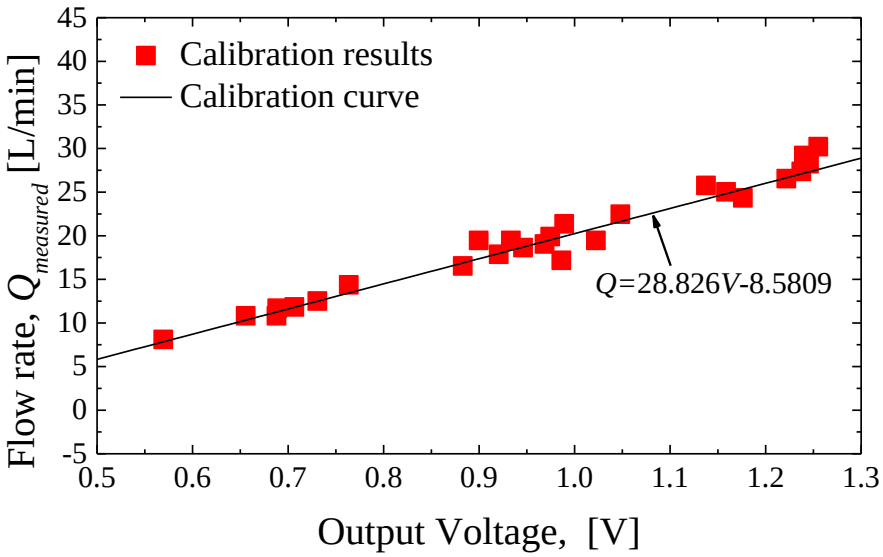

Figure 2-8. (a)Calibration results of vortex flow meter.

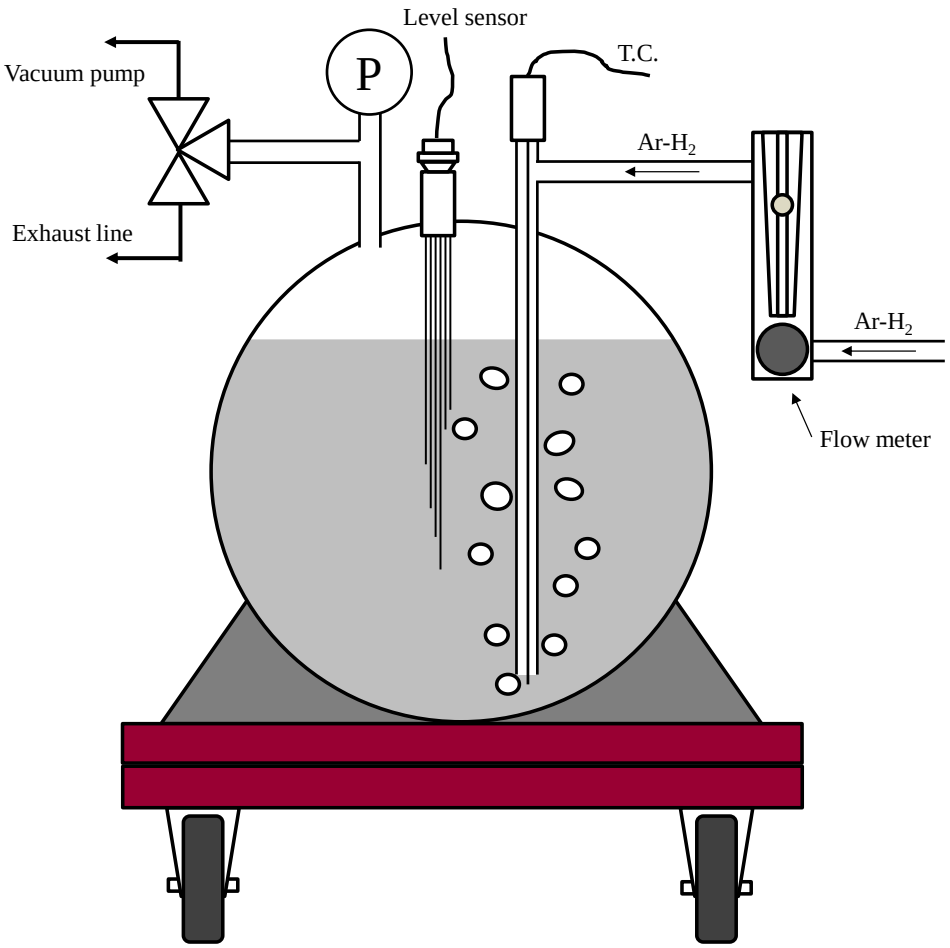

Figure 2-9. Detailed expression of drain tank.

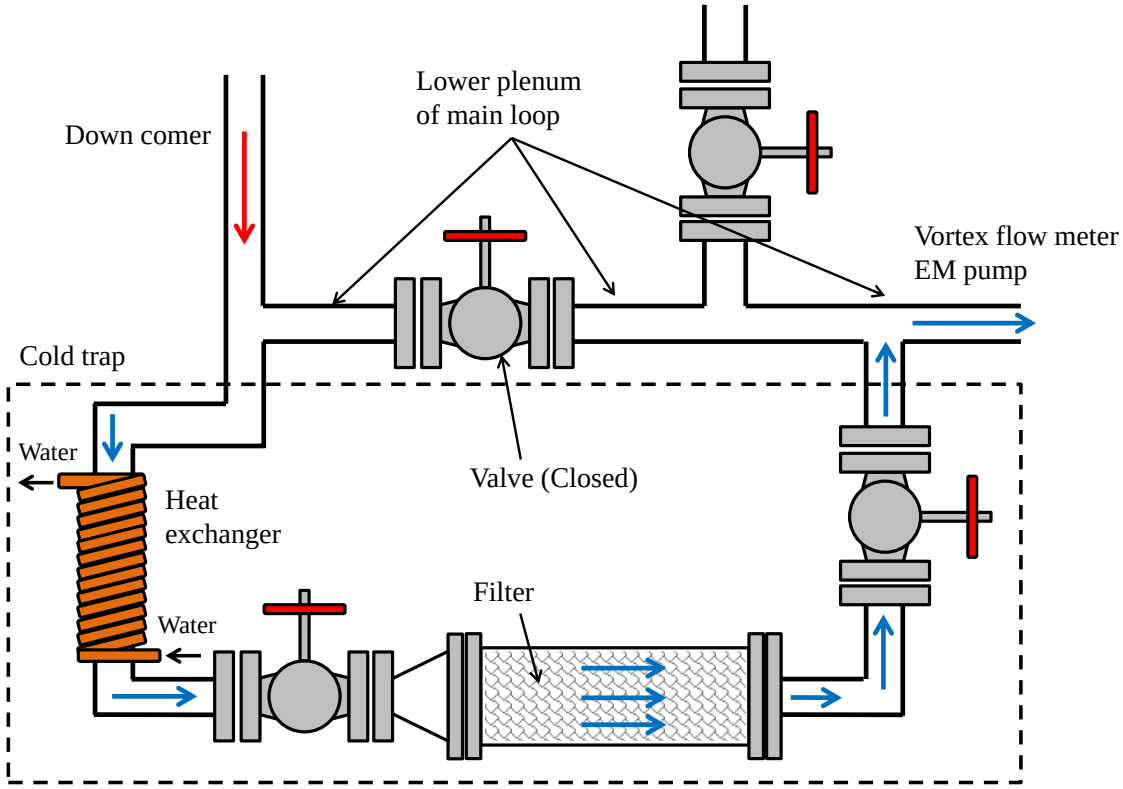

Figure 2-10. Schematic diagram of cold trap installed at lower plenum between outlet of down-comer and inlet of EM pump.

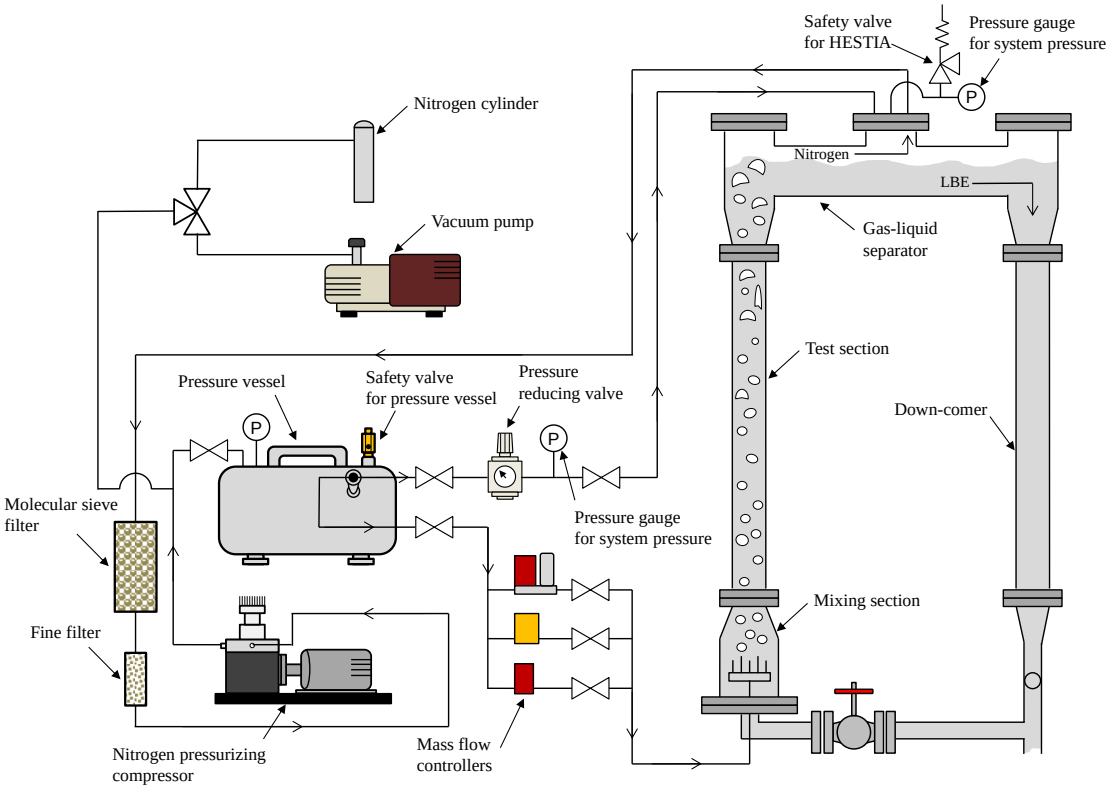

Figure 2-11. Details of nitrogen closed loop.

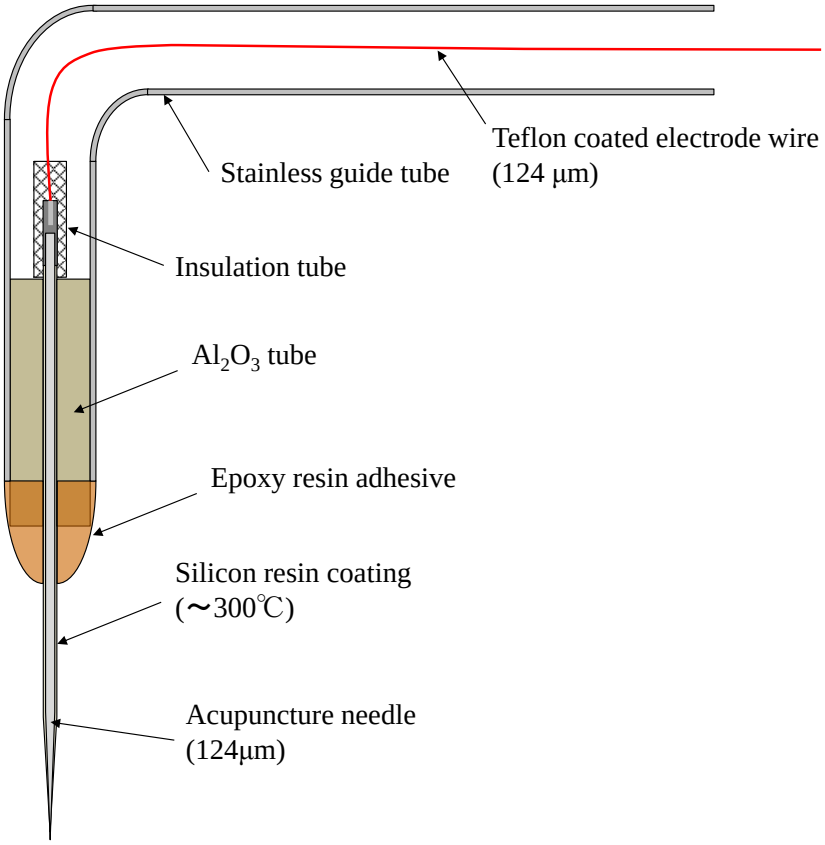

Figure 2-12. Schematic diagram of single-sensor probe.

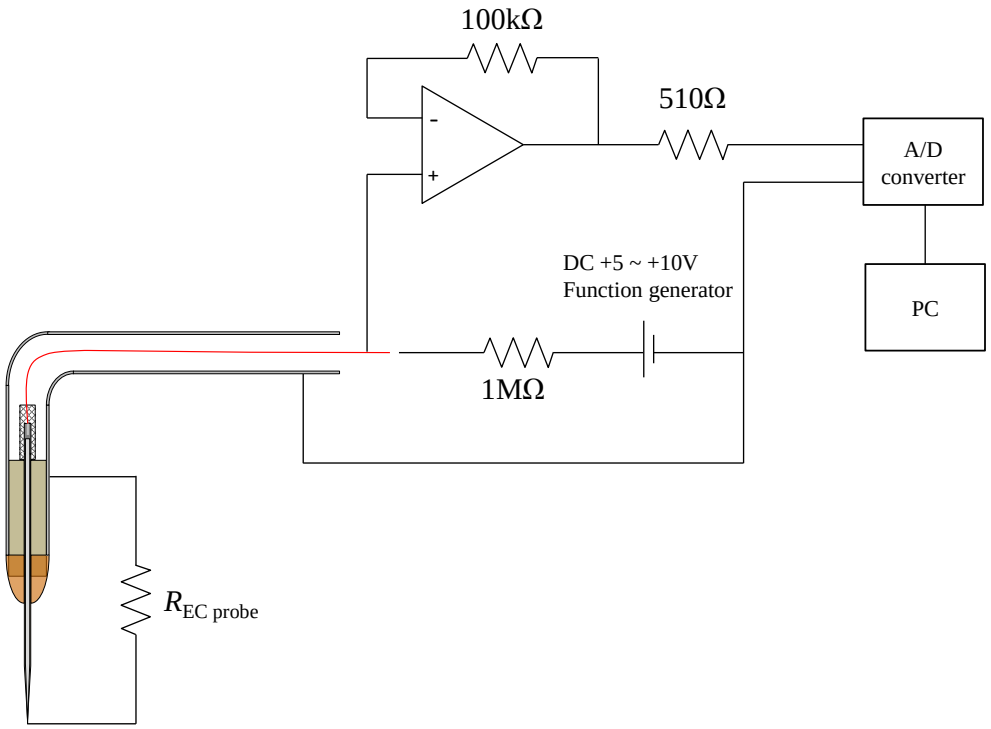

Figure 2-13. Details of measurement system for single-sensor probe.

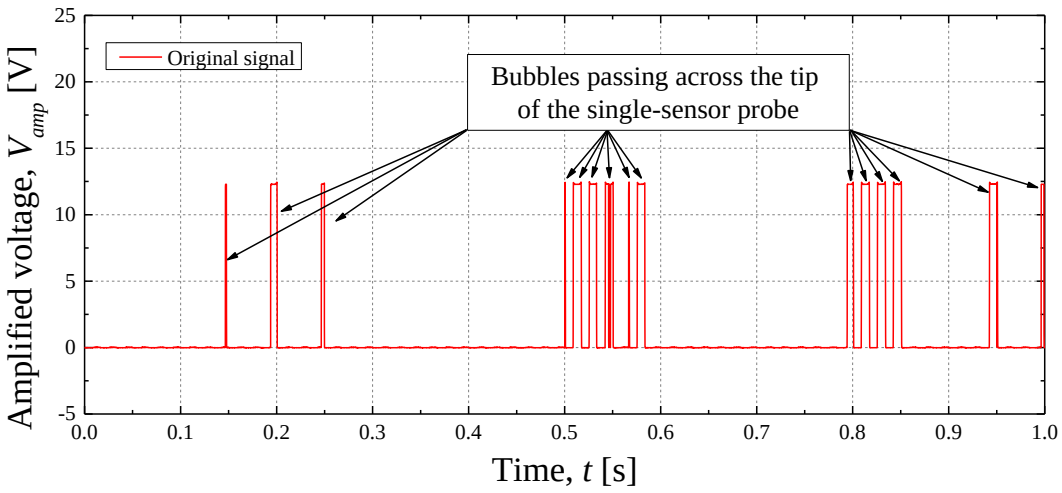

Figure 2-14. Typical output signal of bubbles measured by EC probe.

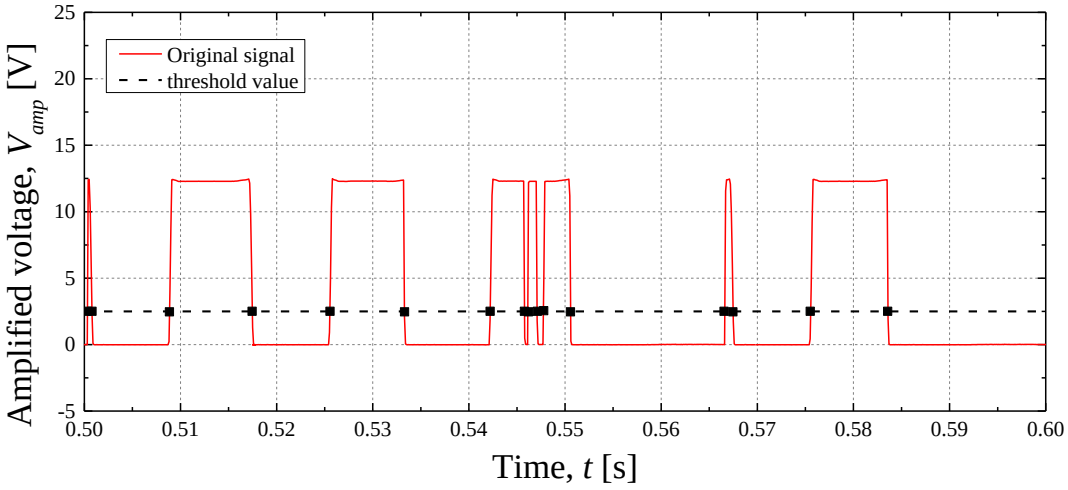

(a)

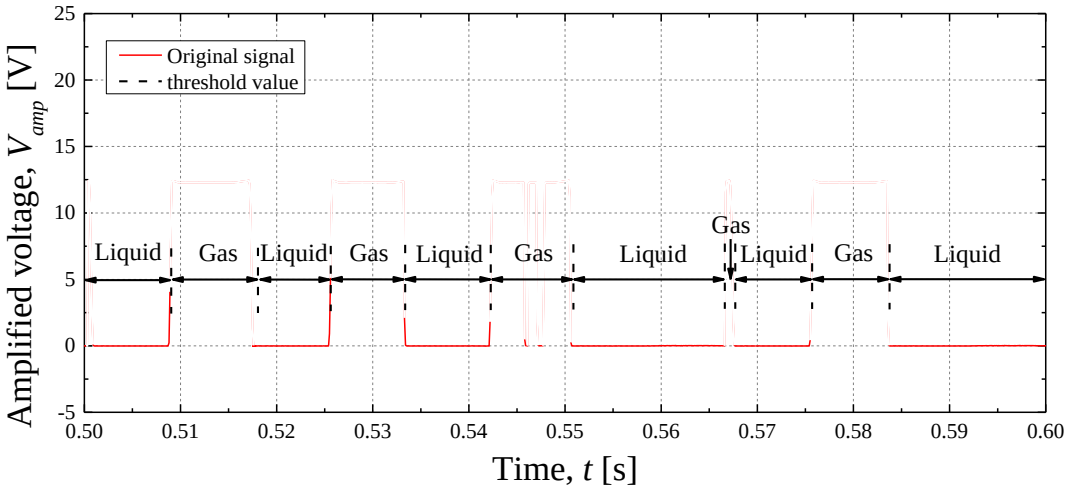

(b)

Figure 2-15. Present signal processing procedure of single-sensor probe for separating gas and liquid phase. (a)First step of signal processing for original signal. (b)Final extracted signal.

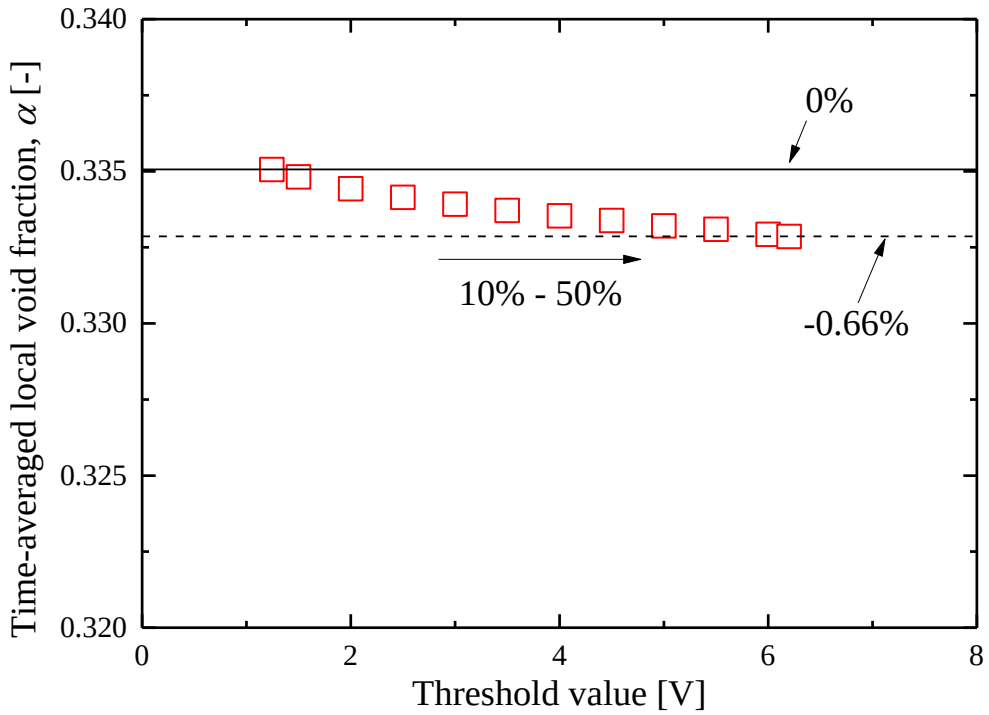

Figure 2-16. Effect of threshold value on estimated time-averaged local void fraction.

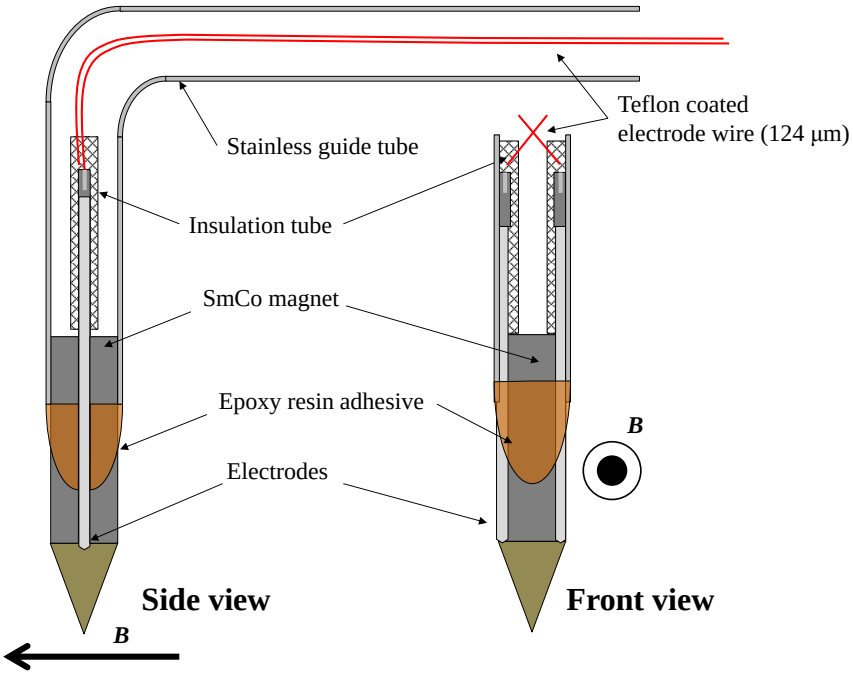

Figure 2-17. Schematic diagram of EM probe.

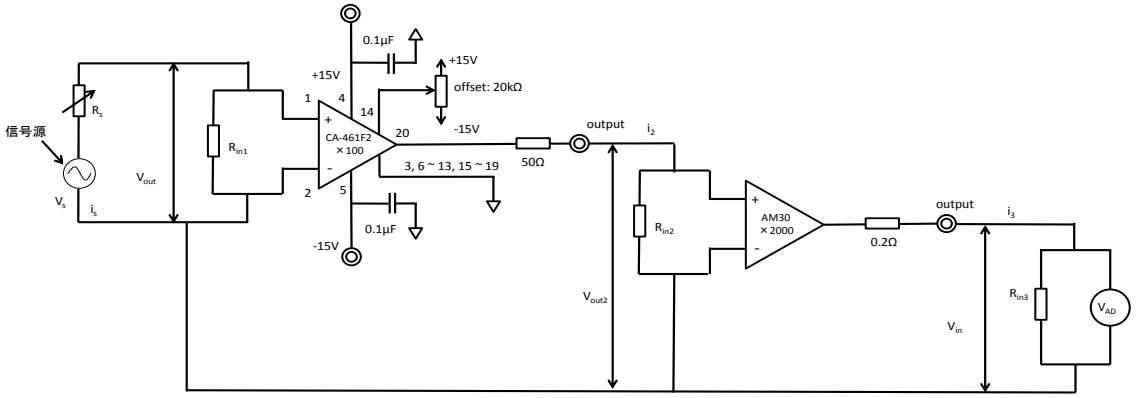

Figure 2-18. Measurement system for EM probe.

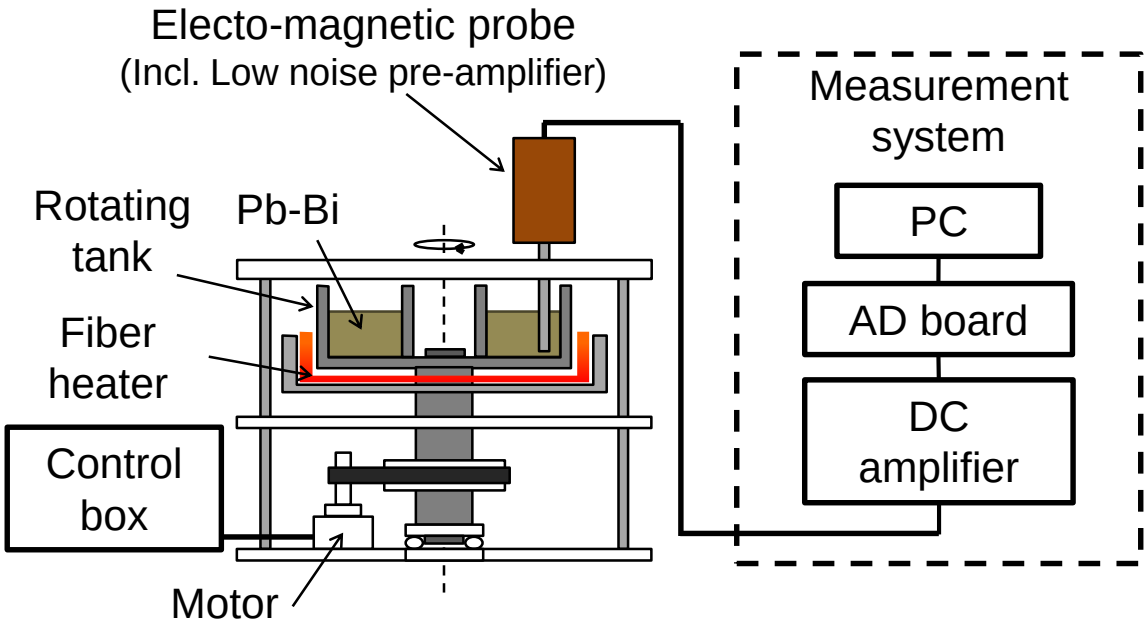

(a)

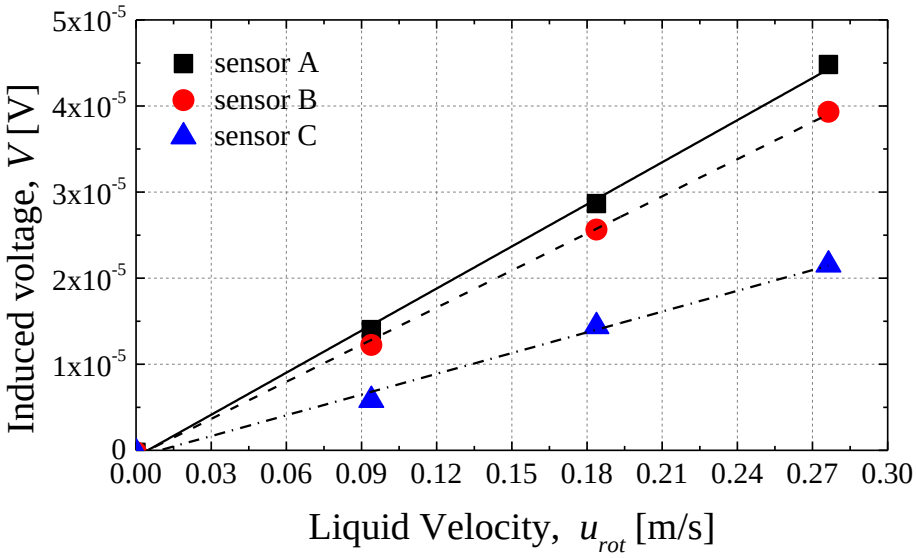

(b)

Figure 2-19. Detail of (a) rotating test apparatus for calibration of EM probe and (b) calibration results of EM probe.

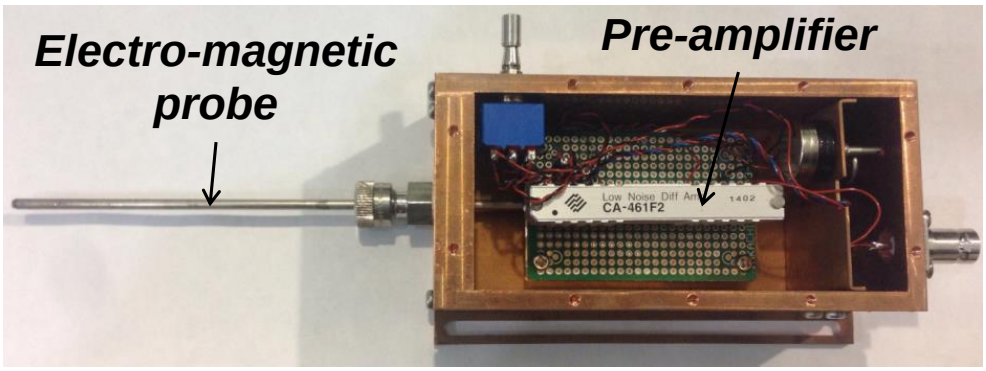

Figure 2-20. Combination of EM probe and pre-amplifier.

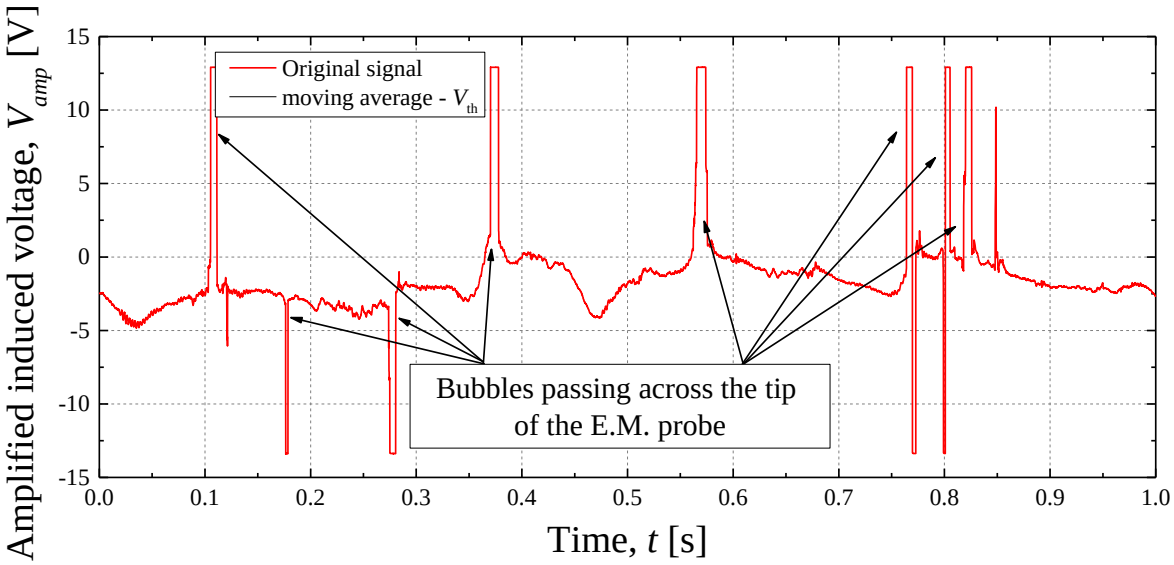

Figure 2-21. Typical output signal of velocity fluctuations measured by EM probe.

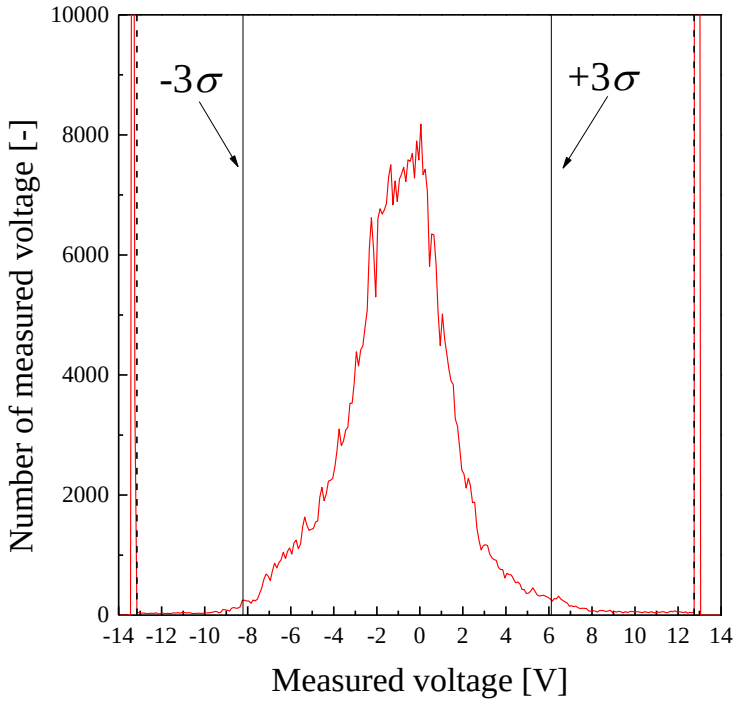

(a)

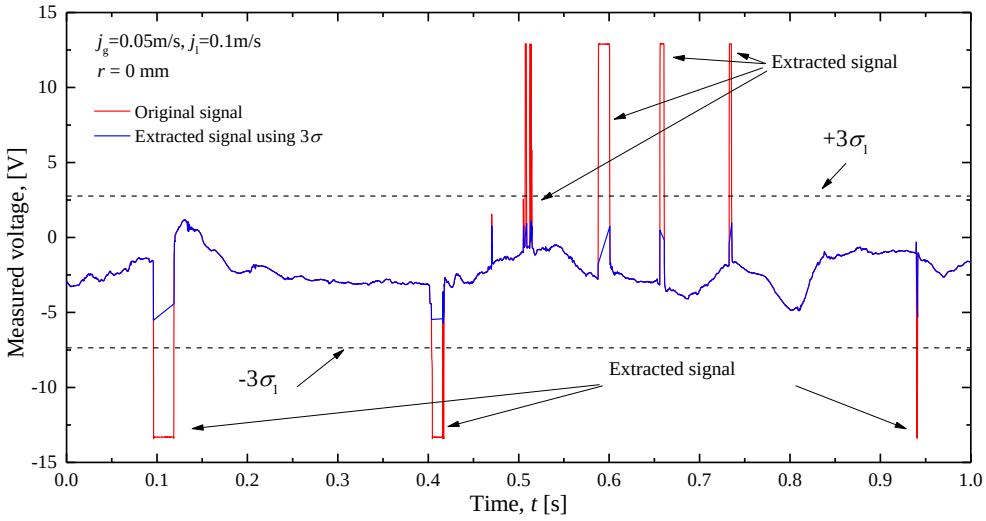

(b)

Figure 2-22. How to decide threshold values of present signal processing procedure for EM probe. (a) Frequency distribution to decide first threshold value of signal processing for original signal (b)Comparison of time derivative of moving averaged voltage to decide second threshold value of signal processing for extracted signal.

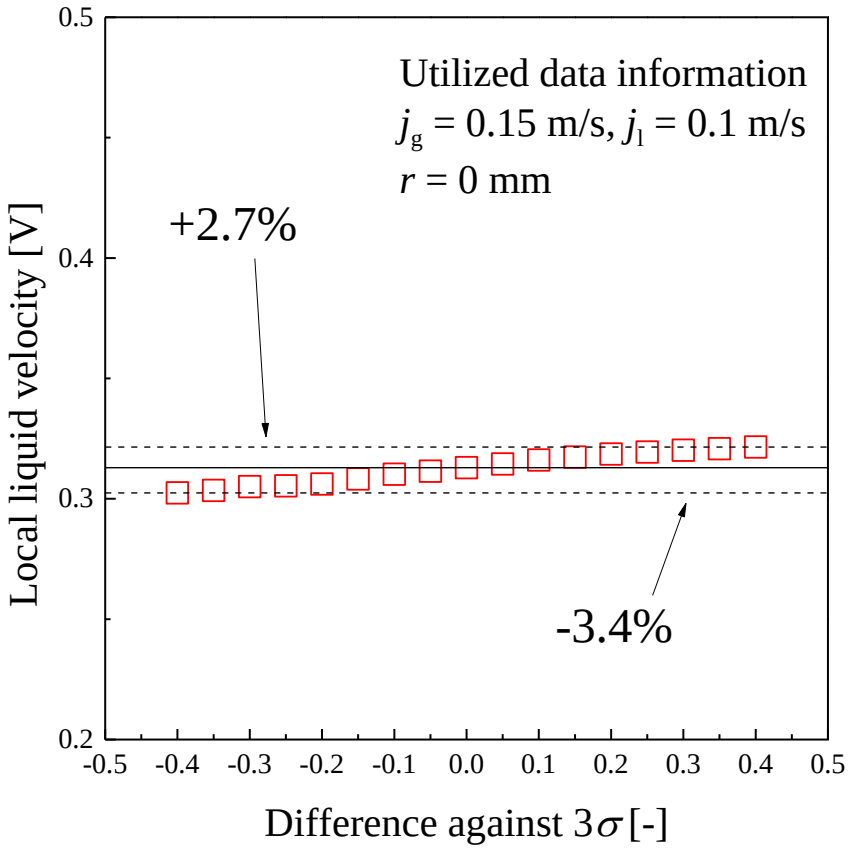

Figure 2-23. How to decide threshold values of present signal processing procedure for EM probe. (a) Frequency distribution to decide first threshold value of signal processing for original signal (b)Comparison of time derivative of moving averaged voltage to decide second threshold value of signal processing for extracted signal.

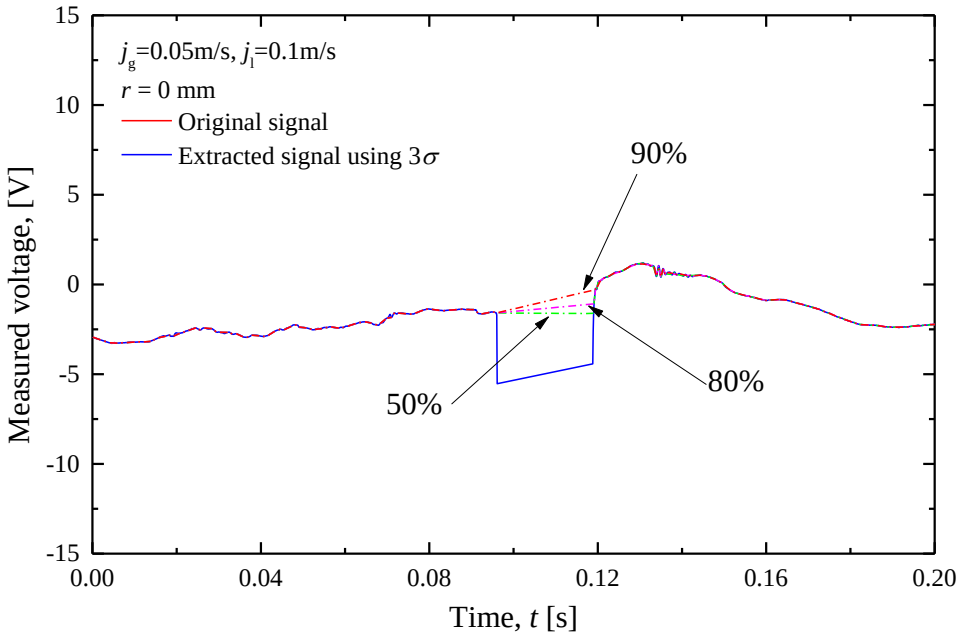

(a)

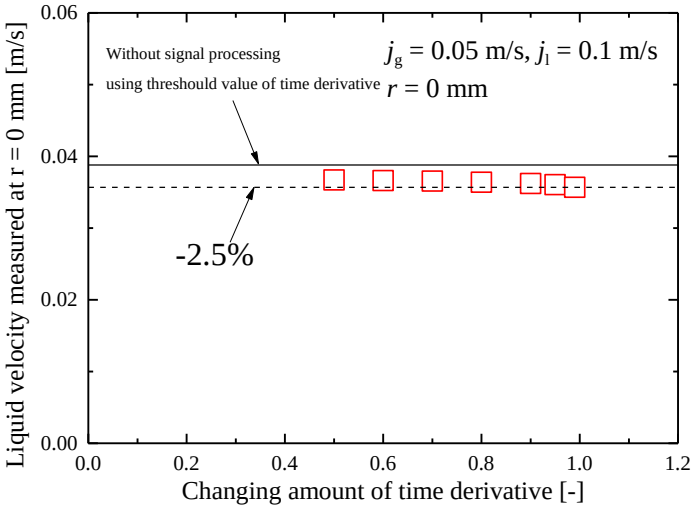

(b)

Figure 2-24. Final extracted signal.

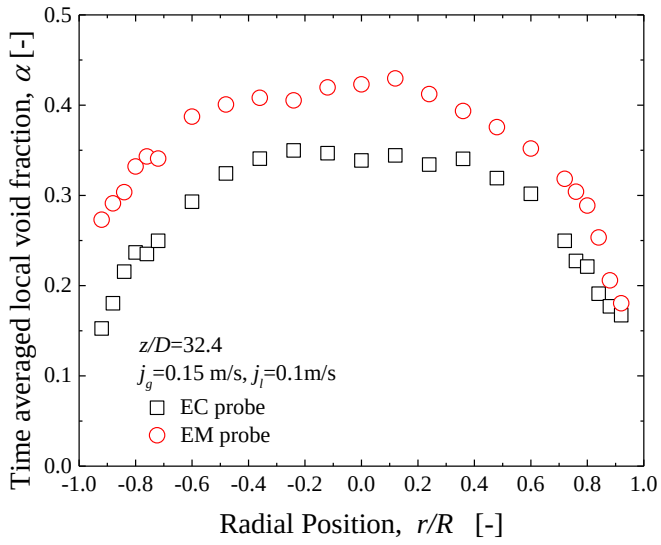

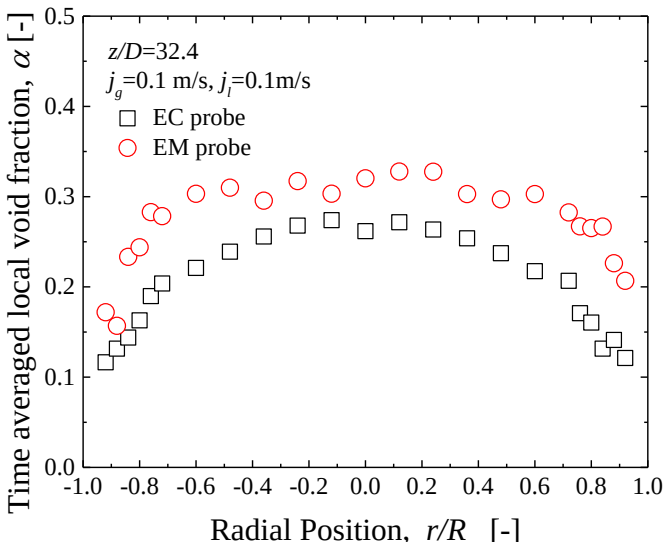

Figure 2-25. Comparison of time averaged local void fraction measured by EC and EM probe.

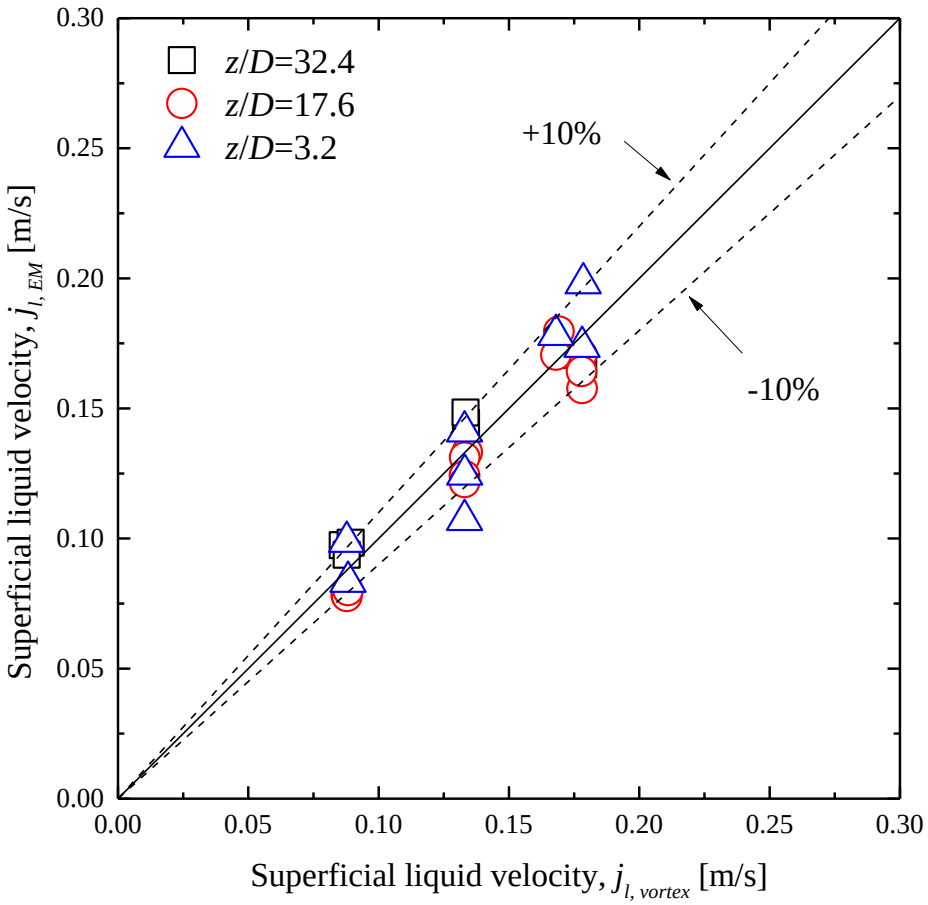

Figure 2-26 Comparison of superficial liquid velocity measured by EM probe and vortex flow meter.

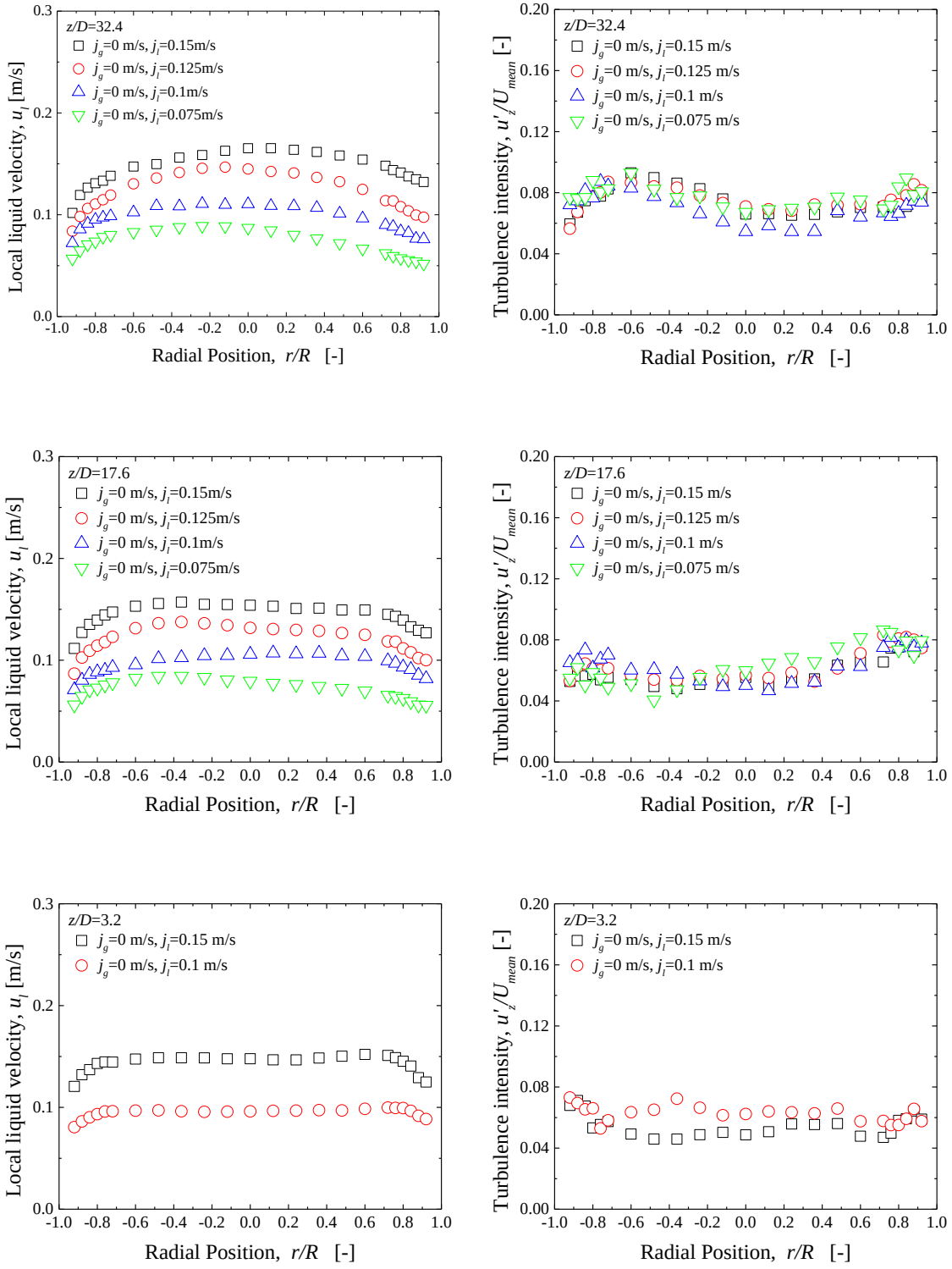

Figure 2-27 Effect of superficial liquid velocity on liquid velocity and turbulence intensity for LBE single-phase flow.

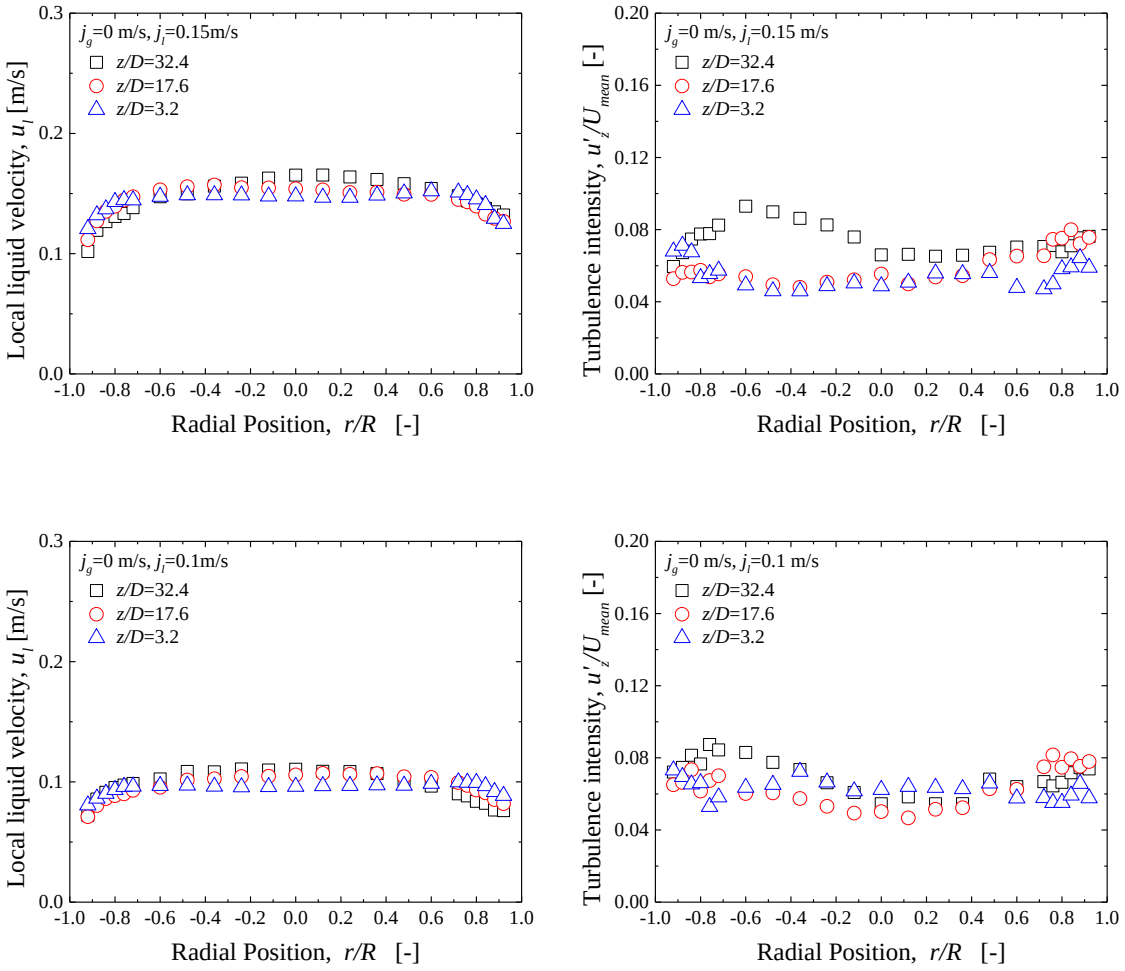

Figure 2-28 Effect of *z/D* on liquid velocity and turbulence intensity for j_l=0.1 m/s.

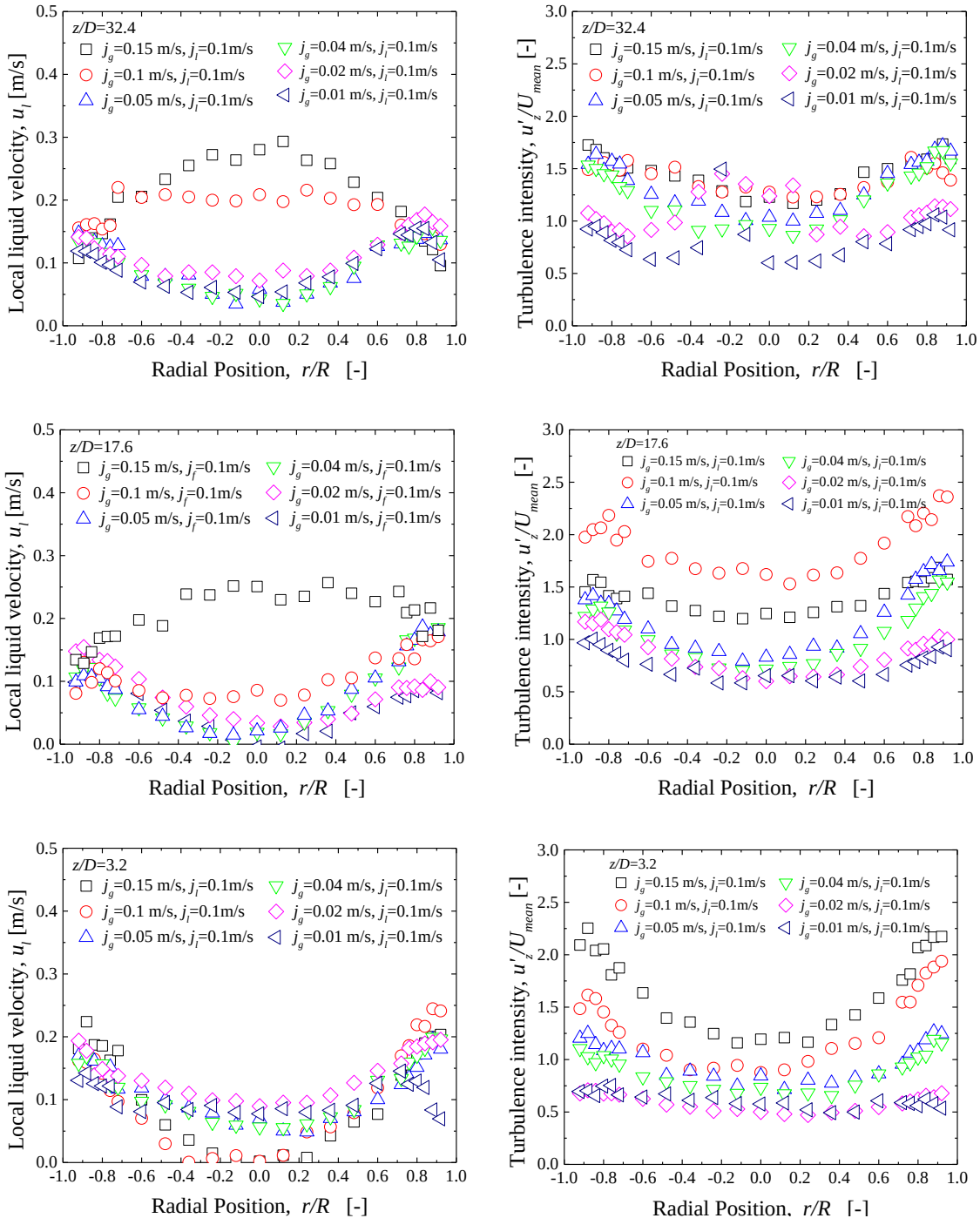

Figure 2-29 Effect of superficial gas velocity on liquid velocity and turbulence intensity for j_l=0.1 m/s.

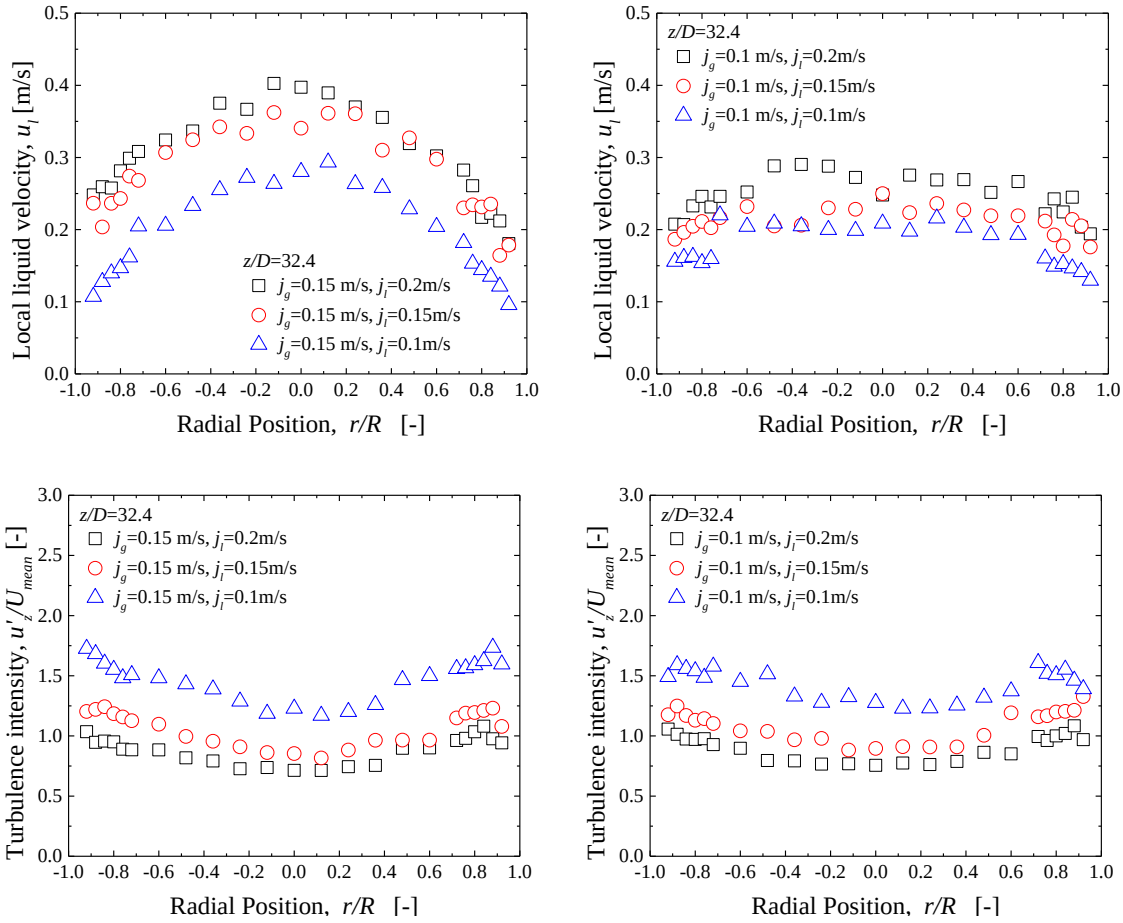

Figure 2-30 Effect of superficial liquid velocity on liquid velocity and turbulence intensity for j_g=0.1 to 0.15 m/s, z/D=32.4.

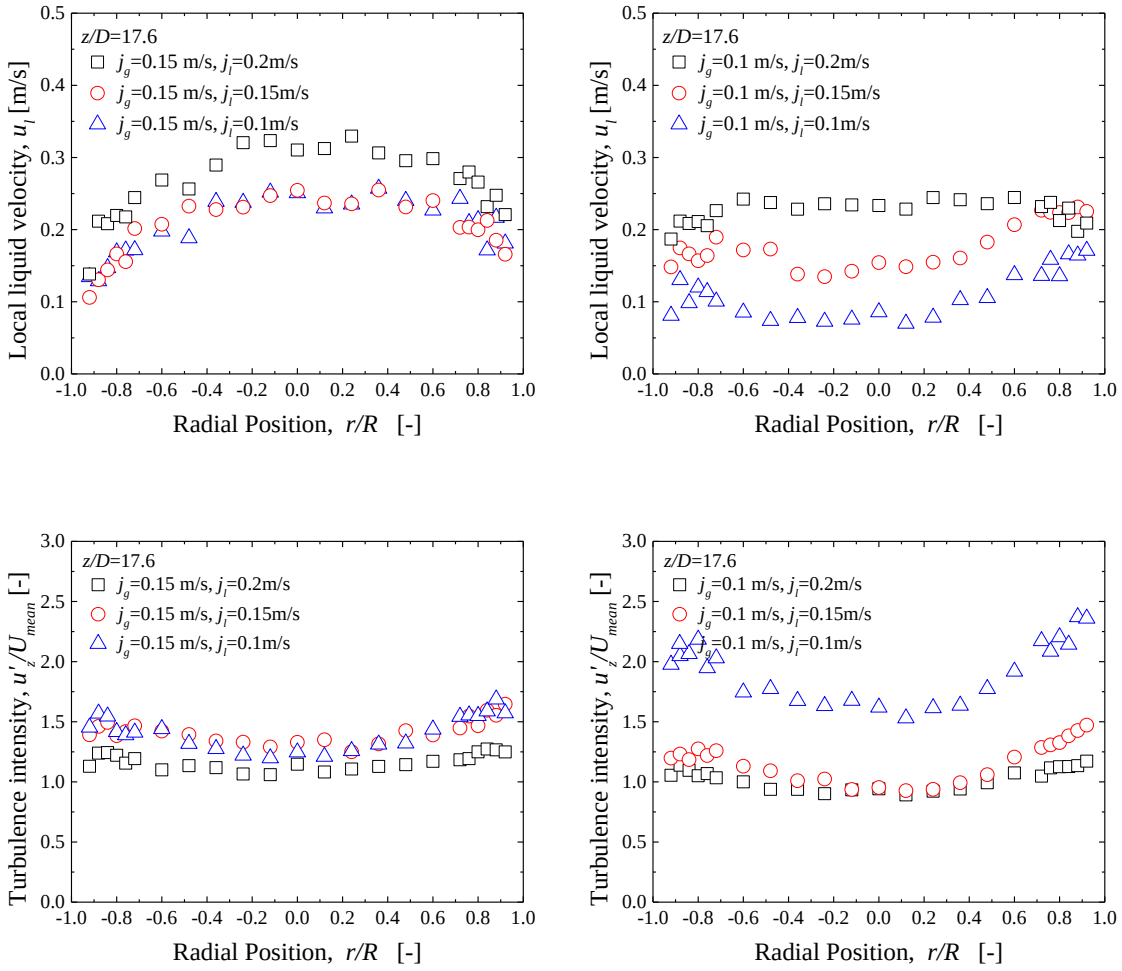

Figure 2-31 Effect of superficial liquid velocity on liquid velocity and turbulence intensity for j_g=0.1 to 0.15 m/s, z/D=17.6.

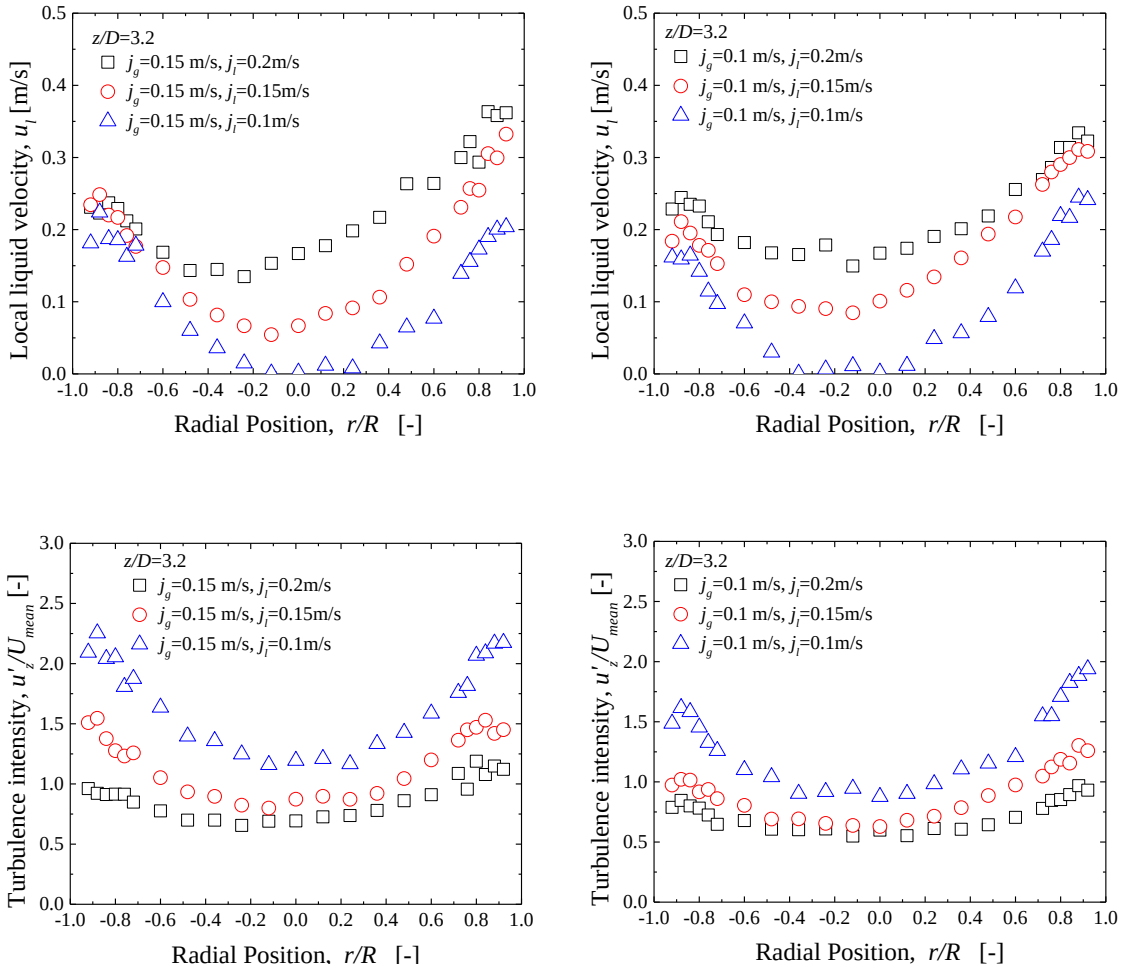

Figure 2-32 Effect of superficial liquid velocity on liquid velocity and turbulence intensity for j_g=0.1 to 0.15 m/s, z/D=3.2.

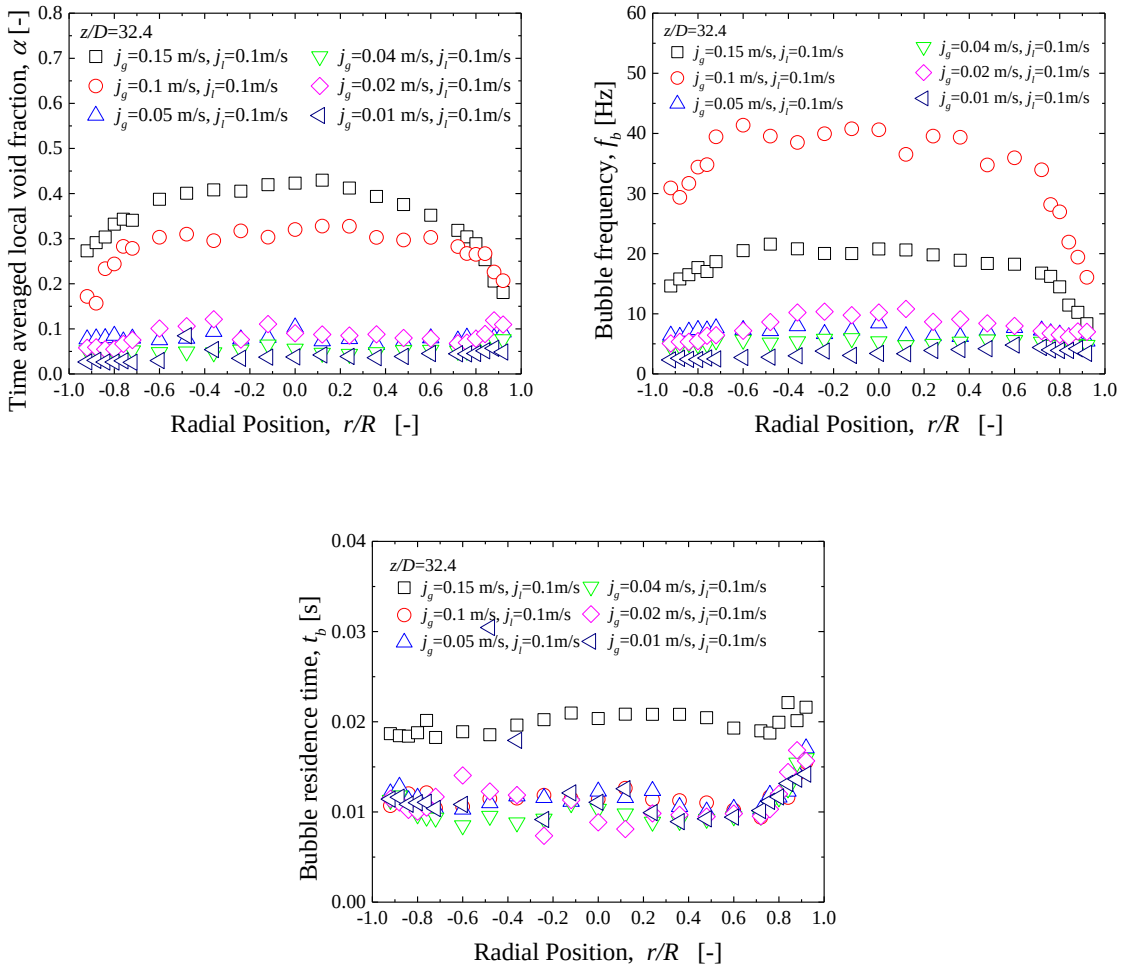

Figure 2-33. Effect of superficial gas velocity on time-averaged local void fraction, bubble frequency and bubble residence time for j_l=0.1 m/s, z/D=32.4.

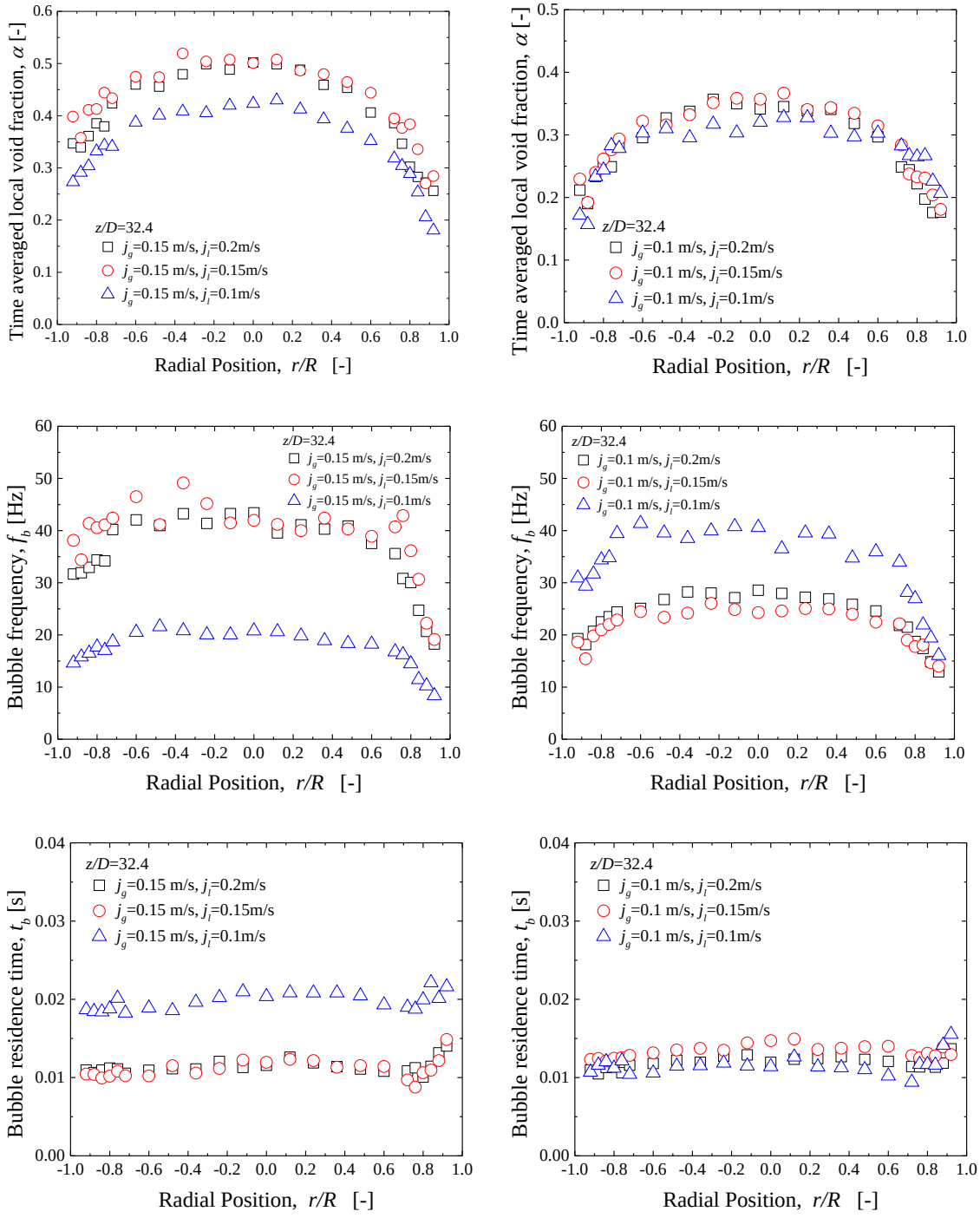

Figure 2-34. Effect of superficial liquid velocity on time-averaged local void fraction, bubble frequency and bubble residence time for j_l=0.1 to 0.15 m/s, z/D=32.4.

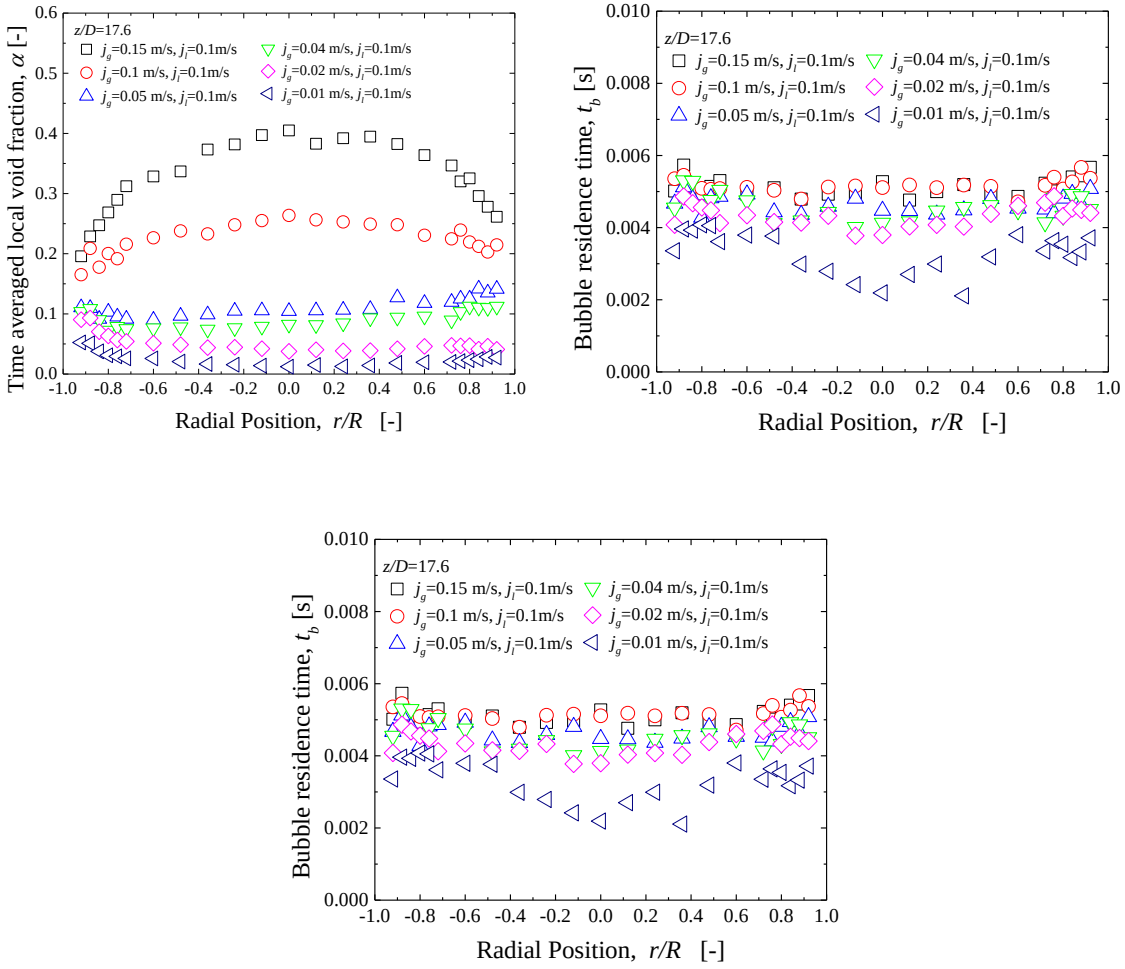

Figure 2-35. Effect of superficial gas velocity on time-averaged local void fraction, bubble frequency and bubble residence time for j_l=0.1 m/s, z/D=17.6.

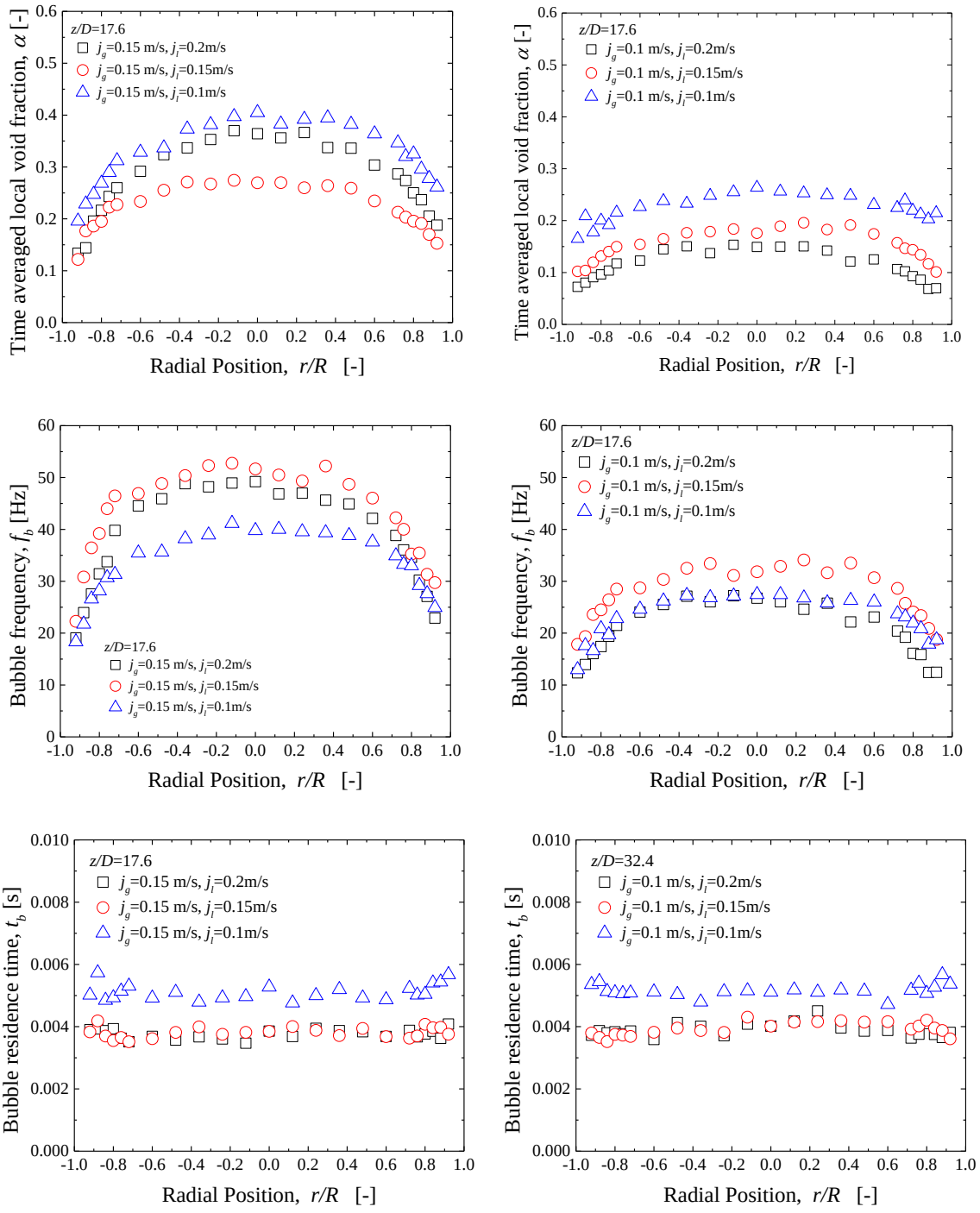

Figure 2-36. Effect of superficial liquid velocity on time-averaged local void fraction, bubble frequency and bubble residence time for j_l=0.1 to 0.15 m/s, z/D=17.6.

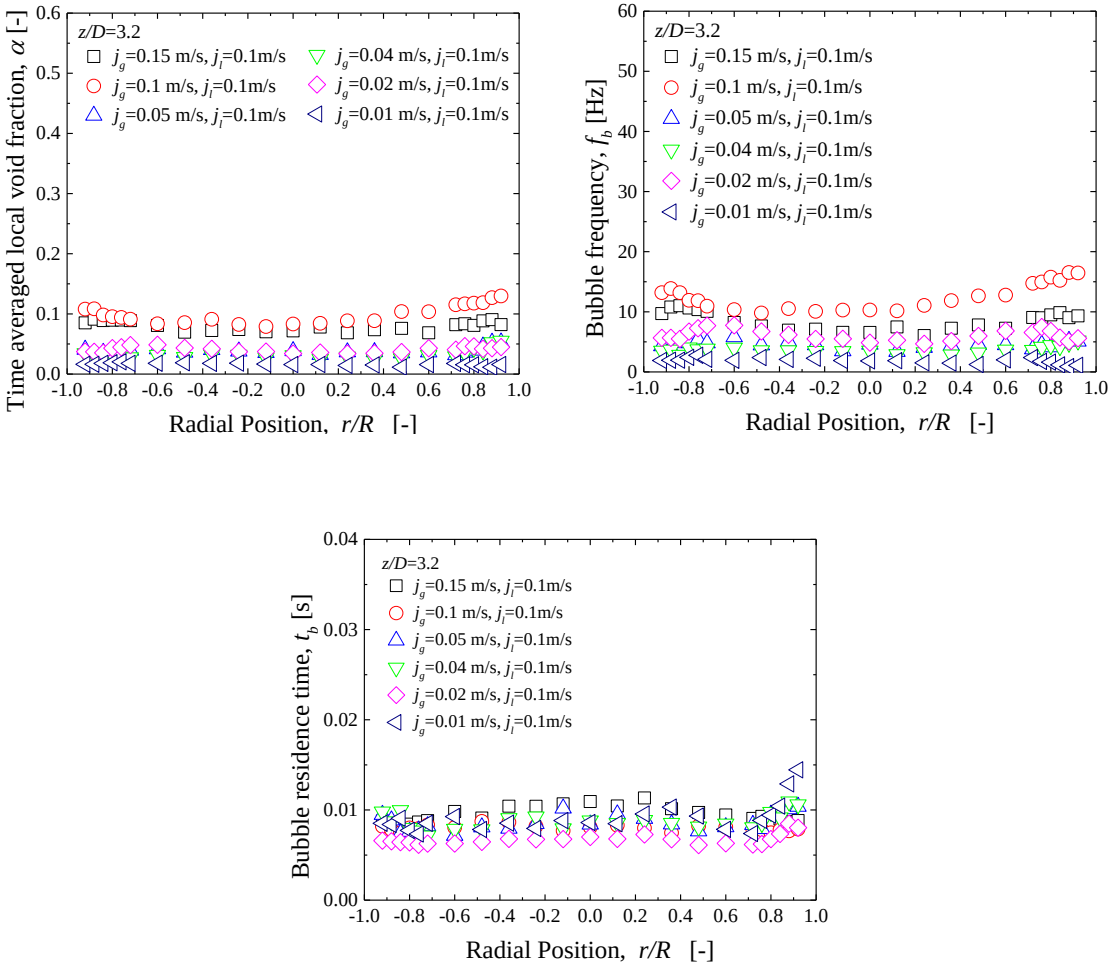

Figure 2-37. Effect of superficial gas velocity on time-averaged local void fraction, bubble frequency and bubble residence time for j_l=0.1 m/s, z/D=3.2.

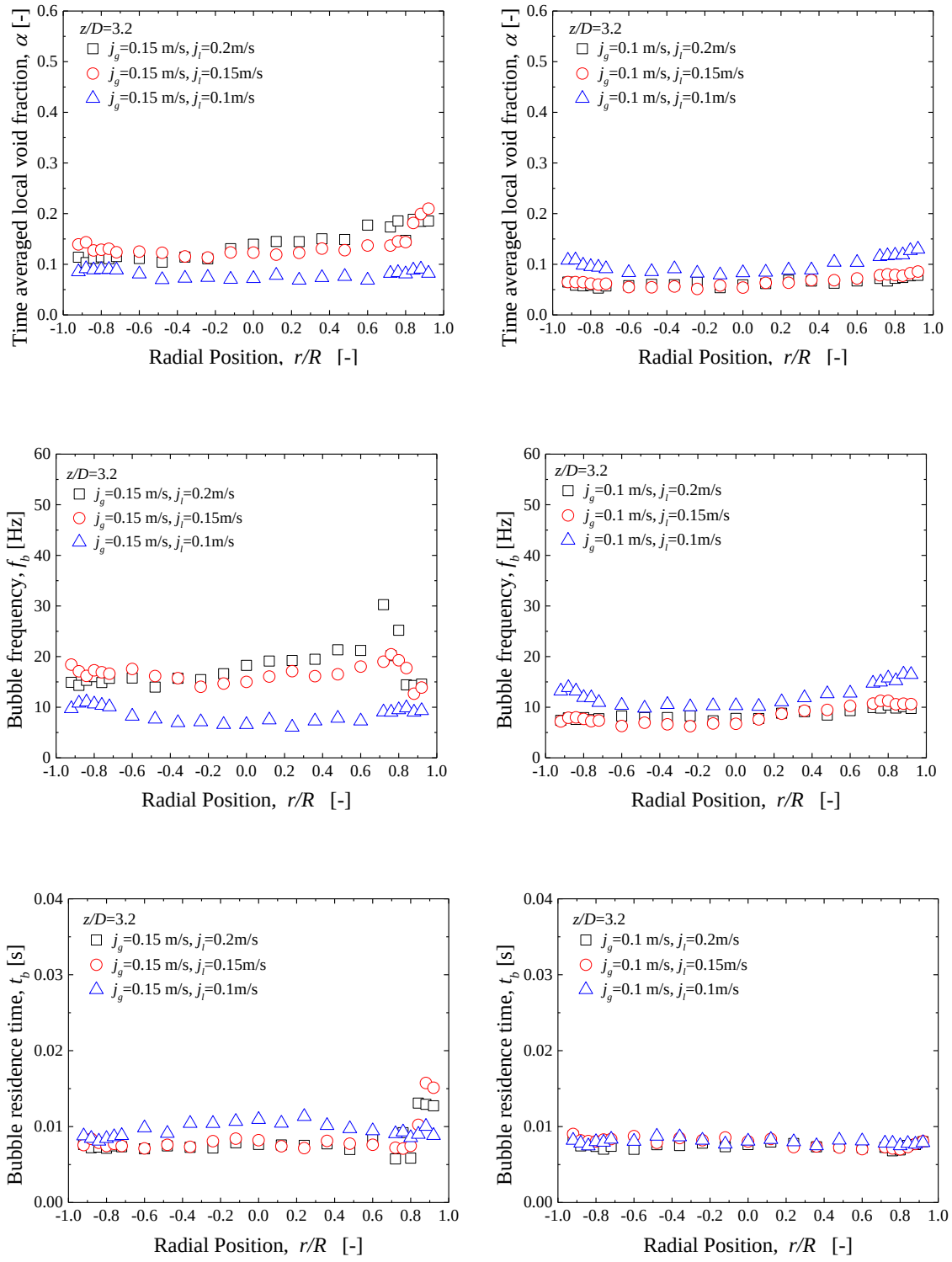

Figure 2-38. Effect of superficial liquid velocity on time-averaged local void fraction, bubble frequency and bubble residence time for j_l=0.1 to 0.15 m/s, z/D=3.2.

Table 2-1 Detailed specification of the A/D converter (ADM-688PCI, Micro Science Co. Ltd.).

ADM-688PCI

Analog input part

Items		
Number of input channel / Singnal mode		8CH / Single end mode (simultaneous measurement)
Input signal ranges (which can be changed by mechanical switch on the A/D bord)		±10V, ±5V, ±2.5V, 0 to +10V, 0 to +5V
Input inpedance		10MΩ
Crosstalk		typ 65dB (between each channel)

A/D converting part

Items		
Resolution		14 or 12 bit (which can be changed by mechanical switch on the A/D bord)
Sampling speed for singlar channel mode	(High speed mode)	2μs (500kHz)
	(Low speed mode)	2μs (500kHz)
Sampling speed for plural channel mode	(High speed mode)	(1μs)+(1μs/CH)
	(Low speed mode)	(1μs)+(4μs/CH)
Temperature drift		±25ppm/˚C

Table 2-2 Physical properties of SmCo magnet.

$d \times l$	2 mm × 9 mm
Residual magnetism	0.240 T
Coercive force	700-750 kA/m
Product (BH) maximum	175-191 kJ/m^3
Curie point	800 °C

Chapter 3

Estimation for axial development of measured void fraction with one-dimensional two-fluid model

3.1 Introduction

In this chapter, development of vertical upward LBE two-phase flow is investigated through one-dimensional analysis along flow direction. Regarding two-phase flow analytical model, there are mainly three typical models to analyze gas-liquid two-phase flow, i.e. homogeneous flow model, drift-flux model and two-fluid model. In the homogeneous flow model, gas-liquid two-phase flow is regarded as homogeneous mixture which has same velocity of gas and liquid phases. Comparing to such homogeneous flow model, difference of velocity between gas and liquid phases is taken into account in the drift-flux model. In the two-fluid model, conservation equations of mass, momentum and energy for gas and liquid phases are introduced to precisely treat two-phase flow. Therefore, the two-fluid model is considered as the most accurate theoretical model in comparison to other analytical models. As for the two-fluid model, one-dimensional simplified two-fluid model was proposed by Satyamurthy et al in 1997 [3-1] and it was applied to vertical upward mercury-nitrogen two-phase flow in a round channel in order to predict void fraction development along flow direction. Hence, in this study, the same prediction method is applied to LBE two-phase flow to predict void fraction development. And then, based on the comparison between the experimental and analytical results, validity of the model will be discussed.

3.2 Numerical analysis using one–dimensional two-fluid model

3.2.1 *Analysis using simplified two-fluid model proposed by Satyamurthy et al* [3-1]

In what follow, simplified analysis with a one-dimensional two-fluid model is explained. The governing equations are the conservation equations of mass and momentum.

Conservation equations of mass for each phase are derived as follows. As shown in **Figure 3-1**, the mass of gas which flows through arbitrary surface during 1 second can be written as below.

$$\rho_g u_g A\alpha$$

This mass of gas should equal to mass flow rate of gas, $\dot{m}_g$. Therefore, Equation (3-1) can be

obtained as the conservation equation of mass for gas phase.

$$\rho_g u_g \alpha A = \dot{m}_g \tag{3-1}$$

Also, the mass of liquid which flows through arbitrary surface during 1 second can be obtained by same consideration with gas phase. So, the mass for liquid phase is as follows.

$$\rho_l u_l A(1-\alpha)$$

This mass of liquid should equal to mass flow rate of liquid. Hence, conservation equation of mass for liquid phase is expressed as following Equation (3-2).

$$\rho_f u_f (1-\alpha) A = \dot{m}_f \tag{3-2}$$

Conservation equation of momentum for two-phase mixture is derived by following procedure. At first, two-phase mixture in vertical round pipe is assumed, which has Δz of thickness toward axial direction, as illustrated in **Figure 3-2**. In this case, conservation of momentum in the mixture is expressed as

$$\dot{m}_g u_{g,z} - \dot{m}_g u_{g,z+\Delta z} + \dot{m}_l u_{l,z} - \dot{m}_l u_{l,z+\Delta z} + P_z A - P_{z+\Delta z} A - \{\alpha\rho_g + (1-\alpha)\rho_l\} A \Delta z g - \tau\pi D \Delta z = 0.$$

Dividing both sides of this equation by $A\Delta z$, the equation is changed to following expression.

$$-\frac{\dot{m}_g}{A}\frac{u_{g,z+\Delta z} - u_{g,z}}{\Delta z} - \frac{\dot{m}_l}{A}\frac{u_{l,z+\Delta z} - u_{l,z}}{\Delta z} - \frac{P_{z+\Delta z} - P_z}{\Delta z} - \{\alpha\rho_g + (1-\alpha)\rho_l\} g - \frac{\tau\pi D}{A} = 0$$

When Δz becomes small enough, above equation can be as follows.

$$-\frac{\dot{m}_g}{A}\frac{du_g}{dz} - \frac{\dot{m}_l}{A}\frac{du_l}{dz} - \frac{dP}{dz} - \{\alpha\rho_g + (1-\alpha)\rho_l\} g - \frac{\tau\pi D}{A} = 0$$

$$\frac{\dot{m}_g}{A}\frac{du_g}{dz} + \frac{\dot{m}_l}{A}\frac{du_l}{dz} = -\frac{dP}{dz} - \{\alpha\rho_g + (1-\alpha)\rho_l\} g - \frac{\tau\pi D}{A}$$

Here, substituting Equations (3-1) and (3-2) into above equation, conservation equation of momentum for two-phase mixture is derived as below.

$$\alpha\rho_g u_g \frac{du_g}{dz} + (1-\alpha)\rho_l u_l \frac{du_l}{dz} = -\frac{dP}{dz} - \{\alpha\rho_g + (1-\alpha)\rho_l\}g - \frac{\tau\pi D}{A}$$

The last term on the right hand side expresses wall friction. In the previous study conducted by Satyamurthy et al. [5-1], the wall friction term is expressed by product between pressure drop assuming entire flow of liquid metal only and the square of two-phase multiplier, Φ_{lo}, where it is based on Friedel correlation [3-2]. Then, Equation (3-3) is derived as the conservation equation of momentum for two-phase mixture.

$$\alpha\rho_g u_g \frac{du_g}{dz} + (1-\alpha)\rho_f u_f \frac{du_f}{dz} = -\frac{dP}{dz} - \{\alpha\rho_g + (1-\alpha)\rho_f\}g - \Phi_{lo}^2\left(\frac{dP}{dz}\right)_{frlo} \tag{3-3}$$

In usual, the conservation equations used in the two-fluid model are completely separated in terms of gas and liquid phases. However, in this two-fluid model, the momentum equation for two-phase mixture is considered for the simplicity. Here, the pressure drop due to liquid metal flow and the square of two-phase multiplier are respectively written by Equations (3-4) and (3-5).

$$\left(\frac{dP}{dz}\right)_{frlo} = \frac{8f_{lo}(\dot{m}_l+\dot{m}_g)^2}{D^5\pi^2\rho_l} \tag{3-4}$$

$$\Phi_{fo}^2 = (1-X)^2 + X^2\frac{\rho_l f_{go}}{\rho_g f_{fo}} + \left[3.24\{X^{0.78}(1-X)^{0.24}\}\left(\frac{\rho_f}{\rho_g}\right)^{0.91}\left(\frac{\mu_g}{\mu_f}\right)^{0.19}\left(1-\frac{\mu_g}{\mu_f}\right)^{0.7} \Big/ F_r^{0.045}W_e^{0.035}\right] \tag{3-5}$$

, where the symbols, i.e. X, f, μ, F_r and W_e, denote quality, friction factor of each phase, viscosity of each phase, Froude number and Weber number. Here, the friction factor f can be given by following Colebrook equation [3-3]

$$\frac{1}{\sqrt{f_{lo}}} = -2\log\left(\frac{\varepsilon}{3.7D} + \frac{2.51}{R_e\sqrt{f_{lo}}}\right) \tag{3-6}$$

, where ε, D, Re indicate roughness at wall surface, diameter of flow channel and Reynolds number of each phase defined by diameter of flow channel. As mentioned in Chapter 2, commercial product of stainless steel pipe without any special surface treatment is used as flow channel. So, in this analysis, the value of roughness for normal stainless steel 304 is applied to Equation (3-6). In the calculation to determine the friction factor, Blasius' equation is utilized to define initial value of the friction factor

$$f_{ini} = 4 \times 0.0791 Re'^{\frac{1}{4}}, \tag{3-7}$$

where Re' means Reynolds number of each phase defined by diameter of flow channel.

Equation (3-4) is momentum equation for single rising bubble. The symbols, i.e. z, P, F_D, F_{VM} and V_b, denote axial position, pressure, interfacial drag force, virtual mass force and bubble diameter, respectively.

$$\rho_g u_g \frac{du_g}{dz} = -\frac{dP}{dz} - \rho_g g - \frac{F_D}{V_b} - \frac{F_{VM}}{V_b} \tag{3-8}$$

In order to use Equation (3-8), it is needed to determine initial bubble diameter. The initial bubble diameter can be given by using Kumar's empirical correlation as follows:

$$D_b = 1.56\left(Re^{0.058}\right)\left\{\frac{\Sigma_f D_h^{\,2}}{(\rho_f - \rho_g)g}\right\}^{\frac{1}{4}} \qquad \text{for } 1 \le Re \le 10 \tag{3-9}$$

$$D_b = 0.32\left(Re^{0.425}\right)\left\{\frac{\Sigma_f D_h^{\,2}}{(\rho_f - \rho_g)g}\right\}^{\frac{1}{4}} \qquad \text{for } 10 \le Re \le 2100 \tag{3-10}$$

$$D_b = 100\left(Re^{-0.4}\right)\left\{\frac{\Sigma_f D_h^{\,2}}{\left(\rho_f - \rho_g\right)g}\right\}^{\frac{1}{4}} \qquad \text{for} \quad 4000 \le Re \le 70000. \qquad (3\text{-}11)$$

Here, note that these equations from (3-9) to (3-11) are derived based on the experimental data of air-water, air-kerosene and air-glycerin systems. And these equations are not for liquid-metal gas-liquid two-phase flow. The symbols, Re, Σ_f and D_h, in these equations indicate Reynolds number in terms of gas phase defined by inner diameter of gas injection nozzle, surface tension of liquid phase and inner diameter of gas injection nozzle, respectively. In this model, spherical bubble and its expansion corresponding to change of absolute pressure are taken into account. To do that, equation of state of gas is used, which is shown below.

$$P = \rho_g RT \qquad (3\text{-}12)$$

, where R is the gas constant and T denotes temperature of gas or liquid phase. In this analysis, the temperature is given as constant value of 200 ˚C since temperature of the LBE two-phase flow in HESTIA was controlled as constant value of 200 ˚C by temperature control units.

Regarding interfacial drag force, Ishii-Mishima's empirical correlations [3-4] for interfacial drag force are utilized, which are shown in Equations (3-13) to (3-15) in this model. These equations can be used corresponding to each flow regime defined by flow regime map that was proposed by Taitel et al. [3-5] and these equation are correspond to bubbly, churn and slug flows, respectively.

$$F_D = 0.5\rho_f V_b \sqrt{\frac{g\left(\rho_f - \rho_g\right)}{\Sigma_f}}\left\{\frac{1+17.67\left(1-\alpha\right)^{\frac{9}{7}}}{18.67\left(1-\alpha\right)^{1.5}}\right\}^2 \left(u_g - u_f\right)\left|u_g - u_f\right| \quad \text{(Bubbly)} \qquad (3\text{-}13)$$

$$F_D = \frac{4}{3}\rho_f A_d \left(1-\alpha\right)^2 \left(u_g - u_f\right)\left|u_g - u_f\right| \quad \text{(Slug)} \qquad (3\text{-}14)$$

$$F_D = 4.9\rho_f A_d \left(1-\alpha\right)^3 \left(u_g - u_f\right)\left|u_g - u_f\right| \quad \text{(Churn)} \qquad (3\text{-}15)$$

In this model, numerical result of void fraction and entrance length shown in Equation (3-16) are utilized to judge flow regimes. So, in the analysis, bubbly flow is judged by condition of

void fraction less than 0.25, churn flow is defined by condition of void fraction larger than 0.25 and condition of axial position, z, less than the entrance length and slug flow can be recognized by condition of void fraction larger than 0.25 and condition of axial position, z, larger than the entrance length, respectively.

$$l_E = 40.6\left\{\frac{\alpha u_g + (1-\alpha)u_f}{\sqrt{gD}} + 0.22\right\}D \tag{3-16}$$

The virtual mass force developed for bubbly flow by Zuber [3-6], expressed as Equation (3-17), is utilized for all of flow regimes in this model.

$$F_{VM} = 0.5\frac{(1+2\alpha)}{(1-\alpha)}V_b\rho_f u_g \frac{d}{dz}(u_g - u_f) \tag{3-17}$$

In this simplified two-fluid model, void fraction and pressure profiles along flow direction can be obtained by conducting integration along flow direction once the initial bubble diameter can be given in this model.

3.2.2 *Simulated systems and condition*

The schematic diagram of simulated system in the analysis is illustrated in **Figure 3-3**. In the analysis, LBE two-phase flow flowing in the vertical circular pipe having inner diameter of 50 mm and length of 1.9 m is simulated. The origin of the z axis is located at 100 mm above the top end of gas-liquid mixing chamber. Although the mixing chamber is located at below from the origin of the z axis, the initial bubble diameter is given approximately at the origin of the z axis. Here, the inner diameter of gas injection nozzles is 0.75 mm. The number of the nozzles is 101.

The flow parameters which used for the analysis are superficial gas velocity in the range from 0.05 to 0.15 m/s and superficial liquid velocity in the range from 0.1 to 0.2 m/s. The physical properties of the LBE and the nitrogen were calculated corresponding to 200℃.

3.2.3 *Computational procedure*

Computational procedure for calculating axial profile of void fraction and pressure is illustrated in **Figure 3-4**. In this procedure, physical properties of nitrogen gas and LBE, corresponding to their temperature of 200 ˚C, are substituted into Equations (3-1) to (3-17). And mass flow rate which can be calculated from densities of nitrogen gas and LBE and

experimental conditions of j_g, j_l and D is given to Equations (3-1) and (3-2) as initial condition. Then, inner diameter of gas injection nozzle, D_h, is substituted into Kumar's formula to estimate initial bubble diameter. After that, initial void fraction and pressure are introduced to Equations (3-1) to (3-17), where experimental results of cross sectional averaged void fraction measured at z/D = 3.2 was applied to this calculation as initial value and absolute pressure estimated by atmospheric pressure and height of LBE was given to this calculation. Then, friction factor, two-phase pressure drop and interfacial drag force are calculated.

Void fraction and pressure are estimated by using Runge-Kutta method iteratively. From Equations (3-1) to (3-17), gradient of void fraction and pressure can be solved as shown in Equations (3-18) and (3-19).

$$\frac{d\alpha}{dz} = func.1(\alpha, P) \tag{3-18}$$

$$\frac{dP}{dz} = func.2(\alpha, P) \tag{3-19}$$

As shown in **Figure 3-4,** in the Runge-Kutta method, 4 sets of gradient for the void fraction and the pressure are respectively estimated from Equations (3-18) and (3-19) and axial step length, Δz by conducting following calculation.

$$S_{\alpha 1} = \frac{d\alpha}{dz} = func.1(\alpha_1, P_1) \tag{3-20}$$

$$S_{P1} = \frac{dP}{dz} = func.2(\alpha_1, P_1) \tag{3-21}$$

$$S_{\alpha 2} = \frac{d\alpha}{dz} = func.1\left(\alpha_1 + \frac{S_{\alpha 1} dz}{2}, P_1 + \frac{S_{P1} dz}{2}\right) \tag{3-22}$$

$$S_{P2} = \frac{dP}{dz} = func.2\left(\alpha_1 + \frac{S_{\alpha 1} dz}{2}, P_1 + \frac{S_{P1} dz}{2}\right) \tag{3-23}$$

$$S_{\alpha 3} = \frac{d\alpha}{dz} = func.1\left(\alpha_1 + \frac{S_{\alpha 2} dz}{2}, P_1 + \frac{S_{P2} dz}{2}\right) \tag{3-24}$$

$$S_{P3} = \frac{dP}{dz} = func.2\left(\alpha_1 + \frac{S_{\alpha 2}dz}{2}, P_1 + \frac{S_{P2}dz}{2}\right) \quad (3\text{-}25)$$

$$S_{\alpha 4} = \frac{d\alpha}{dz} = func.1(\alpha_1 + S_{\alpha 3}dz, P_1 + S_{P3}dz) \quad (3\text{-}26)$$

$$S_{P4} = \frac{dP}{dz} = func.2(\alpha_1 + S_{\alpha 3}dz, P_1 + S_{P3}dz) \quad (3\text{-}27)$$

From those 4 gradients shown in Equations (3-20) to (3-27) and *dz*, the void fraction and the pressure are predicted by using average value of those gradients and *dz*.

$$\alpha_2 = \alpha_1 + \frac{1}{6}(S_{\alpha 1} + 2S_{\alpha 2} + 2S_{\alpha 3} + S_{\alpha 4})dz \quad (3\text{-}28)$$

$$P_2 = P_1 + \frac{1}{6}(S_{P1} + 2S_{P2} + 2S_{P3} + S_{P4})dz \quad (3\text{-}29)$$

These calculations are continued until z = 1.9 m is satisfied.

3.3 Comparison of calculated results with experiments

3.3.1 *Numerical results simulated by simplified two-fluid model proposed by Satyamurthy et al (1997)*[3-1]

Example of comparison of cross sectional averaged void fraction profile between experimental and numerical results in condition of j_g = 0.15 m/s and j_l = 0.2 m/s is shown in **Figure 3-5**. Three plots in the figure indicate experimental results and the solid line represents numerical result. It is found that the numerical result cannot reproduce experimental void fraction profile since the numerical result overestimates the experimental results. Then, it is needed to modify or improve the simplified two-fluid model.

It can be considered that assuming only spherical bubble and no coalescence and break up behaviors of bubble would be one of the causes of this overestimation. No consideration in terms of bubble diameter distribution also would be one of the factors of the overestimation. In addition, making use of interfacial drag force which was derived based on the database in terms of air-water two-phase flow is also one of the causes of the disagreement. Therefore, in this work, modification of drag coefficient in interfacial drag force equations was tried to improve the model.

3.3.2 *Modification method for drag coefficient in the interfacial drag force equations*

Assuming the situation of single rising bubble having rising velocity of u_∞ and project area of A_d in stagnant water, the drag coefficient can be derived from the balance between the buoyancy and drag forces, as shown in Equation (3-30). Also the rising velocity of bubble can be expressed by making use of void fraction weighted mean drift velocity, as shown in Equation (3-31).

$$C_D = \frac{2(\rho_f - \rho_g)g}{\rho_f u_{g\infty}|u_{g\infty}|}\frac{V_b}{A_b}. \tag{3-30}$$

$$u_{g\infty} = \frac{V_{gj}}{(1-\alpha)^k} \tag{3-31}$$

Then following modified drag coefficient is able to be obtained by substituting Equation (3-31) into Equation (3-30).

$$C_D = \frac{2(\rho_f - \rho_g)g}{\rho_f V_{gj}|V_{gj}|}\frac{V_b}{A_b}(1-\alpha)^{2k} \tag{3-32}$$

Then, modified interfacial drag force can be derived, as shown in Equation (3-33)

$$F_D = \frac{1}{2}\frac{2(\rho_f - \rho_g)g}{\rho_f V_{gj}|V_{gj}|}\frac{V_b}{A_b}(1-\alpha)^{2k}\rho_f(u_g - u_f)|u_g - u_f|A_b. \tag{3-33}$$

Here, the drift velocity is given through drift-flux model proposed by Zuber and Findlay [3-7]. The model has been applied to a wide range of two-phase flow problems due to its simplicity in comparison with two-fluid model. In the drift-flux model, velocity difference between gas and mixture is taken into account by introducing following local drift velocity

$$v_{gj} = u_g - j. \tag{3-34}$$

Using Equation (3-34), cross sectional averaged superficial gas velocity is given as

$$\langle j_g \rangle = \langle \alpha u_g \rangle = \langle \alpha j \rangle + \langle \alpha v_{gj} \rangle . \tag{3-35}$$

where j_g, j and α denote the superficial gas velocity, the total superficial velocity and the void fraction, respectively.Then following equation can be derived

$$\frac{\langle j_g \rangle}{\langle \alpha \rangle} = \frac{\langle \alpha u_g \rangle}{\langle \alpha \rangle} = \frac{\langle \alpha j \rangle}{\langle \alpha \rangle} + \frac{\langle \alpha v_{gj} \rangle}{\langle \alpha \rangle}$$

$$\frac{\langle j_g \rangle}{\langle \alpha \rangle} = C_0 \langle j \rangle + V_{gj} \tag{3-36}$$

C_0 and V_{gj} denote the distribution parameter and the void fraction weighted mean drift velocity defined respectively as follows:

$$C_0 = \frac{\langle \alpha j \rangle}{\langle \alpha \rangle \langle j \rangle} \tag{3-37}$$

$$V_{gj} = \frac{\langle \alpha v_{gj} \rangle}{\langle \alpha \rangle} . \tag{3-38}$$

3.3.3 *Comparison of axial void fraction profile between experimental and predicted results by two-fluid model including modified interfacial drag force equation*

Figure 3-6 denotes comparison of simulated axial void fraction profile in terms of change of some drag coefficients, i.e. the void fraction weighted mean drift velocities is regarded as variable. From the figure, it is found that the calculated values of axial void fraction in each case of the void fraction weighted mean drift velocity shows decrease with increasing the drift velocity. Therefore, it is suggested that the drift velocity should be given to Equation (3-24) precisely in order to improve prediction accuracy of the model.

The void fraction weighted mean drift velocity calculated by using experimental data

measured by Yamamoto [3-8] and Asai [3-9] is provided in **Figure 3-7**. In the experimental condition of superficial gas velocity j_g = 0.15 m/s and superficial liquid velocity j_l = 0.2 m/s, the estimated drift velocities are approximately 0.27 m/s. Hence ensemble averaged value of the drift velocity, which is calculated by three data plots shown in the **Figure 3-7** was applied to the simplified two-fluid model in order to confirm the prediction accuracy of the model. **Figure 3-8** shows newly calculated result of axial void fraction using the averaged drift velocity in the same condition of the superficial gas velocity and the superficial liquid velocity. From the **Figure 3-8**, it can be said that the newly estimated result shows good agreement with the experimental results measured by Yamamoto [3-8] at any measurement locations. Other numerical results in different conditions of superficial gas and liquid velocities are provided in **Figure 3-9** and **Figure 3-10**, which show comparison of previous numerical results (a) and newly simulated results. Although the numerical results show slightly underestimated values at the highest measurement location in case of the superficial liquid velocity equals to 0.1 m/s, as shown in **Figure 3-9**, it also can be mentioned from both of **Figures 3-9** and **3-10** that the prediction accuracy of the model for the axial void faction is improved by the modification of the interfacial drag force equation.

3.3.4 *Axial distribution of gas and liquid velocities*

Cross averaged gas and liquid velocities are able to be simulated based on the conservation equation of mass shown as Equations (3-1) and (3-2) by substituting calculated void fraction into each equations. The comparisons of gas velocity in terms of numerical results and experimental results measured by 4-sensor type EC probe are shown in **Figures 3-11** and **3-12**, where **Figures 3-11(a)** and **3-12(a)** denote the comparison before the modification of the interfacial drag force and **Figures 3-11(b)** and **3-12(b)** show the comparison after the modification of the drag force. From these figures, it can be said that there are complete disagreements between the numerical results and the experimental results regardless of the modification of the interfacial drag force.

Also comparisons of numerically simulated liquid velocity with experimental results measured by the EM probe are shown in **Figures 3-13** and **3-14**, where **Figures 3-13(a)** and **3-14(a)** denote the comparison before the modification of the interfacial drag force and **Figures 3-13(b)** and **3-14(b)** show the comparison after the modification. From the **Figure 3-13**, it is found that the numerical result denotes agreement with measured liquid velocities in case of j_g = 0.05 m/s regardless of the modification for the interfacial drag force. However, in case of other superficial gas velocities, which are shown in **Figure 3-13(a)**, numerically calculated liquid velocities show disagreement with the experimentally obtained liquid velocities with increasing the superficial gas velocity. From **Figure 3-13(b)**, it is found that the numerical liquid velocities

indicate values close to the measured liquid velocity at the lowest axial position. However, the numerical results show disagreement with the experimental data at higher axial positions. On the other hand, in case of **Figure 3-14**, better predicted liquid velocities are able to be obtained after the modification of the equation for interfacial drag force in the simplified two-fluid model.

3.4 Conclusion

In this chapter, one-dimensional analysis using simplified two-fluid model proposed by Satyamurthy et al. [3-1] is explained and carried out to obtain numerically simulated axial void fraction, gas velocity and liquid velocity. From the comparisons between the calculated results and experimentally measured results of these parameters show disagreement in case of utilizing the original simplified two-fluid model. In order to improve prediction accuracy of the model for analysis of LBE two-phase flow, the equation of interfacial drag force was modified by using void fraction weighted mean drift velocity. After the modification, the prediction accuracy of axial void fraction was improved. In terms of gas velocity, there is a big disagreement between predicted and measured one. However, as a result, more precise prediction method for axial void fraction profile measured in LBE two-phase flow was established through this work.

References for Chapter 3

[3-1] Satyamurthy, P., et al., “Two-fluid model studies for high density two-phase liquid metal vertical flows”, Int. J. of Multiphase Flow, 24 (1998) 721-737.

[3-2] Friedel L. Improved friction pressure drop correlation for horizontal and vertical two-phase pipe flow. European two-phase group meeting 1979 Jun.

[3-3] Giles, R.V. Fluid mechanics and hydraulics. Schaum's Outline Series. McGraw-Hill, Singapore 1983.

[3-4] Ishii M, Mishima K. Two-fluid model and hydrodynamic constitutive relations. Nuclear Engineering and Design 1984; 82: 107-126.

[3-5] Taitel Y, Bornea D, Duckler A E. Modeling flow pattern transition for steady upward gas-liquid flow in vertical tubes. A. I. Ch. E. Journal 1980; 26: 345-354.

[3-6] Zuber N. On the dispersed two-phase flow on the laminar flow regime. Chemical Engineering Science 1964; 19: 897-917

[3-7] Zuber N, Findlay JA, General Electric Report GEAP-4592.

[3-8] Yamamoto, Y., Study on characteristics of gas-liquid two-phase flow for liquid heavy metal, M.S. thesis 2012; Kyoto University.

[3-9] Asai Y. Study on turbulence characteristics of heavy liquid metal gas-liquid two-phase flow, M.S. thesis 2013; Kyoto University.

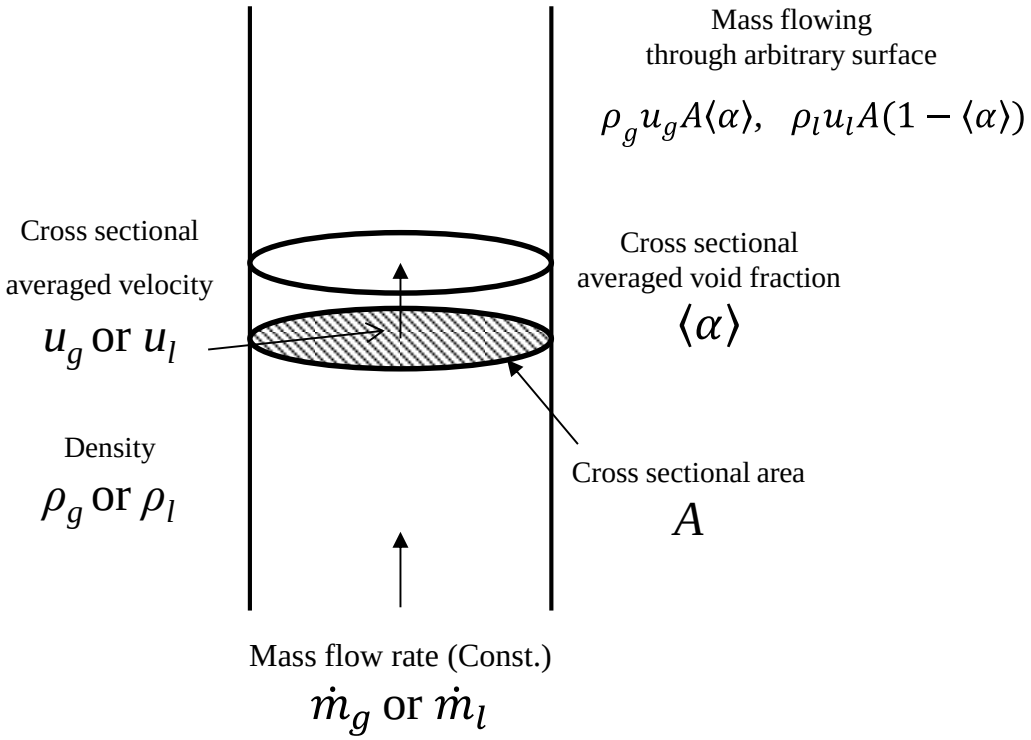

Figure 3-1 Mass of gas or liquid phase flowing through the arbitrary surface during 1 second, which is considered in one-dimensional two-fluid model.

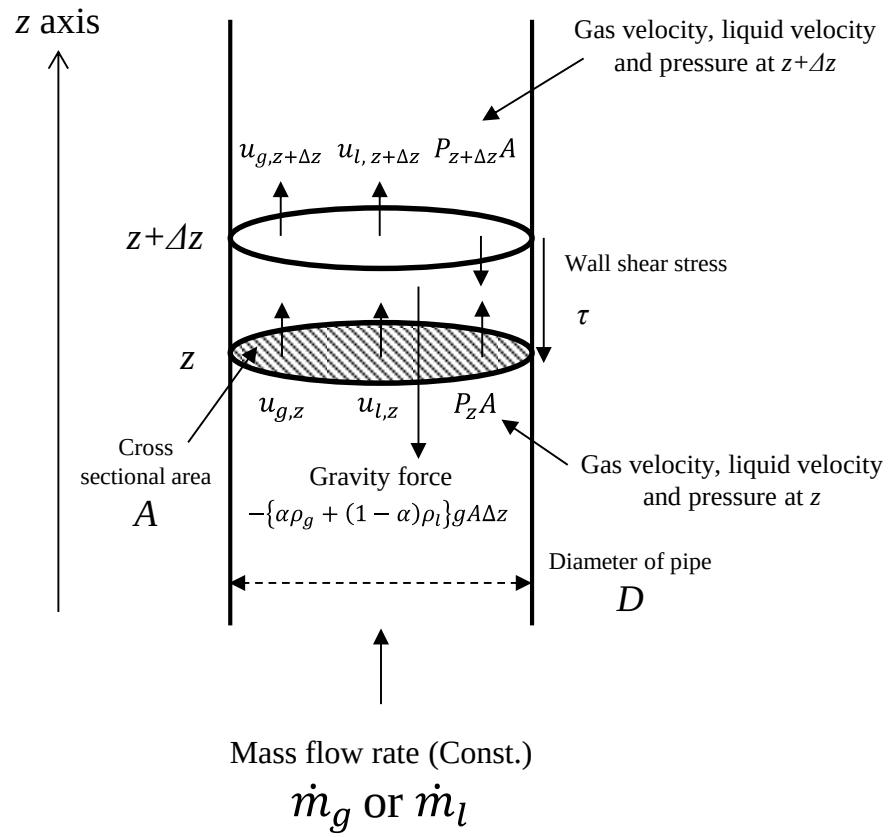

Figure 3-2 Physical quantities for two-phase mixture in a vertical round pipe.

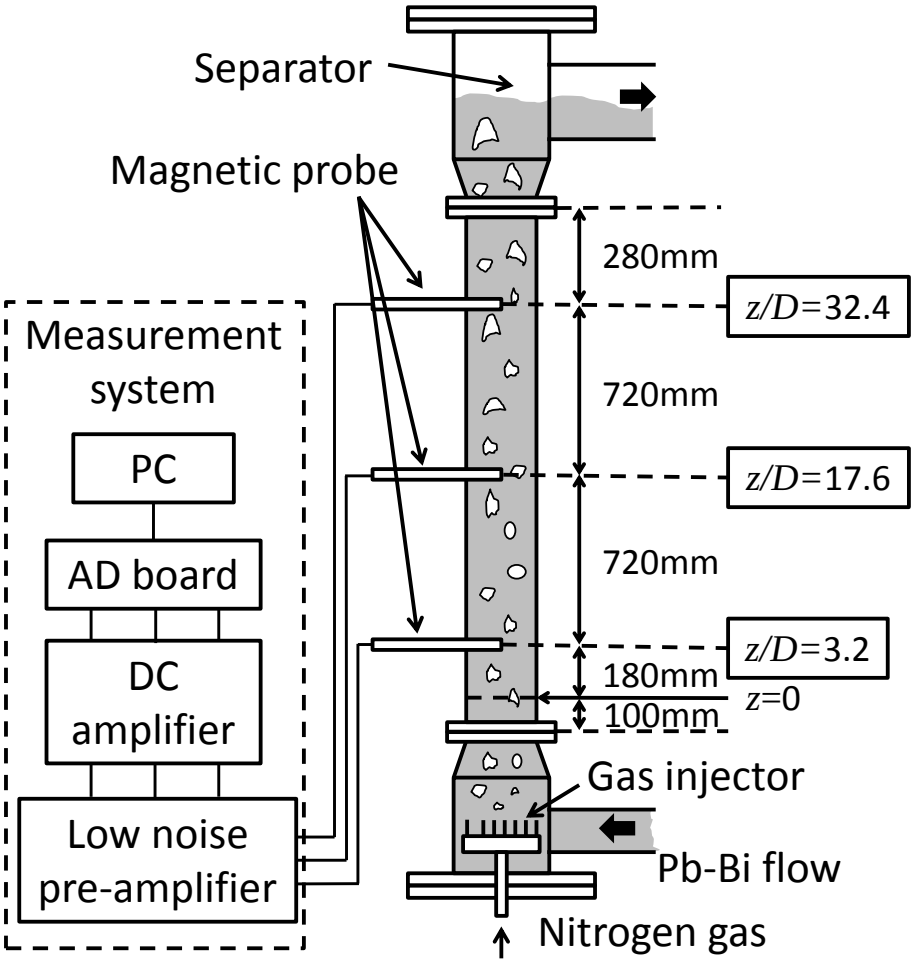

Figure 3-3 Simulated system in the analysis using one-dimensional two-fluid model.

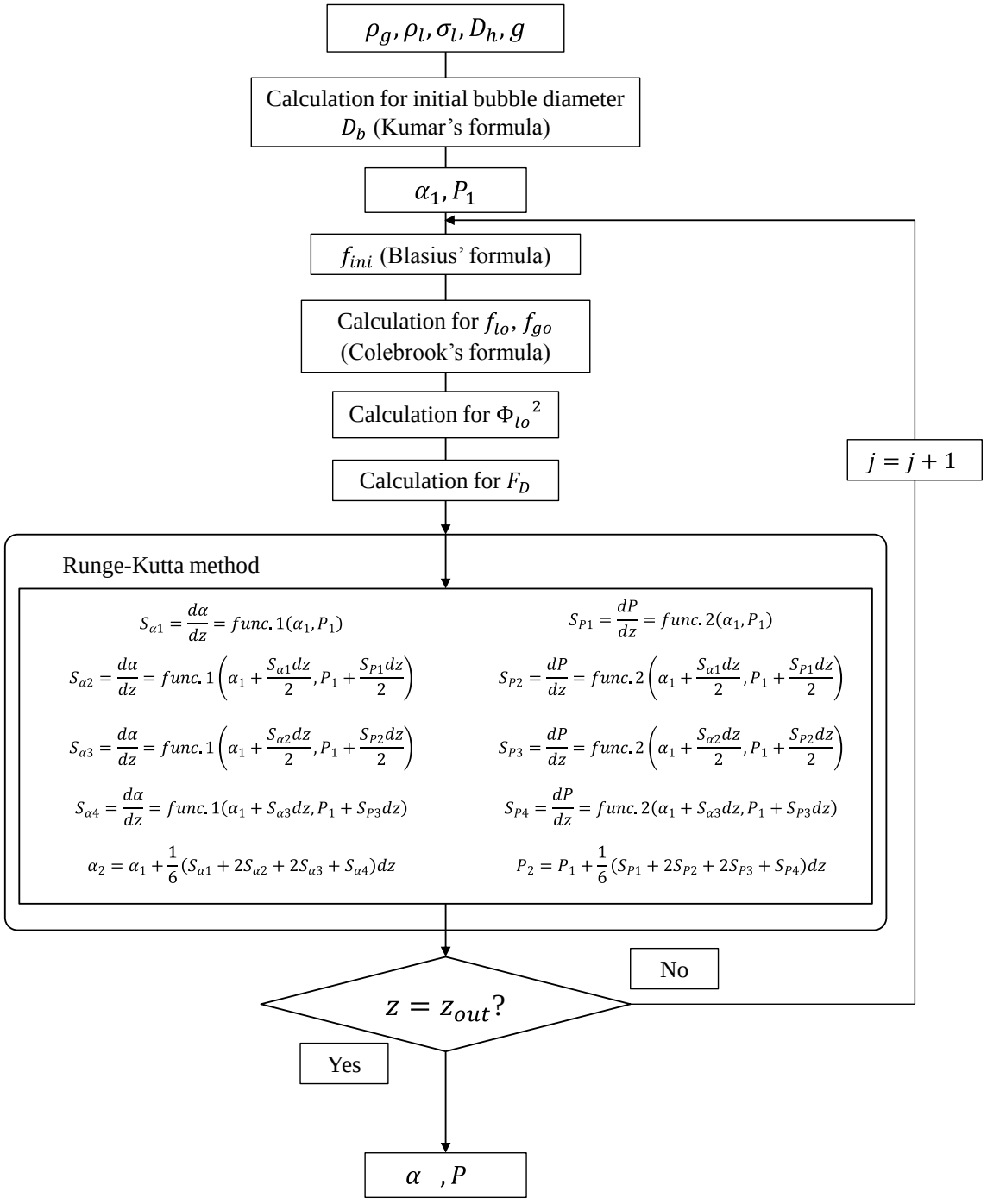

Figure 3-4 Computational procedure for analyzing axial profile of void fraction.

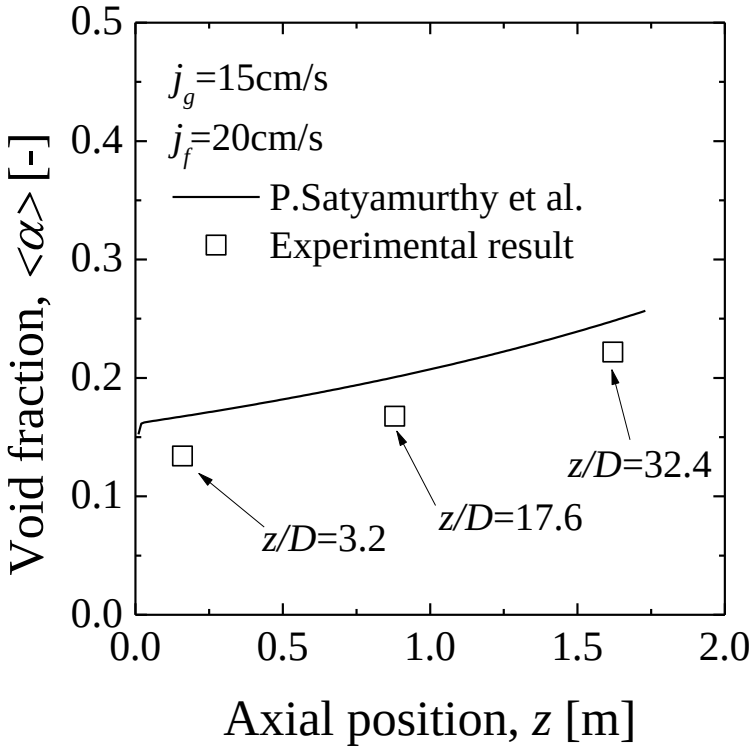

Figure 3-5. Comparison of calculated axial void fraction using the model proposed by Satyamurthy et al. (1997) with experimental results.

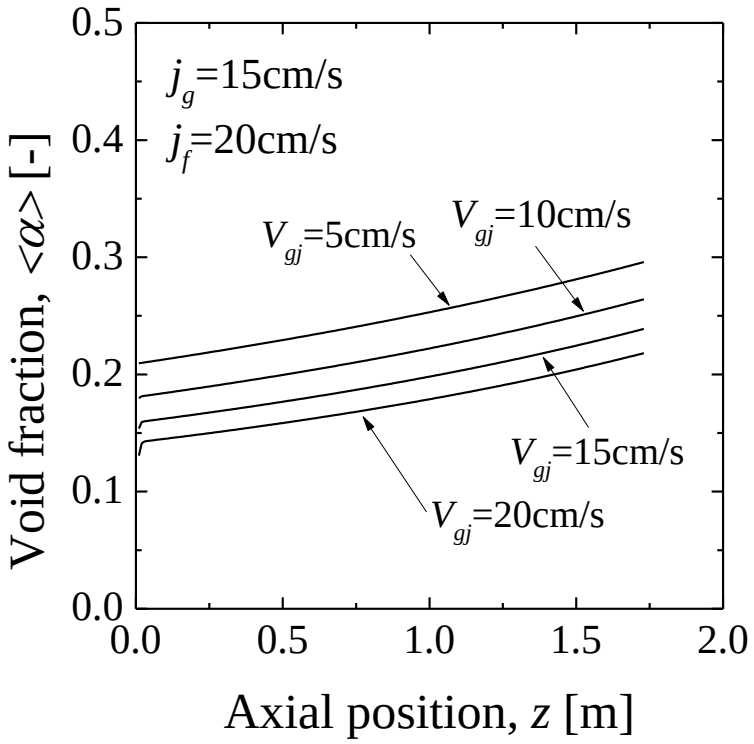

Figure 3-6. Effect of drift velocity on calculated axial void fraction.

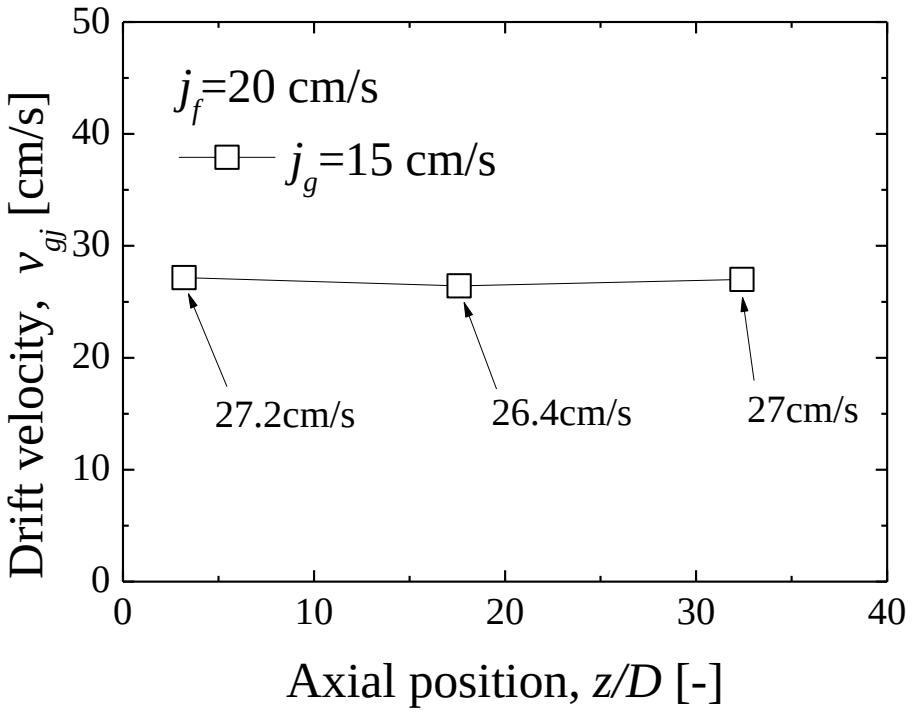

Figure 3-7. Axial profile of drift velocity.

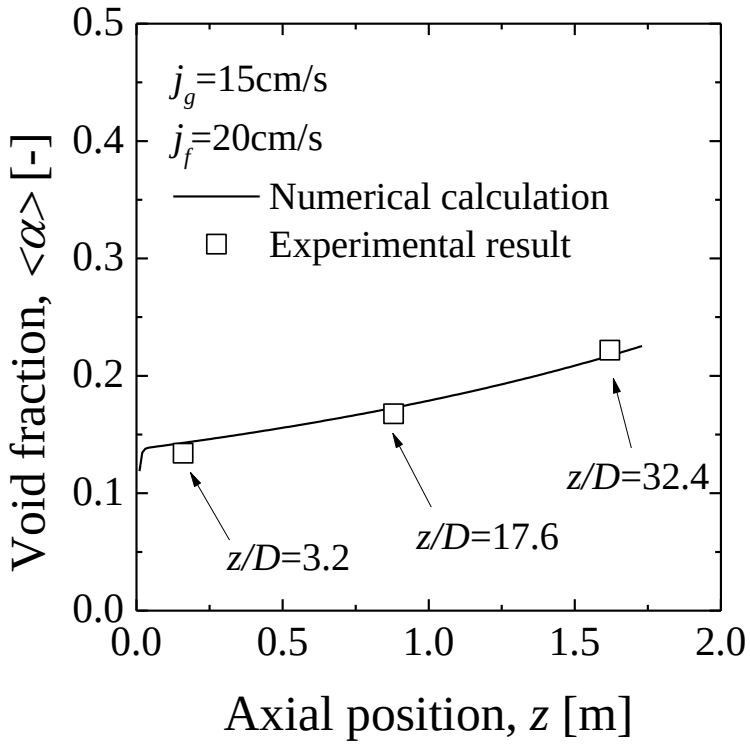

Figure 3-8. Comparison of calculated axial void fraction using the modified model with experimental results.

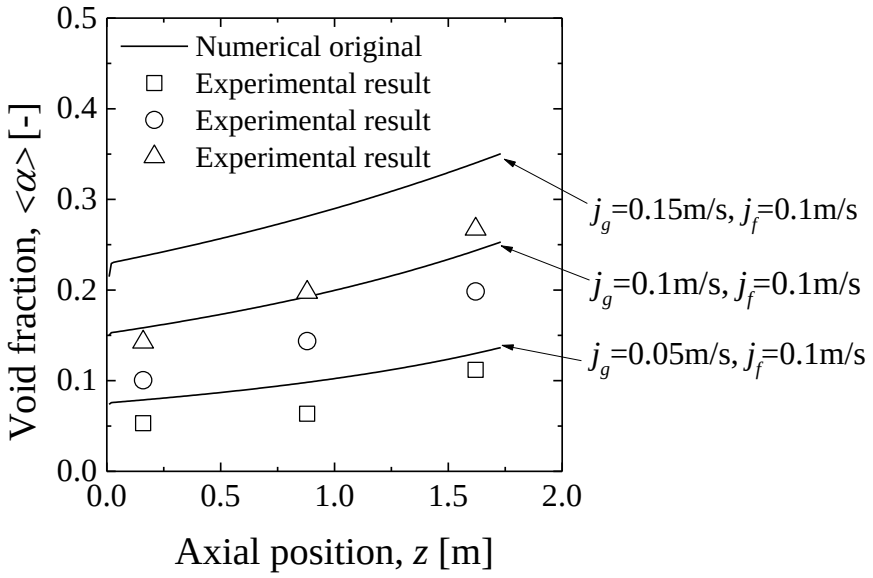

(a)

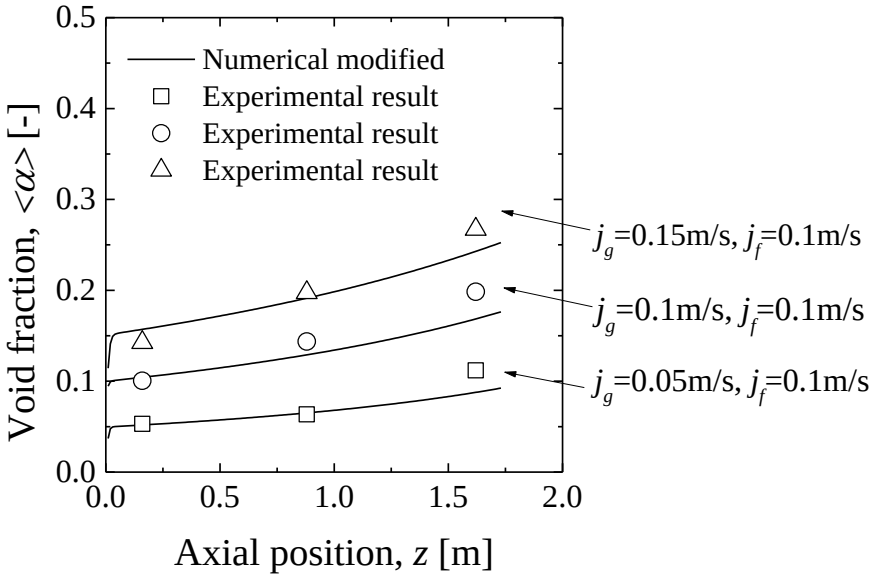

(b)

Figure.3-9 Comparison between (a) original numerical and (b) modified results for V_{gj}=0.35m/s of void fraction development along flow direction.

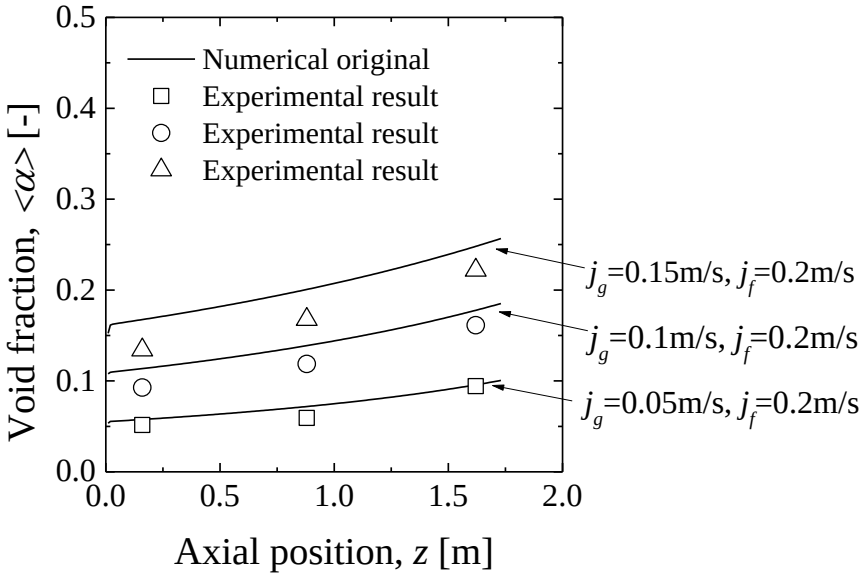

(a)

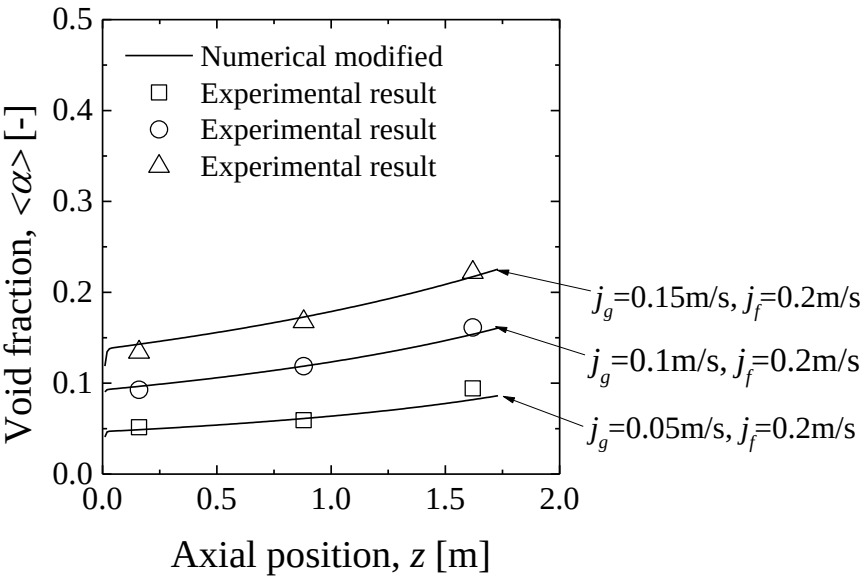

(b)

Figure.3-10 Comparison between (a) original numerical and (b) modified results for V_{gj}=0.27m/s of void fraction development along flow direction.

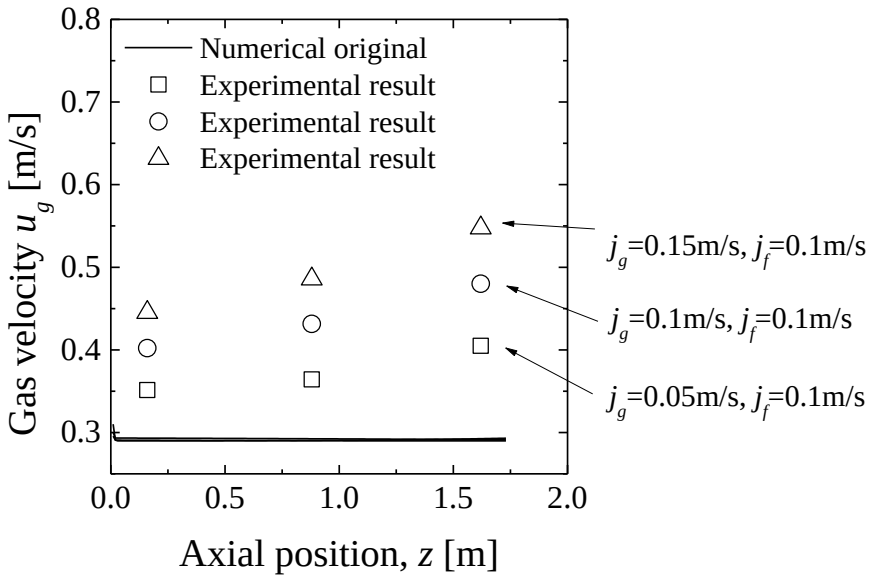

(a)

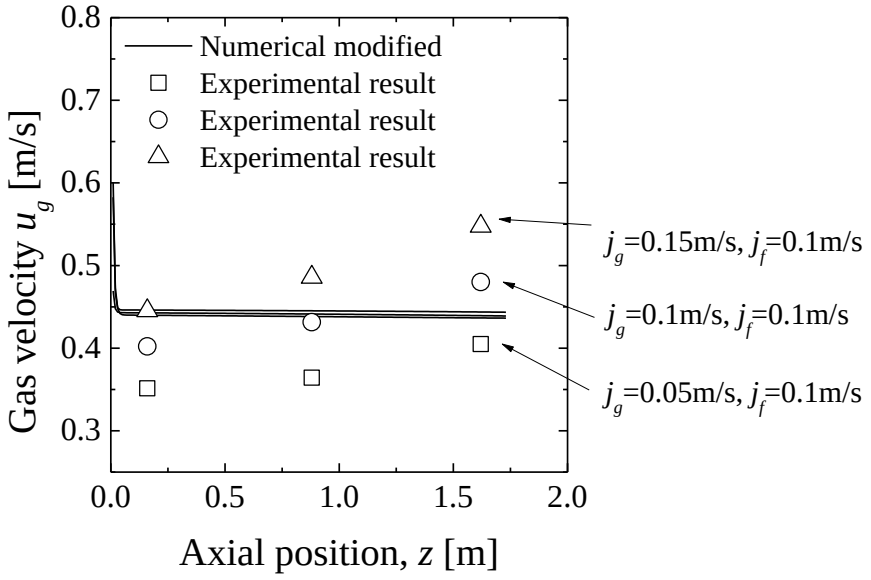

(b)

Figure.3-11 Comparison between (a) original numerical and (b) modified results for V_{gj}=0.35m/s of gas velocity development along flow direction.

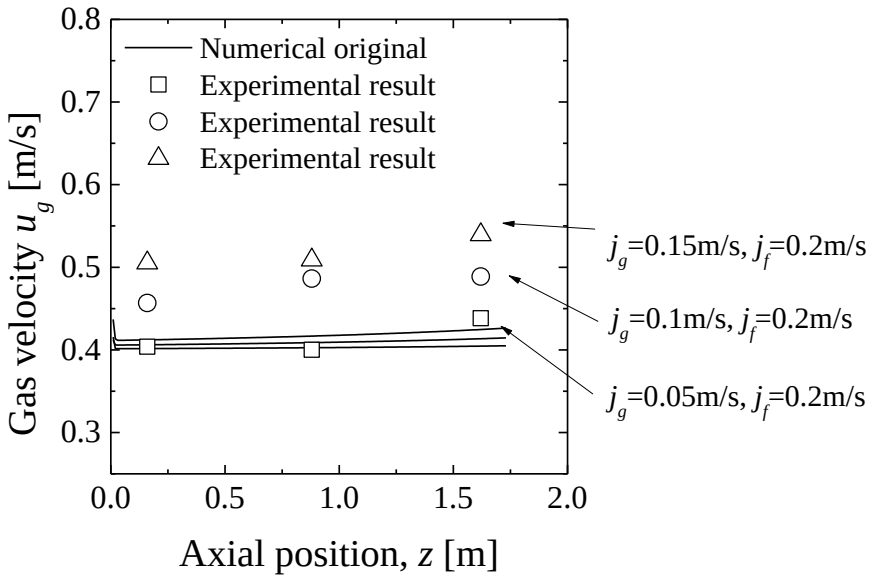

(a)

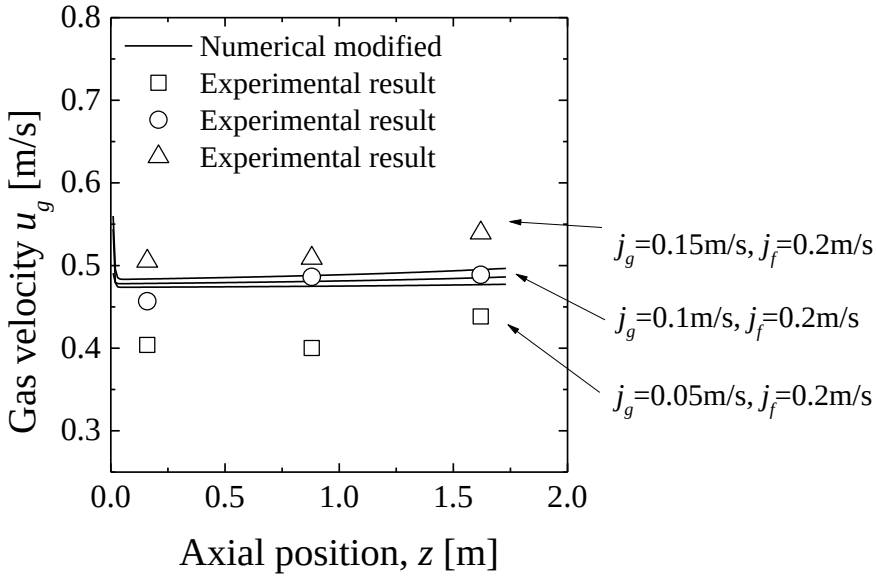

(b)

Figure.3-12 Comparison between (a) original numerical and (b) modified results for V_{gj}=0.27m/s of gas velocity development along flow direction.

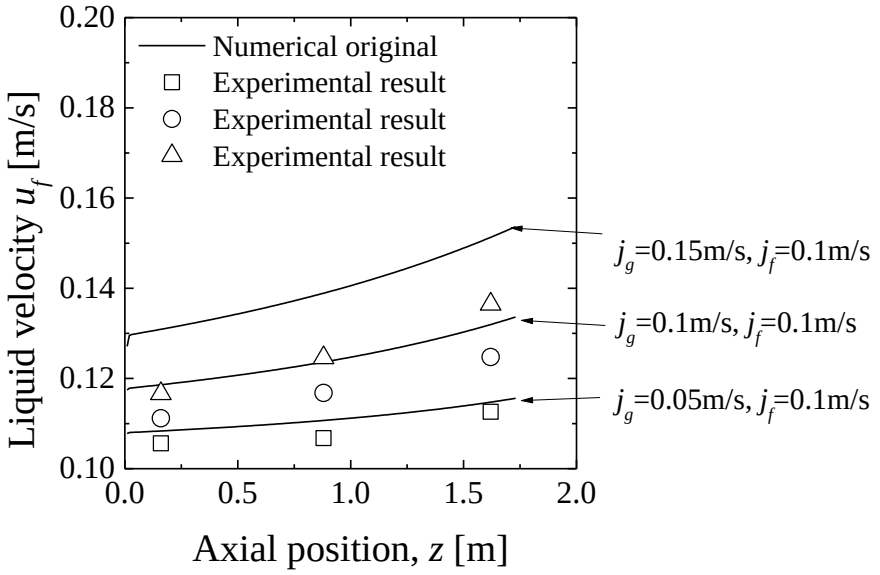

(a)

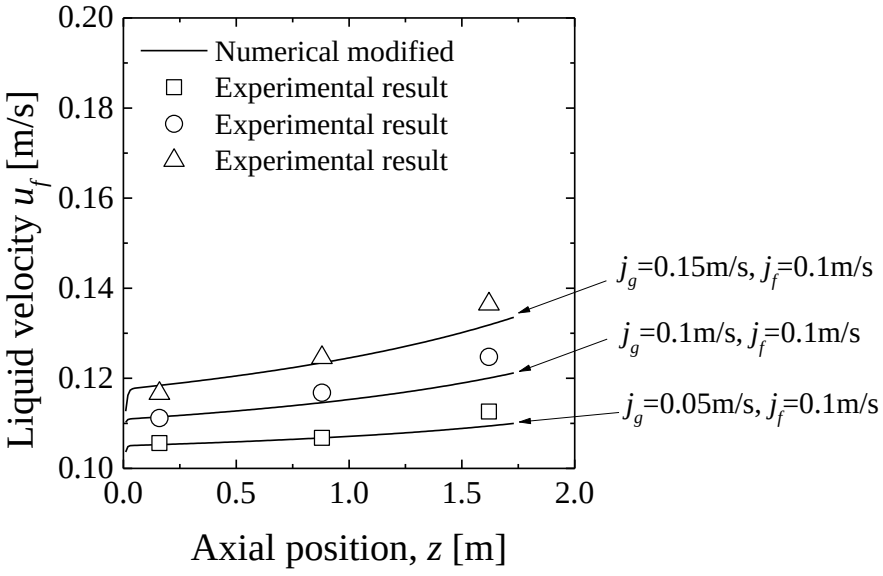

(b)

Figure.3-13 Comparison between (a) original numerical and (b) modified results for V_{gj}=0.35m/s of liquid velocity development along flow direction.

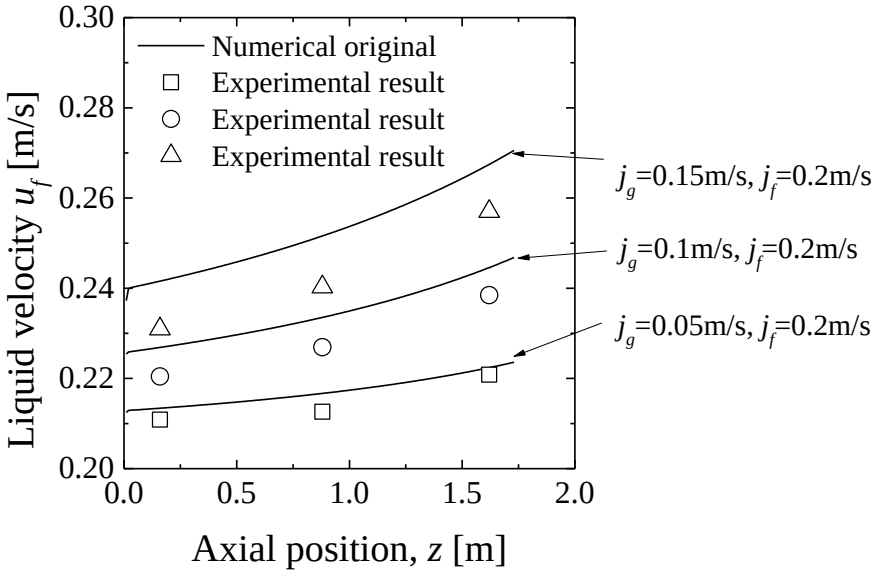

(a)

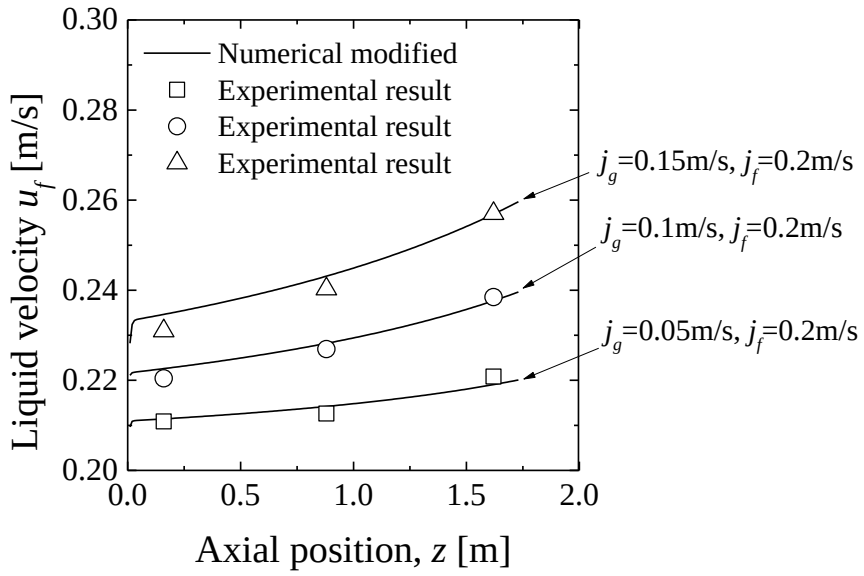

(b)

Figure.3-14 Comparison between (a) original numerical and (b) modified results for V_{gj}=0.27m/s of liquid velocity development along flow direction.

Chapter 4

Effect of wall wettability condition on drift-flux parameters in lead-bismuth two-phase flow in circular and annular bubble columns

4.1 Introduction

In this chapter, LBE two-phase flow in a cylindrical bubble column was studied. In practical condition of ADS, a number of fuel rods are installed. If there is the case of changing wall surface wettability due to flowing LBE or other factor, the effect of wall surface wettability on LBE two-phase flow might be larger. Therefore LBE bubble columns equipping simple circular channel and annular channel were studied to simulate the reactor pool condition and the fuel rods immersed in the pool. In the experiments, measurements of volume averaged void fraction were carried out to evaluate the two-phase flow characteristics of the LBE two-phase flow by varying the wall surface wettability. Also void fraction weighted mean drift velocity and distribution parameter in the bubble column were discussed.

4.2 Experimental apparatus and method

4.2.1 *Experimental apparatus and conditions*

The schematic diagram of LBE bubble column apparatus, HEavy liquid metal Single and Two-phase flows Instrumentation for Accelerator-driven system 2; HESTIA2 which was developed and used for our bubble column experiments is illustrated in **Figure 4-1**. The HESTIA2 consists of a test section, a gas injection system, a drain tank, and a differential pressure gauge. Detailed explanation about the HESTIA2 will be described in following section.

A) Test section of HESTIA2

The test section is a vertical round stainless steel (SS 304) pipe, having an inner diameter of 102.3 mm and a length of 1001.5 mm. As shown in **Figure 4-1**, in order to change the hydraulic equivalent diameter of the test section, three inner concentric rods can be inserted into the test section so that these rods were perpendicular to the bottom of test section. So, four conditions of hydraulic equivalent diameters, including circular pipe condition, can be achieved. Due to those inner concentric pipes, effect of the size of wall surface area on change of wall wettability can be evaluated.

B) Gas distributor

As shown in **Figure 4-1**, the gas distributor is installed at the bottom of the test section and it consists of stainless steel circular plate having 60 holes and 60 pipes having inner diameter of 0.15 mm, which they are arranged and inserted into the plate at even intervals. The schematic of the gas distributor is shown in **Figure 4-2**. Since the operation temperature of the HESTIA2 is from 200 to 280℃, AREMCO-BOND 526N (Aremco Products Inc.) which has sufficient heat resistance in that temperature region, the temperature of heat-resistance is up to 300℃, was utilized to fix the plate and 60 pipes.

C) Drain tank

The drain tank is used for storage of the LBE and is connected to vacuum pump and argon-hydrogen cylinder. Then the air is removed from the tank by the pump and the argon-hydrogen is utilized as a cover gas to prevent oxidation of the LBE. Also the argon-hydrogen is used to transfer the LBE to the test section when the experiments are carried out.

The working fluids are molten LBE (Pb: 44.5wt%, Bi: 55.5wt%) and nitrogen gas. The nitrogen gas was injected from bottom of the test section through the gas distributor. The nitrogen gas was exhausted to the atmosphere from the test section via exhaust line. The gas flow rate was controlled and measured by a mass flow controller (HORIBA STEC Co. Ltd.: SEC-E40, SEC-E50, SEC-E52). In the experiment, superficial gas velocities were changed from 0.014 to 0.129 m/s. Those superficial gas velocities were collected by taking the static pressure at the measurement section into account. The differential pressure was measured by using a differential pressure transmitter (KOBATA GAUGE MFG. CO., LTD: MDC-Y442) for 60 seconds at 100 Hz to estimate the time-averaged volumetric void fraction at the measurement section.

The temperature of working fluids was controlled by temperature controller units and kept at a constant temperature of 200 °C. The flow rate, differential pressure and temperature were monitored by a data acquisition unit connected to a PC.

4.2.2 *Surface treatment for channel wall using soldering flux*

In the LBE cooled ADS, the stainless steel is protected from corrosive nature of the LBE by such a passivate oxide layer. Several researches have been performed to investigate the erosion/corrosion resistance of materials with such oxide layer by changing oxide concentration and temperature of the LBE. It was found that such oxide layer shows an excellent corrosive

resistance up to 600℃, however showing poor wettability to the LBE. Therefore, it is very important to understand the effect of the wettability on the thermal-hydraulics of the LBE.

As mentioned above, oxide layer is formed on the surface of stainless steel with enough oxygen in the LBE showing poor wettability. To achieve good wettability condition, the oxide layer should be removed [4-10, 4-28]. In this experiment, soldering flux (NIPPON WELDING ROD CO., LTD: Wel flux No.51) was used for removing oxide layer from the surface of the test section.

The surface treatment process is as follows:

I. As shown in **Figure 4-3**, soldering flux is poured into the test section by varying the surface level of the LBE.

II. The oxide layer is removed from the wall surface, which is plated by the LBE.

III. The soldering flux and other impurities on the free surface are removed from the test section.

Although LBE free surface shows convex meniscus before conducting these procedures, the meniscus changes to concave after the surface treatment; the surface shows good wettability to LBE, as shown in **Figure 4-4**. Since the activation temperature for the soldering flux was 260℃, the above mentioned surface treatment was carried out at 280℃. The compositions of the soldering flux are shown in **Table 4-1**.

4.2.3 *Differential pressure gauge for void fraction measurement*

Differential pressure gauge is useful tool for measuring volumetric void fraction in gas-liquid two-phase flow because of its simplicity. As shown in **Figure 4-5**, when pressures are measured at different locations in a vertical pipe, absolute pressures at each pressure port and differential pressure between the ports can be calculated by following equations.

$$P_1 = P_0 + \rho_l h_1 (1-\alpha_1) g \tag{4-1}$$

$$P_2 = P_0 + \rho_l h_1 (1-\alpha_1) g + \rho_l (h_2 - h_1)(1-\alpha_2) g \tag{4-2}$$

$$\Delta P = \rho_l (h_2 - h_1)(1-\alpha_2) g \tag{4-3}$$

Then, the volumetric void fraction is obtained by the following equation.

$$\alpha_2 = 1 - \frac{\Delta P}{\rho_l (h_2 - h_1) g} \tag{4-4}$$

Selection of the differential pressure gauge

In the present experiments, the pressure receiver of the differential pressure gauge is exposed to a high temperature since the operating temperature of the experimental apparatuses is 200 – 280℃. Also, in general, as mentioned in Chapter 1, the LBE has strong corrosion characteristics to some kinds of metal [1-15 – 1-16]. Therefore, the differential pressure gauge should have high heat-resistance and corrosion-resistance. In this study, the diaphragm pressure gauge made of stainless steel was selected to prevent the heat damage and the corrosion attack from the LBE.

The length of measurement section, i.e. distance between the pressure ports, installed in the HESTIA2 is 350 mm. So, differential pressure between the pressure ports can be calculated based on Equation (2-3). The maximum differential pressure which is achieved in case of $\alpha_2 = 0$ is estimated as 35.9 kPa.

Hence, in this study, the diaphragm type differential pressure gauge that has measuring range from 0 to 50 kPa was used for measurement of volumetric void fraction (KOBATA GAUGE MFG. CO., LTD: MDC-Y442). The schematic expression of the differential pressure gauge is shown in **Figure 4-6** and the detailed information is summarized on **Table 4-2**.

Calibration method for the differential pressure gauge

The differential pressure gauge can output current signal from 4 to 20 mA corresponding to the differential pressure from 0 to 50 kPa. Then, in order to obtain the relationship between the differential pressure and the signal, calibration test was carried out by using water instead of the LBE. The test apparatus for the calibration is shown in **Figure 4-**7. This apparatus consists of two transparent tubes, the differential pressure gauge and data acquisition unit. The output current signal from the differential pressure gauge is converted to voltage signal by using shunt resistance. In order to prevent effect of temperature drift of the resistance due to Joule heat, the shunt resistance of 75 Ω was selected in this study.

In the calibration, water level in one of the tube remains constant. Then water level in the other tube can be changed so that the differential pressure from 0 to 50 kPa can be achieved based on the difference of the water level. The calibration result is shown in **Figure 4-8**. The dotted line indicates approximating curve calculated by least-square method. From the calibration test, following result was obtained.

$$\Delta P = 42064V - 10168 \quad (4\text{-}5)$$

In the experiments explained in Chapter 4, the value of 42064 Pa/V was utilized to estimate differential pressure. The offset voltage of the differential pressure gauge was measured in every experiment to remove the effect of the offset voltage.

4.3 Experimental results and discussion

4.3.1 *Volume averaged void fraction distribution*

Figure 4-9(a) shows variation of measured volumetric averaged void fraction with the gas superficial velocity for poor wettability condition. As shown in this figure, measured void fraction increases with increasing superficial gas velocity and the relationship between void fraction and gas velocity is not linear but concave.

As Ruizicka et al. [4-29] pointed out, the flow behavior in a bubble column could be classified into homogeneous and heterogeneous flows depending on its flow regime. They measured volumetric void fraction in a bubble column using two different pore sizes for bubble distributers, and concluded that the void fraction could be expressed as function of j_g^2 for homogeneous flow or j_g / (1+j_g) for heterogeneous flow, respectively. The obtained tendency of measured void fraction could be attributed to the heterogeneous flow. It is also found that the measured void fraction slightly increases with increasing hydraulic diameter, except for the hydraulic diameter of 26 mm.

Figure 4-9(b) shows variation of measured volumetric averaged void fraction with the gas superficial velocity for good wettability condition. As shown in this figure, measured results show almost similar tendency to those for poor wettability condition. However, the effect of the hydraulic diameter on the void fraction was not distinct for good wettability condition.

Figures 4-10 denotes the variation of the measured gas velocity with increase of superficial gas velocity so that the comparison with existing drift flux correlations can be made. In each figure, the open and close symbols denote the measured results for poor and good wettability conditions, respectively. The solid, broken and dotted lines denote the predicted values for cap bubbly, slug, bubbly and churn-turbulent flows, assuming C_0 = 1.19 proposed by Ishii for ordinary two-phase flow. In addition to the existing correlations, the fitted lines are also shown by using the least square method. In any cases shown in **Figure 4-10**, it can be found that those predicted values underestimate experimental results. The difference between those predictions and experimental results is relatively larger for D_H = 0.026 m as shown in **Figure 4-10(d)**.

In **Figures 4-10(a) (b)**, it can be seen that measured gas velocities in poor wettability condition show slightly larger values than those in good wettability condition. For smaller gas

superficial velocity j_g < 0.03 m/s, it is found that there is relatively large difference of gas velocities in comparison regarding wall wettability condition on each figure. From the difference, it can be considered that the effect of the wettability on the measured gas velocity seems to be relatively larger than for larger superficial velocity. However, since no flow visualization has been conducted at the present study, the detail observation should be made to clarify the difference. From **Figures 4-10(a)-(d)**, it can be expected that the dispersion of measured gas velocities at each j_g might indicate formation of unstable flow condition in the LBE bubble column.

4.3.2 *Drift velocity and distribution parameter*

Drift velocity V_{gj} and distribution parameter C_0 were estimated by using experimental results shown in **Figures 4-10**. The drift velocity and the distribution parameter obtained from this work are shown in **Figures 4-11**. Each figure indicates comparisons of V_{gj} and C_0 depending on the different wall wettability conditions. In **Figure 4-11(a)**, the solid line denotes the existing correlation for cap bubbly. In good wettability condition, the measured drift velocity shows good agreement with the existing correlation for cap bubbly flow except the case of D_H = 0.026 m. In poor wettability condition, however, the drift velocity shows larger values than that in good wettability condition and also shows increase with decreasing hydraulic equivalent diameter. Hasan and Kabir [4-30] reported that the bubble rising velocity increases with decreasing annular gap in case of slug and cap bubbly flows. Also, it was reported that bubble rising velocity in annular channel is larger in comparison with that in circular pipe since the top shape of bubbles becomes incisive against cross section of the annulus [4-31]. Therefore, the bubble rising velocity also in the LBE two-phase flow could increase with decreasing annular gap in case of annular channel. In that case, drift velocity might increase too. However, in good wettability condition, such trend cannot be observed in measured results. Hence, in case of LBE two-phase flow, it can be considered that effect of decreasing annular gap on drift velocity is small. However, as mentioned before, the drift velocity measured in poor wettability condition shows increase with decreasing annular gap. Therefore it would be considered that increase of the measured drift velocity might be caused by the changing of wall wettability conditions. The reason why the drift velocity can take higher value in poor wettability condition would be that a number of bubbles can easily touch to the wall surface and flow close to inner wall region, as mentioned above [4-11, 4-12].

As for the distribution parameter C_0, it is found that the effect of wall wettability on C_0 is not so distinct as shown in **Figure 4-11(b)**. However, the distribution parameter C_0 takes higher values of about 4 regardless of the wettability of the wall, where the solid line denotes the Ishii's correlation. Those values are larger in comparison with Ishii's correlation. In case of gas-liquid

two-phase flow in stagnant water, it has been known that the distribution parameter C_0 takes larger values than 1.2 [4-20, 4-32, 4-33]. Therefore, the distribution parameter C_0 at present work might take larger value due to the low liquid velocity. Validity of these distribution parameters will be considered in section 4.4.

Figure 4-12 denotes comparison of the measured void fraction with predicted void fraction by drift flux model for both wettability conditions, where ensemble averaged values of V_{gj} and C_0 estimated from present experiments were used to obtain predicted values of volumetric averaged void fraction. From this figure, it is found that standard deviation estimated by the measured and predicted void fractions is 10.6% in poor wettability condition and is larger than that in good wettability condition. Such difference might be caused by increase of gas velocity in case of lower superficial gas velocity less than 0.03 m/s and poor wettability condition, as shown in Figures 4-6(a) and (b). However, it can be found that the drift flux model can provide reasonable prediction results less than 11% of error.

4.4 Numerical analysis for distribution parameter based on momentum transfer and drift flux model

As mentioned in the introduction, Clark et al. [4-20] predicted liquid velocity distribution in the bubble column with assuming local void fraction profile and considering force balance and momentum transfer in the fluid. Using those numerically predicted results, distribution parameters in the bubble column were estimated based on the drift flux model. From their work, it was found that the numerically predicted distribution parameters could be higher than 1.2 when the liquid recirculation developed. In this paper, the local liquid velocity distributions and the distribution parameter in the annular bubble column are investigated as well as those parameters in the circular bubble column by utilizing such useful prediction methods in order to evaluate the wall wettability effect on those parameters. However, such one-dimensional numerical simulations for predicting the local liquid velocity distribution have not been applied to two-phase flows in annular bubble column although the analysis have been adopted by many researchers [4-14 - 4-18, 4-34 - 4-35] to investigate the turbulent momentum transport in the two-phase flows. Therefore, the one-dimensional simulation proposed by Clark et al. [4-20] was extended to annular channel in this paper. Regarding single-phase flow in annulus, it has been pointed that the maximum point of local liquid velocity is located closer to inner wall in the annular gap, and that radial position of zero shear stress does not always correspond to the maximum location of local liquid velocity. However, experimental results available for two-phase flow has been limited to predict the maximum position in the liquid velocity profile. Hence, at present analysis, it is assumed that the maximum location of local liquid velocity

agrees with that of zero shear stress and with the location of the maximum void fraction with above mentioned assumptions, the simplified equations for annular bubble column have been derived. Both of the liquid velocity and the void fraction profile are defined for the inner and outer regions, which is divided by the location of zero shear stress, R_m, as shown in **Figure 4-13**. If one assumes parabolic shape profiles in radial direction, the local void fraction and the local mixture density can be written by Equations (4-6)-(4-9)

$$\alpha(r) = \alpha_m \left\{ 1 - \left(\frac{r - R_m}{R_1 - R_m} \right)^2 \right\} \qquad (R_1 \le r < R_m) \tag{4-6}$$

$$\alpha(r) = \alpha_m \left\{ 1 - \left(\frac{r - R_m}{R_2 - R_m} \right)^2 \right\} \qquad (R_m \le r < R_2) \tag{4-7}$$

$$\rho_l(r) = \rho_l \left[1 - \alpha_m \left\{ 1 - \left(\frac{r - R_m}{R_1 - R_m} \right)^2 \right\} \right] \qquad (R_1 \le r < R_m) \tag{4-8}$$

$$\rho_l(r) = \rho_l \left[1 - \alpha_m \left\{ 1 - \left(\frac{r - R_m}{R_2 - R_m} \right)^2 \right\} \right] \qquad (R_m \le r < R_2) \tag{4-9}$$

where these equations are given as quadratic functions for simplicity. Considering force balance in terms of intervals from R_1 to R_2 and from R_1 to r, Equations (4-10)-(4-11) can be obtained, respectively

$$\frac{2R_1}{r^2 - R_1^2}\tau_1 - \frac{2r}{r^2 - R_1^2}\tau(r) - \rho_{l,i(R_1 \to r)}(r)g - \frac{\Delta P}{\Delta z} = 0, \tag{4-10}$$

where subscripts, $R_1 \to r$, indicate the intervals of integrations for the mixture density; subsequent integrations implemented

$$\rho_{l,i(R_1 \to r)}(r) = \frac{\int_{R_1}^{r} \rho_l(r) 2\pi r dr}{\int_{R_1}^{r} 2\pi r dr}. \tag{4-11}$$

Then, the shear stress can be obtained from force balance as shown in the following equation:

$$\tau(r)=\frac{R_m^2-r^2}{r(R_m^2-R_1^2)}R_1\tau_1+\frac{(r^2-R_1^2)g}{2r}\left\{\overline{\rho_{l,R_1\to R_m}}-\rho_{l,i(R_1\to r)}(r)\right\}, \tag{4-12}$$

where the shear stress at $r=R_m$ is assumed as zero. In addition, Equation (4-13) can be derived from momentum transfer

$$\tau(r)=-\mu_l\frac{du(r)}{dr}-l^2\rho_l(r)\left|\frac{du(r)}{dr}\right|\frac{du(r)}{dr}. \tag{4-13}$$

Finally, the equation in terms of local liquid velocity gradient can be obtained as shown in Equation (4-14) when it can be assumed that Equation (4-12) is equal to Equation (4-13),

$$\frac{R_m^2-r^2}{r(R_m^2-R_1^2)}R_1\tau_1+\frac{(r^2-R_1^2)g}{2r}\left\{\overline{\rho_{l,R_1\to R_m}}-\rho_{l,i(R_1\to r)}(r)\right\}+\mu_l\frac{du(r)}{dr}+l^2\rho_l(r)\left|\frac{du(r)}{dr}\right|\frac{du(r)}{dr}=0. \tag{4-14}$$

$$(R_1\le r<R_m)$$

Regarding the outer region, following similar equation also can be derived by the same manner:

$$\frac{r^2-R_m^2}{r(R_2^2-R_m^2)}R_2\tau_2+\frac{(r^2-R_m^2)g}{2r}\left\{\overline{\rho_{l,R_m\to R_2}}-\rho_{l,i(R_m\to r)}(r)\right\}+\mu_l\frac{du(r)}{dr}+l^2\rho_l(r)\left|\frac{du(r)}{dr}\right|\frac{du(r)}{dr}=0 \tag{4-15}$$

$$(R_m\le r<R_2)$$

, where subscripts, $R_m\to R_2$ and $R_m\to r$, indicate intervals of integrations for the mixture density. For the purpose of lucidity and efficiency to calculate the liquid velocity distribution and the distribution parameter, non-dimensional equations shown in Equations (4-16)-(4-17) are also derived by using several non-dimensional values summarized in **Table 4-3**.

$$0=\frac{A(C^2-r^{*2})}{r^*(C^2-A^2)}N\tau_1+\frac{Ga}{2}\frac{\alpha_m}{2}\left(r^*-\frac{A^2}{r^*}\right)\frac{1}{6\alpha_m}\left[\frac{3(2-\alpha_m)A+(6-5\alpha_m)C}{C+A}\right.$$

$$-\frac{1}{r^*+A}\left[3\left\{\alpha_m\left(\frac{r^*-C}{A-C}\right)^2-\alpha_m+2\right\}(A-C)\left(\frac{r^*-C}{A-C}+1\right)\right.$$

$$\left.+\left\{4\alpha_m\left(\frac{r^*-C}{A-C}\right)^2+4\alpha_m\left(\frac{r^*-C}{A-C}\right)-8\alpha_m+12\right\}C\right]+2\frac{du^*}{dr^*}+\left(\frac{l}{R_H}\right)^2 Ga\{1-\alpha(r^*)\}\left|\frac{du^*}{dr^*}\right|\frac{du^*}{dr^*}$$

$$(A\le r^*<C) \qquad (4\text{-}16)$$

$$0=\frac{B(r^{*2}-C^2)}{r^*(B^2-C^2)}N\tau_2+\frac{Ga}{2}\frac{\alpha_m}{2}\left(r^*-\frac{A^2}{r^*}\right)\frac{1}{6\alpha_m}\left[\frac{3(2-\alpha_m)B+(6-5\alpha_m)C}{B+C}\right.$$

$$-\frac{B-C}{r^{*2}-C^2}\left\{3\alpha_m(B-C)\left(\frac{r^*-C}{B-C}\right)^4+4\alpha_m C\left(\frac{r^*-C}{B-C}\right)^3\right.$$

$$\left.\left.+6(1-\alpha_m)(B-C)\left(\frac{r^*-C}{B-C}\right)^2+12(1-\alpha_m)C\left(\frac{r^*-C}{B-C}\right)\right\}\right]+2\frac{du^*}{dr^*}+\left(\frac{l}{R_H}\right)^2 Ga\{1-\alpha(r^*)\}\left|\frac{du^*}{dr^*}\right|\frac{du^*}{dr^*}$$

.

$$(C\le r<B) \qquad (4\text{-}17)$$

In above equations, the following Nikuradse's empirical expressions [4-36] for mixing length are assumed:

$$\frac{l}{R_H}=0.02(1-\eta_1{}^2)(7+3\eta_1{}^2)\{1-(1-S^*)\eta_1\}(B-C) \qquad (A\le r^*<C) \qquad (4\text{-}18)$$

$$\frac{l}{R_H}=0.02(1-\eta_2{}^2)(7+3\eta_2{}^2)(B-C). \qquad (C\le r<B) \qquad (4\text{-}19)$$

As mentioned above, disagreement between the maximum point R_m and the center of the annular gap had been observed in a lot of previous investigations. Rothofus et al. [4-37] have reported that the radius of zero shear stress was observed to take the same value in fully developed turbulent flow as predicted from theory for fully viscous flow. On the other hand, Kays and Leung [4-38] have proposed an empirical correlation of r_m^* as follows:

$$\frac{r_m^* - a}{1 - r_m^*} = a^{0.343} \tag{4-20}$$

, where a is the inner-outer radius ratio R_1/R_2. Michiyoshi and Nakajima [4-36] compared those two relations proposed by Rothofus et al. [4-37] and by Keys and Leung [4-38] with available experimental results. They reported that Kays and Leung's correlation agrees much better with the measured results. Therefore, also in this work, Kays and Leung's correlation shown in Equation (4-18) was employed to evaluate the radius of zero shear r_m^*. At present analysis, the empirical correlation by Kays and Leung was assumed to determine the void and mixing length distributions. However, it should be noted that the velocity profile would be affected by the void fraction profile and the recirculation flow in the annular channel and that such effect was neglected at the present calculations. Using above equations, du^*/dr^* were then solved by the quadratic formula. Integrating from the inner wall boundary condition, $u_1^* = 0$ at $r^* = R_1/R_H = A$, the liquid velocity profile $u^*(r^*)$ can then be obtained. The integrating is repeated with varying assumed outer wall shear stress, τ_2 so that zero local liquid velocity can be achieved at outer wall surface, $r^* = R_2/R_H = B$. Integrating $u^*\{1-\alpha(r^*)\}$ over the cross section of annular gap gives non-dimensional superficial liquid velocity; namely

$$\frac{< j_l >}{\pi(B^2 - A^2)} = \frac{\int_A^B u^* \{1-\alpha(r^*)\} 2\pi r^* dr^*}{\int_A^B 2\pi r^* dr^*}. \tag{4-21}$$

Such integrating is also repeated with varying assumed inner wall shear stress, τ_1 so that zero velocity of cross sectional averaged non-dimensional superficial liquid velocity can be satisfied. Appropriate local liquid velocity profiles are then determined, finally. Distribution parameters are estimated with the assumed void fraction profile $\alpha(r)$, the predicted local liquid velocity $u(r)$ and the local drift velocity v_{gj} via Equation (4-22)

$$C_0 = \frac{R_2^2 - R_1^2}{2} \frac{\int_{R_1}^{R_2} \left\{ \alpha(r) \cdot u(r) + \frac{\alpha(r)^2}{1-\alpha(r)} v_{gj} \right\} r dr}{\int_{R_1}^{R_2} \alpha(r) r dr \int_{R_1}^{R_2} \left\{ u(r) + \frac{\alpha(r)}{1-\alpha(r)} v_{gj} \right\} r dr} \tag{4-22}$$

At our present experiments, the local gas velocity has not been measured. To estimate the distribution parameter, void fraction weighted mean drift velocity V_{gj} is applied to the Equation

(4-22) as the approximate value of the local drift velocity v_{gj}. Here, the definition of Froude number is as follows:

$$Fr \equiv \frac{V_{gj}}{\sqrt{gD_H}}. \tag{4-23}$$

Using this Froude number, Equation for the distribution parameter can be obtained as the non-dimensional formula

$$C_0 = \frac{B^2 - A^2}{2} \frac{\int_A^B \left\{ \alpha(r^*) \cdot u(r^*) + \frac{\alpha(r^*)^2}{1-\alpha(r^*)} Fr \right\} r^* dr^*}{\int_A^B \alpha(r^*) r^* dr^* \int_A^B \left\{ u^*(r^*) + \frac{\alpha(r^*)}{1-\alpha(r^*)} Fr \right\} r^* dr^*}. \tag{4-24}$$

The distribution parameters corresponding to the various Froude numbers (various drift velocities) can calculated with given Froude numbers.

4.5 Comparison of calculated results with experimental results

As mentioned above, analytical method for predicting liquid velocity profile and distribution parameter for large diameter bubble column proposed by Clark et al. [4-20] has been modified so that liquid velocity profile and distribution parameter in annular bubble column can be calculated. If the inner diameter is zero; simple circular pipe condition, Equations (4-14) and (4-15) result in the same formula proposed by Clark et al. [4-20]. **Figure 4-14(a)** shows predicted distribution parameters depending on variation of Galileo numbers and Froude numbers in terms of simple circular bubble column condition. As shown in the figure, it can be found that the prediction value shows good agreement with experimental results measured in simple circular channel condition when the Froude number equal to 0.38, which is the same condition with present experiments. **Figure 4-15(b)** presents numerical results of liquid velocity profile in a simple circular channel. In this figure, there are upward and downward flow regions in inner area and outer area, respectively. Such trend of this liquid velocity profile is consistent with Clark's results [4-20].

In case of analysis for annulus condition, however, predicted values of C_0 show much smaller in comparison with experimental results as shown in **Figure 4-15(a)**. The calculated liquid velocity profiles are also shown in **Figure 4-15(b)**. As shown in this figure, upward flow exists in the central region and downward flow can be seen at the both sides of wall, corresponding to

the non-slip conditions at each boundary condition. Disagreement in the prediction of distribution parameter may be caused by the inaccurate estimation in liquid velocity profiles. As mentioned before, void fraction profile need to be assumed in advance for prediction of liquid velocity profile. This is one of the weakness points of this kind of analysis. However the prediction accuracy can be better if void fraction profile can be measured before conducting analysis.

In case of single-phase flow in annulus, it was reported that the position of maximum velocity in turbulent flow was closer to the inner wall than in laminar flow [4-39]. In addition, it might be supposed that the maximum position of liquid velocity in two-phase flow could be closer than that in single-phase turbulent flow. Hence, in this work, numerical estimations have been conducted with modified void distributions by changing the location of the maximum point in the void fraction profile, as shown in **Figure 4-16(a)** and the corresponding liquid velocity profiles are shown in **Figure 4-16(b)**. As can be seen from those figures, maximum positions of the calculated liquid velocity profiles are also closer than that for original calculated liquid velocity profile. Predicted values of C_0 calculated by using such modified profiles are shown in **Figure 4-17**. As explained above, remembering those experimental values are almost 4.0, it is found that predicted C_0 becomes more than 3.0 and are getting closer to the experimental values; almost 4.0 in condition of D_H =0.751 m. In other condition of D_H, it is able to see that predicted C_0 become closer values to the experimental values as shown in **Figure 4-17**. However, the predicted C_0 still shows smaller values in comparison with those experimental results even though such extreme situation of void fraction profile shown as condition of $r_m^* - R_1/R_2 = 0.003$ is assumed. Such disagreement might be suggestive of inaccurate assumption for void fraction profile. Actual void fraction profile might be steeper distribution near inner wall. In that case, it could be able to be considered that the C_0 might be getting closer to the experimental results.

As shown in **Figure 4-11(b)**, the wall wettability effect on C_0 is not so distinct at present experimental conditions, however the measured drift velocity is strongly affected by the wall wettability. From these results, it could be considered that those results might be attributed to the difference in the phase distribution due to the wall wettability. In poor wettability condition, there may be a possibility of existence of sliding or slipping bubbles on the inner wall surface in comparison with good wettability condition resulting in increase of the drift velocity.

However experimental results of C_0 are almost constant regardless of the increasing V_{gj} even though the predicted C_0 shows decrease with increasing the V_{gj}, as shown in **Figure 4-18**, where those distribution parameters C_0 are calculated by utilizing the assumed void fraction profile and the predicted local liquid velocity profile via Equation (4-24) and by varying Froude numbers; drift velocities. Therefore, steeper void fraction profile might be formed due to the

sliding bubble or slipping bubble near the wall for poor wettability condition.

4.6 Conclusion

LBE bubble columns with a simple circular channel and annulus were experimentally investigated by varying the surface wettability of the channel wall and the measured results are compared with existing correlations and with one-dimensional momentum transfer model. Results can be summarized as follows:

(1) The surface wettability affects the drift velocity in the LBE two-phase flow in the annular channels due to enhancement of circulation flow by bubbles flowing close to inner wall surface. However, the effect of the surface wettability on the two-phase flow in a cylindrical vessel was not distinct, which might be attributed to the small void fraction in the near wall region caused by the circulation flow.

(2) The distribution parameter in the LBE two-phase flow in a cylindrical vessel can be well reproduced by using one dimensional simulation with assumed void fraction and mixing length for single phase flow. In case of the annular channels, the one-dimensional simulation gives underestimation in the distribution parameters, because the assumed void fraction profiles may affect the circulation flow in the annular channel.

(3) Although the C_0 obtained from experiments shows almost constant values with increasing the experimental V_{gj}, the predicted C_0 shows decreasing with increasing the V_{gj},. This difference might be caused by assuming incorrect void fraction profiles in the analysis. It can be expected that shapes of actual void fraction profiles might show more different shapes and would seem to be steeper. In that case, predicted values of C_0 would take higher values and would be getting closer to present experimental results.

References for Chapter 4

[4-1] Handbook on lead-bismuth eutectic alloy and lead properties, materials compatibility, thermal-hydraulics and technologies 2015 edition. Nuclear Energy Agency Organisation for Economic Co-operation and Development. 2015, No. 7268.

[4-2] Gromov BF, Belomitcev YuS, Yefimov EI, Leonchuk MP, Martinov PN, Orlov YuI, Pankratov DV, Pashkin YuG, Toshinsky GI, Chekunov VV, Shmatko BA, Stepanov VS. Use of lead-bismuth coolant in nuclear reactors and accelerator-driven systems. Nucl. Eng. and Des. 1997 Oct; 173: 207-217.

[4-3] Abderrahim HA, Kupschus P, Malambu E, Benoit Ph, Tichelen KV, Arien B, Vermeersch F, D'hondt P, Jongen Y, Ternier S, Vandeplassche D. MYRRHA: A multipurpose accelerator driven system for research & development. Nucl. Instrum. Meth. A. 2001 May; 463: 487-494.

[4-4] Mukaiyama T, Takizuka T, Mizimoto M, Ikeda Y, Ogawa T, Hasegawa A, Tkada H, Takano H. Review of research and development of accelerator-driven system in Japan for transmutation of long-lived nuclides. Prog. Nucl. Energ. 2001 Mar; 38: 107-134.

[4-5] Sasa T, Oigawa H. Studies on Accelerator-Driven System in JAEA. Plasma and Fusion Research. 2014 May; 9: 4401113-1- 4401113-5.

[4-6] Coccoluto G, Gaggini P, Labanti V, Tarantino M, Ambrosini W, Forgione N, Napoli A, Orioro F. Heavy liquid metal natural circulation in a one-dimensional loop. Nucl. Eng. and Des. 2011 May; 241: 1301-1309.

[4-7] Abanades A, Pena A. Steady-state natural circulation analysis with computational fluid dynamic codes of a liquid metal-cooled accelerator driven system. Nucl. Eng. and Des. 2009 Feb; 239: 418-424.

[4-8] Weisenburger A, Mansani L, Schumacher G, Muller G. Oxygen for protective oxide scale formation on pins and structural material surfaces in lead-alloy cooled reactors. Nucl. Eng. and Des. 2014 Jul; 273: 584-594.

[4-9] Martinelli L, Courouau JL, Fanny BC. Oxidation of steels in liquid lead bismuth: Oxygen control to achieve efficient corrosion protection. Nucl. Eng. and Des. 2011 May; 241: 1288-1294.

[4-10] Giuranno D, Gnecco F, Ricci E, Novakovic R. Surface tension and wetting behaviour of molten Bi-Pb alloys. Intermetallics. 2003 Oct; 11: 1313-1317.

[4-11] Terauchi Y, Iguchi M, Kosaka H, Yokoya S, Hara S. [Wettability Effect on the Flow Pattern of Air-water Two-phase Flows in a Vertical Circular Pipe]. Tetsu-To-Hagane. 1999 Jun; 85: 7-13 [in Japanese].

[4-12] Takamasa T, Hazuku T, Hibiki T. Experimental study of gas-liquid two-phase flow

affected by wall surface wettability. Int. J. Heat Fluid Fl. 2008 Dec; 29: 1593-1602.

[4-13] Kudoh H, Zhao D, Sugiyama K, Narabayashi T, Ohshima H, Kurihara A. Void fraction distributions of inert gas jets across a single cylinder with non-wetting surface in liquid sodium. J. Nucl. Sci.Technol. 2012 Nov; 49: 1175-1185.

[4-14] Clark NN, Atkinson CM, Flemmer RLC. Turbulent circulation in bubble columns. AlChE Journal. 1987 Apr; 33: 515-518.

[4-15] Ueyama K, Miyauchi T. Properties of recirculating turbulent two phase flow in gas bubble columns. AlChE Journal; 1979 Mar; 25: 258-266.

[4-16] Koide K, Kubota H. Gas holdup distribution and liquid velocity distribution on bubble flow in vertical column. 1966; 30: 806-813 [in Japanese].

[4-17] Sato Y, Sadatomi M, Horita K, Sekoguchi K. Momentum and heat transfer in two-phase bubble flow : 1st report, theory. Transaction of the Japan Society of Mechanical Engineers Series B. 1980; 46: 1780-1789 [in Japanese].

[4-18] Sato Y, Sadatomi M, Horita K, Nakazatomi M, Sekoguchi K. Momentum and heat transfer in two-phase bubble flow: 2nd report, A comparison between experimental data and theoretical calculations. Transaction of the Japan Society of Mechanical Engineers Series B. 1980; 46: 1790-1796 [in Japanese].

[4-19] Ozar B, Jeong JJ, Dixit A, Julia JE, Hibiki T, Ishii M. Flow structure of gas-liquid two-phase flow in an annulus. Chem. Eng. Sci. 2008 May; 63: 3998-4011.

[4-20] Clark NN, Egmond JWV, Nebiolo EP. The drift-flux model applied to bubble columns and low velocity flows. Int. J. Multiphase Flow. 1990 Mar - Apr; 16: 261-279.

[4-21] Schlegel JP, Macke CJ, Hibiki T, Ishii M. Modified distribution parameter for churn-turbulent flows in large diameter channels. Nucl. Eng. and Des. 2013 Oct; 263; 138-150.

[4-22] Chen SW, Liu Y, Hibiki T, Ishii M, Yoshida Y, Kinoshita I, Murase M, Mishima K. Experimental study of air-water two-phase flow in an 8 × 8rod bundle under pool condition for one-dimensional drift-flux model. Int. J. Heat Fluid Flu. 2012 Feb; 33: 168-181.

[4-23] Mishima K, Hibiki T, Saito Y, Nishihara H, Tobita Y, Konishi K, Matsubayashi M. Visualization and measurement of gas-liquid metal two-phase flow with large density difference using thermal neutrons as microscopic probes. Nucl. Instrum. Meth. A. 1999 Nov; 424: 229-234.

[4-24] Kataoka I, Ishii M. Drift flux model for large diameter pipe and new correlation for pool void fraction. Int. J. Heat Mass Transfer. 1987 Sep; 30: 1927-1939.

[4-25] Saito M, Sawada T, Teraoka Y, Nezu A. Dispersion characteristics of gas-liquid

two-phase pool. Proc. 6th ICONE; 1998 May 10-14; ICONE-6118.

[4-26] Nishi Y, Kinoshita I, Nishimura S. Experimental study on the gas lift pump in lead-bismuth eutectic. Transactions of the Japan Society of Mechanical Engineers Series B. 2004; 70; 715-722 [in Japanese].

[4-27] Ishii M, One-dimensional drift-flux model and constitutive equations for relative motion between phases in various two-phase flow regimes. USA: Argonne National Laboratory; 1977, ANL-77-47.

[4-28] Klecka J, Gabriele FD, Hojna A. Mechanical properties of the steel T91 in contact with lead. Nucl. Eng. and Des. 2015 Mar; 283: 131-138.

[4-29] Ruzicka MC, Zahradnik J, Drahos J, Thomas NH. Homogeneous-heterogeneous regime transition in bubble columns. Chem. Eng. Sci. 2001 Aug; 56: 4609-4626.

[4-30] Hasan AR, Kabir CS. Two-phase flow in vertical and inclined annuli. Int. J. multiphase Flow. 1992 Mar; 18; 279-293.

[4-31] Furukawa T, Sekoguchi K. Phase distribution for gas-liquid two-phase flow in annuli. Transactions of the Japan Society of Mechanical Engineers Series B. 1986; 52: 199-207.

[4-32] Kataoka Y, Suzuki H, Murase M. Drift-flux parameters for upward gas flow in stagnant liquid. J. Nucl. Sci. Technol. 1987 Jul; 24: 580-586.

[4-33] Hibiki T, Ishii M. One-dimensional drift-flux model for two-phase flow in a large diameter pipe. Int. J. Heat Mass Transfer. 2003 May; 46: 1773-1790.

[4-34] Menzel T, Weide TID, Staudacher O, Wein O, Onken U. Reynolds shear stress for modeling of bubble column reactors. Ind. Eng. Chem. Res. 1990 Jan; 29: 988-994.

[4-35] Kumar BS, Devanathan N, Moslemian D, Dudukovic M. Effect of scale on liquid recirculation in bubble columns. Chem. Eng. Sci. 1994 Dec; 49: 5637-5652.

[4-36] Michiyoshi I, Nakajima T. Fully developed turbulent flow in a concentric annulus. J. Nucl. Sci.Technol. 1968 Jul; 5: 354-359.

[4-37] Rothofus RR, Mornarad CC. Correlation of turbulent velocities for tubes and parallel plates. Ind. Eng. Chem. 1955 Jun; 47: 1144-1149.

[4-38] Kays MW, Leung YE. Heat transfer in annular passages–hydrodynamically developed turbulent flow with arbitrarily prescribed heat flux. Int. J. Heat Mass Transfer. 1963 Jul; 6: 537-557.

[4-39] Rehme K. Turbulent flow in smooth concentric annuli with small radius rations. J. Fluid Mech. 1974 Jun; 64: 263-287.

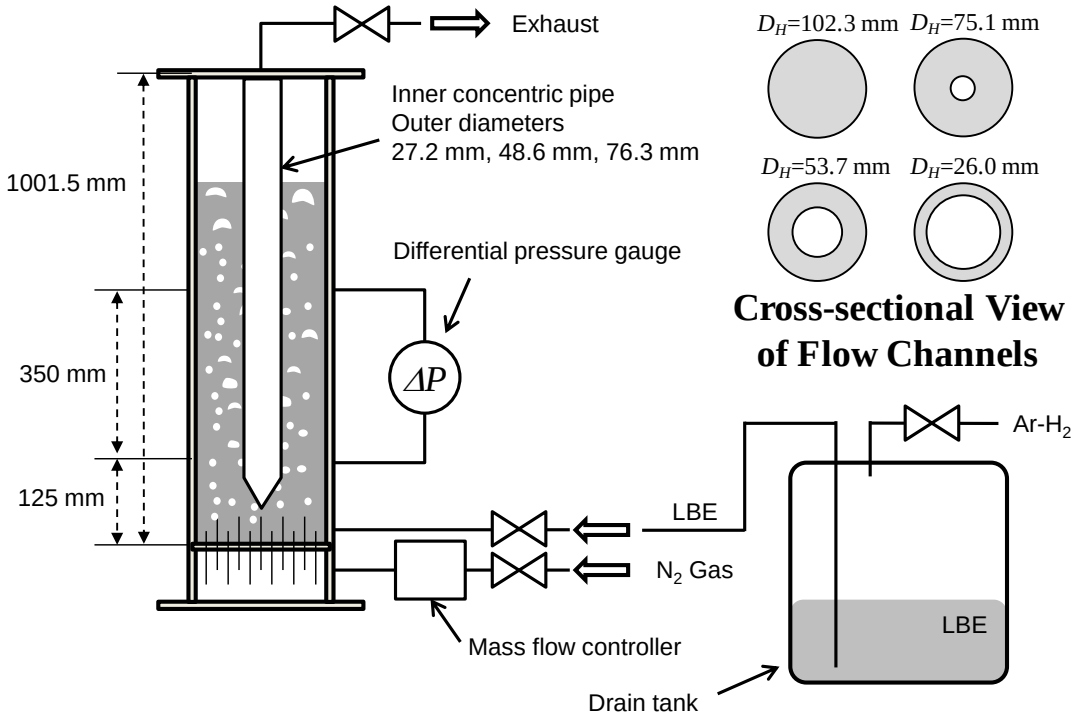

Figure 4-1. Schematic diagram of LBE bubble column apparatus HESTIA2

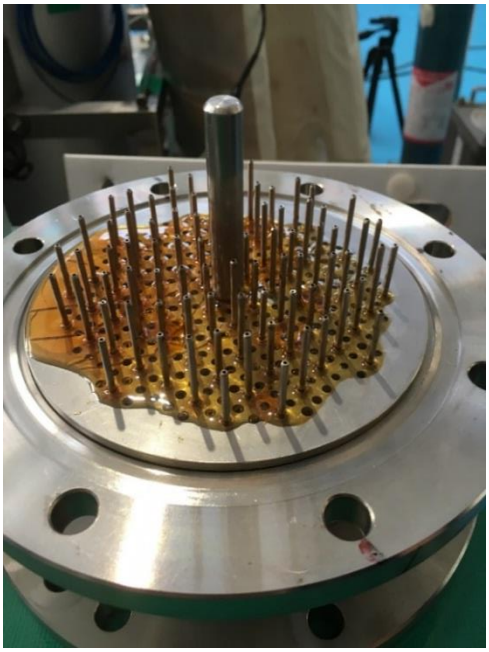

(a)

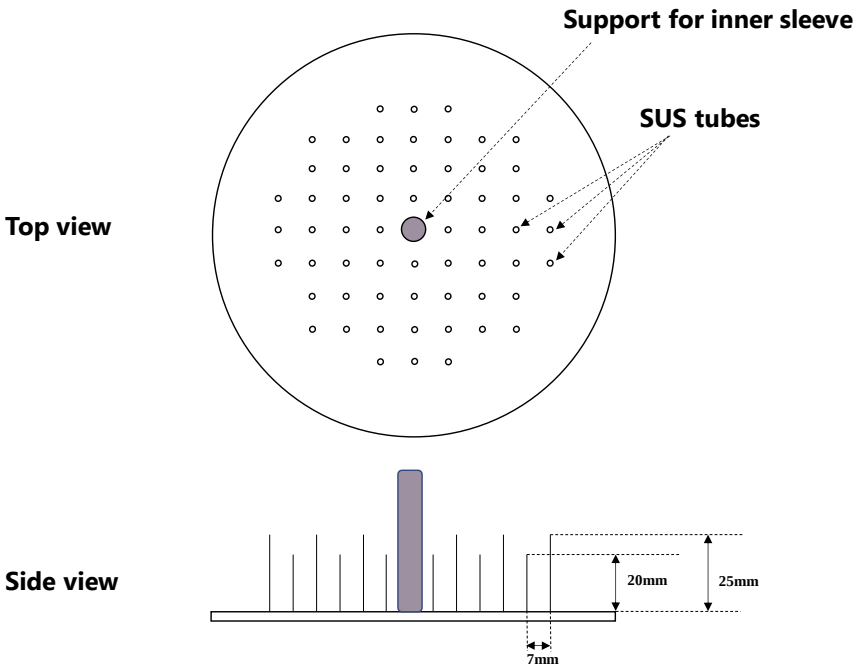

(b)

Figure 4-2. Photograph (a) and schematic diagram (b) of gas distributor

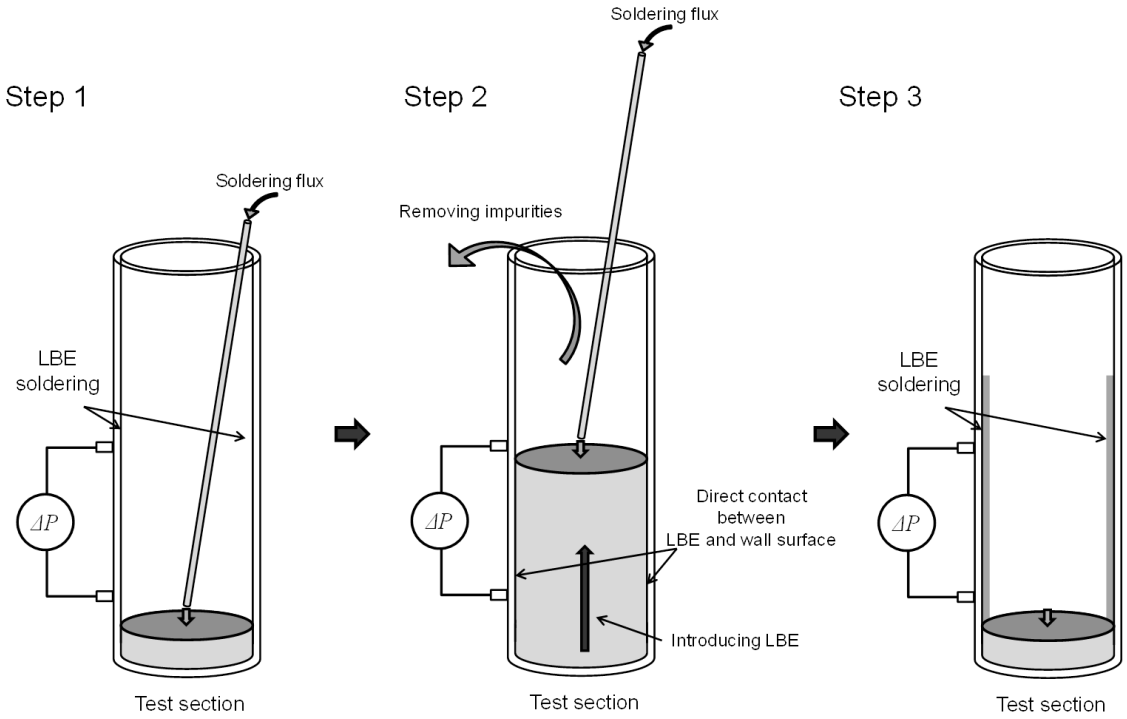

Figure 4-3. Method for improving wall wettability to LBE.

(a)

(b)

Figure 4-4. Difference of meniscus of LBE free surface (a)before and (b)after surface treatment using soldering flux.

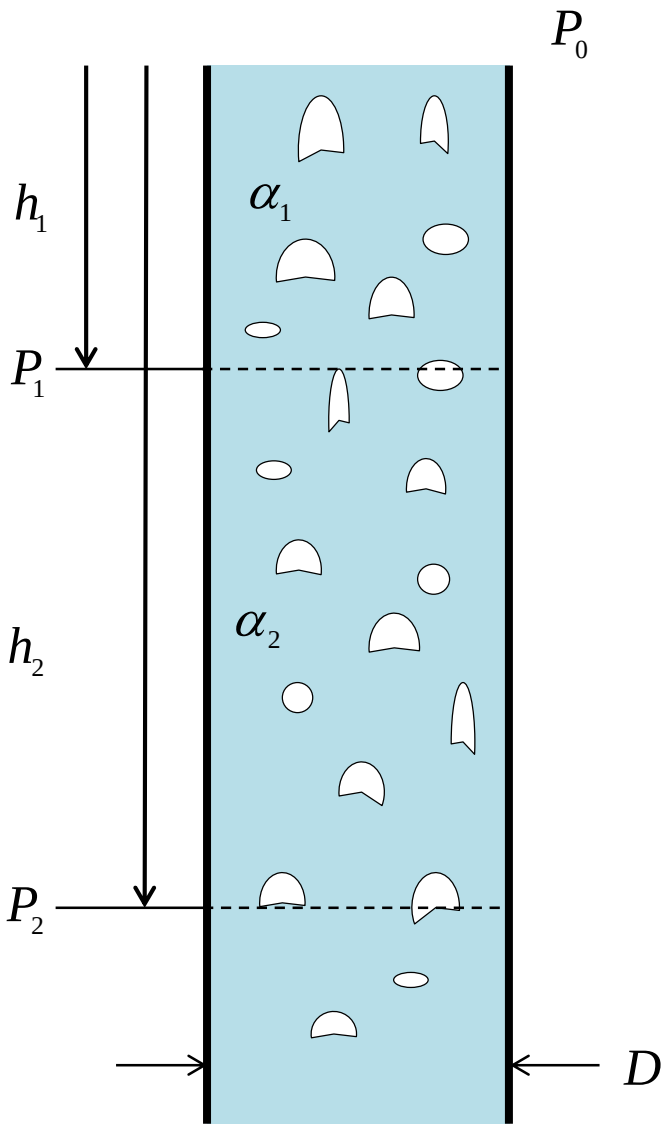

Figure 4-5. Principle of void fraction measurement by means of differential pressure gauge.

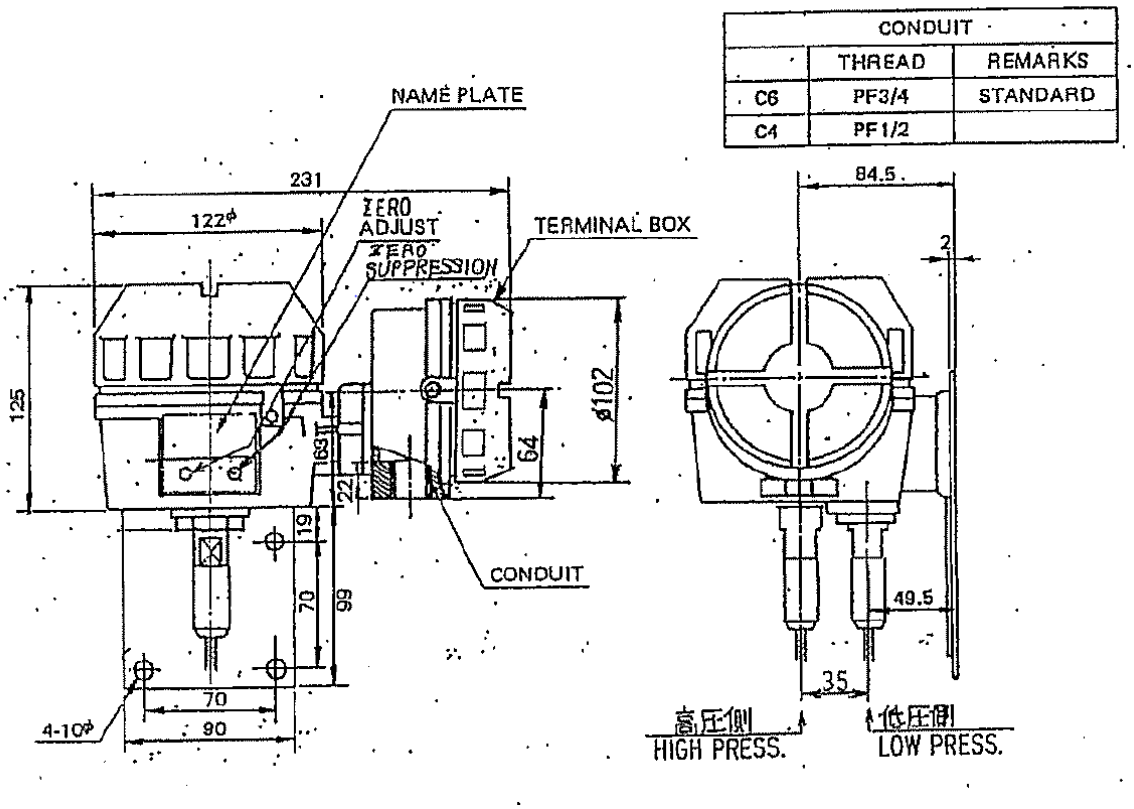

Figure 4-6. Schematic expression of differential pressure gauge.

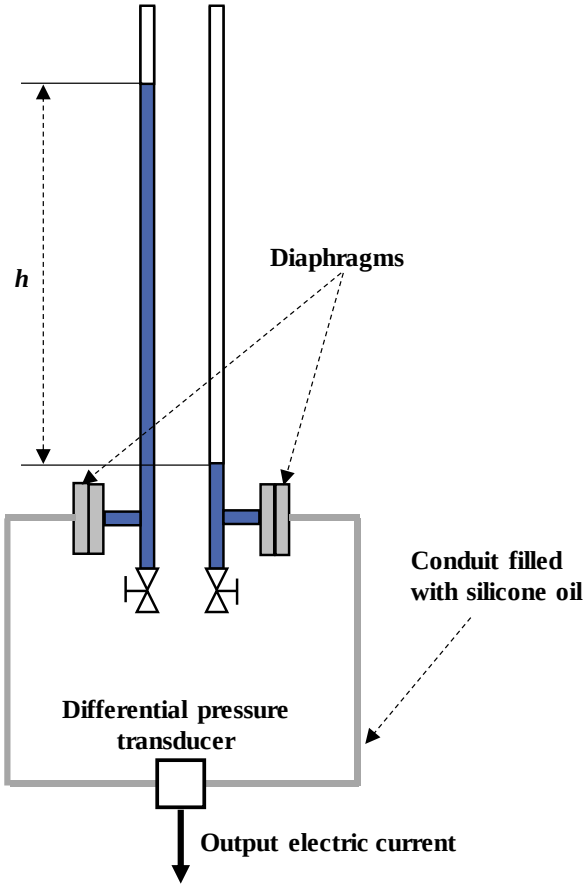

Figure 4-7. Calibration method of differential pressure gauge.

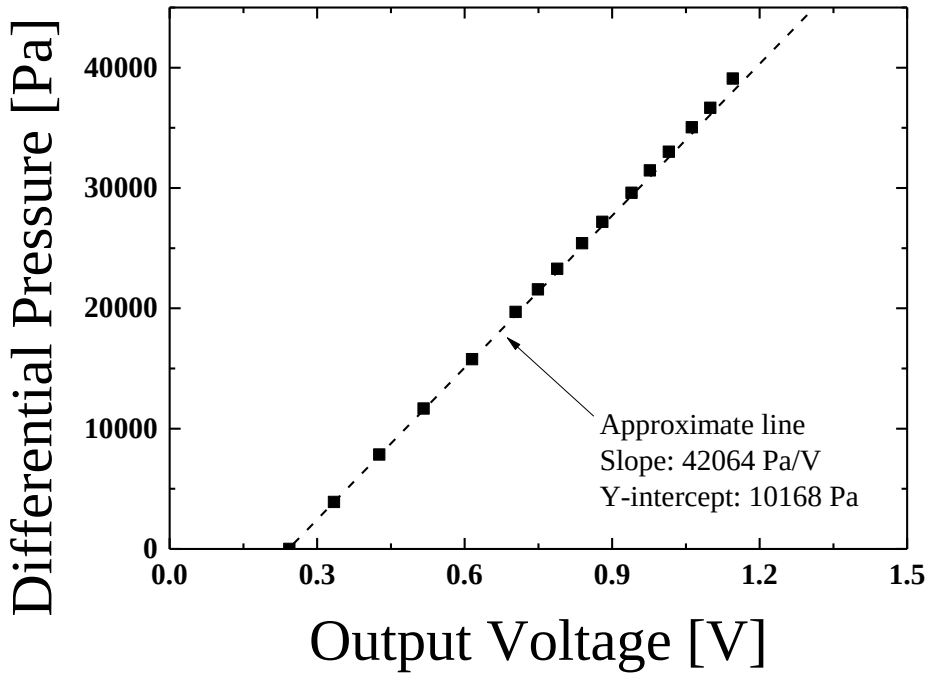

Figure 4-8. Calibration result of differential pressure gauge.

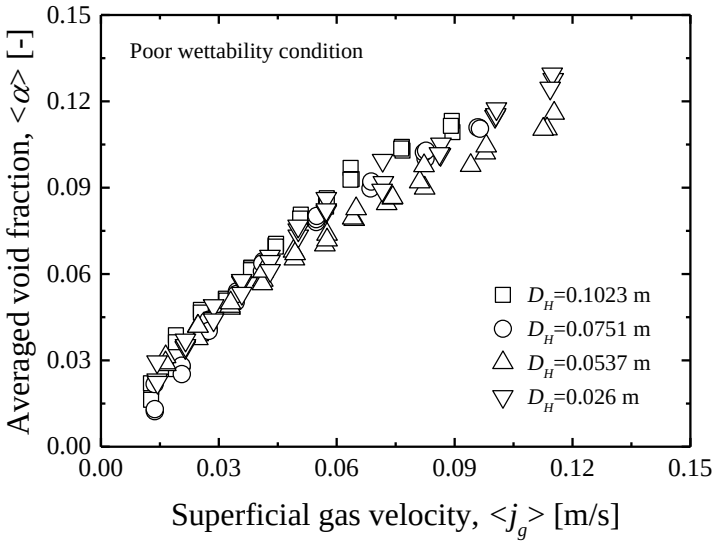

(a)

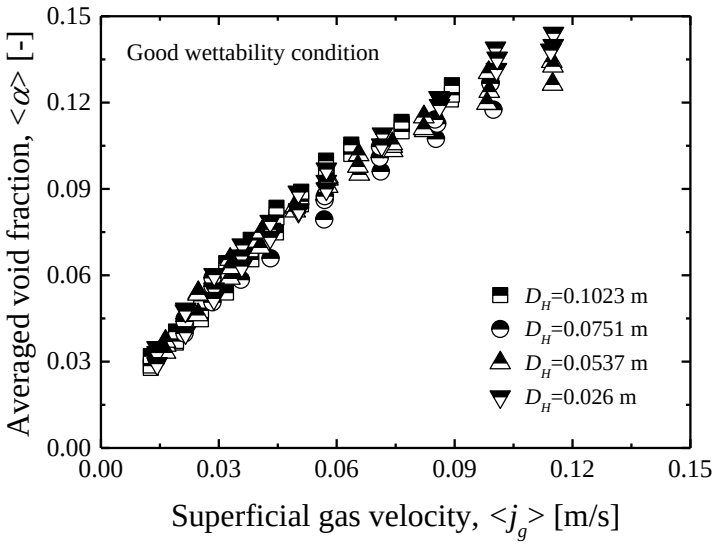

(b)

Figure 4-9. Variation of averaged void fraction with superficial gas velocity for (a)poor wettability condition and (b)good wettability condition.

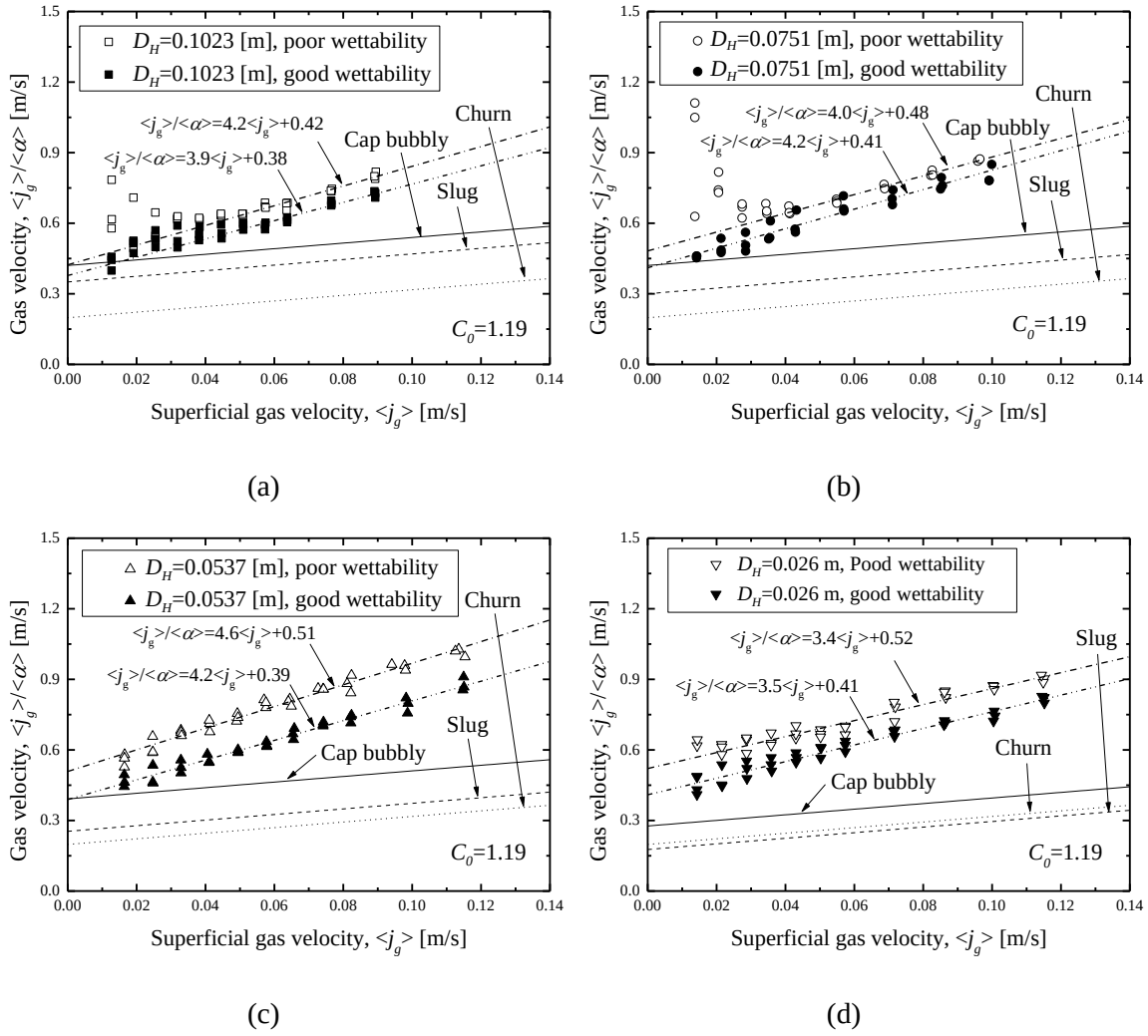

Figure 4-10. Comparison of drift flux plot assuming C_0 = 1.19 with measurements for (a)D_H=0.01023 m, (b) D_H=0.0751 m, (c) D_H=0.0537 m and (d) D_H=0.026 m.

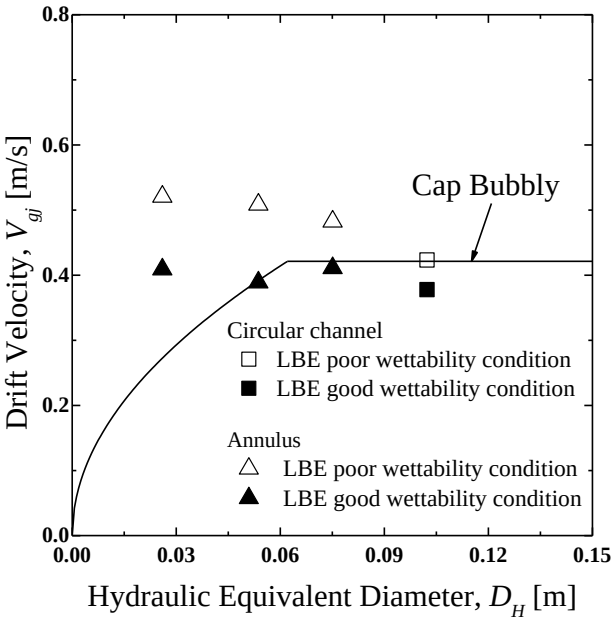

(a)

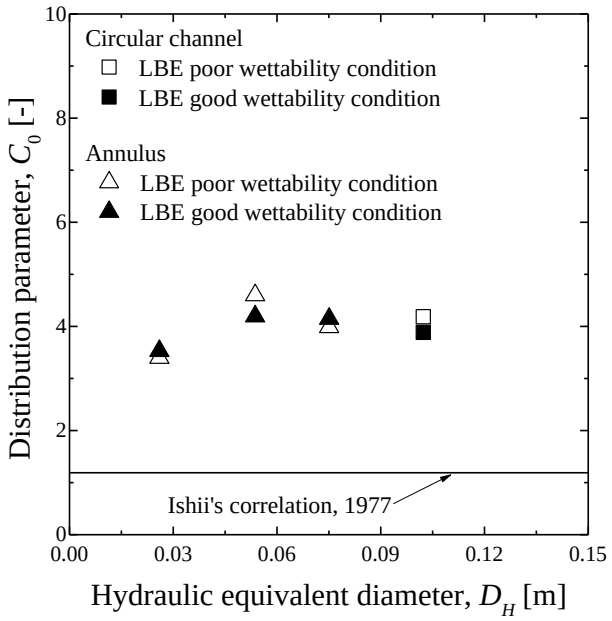

(b)

Figure 4-11. Effect of hydraulic equivalent diameter on measured drift flux model parameters; (a)drift velocities and (b)distribution parameters.

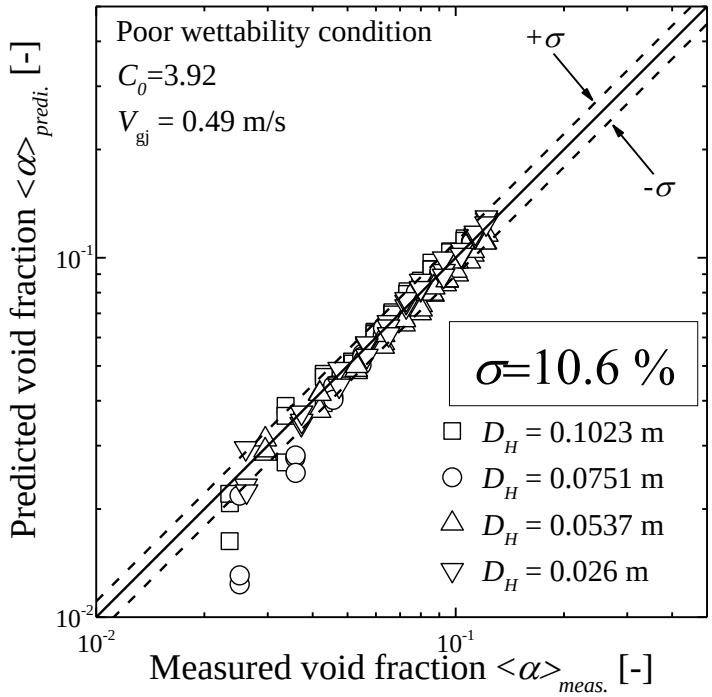

(a)

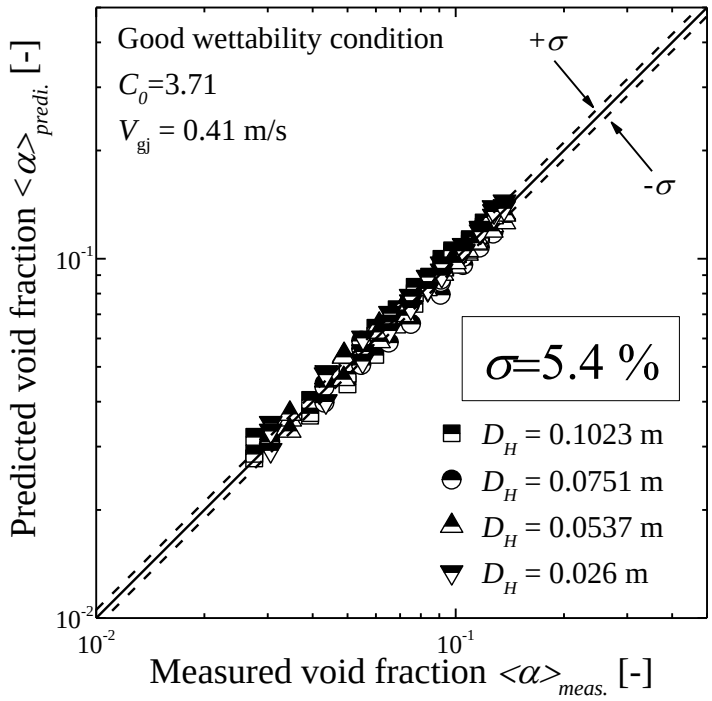

(b)

Figure 4-12. Comparison of void fraction with predicted void fraction by drift-flux model for (a)Poor wettability condition, and (b)Good wettability condition.

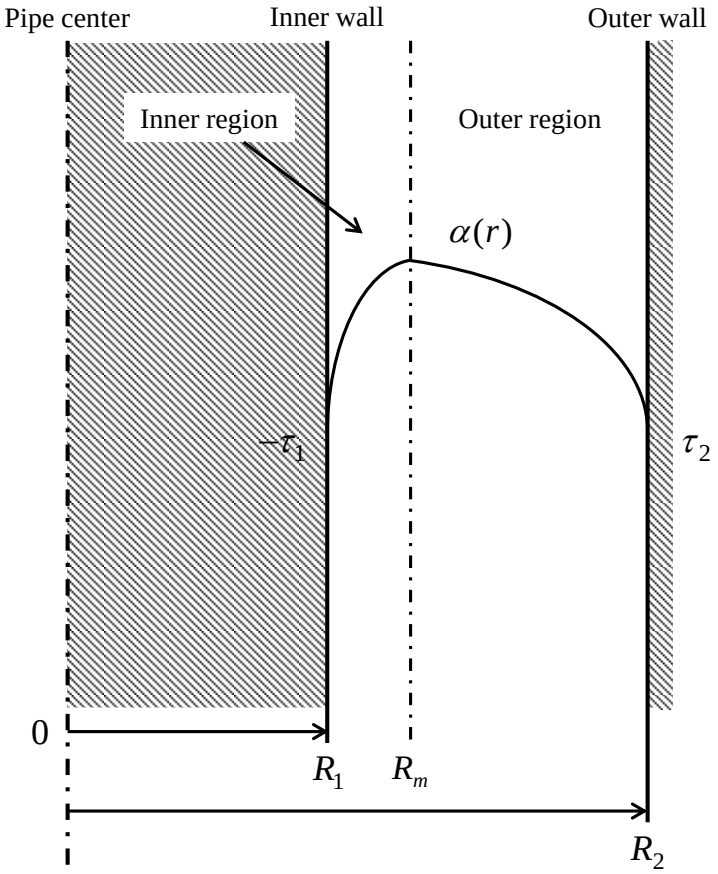

Figure 4-13. Coordinates in bubble column apparatus HESTIA2

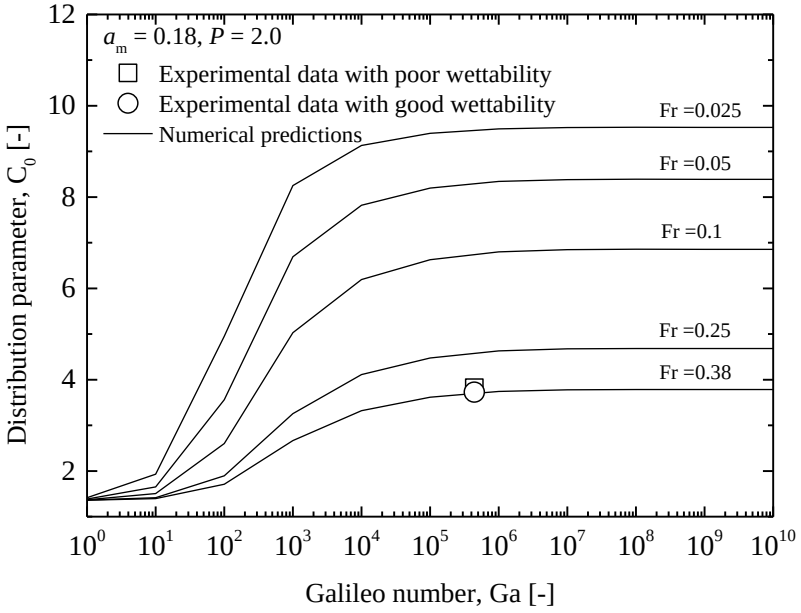

(a)

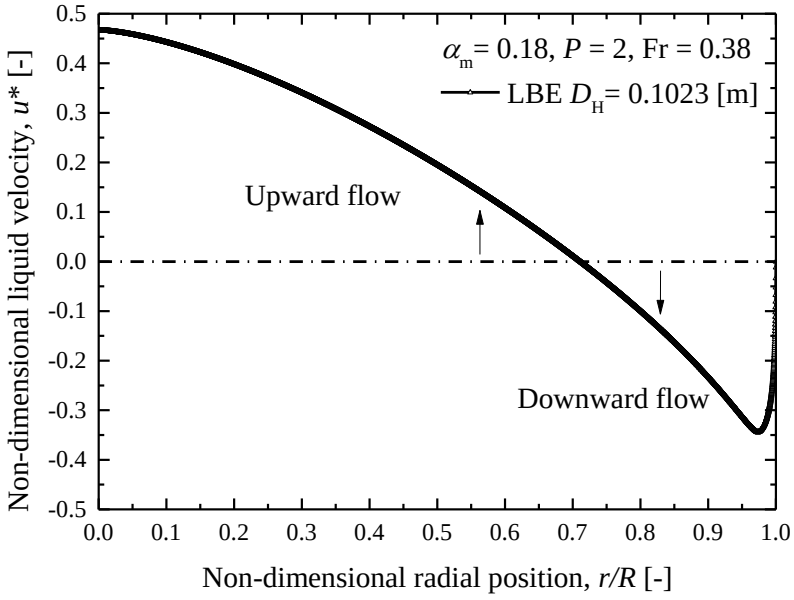

(b)

Figure 4-14. Numerical predictions for D_H =0.1023 [m] by Clark et al.'s method (circular cross section) (a) Comparison of predicted C_0 with measurement results (b) Predicted liquid velocity distribution.

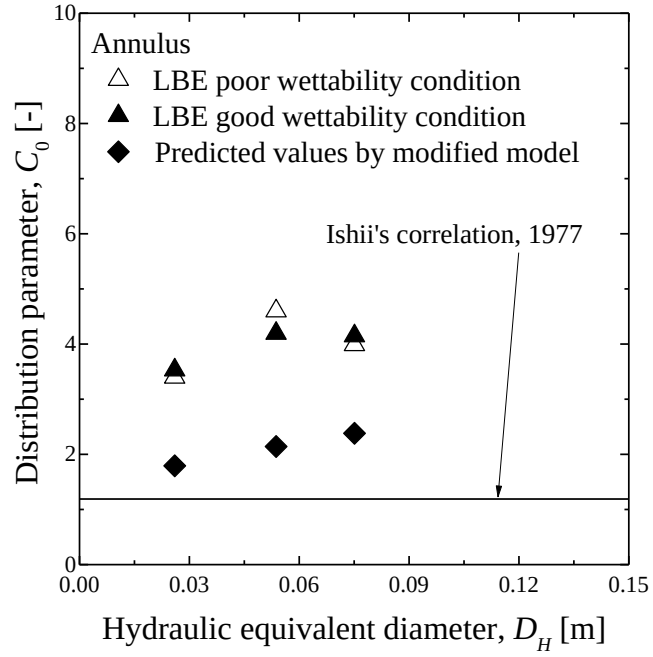

(a)

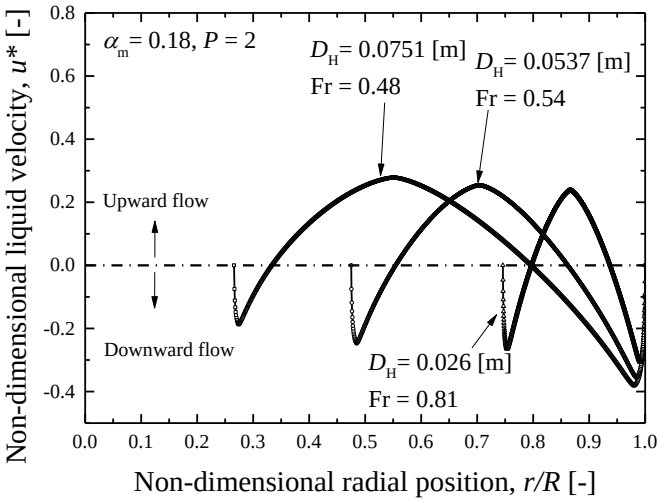

(b)

Figure 4-15. Calculated results for annular channel (a)comparison of calculated distribution parameters with measured distribution parameters and (b)calculated liquid velocity profile.

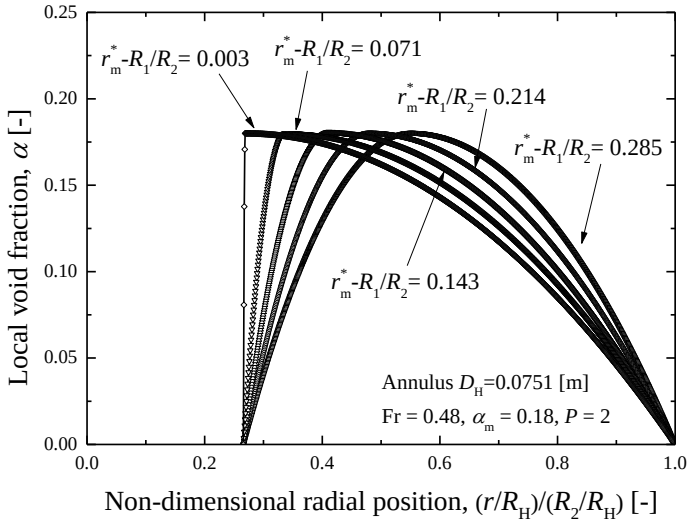

(a)

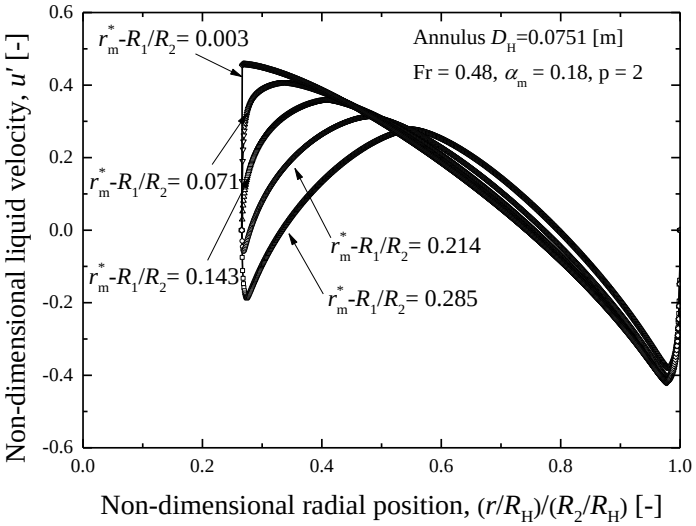

(b)

Figure 4-16. (a)Assumed void fraction profile by varying r^*, (b)calculated liquid velocity distribution based on modified void fraction profile.

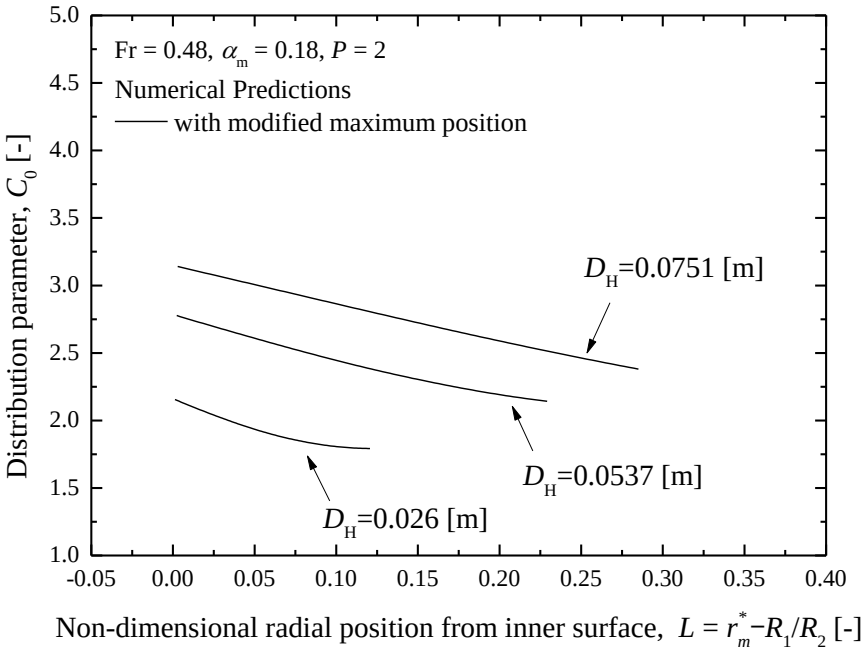

Figure 4-17. Effect of maximum location of void fraction on numerical predicted distribution parameter

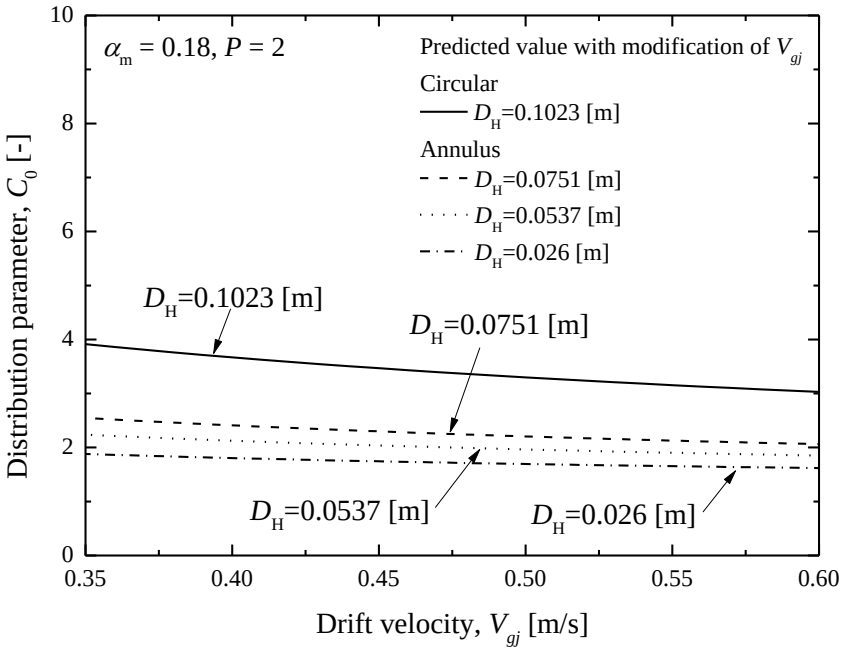

Figure 4-18. Effect of drift velocity on predicted distribution parameter.

Table 4-1. Composition and content of soldering flux.

Soldering flux	
Composition	Content wt [%]
Phosphoric acid (H_3PO_4)	55%
Methanol (CH_3OH)	10%
Aniline hydro chloride (C_6H_8ClN)	5%
Water (H_2O)	30%
Surfactant	Some quantities

Table 4-2. Detailed specification of the diaphragm type differential pressure gauge.

Measuring range	0 ～50 [kPa]
Withsranding pressure	150% F.S.
Line pressure	max 1 [MPa]

Materials

Diaphram	Stainless steel 316L
Flange	Stainless steel 316
Capillary tube	Stainless steel 316
Flexible tube	Stainless steel 316
Box for amplifier	ADC

Length of capillary tube	1 [m]
Sealing liquid	Silicon oil
Conversion method	Diffusion type semiconductor pressure sensor
Input power supply	AC 100 [V]
Output signal	DC 4 ～ 20 [mA]
Load resistance	max 500 [Ohm]
Power consumption	Approx. 2.5 [W]
Offset adjustable range	±10 [%]F.S.
Span adjustable range	±10 [%]F.S.
Span coarse adjustable range	±30 [%]F.S.
Suppression renge	120 [%]F.S.
Temperature range of the surrounding enviroment	- 10 ～ 60 ℃
Temperature range of the pressure transducer	- 10 ～ 60 ℃
Accuracy of output	±1.0 [%]F.S. (at 20 ℃)

Table 4-3. Non-dimensional values defined in equations

Non-dimensional values		
a	ratio between R_1 and R_2 [-]	$a = \frac{R_1}{R_2}$
A	non-dimensional value in force balance equation [-]	$A = \frac{R_1}{R_H}$
B	non-dimensional value in force balance equation [-]	$B = \frac{R_2}{R_H}$
C	non-dimensional value in force balance equation [-]	$C = \frac{R_m}{R_H}$
Fr	Froude number [-]	$Fr \equiv \frac{V_{gj}}{\sqrt{gD_H}}$
Ga	Galileo number [-]	$Ga \equiv \frac{\sqrt{gD_H}D_H\rho_l}{\mu_l}$
$N_{\tau 1}$	non-dimensional inner wall shear stress on outer pipe [-]	$N\tau_1 = \frac{\tau_1}{\mu_l}\sqrt{\frac{D_H}{g}}$
$N_{\tau 2}$	non-dimensional outer wall shear stress on inner pipe [-]	$N\tau_2 = \frac{\tau_2}{\mu_l}\sqrt{\frac{D_H}{g}}$
r^*	non-dimensional radial position [-]	$r^* = \frac{r}{R_H}$

r_m^*	ratio between R_m and R_2 [-]	$r_m^* = \frac{R_m}{R_2} = \frac{C}{B}$
S^*	non-dimensional value for mixing length [-]	$S^* = \frac{R_m - R_1}{R_2 - R_m} = \frac{C - A}{B - C}$
u^*	non-dimensional liquid velocity [-]	$u' = \frac{u}{\sqrt{g \cdot D_H}}$
η_1	non-dimensional value for mixing length [-]	$\eta_1 = \frac{R_m - r}{R_m - R_1} = \frac{C - r^*}{C - A}$
η_2	non-dimensional value for mixing length [-]	$\eta_2 = \frac{r - R_m}{R_2 - R_m} = \frac{r^* - C}{B - C}$

Chapter 5

Prediction of radial distribution of local liquid velocity using momentum transfer model

5.1 Introduction

As explained in Chapter 2, it was found from the experimental results that the void fraction and the local liquid velocity in the LBE two-phase flow take the maximum value near the wall region at low void fraction conditions. On the other hand, in higher void fraction conditions, the local void fraction and the local liquid velocity in the LBE two-phase flow show core-peak distributions. These experimental results might be affected by wall wettability effect and lift force effect on bubbles in the LBE two-phase flow. In respect to wall wettability effect on LBE two-phase flow, it was found from the experiments and numerical prediction using momentum transfer model that volume averaged void fraction in LBE two-phase flow is increased in the case of poor wall wettability condition and the location of maximum point of local void fraction is inferred to be located close to poor wetted inner wall surface in case of annular bubble column condition, as explained in Chapter 4. So, wettability effect on the LBE two-phase flow was confirmed through the Chapter 4.

In this chapter, analytical model used in Chapter 4 is applied to forced convection condition. And then, radial distribution of local liquid velocity measured in the LBE two-phase flow in a round tube was numerically investigated by conducting one-dimensional numerical simulation using momentum transfer model toward the radial direction. Through this chapter, reproduction of the measured local liquid velocity distributions was tried by taking inferred wettability and lift force effects on bubbles into account to the momentum transfer model.

5.2 Numerical analysis for predicting liquid velocity profile in LBE two-phase flow with Clark's model

5.2.1 *Basic equations of Clark's model*

In this section, the local liquid velocity distributions in the LBE two-phase flow are investigated by utilizing useful prediction methods based on momentum transfer model proposed by Clark et al. [5-1, 5-2]. Detailed explanations of basic equations are given in following part.

In this analysis, the radial distribution of void fraction is assumed and given as a

polynomial expression corresponding to measured void fraction profile by using a least squares method. The mixture density described as a function of radial position is given by following equation:

$$\rho(r) = \rho_l \{1-\alpha(r)\} + \rho_g \alpha(r) \tag{5-1}$$

Since, generally, the density of gas can be neglected, the following equation is obtained as the mixture density

$$\rho(r) = \rho_l \{1-\alpha(r)\} \tag{5-2}$$

The axial shear stress may be found using a force balance as shown in Equation (5-3), where $\overline{\rho}$ indicates the cross sectional average density over the whole radius defined as Equation (5-4), and $\rho_{l,i(0\to r)}(r)$ also denotes cross sectional average density calculated by integration in terms of the densities from pipe center to certain radial point, as defined as Equation (5-5).

$$\tau(r) = \frac{r}{R}\tau_w + \frac{rg}{2}(\overline{\rho} - \rho_i) \tag{5-3}$$

$$\overline{\rho_{l,0\to R}} = \frac{\int_0^R \rho_l(r) 2\pi r dr}{\int_0^R 2\pi r dr} \tag{5-4}$$

$$\rho_{l,i(0\to r)}(r) = \frac{\int_0^r \rho_l(r) 2\pi r dr}{\int_0^r 2\pi r dr}. \tag{5-5}$$

As used in Chapter 4, using the mixing length for single-phase turbulent flow, the share stress is given by Equation (5-6).

$$\tau(r) = -\mu\frac{du}{dr} - \rho l^2 \left|\frac{du}{dr}\right| \frac{du}{dr} \tag{5-6}$$

, where *l* is Nikuladse's mixing length for single-phase turbulent flow.

$$\frac{l}{R} = 0.14 - 0.08\left(\frac{r}{R}\right)^2 - 0.06\left(\frac{r}{R}\right)^4 \tag{5-7}$$

From Equation (5-3) and Equation (5-6), the following equation in terms of velocity gradient is obtained.

$$0 = \tau_w\left(\frac{r}{R}\right) + \frac{1}{2}rg\{\bar{\rho} - \rho_i(r)\} + \mu_l\frac{du}{dr} + \rho l^2\left|\frac{du}{dr}\right|\frac{du}{dr} \tag{5-8}$$

Then non-dimensional equation corresponding to Equation (5-8) is as follows:

$$0 = \left\{N_{\tau_w} + \frac{Ga}{2}\frac{1}{2}(X - Y)\right\}r^* + 2\frac{du^*}{dr^*} + \{1 - \alpha(r^*)\}Ga\left(\frac{l}{R}\right)^2\left|\frac{du^*}{dr^*}\right|\frac{du^*}{dr^*} \tag{5-9}$$

, where non-dimensional values used in Equation (5-9) are listed on Table 5-1. From Equation (5-9), the local liquid velocity gradient can be calculated. As can be seen in Equation (5-9), the equation is quadratic function of velocity gradient. So, in this study, the velocity gradients were solved by using quadratic formula for simplicity. Then, by integrating the velocity gradients calculated by Equation (5-9) toward the radial direction, the local liquid velocity distribution can be obtained, where boundary condition is 0 velocity at wall surface.

$$u_l(r^*) = \int_1^0 \frac{du_l}{dr^*}dr^* \tag{5-10}$$

Flow chart of practical computational procedure for this analysis is shown in **Figure 5-1**. As can be seen from this figure, radial distribution of void fraction, viscosity of LBE, density of LBE, radius of flow channel and wall share stress are given as initial conditions for the analysis. Then, using velocity gradient calculated by Equation (5-9) and boundary condition for velocity at wall surface, simulated radial distribution of liquid velocity can be obtained. From such estimated liquid velocity distribution and assumed void fraction profile, superficial liquid velocity can be obtained. In this analysis, by varying the initial condition of the shear stress at the wall, convergent calculation is conducted so that the given superficial liquid velocities are satisfied. Then finally, optimized radial distribution of local liquid velocity is obtained. In the section, calculated radial distribution of liquid velocity is compared with liquid velocity distribution measured in LBE flows.

5.2.2 *Simulated systems and condition*

The schematic diagram of the simulated system in this analysis is illustrated in **Figure 5-2**. The system simulates the experimental setup in HESTIA, which consists of the vertical circular pipe having inner diameter of 50 mm and length of 1.9 m. The flow parameters are the superficial gas velocity in the range from 0.01 to 0.15 m/s and the superficial liquid velocity in the range from 0.1 to 0.2 m/s. The physical properties of the LBE and the nitrogen were calculated corresponding to liquid temperature of 200℃. In the analysis, liquid velocity profiles measured at z/D=32.4 were analyzed because flow field in the LBE two-phase flow can be considered as developed flow field.

5.2.3 *Local liquid velocity profiles predicted by Clark's model using mixing length for single phase turbulent flow*

First of all, Clark's model was examined for LBE single phase flow by substituting 0 for the void fraction in Equation (5-9). Comparisons of the measured and calculated liquid velocity profiles for LBE single phase flow are shown in **Figure 5-3.** It should be noted that these velocity profiles were calculated by using Equation (5-9), by assuming Nikuradse's mixing length. As indicated in **Figure 5-3**, the calculated liquid velocity profiles show good agreement with experimental results over all of the present experimental conditions. From these results, the mixing length model can be applied to simulate LBE single phase turbulent flow without any special assumptions.

Using the Clark's model, liquid velocity profiles in LBE two-phase flow were calculated. The results are shown in **Figures 5-4** to **Figure 5-7**. These figures indicate the comparisons of liquid velocity between measurements and calculations, where Nikuradese's mixing length was used for the calculation and ranges of superficial gas and liquid velocity are 0.01 to 0.15 m/s and 0.1 to 0.2 m/s, respectively. It is found that calculated liquid velocity profiles show relatively good agreement with liquid velocity profiles measured at conditions of superficial gas velocity from 0.01 and 0.02 m/s. However, the calculated liquid velocity profiles show disagreement with experimental results measured higher superficial gas velocity conditions; calculated velocities overestimate experimental results at core region and also underestimate experimental results at wall side region. These disagreements may arise from the underestimation of momentum transfer term calculated by Nikuladse's mixing length. As shown in Chapter 2, measured turbulence intensities for two-phase flow show quite larger values than those for single phase flow. Such tendency indicates that bubble induced turbulence might be dominant in LBE two-phase flow measured at present experimental conditions. Therefore, in the following section, bubble induced turbulence is taken into account to predict measured liquid velocity profiles.

5.3 Numerical analysis for predicting liquid velocity profile in LBE two-phase flow with Sato's model

5.3.1 *Basic equations of Sato's model*

In order to take the turbulence in two-phase flow into account to momentum transfer model, the share stress derived from momentum transfer is given by Equation (5-11), where the turbulence is composed of the wall turbulence and the bubble induced turbulence,

$$\tau = (1-\alpha)\left(\mu_l \frac{du_l}{du} - \rho_l \overline{u'v'} - \rho_l \overline{u''v''} \right)$$

$$\tau = (1-\alpha)\left(\mu_l \frac{du_l}{du} + \rho_l \varepsilon' \frac{du_l}{dy} + \rho_l \varepsilon'' \frac{du_l}{dy} \right)$$

$$\tau = \rho_l (1-\alpha)(\upsilon_l + \varepsilon' + \varepsilon'') \frac{du_l}{dy} \tag{5-11}$$

, where υ_l, ε' and ε'' are the kinetic viscosity, the eddy diffusivity for the wall turbulence and the eddy diffusivity for the bubble induced turbulence, respectively. At present analysis, Equation (5-12) is used as the eddy diffusivity for the wall turbulence

$$\varepsilon' = \left\{ 1 - \exp\left(-\frac{y^+}{A^+} \right) \right\}^2 \kappa y^+ \left\{ 1 - \frac{11}{6}\left(\frac{y^+}{R^+} \right) + \frac{4}{3}\left(\frac{y^+}{R^+} \right)^2 - \frac{1}{3}\left(\frac{y^+}{R^+} \right)^3 \right\} \upsilon, \tag{5-12}$$

$$y^+ = \frac{yu^*}{\upsilon},\ R^+ = \frac{Ru^*}{\upsilon},\ A^+ = 16,\ \kappa = 0.4$$

where y^+, R^+, A^+ and κ are the non-dimensional distance from wall, the non-dimensional radius, the experimental constant and the mixing length constant, respectively. The eddy diffusivity for the bubble induced turbulence is given as following Equation (5-13):

$$\varepsilon'' = \left\{ 1 - \exp\left(-\frac{y^+}{A^+} \right) \right\}^2 K_1 \alpha \left(\frac{d_B}{2} \right) U_B, \tag{5-13}$$

where $K_1 = 1.2$ is the experimental constant. U_B is the terminal velocity of a single bubble rising in a stagnant liquid. At present analysis, U_B was given as the difference between cross sectional averaged gas velocity measured by EC probe [5-5] and superficial liquid velocity measured by EM probe. In addition, d_B is the bubble diameter which is given by the following Equation (5-14)

$$d_B = \begin{cases} 0 & : (0 < y \le 20\mu\text{m}) \\ 4y(\hat{d}_B - y)/\hat{d}_B & : (20\mu\text{m} < y \le \hat{d}_B/2) \\ \hat{d}_B & : (\hat{d}_B/2 < y \le R) \end{cases} \quad (\hat{d}_B : \text{average bubble diameter}). \tag{5-14}$$

On the other hand, the axial shear stress may be expressed by same expression with Equation (5-3) from relationship for a force balance. Substituting Equation (5-3) for the shear stress in Equation (5-10), the following equation can be obtained:

$$0 = \tau_w\left(\frac{r}{R}\right) + \frac{1}{2}rg\left\{\overline{\rho} - \rho_i(r)\right\} + \rho_l(1-\alpha)\left(\frac{\mu_l}{\rho_l} + \varepsilon' + \varepsilon''\right)\frac{du_l(r)}{dr} \tag{5-15}$$

Finally, the following non-dimensional equations can be obtained:

$$0 = \left(\frac{r}{R}\right)\frac{\tau_w}{\mu_l}\sqrt{\frac{D}{g}} + \frac{1}{2}rg\frac{1}{\mu_l}\sqrt{\frac{D}{g}}\left\{\overline{\rho} - \rho_i(r)\right\} + \rho_l\frac{1}{\mu_l}\sqrt{\frac{D}{g}}(1-\alpha)\left(\frac{\mu_l}{\rho_l} + \varepsilon' + \varepsilon''\right)\frac{du_l(r)}{dr}$$

$$0 = \left(\frac{r}{R}\right)\frac{\tau_w}{\mu_l}\sqrt{\frac{D}{g}} + \frac{1}{2}r\frac{\sqrt{gD}}{\mu_l}\frac{2R\rho_l}{2R}\left\{\frac{1}{\pi R^2}\int_0^R(1-\alpha)2\pi r dr - \frac{1}{\pi r^2}\int_0^r(1-\alpha)2\pi r dr\right\}$$

$$+ \frac{\rho_l}{\mu_l}\sqrt{\frac{D}{g}}(1-\alpha)\left(\frac{\mu_l}{\rho_l} + \varepsilon' + \varepsilon''\right)\frac{du_l(r)}{dr}$$

$$0 = N_{\tau_w}r^* + \frac{Ga}{2}\frac{1}{2}\left[\frac{1}{\pi}\int_0^1\left\{1-\alpha(r^*)\right\}2\pi r^* dr^* - \frac{1}{\pi r^{*2}}\int_0^{r^*}\left\{1-\alpha(r^*)\right\}2\pi r^* dr^*\right]r^*$$

$$+\frac{\rho_l}{\mu_l}\sqrt{\frac{D}{g}}\frac{\sqrt{gD}}{R}(1-\alpha)\left(\frac{\mu_l}{\rho_l}+\varepsilon'+\varepsilon''\right)\frac{du_l^*(r^*)}{dr^*}$$

$$0=\left(N_{\tau_w}+\frac{Ga}{2}\frac{X-Y}{2}\right)r^*+2(1-\alpha)\frac{\rho_l}{\mu_l}\left(\frac{\mu_l}{\rho_l}+\varepsilon'+\varepsilon''\right)\frac{du_l^*(r^*)}{dr^*}$$

$$0=\left(N_{\tau_w}+\frac{Ga}{2}\frac{X-Y}{2}\right)r^*+2Z\frac{du_l^*(r^*)}{dr^*}$$

$$\frac{du_l^*(r^*)}{dr^*}=-\frac{1}{2Z}\left(N_{\tau_w}+\frac{Ga}{2}\frac{X-Y}{2}\right)r^*, \tag{5-16}$$

where the non-dimensional values used in Equation (5-16) are listed also on Table 5-1. As can be seen in Equation (5-16), the equation is linear function. So, the local liquid velocity gradient can be easily calculated. And then, by integrating the velocity gradients in the radial direction, the local liquid velocity distribution can be obtained. By varying the initial value of the shear stress at the wall, convergent calculation is also conducted so that the given superficial liquid velocities are satisfied. In the following section, the liquid velocity distributions calculated by Equations (5-16) are compared with measured liquid velocity distributions.

5.3.2 *Local liquid velocity profiles predicted by Sato's model using eddy diffusivities for single phase turbulence and bubble induced turbulence*

In order to take the bubble induced effect on momentum transfer toward radial direction into account, Sato's model explained in section 5.3.1 was applied to the analysis. As mentioned in section 5.3.1, turbulence in two-phase flow is assumed to be sum of single phase turbulence and bubble induced turbulences. And then, eddy diffusivities corresponding to each turbulence are introduced to momentum transfer model, as written in Equation (5-16).

Predicted liquid velocity profiles are shown in **Figures 5-8** to **5-11**. It is found that tendency of calculated liquid velocities are changed to be flatter shape in conditions of superficial gas velocity larger than 0.1 m/s and roughly agree with experimental results in such superficial gas velocity conditions. It is considered that such change of the tendency is caused by larger momentum transfer toward radial direction than that estimated by Clark's model using only mixing length for single phase turbulent flow. Such larger momentum transfer is estimated by introducing eddy diffusivity due to bubble induced turbulence. As mentioned in Chapter 2,

measured turbulence intensities for two-phase flow show quite larger values than those for single phase flow. And such difference of intensity is proportional to superficial gas velocity. Such results indicate that larger effect of bubble induced turbulence on the velocity profile might exist in LBE two-phase flow at present experimental conditions. Therefore, as shown in Chapter 2, it is considered that core-peak velocity distributions measured at condition of superficial gas velocity larger than 0.1 m/s may be formed by larger effect of bubble induced turbulence. So, it can be considered that tendencies between calculated and measured liquid velocity distribution are valid in the case of superficial gas velocity lager than 0.1 m/s.

On the other hand, it is found that measured liquid velocity distributions at condition of superficial gas velocity less than 0.05 m/s are not predicted well. Such measured liquid velocity distributions indicate same tendency in terms of distribution shape; those liquid velocity distributions have maximum value near the wall side, wall-peak distribution. One of the possibilities of cause for such wall-peak distribution is considered below.

As mentioned in Chapter 1, LBE has poor wettability characteristics to stainless steel. At present work, commercial stainless steel pipe without any surface treatment is utilized as the test section of HESTIA. So, it can be considered that there exists a poor wettability condition in the LBE two-phase flow measured in this study. Here, as for the case of air-water two-phase flow, it was reported that bubbles rising in a two-phase flow tend to be close to and to attach to and detach from the wall surface in such poor wettability condition to the wall surface [5-6, 5-7, 5-8]. Hence, it may be able to consider that similar phenomenon can arise also in the LBE two-phase flow. In fact, as shown in Chapter 2, void fraction measured at condition of superficial gas velocity less than 0.05 m/s indicated wall-peak distribution too. Therefore, it can be guessed that bubbles tend to flow near the wall side. Such bubbles may continue to flow near the wall surface once the bubble can touch to the wall surface due to poor wettability effect on the bubbles. At the same time, rising velocity of such bubbles is faster than that of liquid phase. So, velocity gradient becomes larger near the wall surface. Therefore, bubbles may be accumulated by lift force due to such velocity gradient. And then, it might be guessed that liquid phase flowing near the wall side is accelerated by accumulated bubbles existing near the wall side.

As shown in **Figure 5-3**, measured liquid velocity can be predicted by momentum transfer model without any newly assumption at wall surface in case of LBE single phase flow. From that calculation results, it may be able to consider that liquid velocity at wall surface is almost 0 m/s. However, as explained above, liquid phase flowing near the wall side may be accelerated by accumulated bubbles existing near the wall side. Hence, there may be a possibility to exist finite liquid velocity at wall surface in case of LBE two-phase flow. In the practical condition, it can be considered that bubbles discretely exist on the wall surface, as

shown in **Figure 5-12**. Hence, there might be repetition of dry and wet due to such bubbles on the wall surface. Due to these bubbles, liquid phase may be accelerated. From space-time average point of view, this situation might be considered as slip condition at wall surface. Therefore, the finite velocity might be regarded as some kind of slip velocity at wall surface. In the following section, such slip velocity is taken into account to Sato's model.

5.3.3 *Local liquid velocity profiles predicted by Sato's model with assumption of slip velocity on the wall surface*

To take the slip condition into account to Sato's model, void fraction at wall surface was assumed because the slip velocity may be caused by bubbles accumulated on the wall surface. The void fraction was given by polynomial expression of even function. And also, as indicated in **Figure 5-13**, boundary condition for liquid velocity at $r^* = 1$ was changed so that the calculated liquid velocity distribution agrees with measured liquid velocity distribution. Calculated results are shown in **Figures 5-14** (right) to **Figure 5-17** (right), where Figures located left side denotes void fraction profiles assumed in this analysis. It is found that predicted liquid velocity profiles show agreement with experimental results in all of experimental conditions.. Therefore, there might be slip condition on the wall surface. Such slip conditions should be assumed to predict the liquid velocity profiles for poor wettability condition.

From those calculation results shown in **Figures 5-14** to **5-17**, the slip velocities assumed in this analysis can be obtained. Such slip velocity might come from bubbles accumulated on the wall surface by wettability effect and velocity gradient toward the wall surface, as explained above section. In that case, it is considered that there might be some relationships between the assumed slip velocities and gas velocities. Therefore, in this study, void fraction weighed mean gas velocities, $\langle\langle u_g \rangle\rangle$, are estimated in order to find relationship between such gas velocities and the assumed slip velocity. Here, to estimate void fraction weighed mean gas velocity, void fraction weighed mean drift velocity, V_{gj}, is needed. Here, the $\langle\langle v_{gj} \rangle\rangle$ was given as constant value of 0.27 m/s since the V_{gj} are about 0.27 m/s, as denoted in Chapter 3. In addition, it was reported in the previous study that the distribution parameter C_0 was approximately 1 [5-5]. Hence, the C_0 was given as same value of 1, in present work. Using Equation (3-18), $\langle\langle u_g \rangle\rangle$ are estimated.

Figure 5-18 shows the relationship between estimated $\langle\langle u_g \rangle\rangle$ and the slip velocity assumed at wall surface. It is found that the assumed slip velocities are proportional to $\langle\langle u_g \rangle\rangle$. And also, slip velocities are about 30% of $\langle\langle u_g \rangle\rangle$. From this result, radial distribution of local liquid velocity may be able to be predicted by using Sato's momentum transfer model if the slip velocity given as about 30% value of $\langle\langle u_g \rangle\rangle$ and void fraction on the wall surface are

introduced to the model.

As for the meaning of the 30%, it might be considered that there exist starting point of bubble coalescence to become larger bubble. Mishima and Ishii [5-??] derived result of α = 0.3 from simple geometrical consideration only. And they reported that the value, 0.3, of void fraction can be given as boundary of bubbly to slug flows transition because not only bubble collision but also bubble coalescence arise if the void fraction becomes larger than 0.3. Based on their consideration, it is considered that similar condition for bubbles might be formed near the wall surface in the LBE two-phase flow. At present experimental condition, the accumulation of bubbles is inferred from the consideration of wettability effect and lift force effect on bubbles in the LBE two-phase flow. Then, formation of larger bubbles might be started by bubbles which are going to be close to the wall surface if the void fraction becomes larger than 0.3. The formed larger bubbles might break up due to interfacial instability of bubbles. After that, at wall region, such phenomena might be repeated in case of LBE two-phase flow flowing poor wetted channel. At present work, above mentioned phenomena is inferred. However, in this study, measurements of liquid velocity and void fraction at wall surface have not been conducted so far due to problem for dimensions of EM and EC probes. Therefore, further investigation for the liquid velocity and the void fraction close to the wall surface should be needed to clarify detailed mechanism of slip velocity.

5.4 Conclusion

To investigate the effect of wall surface condition on flow structure in LBE two-phase flow, the local void fraction and local liquid velocity in LBE two-phase flow were measured by using intrusive probe method. From measurement and analytical results, the following conclusions are obtained.

From the comparison of liquid velocity distributions between measured and calculated one, liquid velocity distributions predicted by Clark's model using mixing length for single phase turbulent flow show agreement with velocity distributions measured in the LBE single phase flow However, in case of two-phase flow, it is found that predicted liquid velocity profiles show disagreement with experimental results measured higher superficial gas velocity conditions. This means that amount of momentum transfer is underestimated in case of using mixing length for single-phase flow. That means bubble induced turbulence might be dominant in LBE two-phase flow measured at present experimental conditions.

In case of using Sato's model which introduce eddy viscosities for single phase turbulent flow and bubble induced turbulence, predicted liquid velocity profiles show roughly agreement with experimental results measured higher superficial gas velocity conditions.

Good agreement was obtained between experimental and predicted velocity profiles by assuming slip velocity on the wall surface. In case of poor wettability condition, there is repetition of dry and wet due to bubble on the wall surface. Therefore, macroscopic point of view, such slip conditions should be assumed to predict the velocity profiles for poor wettability conditions.

From the consideration in term of wettability effect and lift force effect on the bubbles, it is considered that the slip velocities on the wall surface might come from bubbles accumulated on the wall surface. In that case, it is considered that there might be some relationships between the assumed slip velocities and gas velocities. From the relationship between estimated $<<u_g>>$ and the slip velocity assumed at wall surface, it is found that the assumed slip velocities are proportional to $<<u_g>>$ and that slip velocities are about 30% of $<<u_g>>$. From this result, radial distribution of local liquid velocity may be able to be predicted by using Sato's momentum transfer model if the slip velocity given as about 30% value of $<<u_g>>$ and void fraction on the wall surface are introduced to the model.

However, in this study, measurements of liquid velocity and void fraction at wall surface have not been conducted so far due to problem for dimensions of EM and EC probes. Therefore, further investigation for the liquid velocity and the void fraction close to the wall surface should be needed to understanding detailed mechanism of slip velocity

References for Chapter 5

[5-1] Clark NN, Atkinson CM, Flemmer RLC. Turbulent circulation in bubble columns. AlChE Journal. 1987 Apr; 33: 515-518.

[5-2] Clark NN, Egmond JWV, Nebiolo EP. The drift-flux model applied to bubble columns and low velocity flows. Int. J. Multiphase Flow. 1990 Mar - Apr; 16: 261-279.

[5-3] Sato Y, Sadatomi M, Horita K, Sekoguchi K. Momentum and heat transfer in two-phase bubble flow : 1st report, theory. Transaction of the Japan Society of Mechanical Engineers Series B. 1980; 46: 1780-1789 [in Japanese].

[5-4] Sato Y, Sadatomi M, Horita K, Nakazatomi M, Sekoguchi K. Momentum and heat transfer in two-phase bubble flow: 2nd report, A comparison between experimental data and theoretical calculations. Transaction of the Japan Society of Mechanical Engineers Series B. 1980; 46: 1790-1796 [in Japanese].

[5-5] Yamamoto Y, Master thesis, Kyoto university, 2012 [in Japanese].

[5-6] Iguchi M, Terauchi Y. Boundaries among bubbly and slug flow regimes in air-water two-phase flows in vertical pipe of poor wettability. Int. J. Multiphase Flow 2001 27 729-735.

[5-7] Iguchi M and Terauchi Y. Rising behavior of air-water two-phase flows in vertical pipe of poor wettability. ISIJ International 2000 Feb; 40: 567-571.

[5-8] Terauchi Y, Iguchi M, Kosaka H, Yokoya S, Hara S. [Wettability Effect on the Flow Pattern of Air-water Two-phase Flows in a Vertical Circular Pipe]. Tetsu-To-Hagane. 1999 Jun; 85: 7-13 [in Japanese].

[5-9] Mishima K, and Ishii M. Flow regime transition criteria for upward two-phase flow in vertical tubes. Int. J. Heat Mass Transfer 1984 27 723-737.

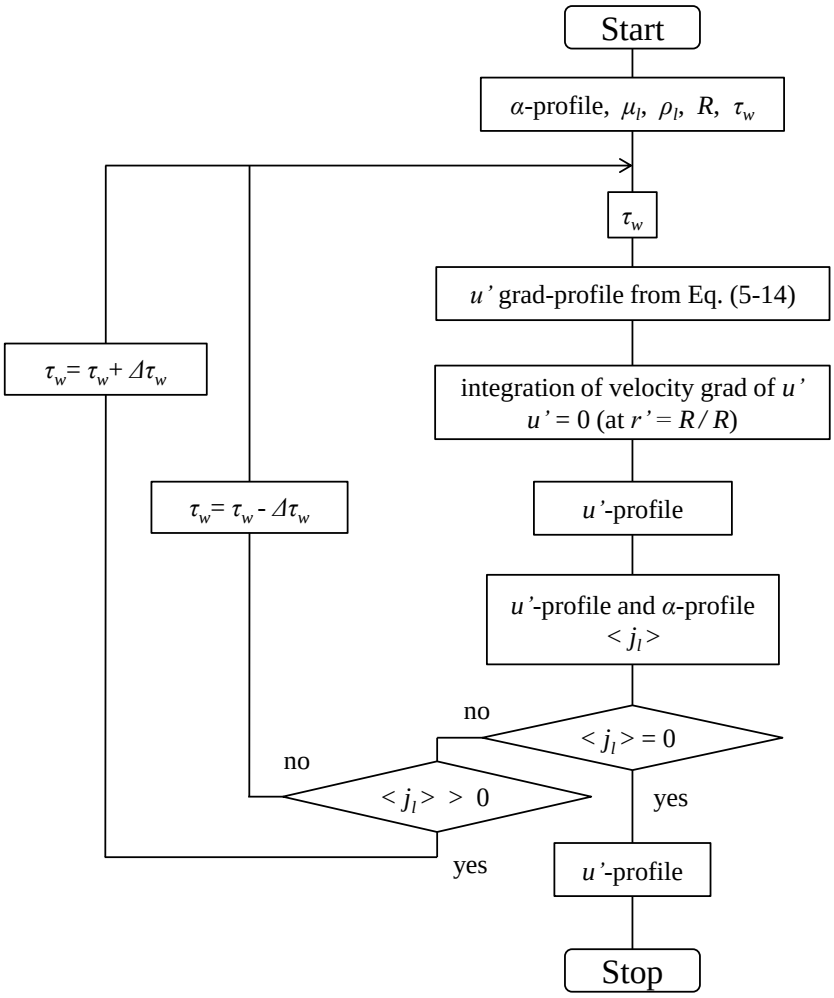

Figure 5-1 Flow chart for numerical analysis using Clark's model.

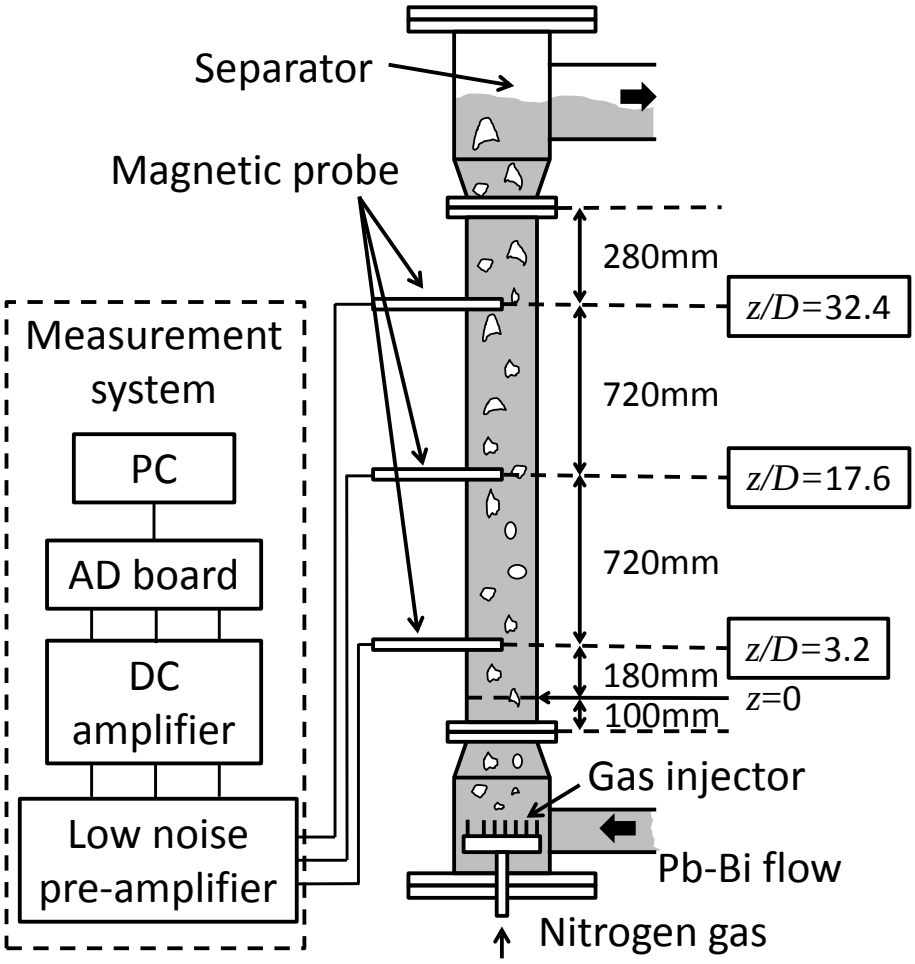

Figure 5-2 Simulated system in the analysis using momentum transfer model.

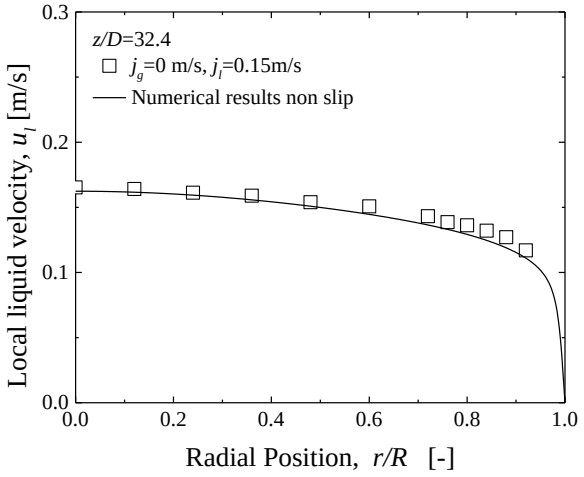

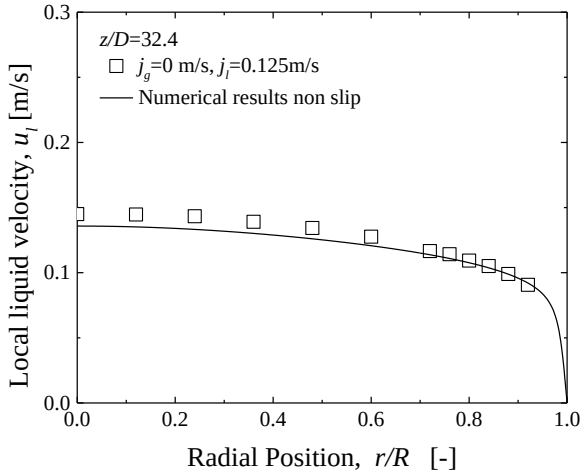

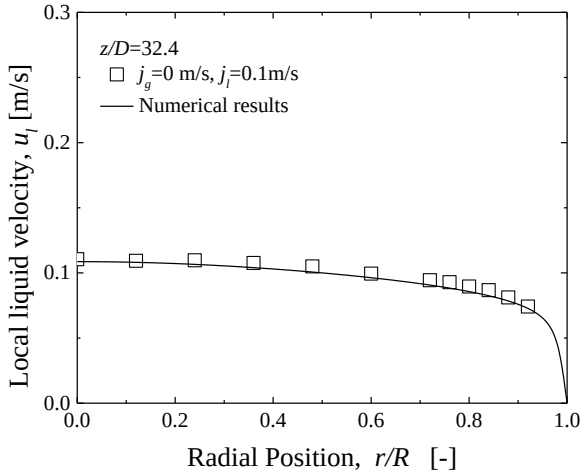

Figure 5-3 Comparison of liquid velocity between experimental one and calculated one, where Nikuradese's mixing length was used for the calculation.
(for j_g =0 m/s, j_l = 0.1 m/s)

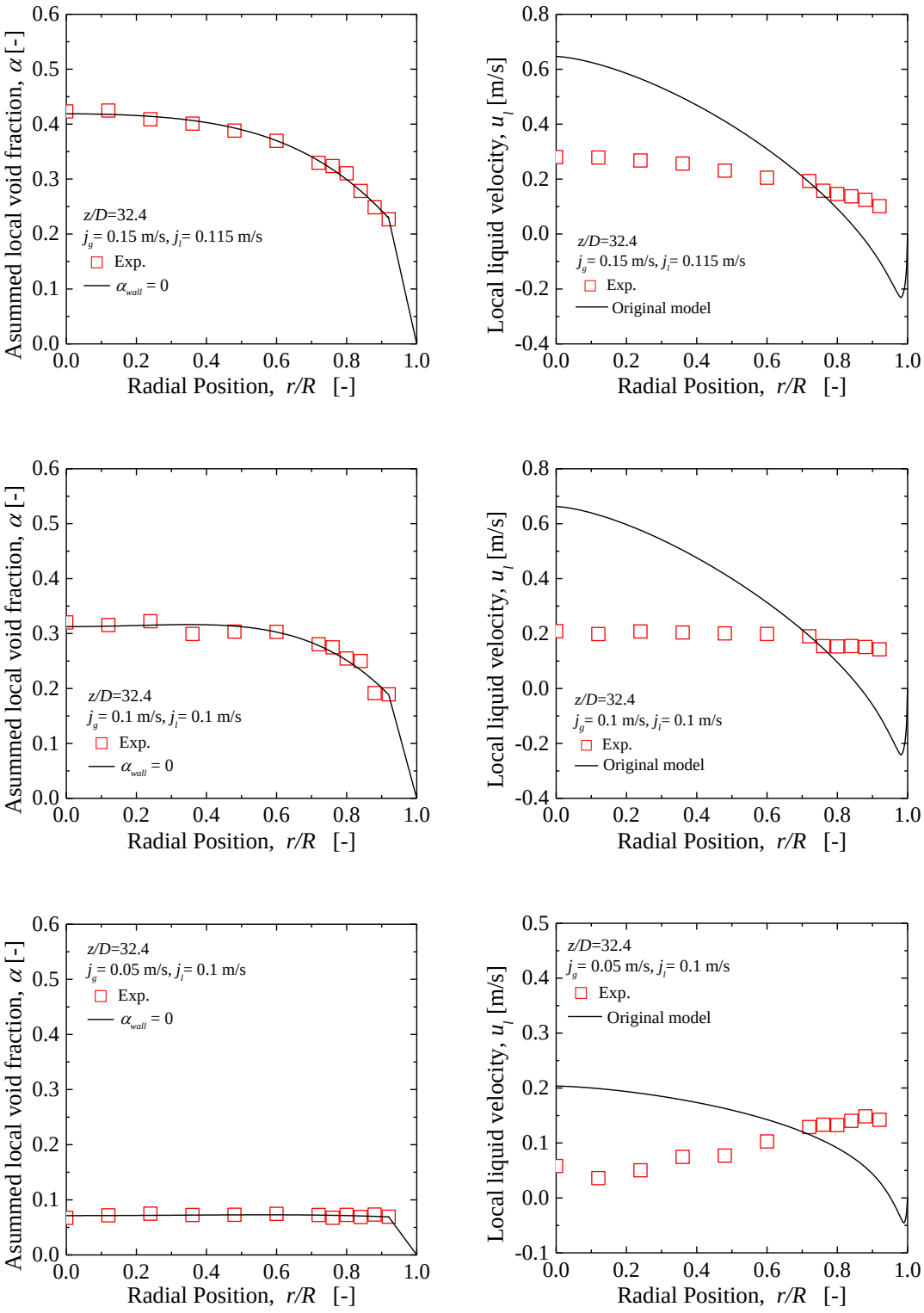

Figure 5-4 Comparison of liquid velocity between experimental one and calculated one, where Nikuradese's mixing length was used for the calculation. (for j_g =0.05 to 0.15 m/s, j_l = 0.1 m/s)

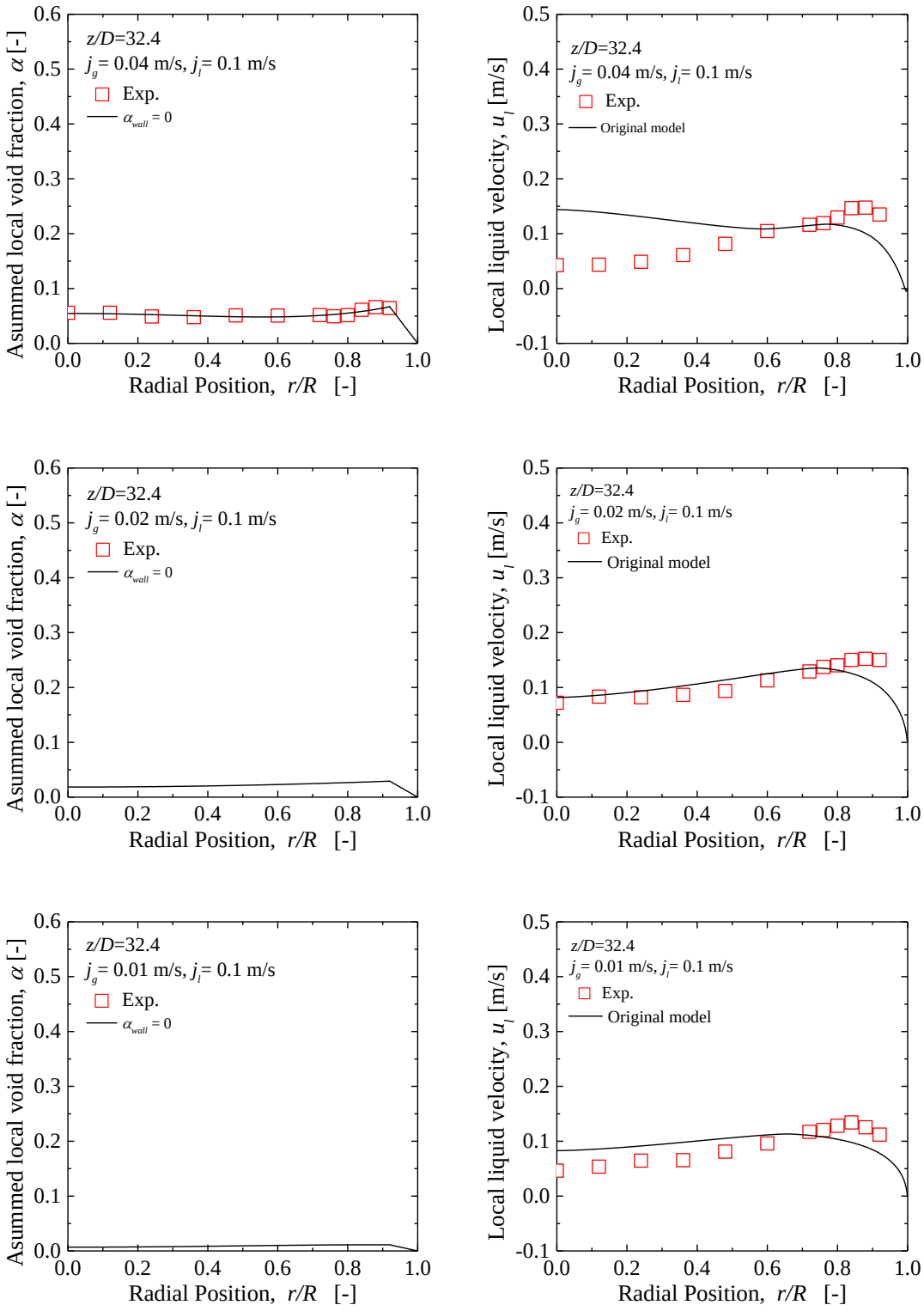

Figure 5-5 Comparison of liquid velocity between experimental one and calculated one, where Nikuradese's mixing length was used for the calculation. (for j_g =0.01 to 0.04 m/s, j_l = 0.1 m/s)

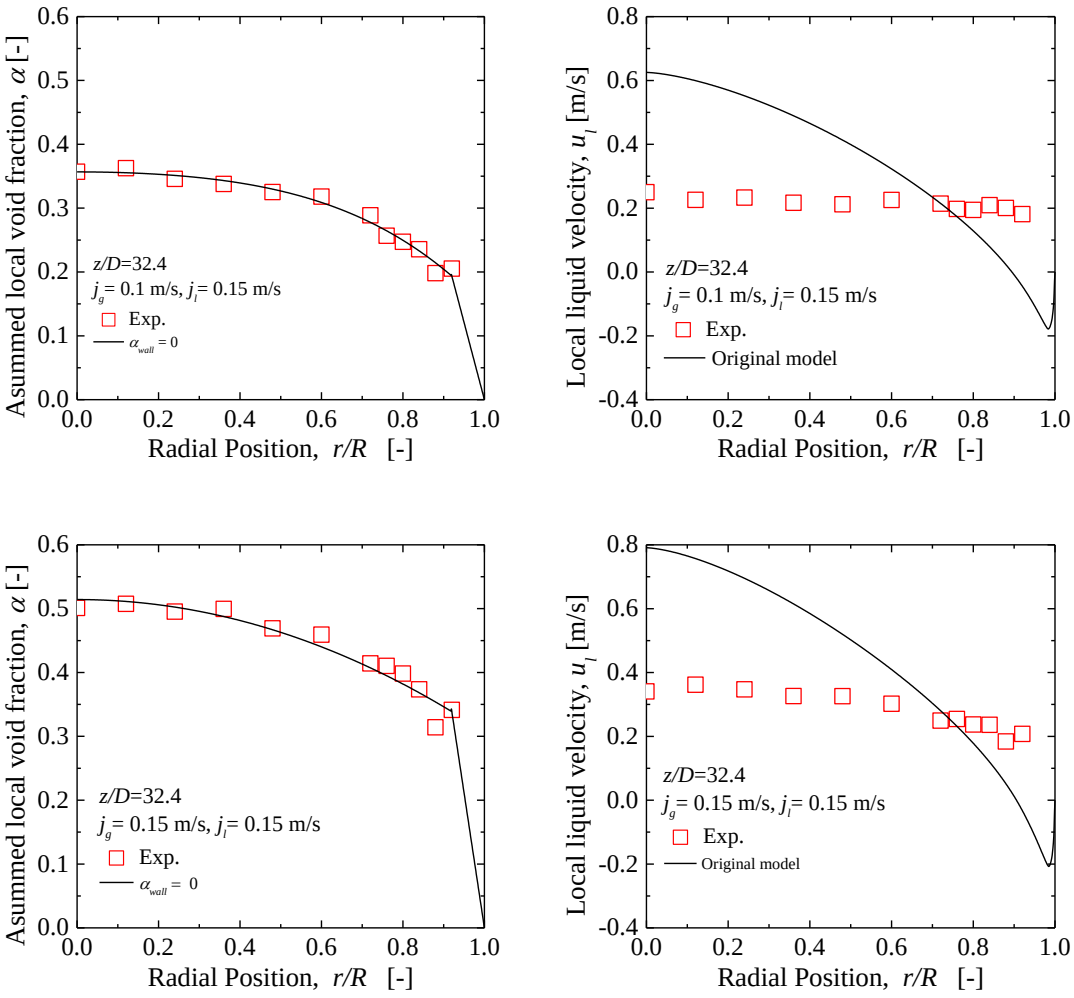

Figure 5-6 Comparison of liquid velocity between experimental one and calculated one, where Nikuradese's mixing length was used for the calculation. (for j_g =0.1 to 0.15 m/s, j_l = 0.15 m/s)

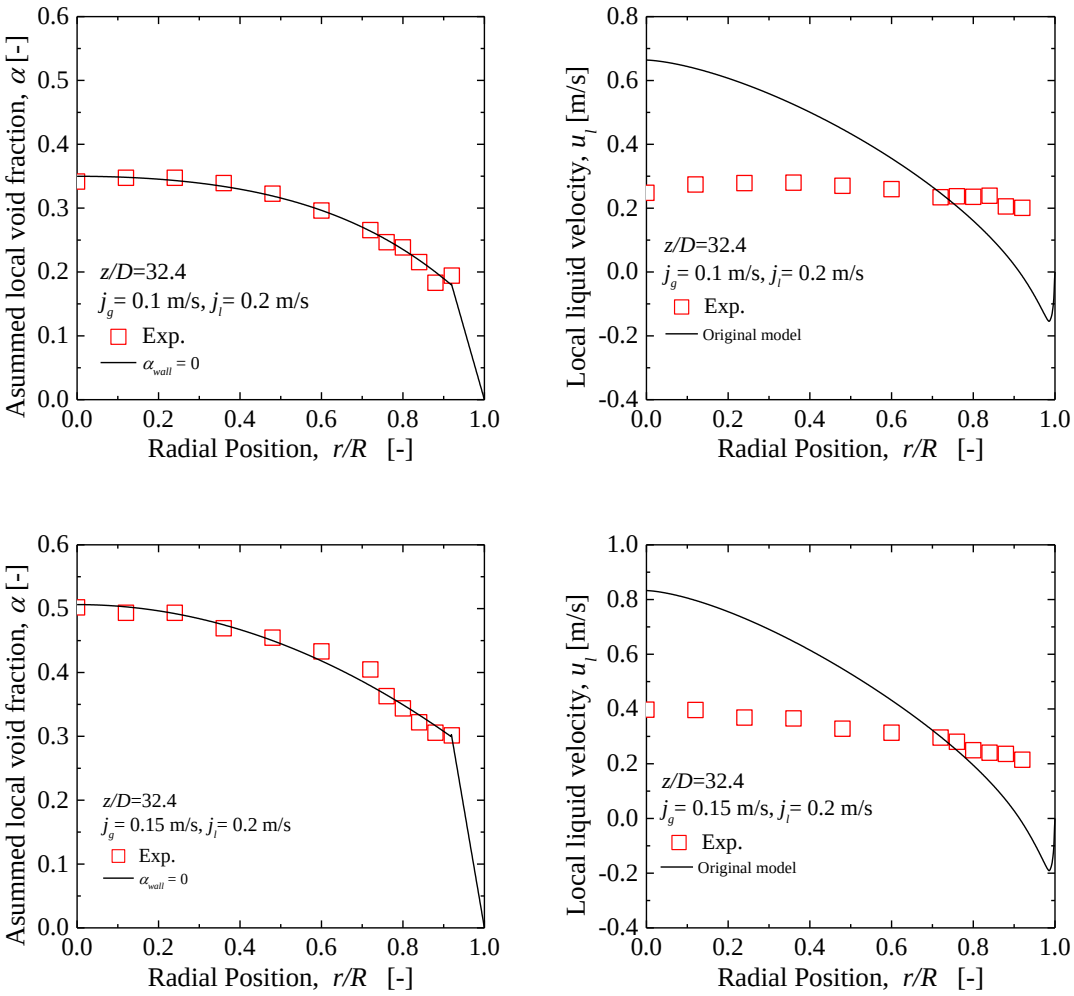

Figure 5-7 Comparison of liquid velocity between experimental one and calculated one, where Nikuradese's mixing length was used for the calculation (for j_g =0.1 to 0.15 m/s, j_l = 0.2 m/s)

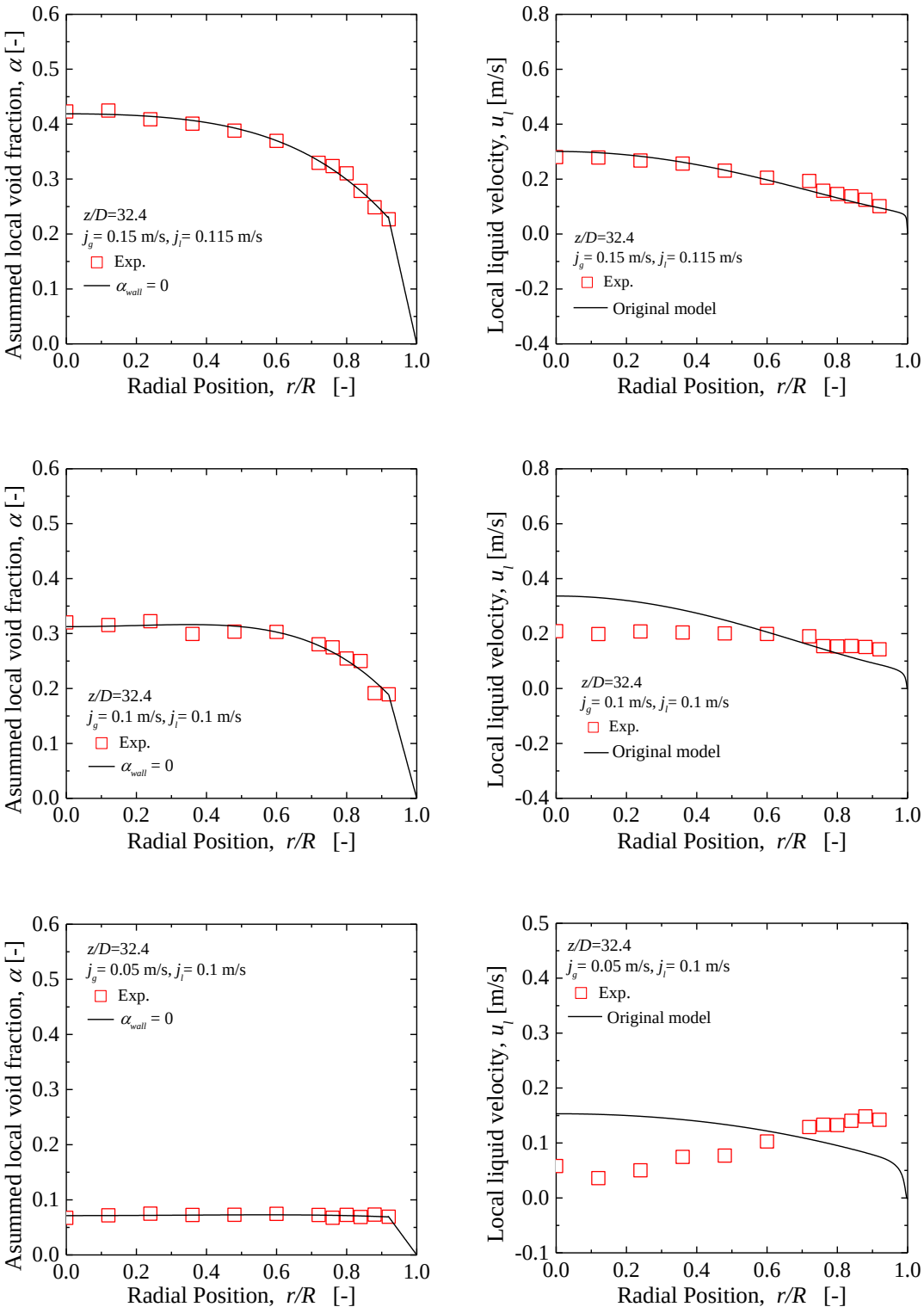

Figure 5-8 Comparison of liquid velocity between experimental one and calculated one, where eddy diffusivities, ε' and ε'', were used for the calculation.
(for j_g =0.05 to 0.15 m/s, j_l = 0.1 m/s)

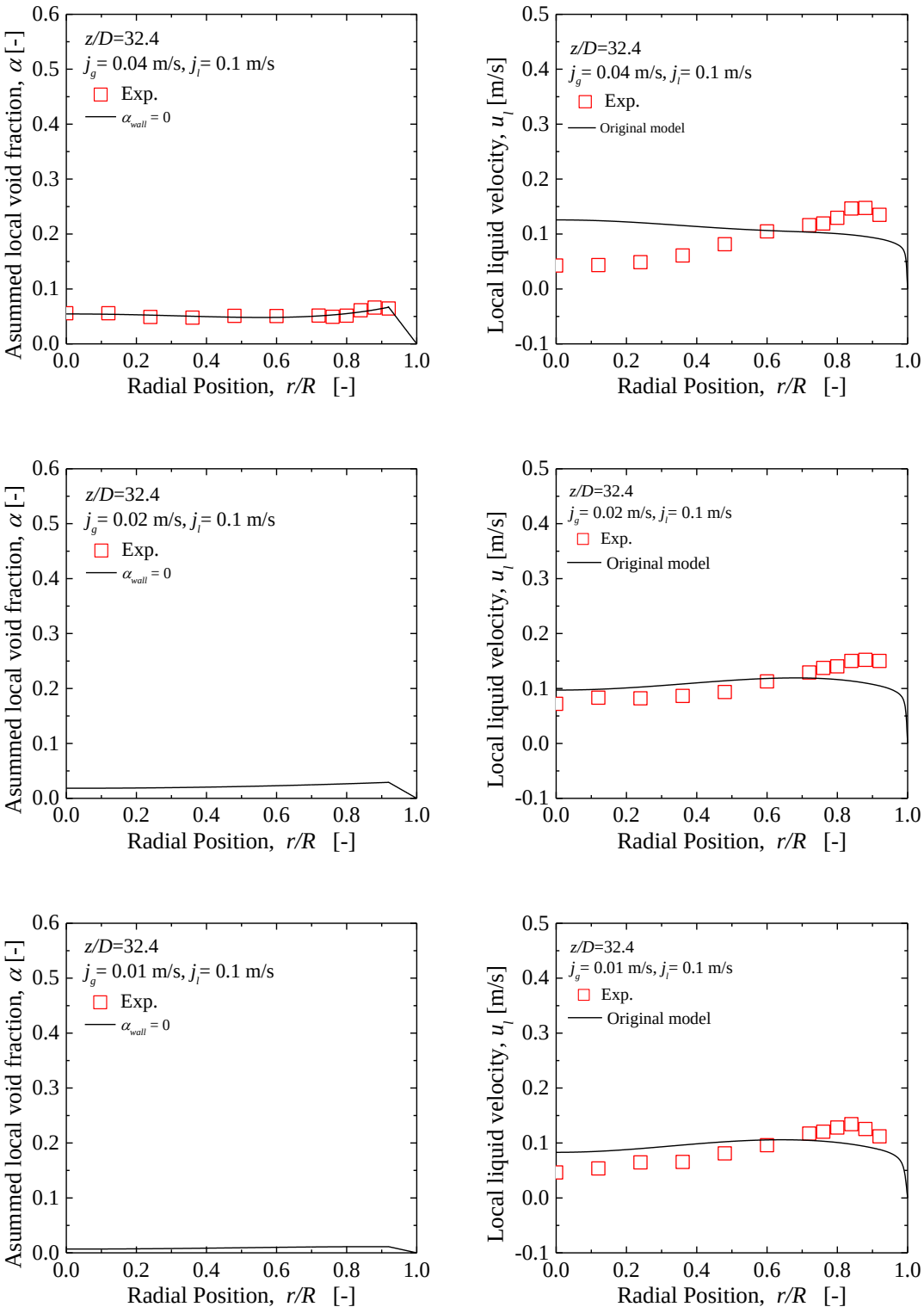

Figure 5-9 Comparison of liquid velocity between experimental one and calculated one, where eddy diffusivities, ε' and ε", were used for the calculation.
(for j_g =0.01 to 0.04 m/s, j_l = 0.1 m/s)

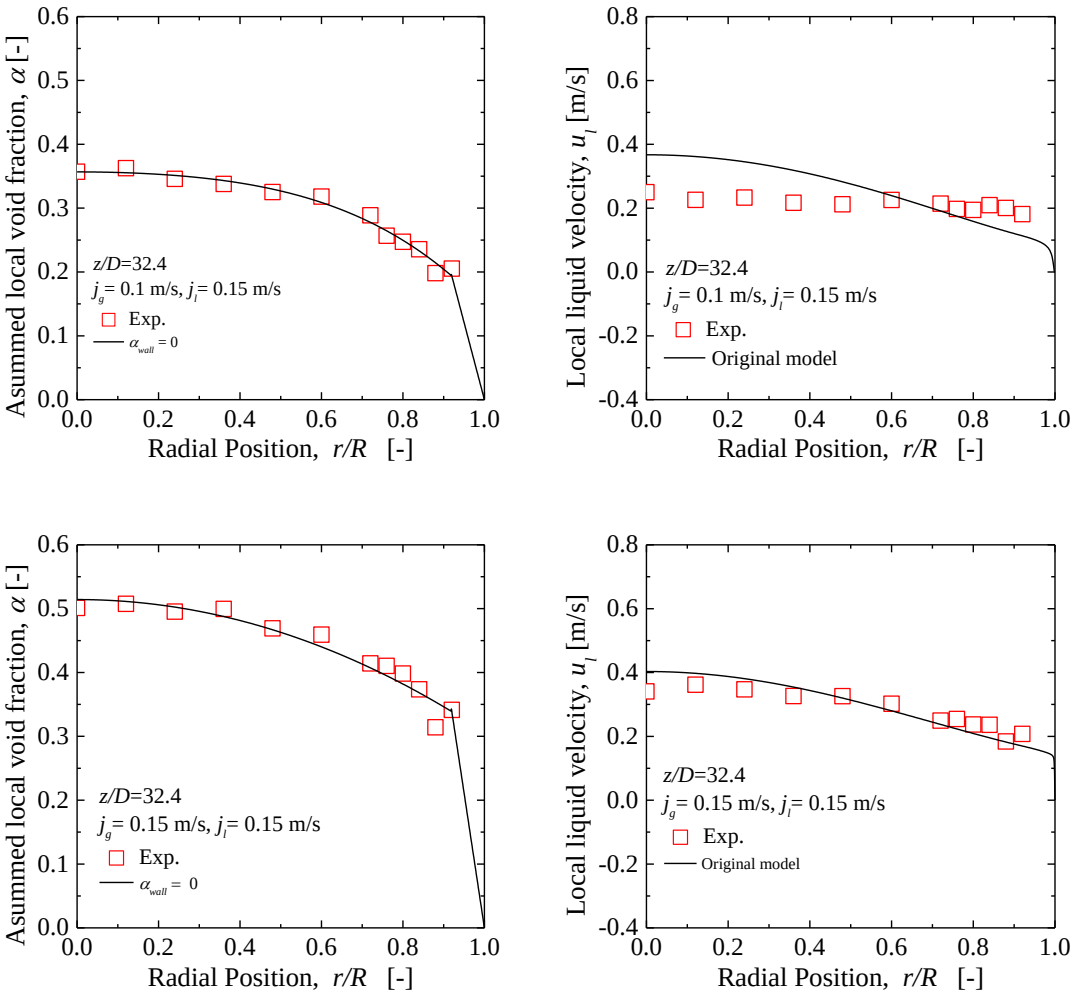

Figure 5-10 Comparison of liquid velocity between experimental one and calculated one, where eddy diffusivities, ε' and ε'', were used for the calculation.
(for j_g =0.1 to 0.15 m/s, j_l = 0.15 m/s)

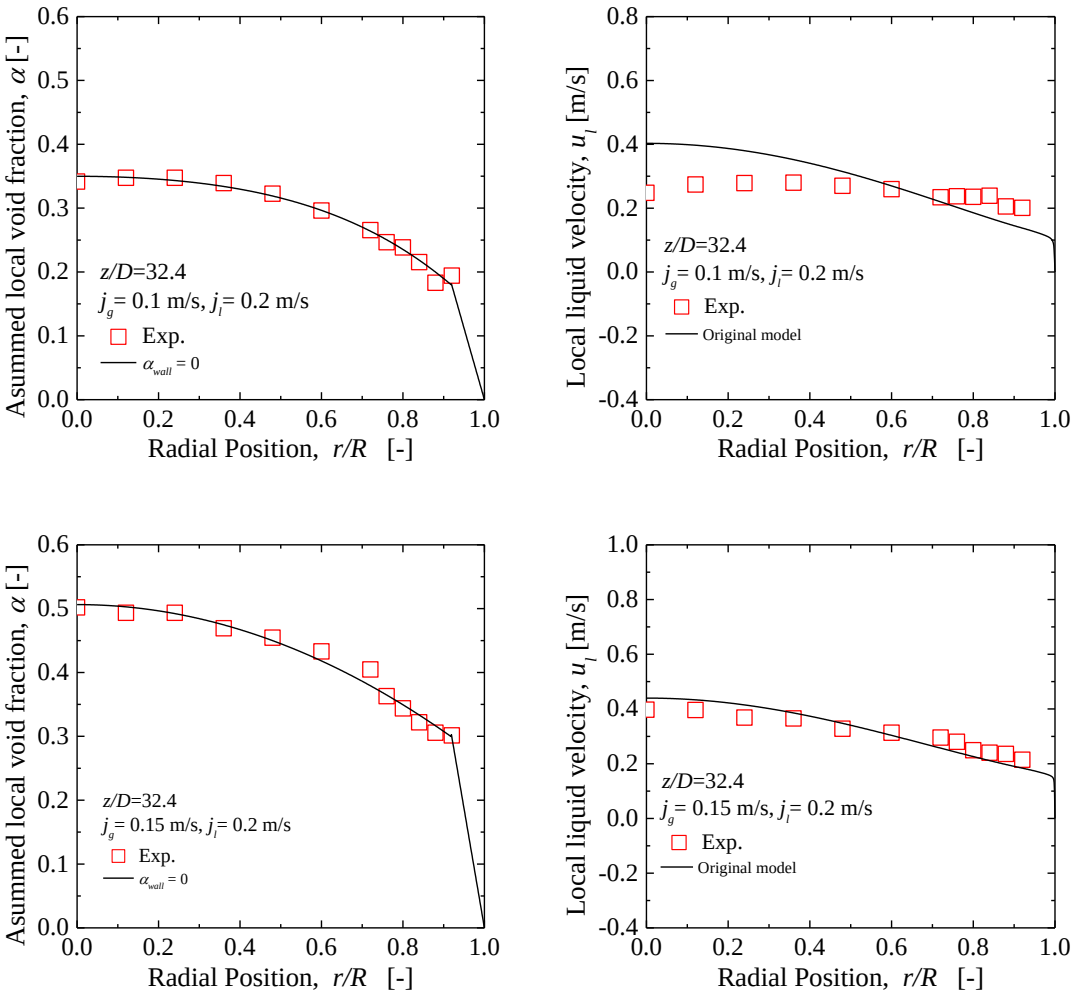

Figure 5-11 Comparison of liquid velocity between experimental one and calculated one, where eddy diffusivities, ε' and ε'', were used for the calculation.
(for j_g =0.1 to 0.15 m/s, j_l = 0.2 m/s)

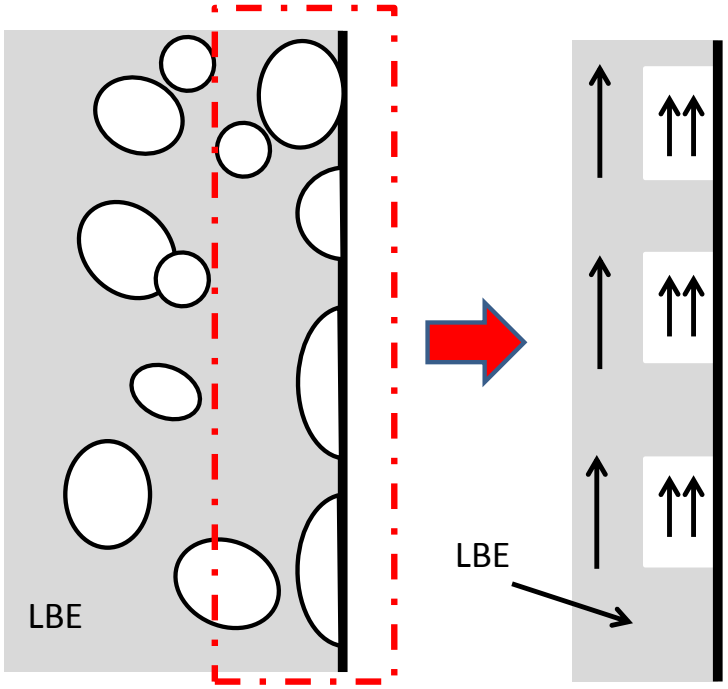

Figure 5-12 Inferred situation of bubbles near the wall region.

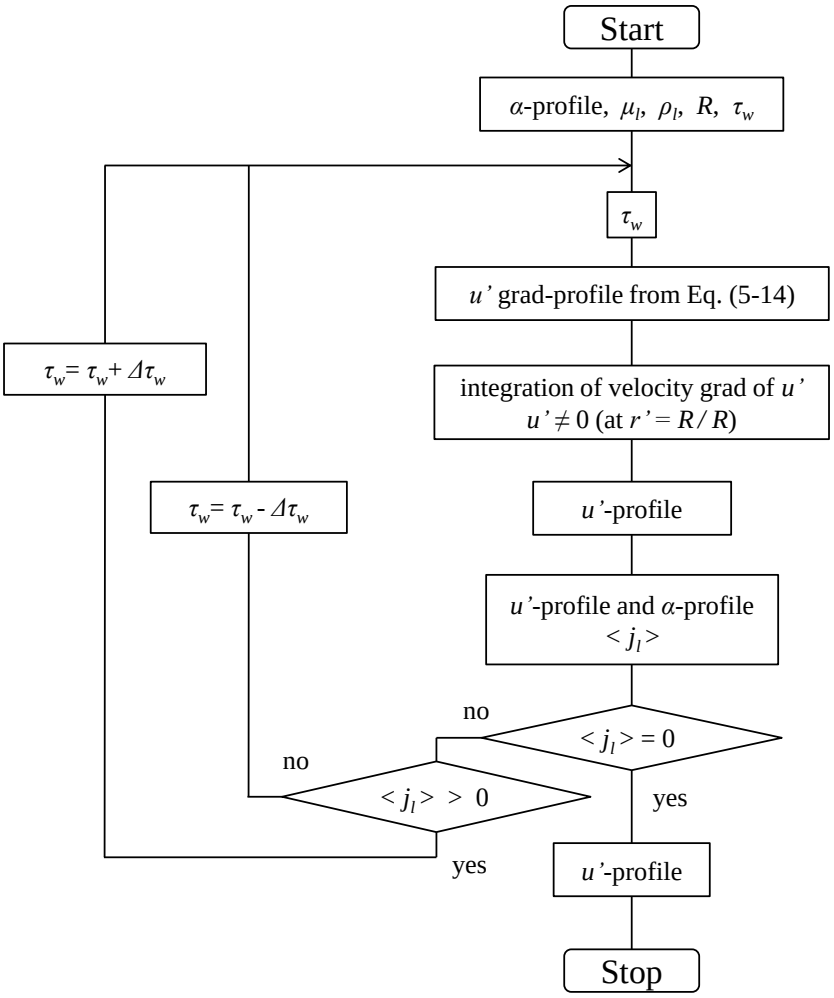

Figure 5-13 Flow chart for numerical analysis using Sato's model with slip condition.

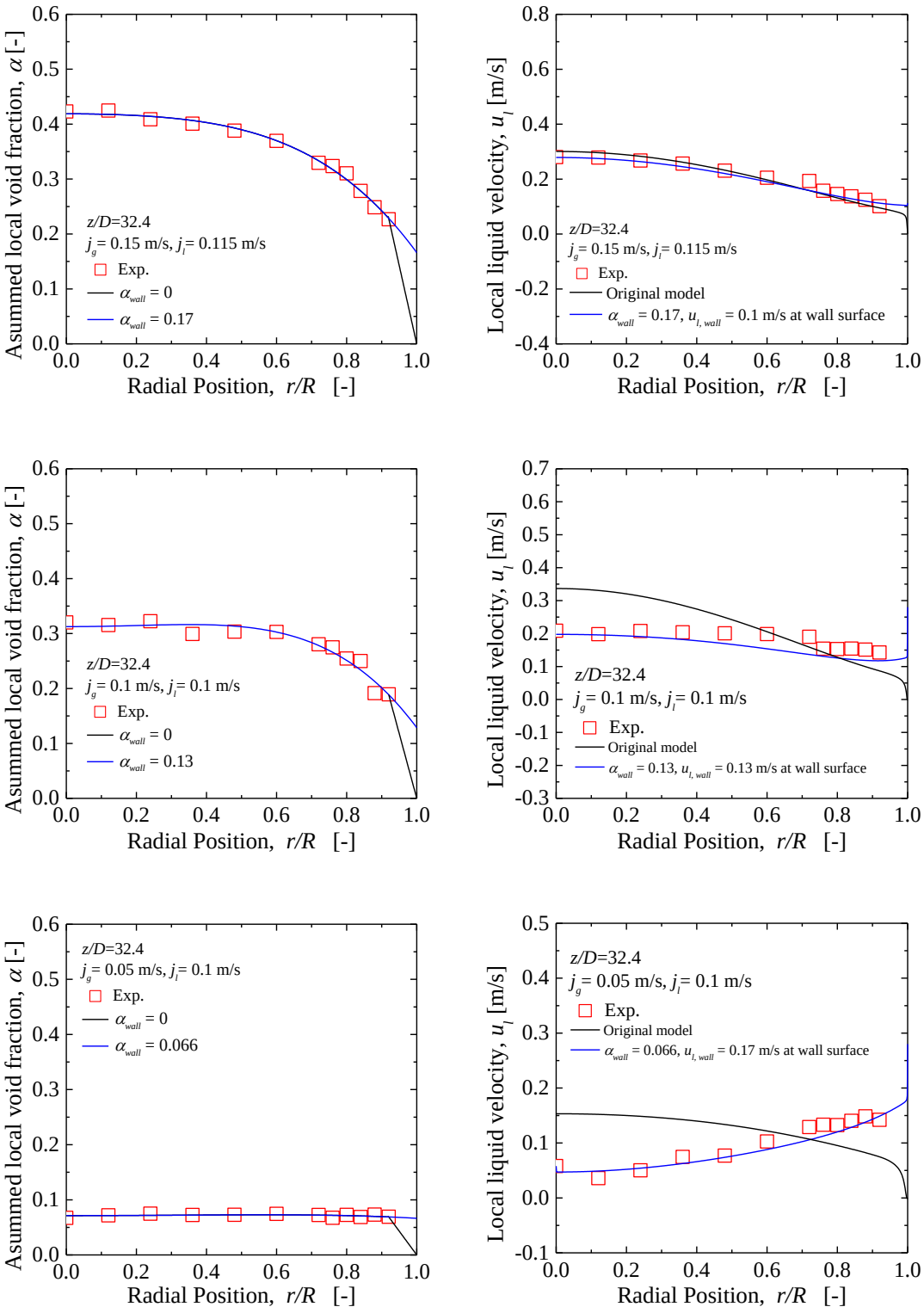

Figure 5-14 Comparison of liquid velocity between experimental one and calculated one, where eddy diffusivities, ε' and ε'', were used for the calculation.
(for j_g =0.05 to 0.15 m/s, j_l = 0.1 m/s)

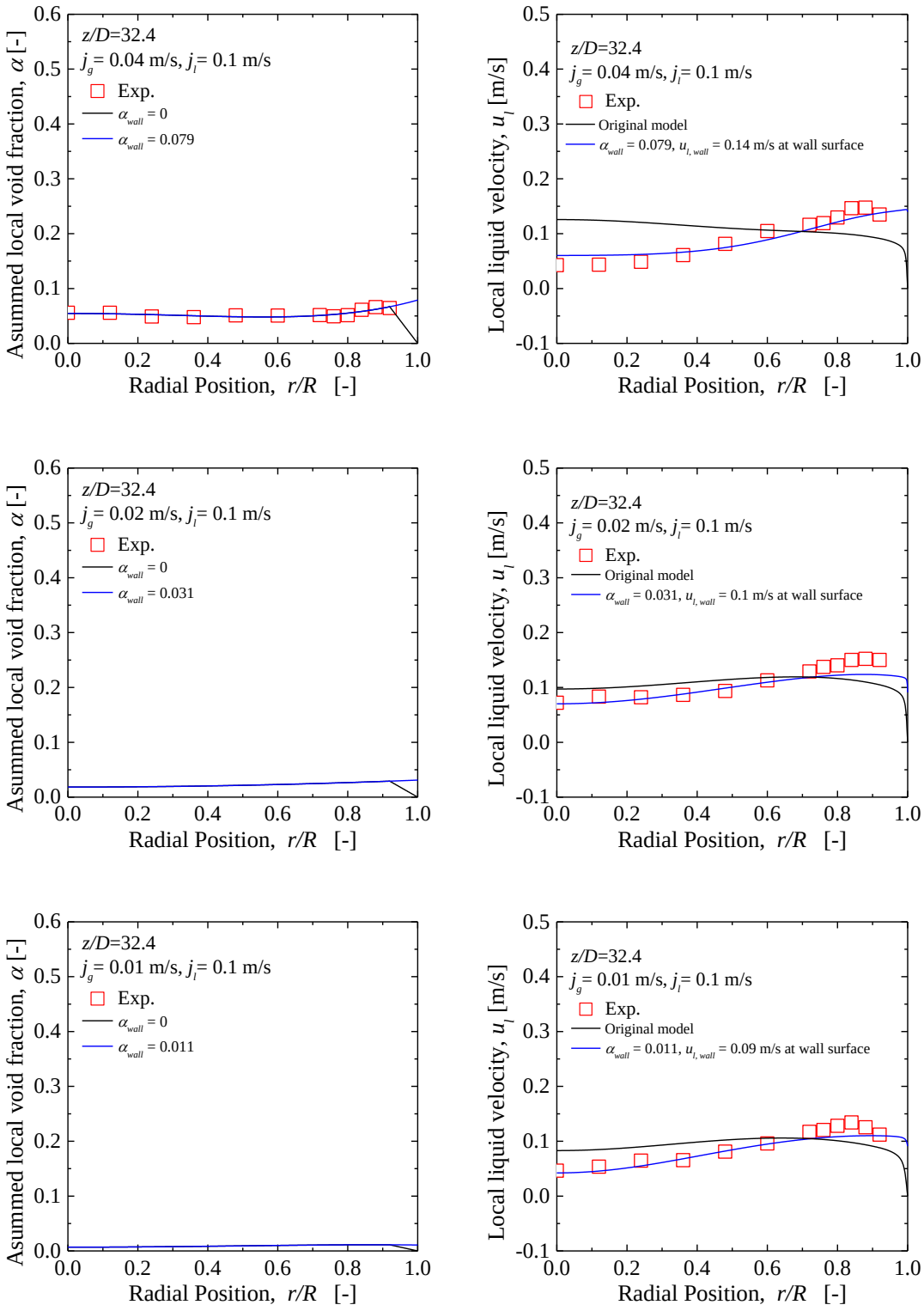

Figure 5-15 Comparison of liquid velocity between experimental one and calculated one, where eddy diffusivities, ε' and ε'', were used for the calculation.
(for j_g =0.01 to 0.04 m/s, j_l = 0.1 m/s)

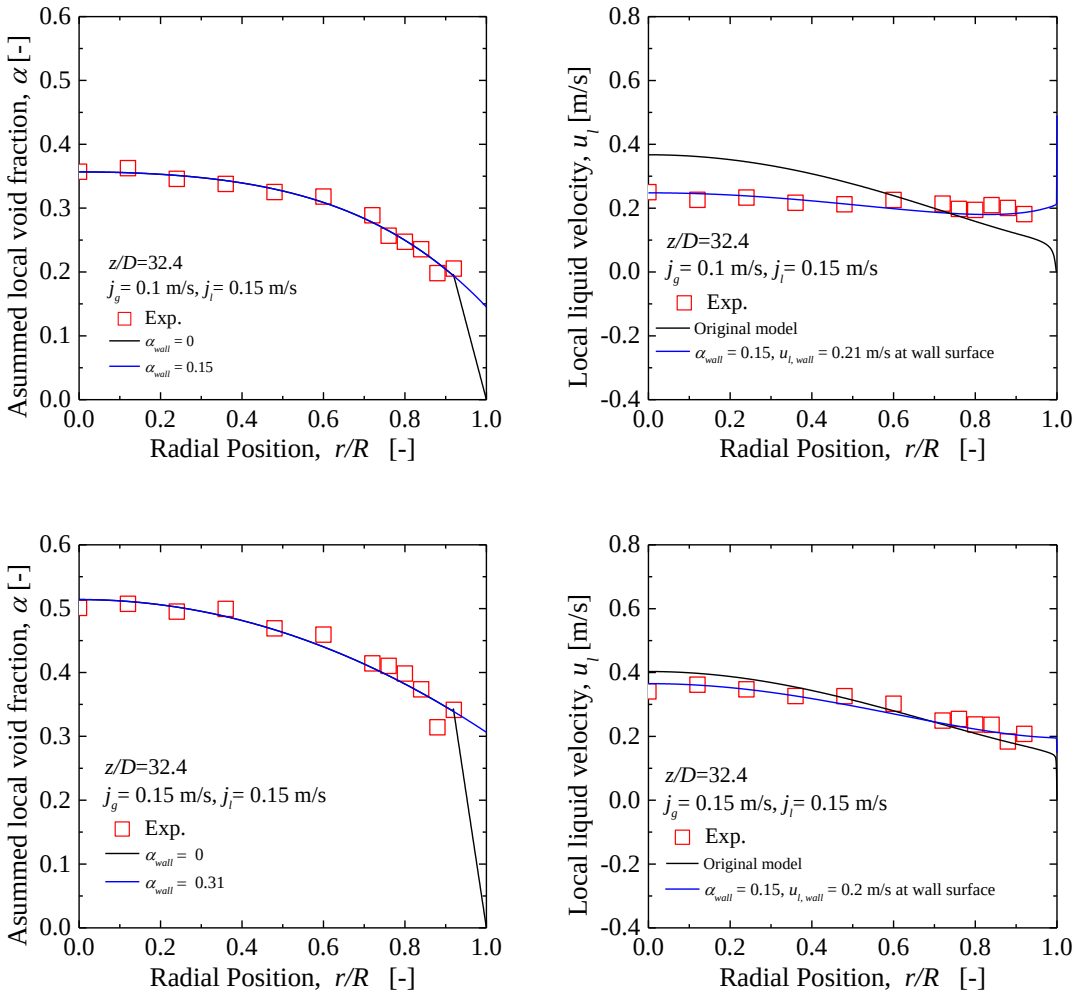

Figure 5-16 Comparison of liquid velocity between experimental one and calculated one, where eddy diffusivities, ε' and ε'', were used for the calculation.
(for j_g =0.1 to 0.15 m/s, j_l = 0.15 m/s)

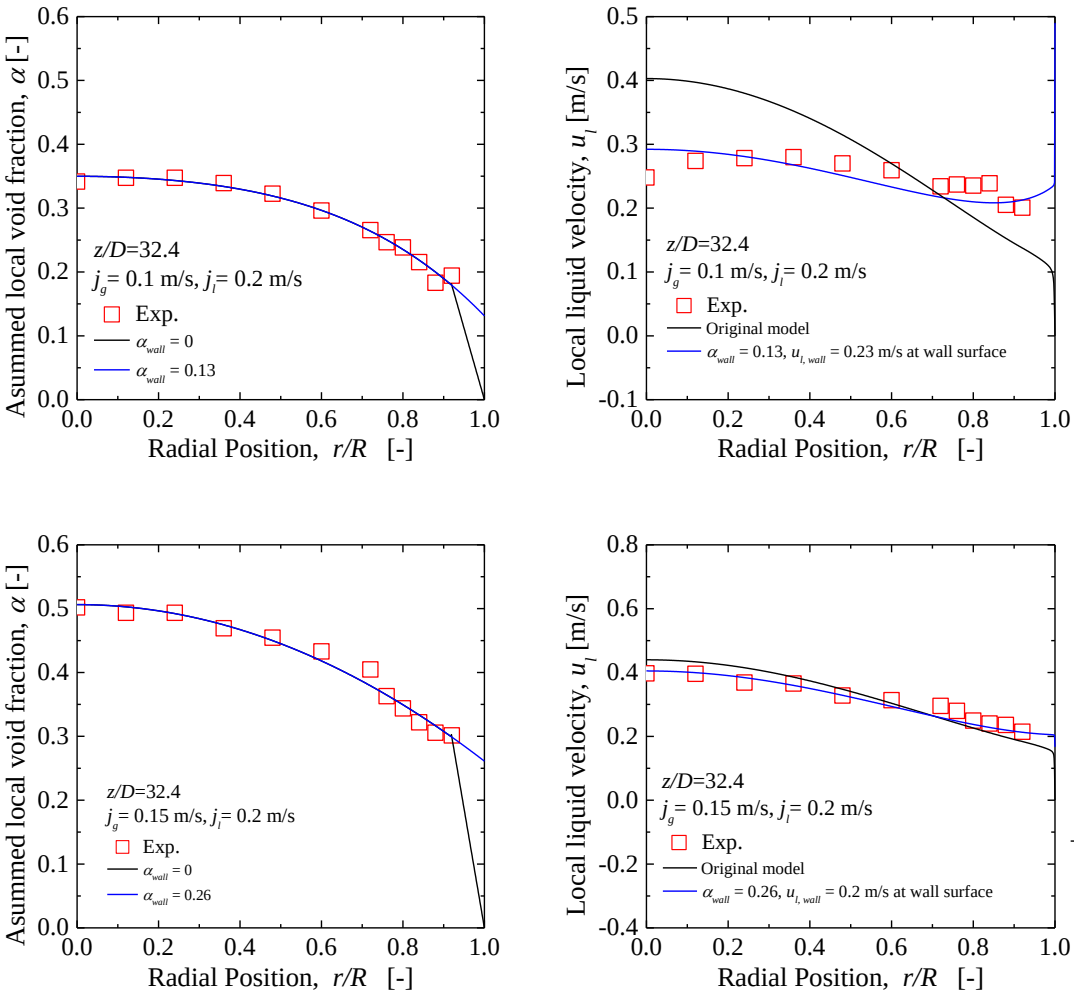

Figure 5-17 Comparison of liquid velocity between experimental one and calculated one, where eddy diffusivities, ε' and ε'', were used for the calculation.
(for j_g =0.1 to 0.15 m/s, j_l = 0.2 m/s)

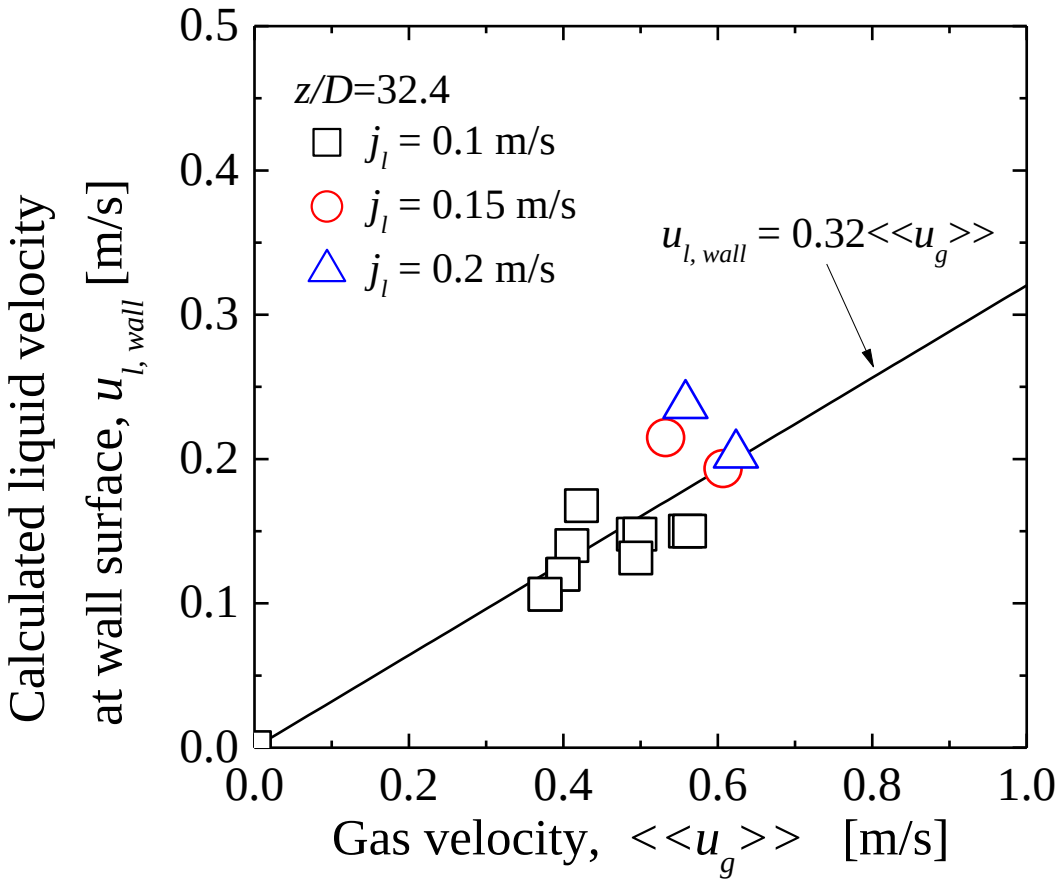

Figure 5-18 Relationship between gas velocity and liquid velocity calculated at wall surface.

Table 5-1 Non-dimensional values used in Equation (5-15).

$X = \frac{1}{\pi}\int_0^1 \{1-\alpha(r^*)\} 2\pi r^* dr^*$	$Y = \frac{1}{\pi r^{*2}}\int_0^{r^*} \{1-\alpha(r^*)\} 2\pi r^* dr^*$	$Z = (1-\alpha)\frac{\rho_l}{\mu_l}\left(\frac{\mu_l}{\rho_l} + \varepsilon' + \varepsilon''\right)$
$N\tau_w = \frac{\tau_w}{\mu_l}\sqrt{\frac{D}{g}}$	$r^* = \frac{r}{R}$	$Ga \equiv \frac{\sqrt{gD}D\rho_l}{\mu_l}$
$u_l^*(r^*) = \frac{u_l(r^*)}{\sqrt{gD}}$	$y^+ = \frac{U_l^* y}{\nu_l}$	$A^+ = \frac{AU^*}{\nu}$
$U^* = \sqrt{\frac{\tau_w}{\rho}}$		

Chapter 6
Conclusion

Understanding of the LBE gas-liquid two-phase flow has essential importance to estimate safety of the heavy liquid metal cooled reactors such as ADSs and LFRs in PRASG condition. Experimental efforts have been made in this study to clarify the two-phase flow characteristics, such as void fraction profile, liquid velocity profile, and turbulent quantities. Intensive review of existing works in relation to the liquid-metal flows, it was found that the gas-liquid density ratio and wall wettability might affect the two-phase flow behavior of LBE. To measure the void fraction and liquid velocity fluctuations of LBE two-phase flows, an electrical conductivity probe (EC probe) and an electro-magnetic probe (EM probe) have been developed. From experimental data, basic characteristics of its two-phase flow have been theoretically analyzed, including wall wettability effects.

Experiments and measurements have been performed using a LBE test loop named as HEavy liquid metal Single and Two-phase flow Instrumentation for Accelerator-driven system (HESTIA). The test section was a vertical round stainless steel (Type 304) pipe and it has an inner diameter of 50 mm and a length of 2,000 mm. The stainless steel pipe is commercially available without any special surface treatment, which has a passivation film on its surface, showing poor wettability to the LBE. The superficial gas velocity j_g was varied from 0.05 to 0.15 m/s and the superficial liquid velocity j_l was varied from 0.1 to 0.2 m/s,

As a result, it was found that the local liquid velocity can be measured by the EM probe with less than ±10% of measurement error for the vortex flow meter - even in the two-phase flows. The measured void fraction by the EM probe was slightly larger than that by the EC probe due to the larger measurement area of EM probe. However, the measurement error of void fraction by EM probe can be minimized by adjusting the threshold value in the signal processing. Measurement results show the transition from wall-peak to core-peak profile in the void fraction and the liquid velocity at low liquid flow rate. Wall-peak profile might be formed by the bubble accumulations in the wall regions due to the poor wettability of LBE.

One-dimensional analysis using simplified two-fluid model was carried out to obtain numerically simulated axial void fraction, gas velocity and liquid velocity. From the comparisons between the calculated results and experimentally measured results of these parameters show disagreement in case of utilizing the existing simplified two-fluid model. Such

disagreement might be caused by the difference in the gas-liquid interfacial force between LBE two-phase flow and air-water two-phase flow. In order to improve prediction accuracy of the model for analysis for LBE two-phase flow, the equation of interfacial drag force was modified by using void fraction weighted mean drift velocity. Axial development of measured void fraction in HESTIA can be well reproduced with above mentioned modifications.

LBE bubble columns, HESTIA2, with a simple circular channel and annulus were experimentally investigated by varying the surface wettability of the channel wall and the measured results were compared with existing correlations and with one-dimensional simulation based on momentum transfer model toward radial direction and drift flux models. The inner dimeter of the test section was 102.3mm and the height was 1001.5 mm. From measurement results, it was found that the surface wettability affected the drift velocity in the LBE two-phase flow in the annular channels. As the possible cause, it might be considered that LBE circulation flow in the annular channels is enhanced by bubbles flowing close to inner wall surface in case of poor wettability condition. However, the effect of the surface wettability on the two-phase flow in a cylindrical vessel was not distinct, which might be attributed to the small void fraction in the near wall region caused by the circulation flow. The distribution parameter in the LBE two-phase flow in a cylindrical vessel can be well reproduced by using one dimensional momentum transfer model with assumed void fraction and mixing length for single phase flow. In case of the annular channels, the one-dimensional simulation gives underestimation in the distribution parameters. Such underestimation was revised by the one-dimensional simulation assuming void fraction profile showing maximum value near the inner wall surface.

Based on the void fraction and liquid velocity distributions measured in HESTIA loop, the momentum transfer models have been compared. From comparison of the liquid velocity profile between measured and calculated one, measured liquid velocity can be reproduced by momentum transfer model with assumption of local void fraction and slip velocity at wall surface. Measured liquid velocity cannot be predicted by using mixing length model for single phase flow. Similar eddy viscosity model developed for gas-liquid two-phase flow to mixing length model have been applied to the measurement results. Good agreement was obtained between experimental and predicted velocity profiles by assuming slip velocity on the wall surface. In case of poor wettability condition, it is inferred that there might be repetition of dry and wet due to bubble on the wall surface. Therefore, macroscopic point of view, such slip conditions should be assumed to predict the velocity profiles for poor wettability conditions.
The main results are summarized as follows:

1) In order to obtain local flow structure in the LBE two-phase flow, EC and EM probe methods were established. Measurement error of the local liquid velocity by the EM probe was about 10%.
2) Measured void fraction and liquid velocity profiles show transition from wall-peak to core-peak distribution in condition of low superficial gas and liquid velocities. The wall-peak distribution might be caused by bubble accumulation near the wall surface due to the poor wettability between LBE and stainless steel wall.
3) In the LBE two-phase flow, gas-liquid interfacial drag force might be small. In the case of assuming such interfacial drag force, axial development of void fraction can be reproduced by utilizing one-dimensional two-fluid model.
4) The wall surface wettability can affect void fraction profile and liquid velocity profile also in the LBE two-phase flow. Tendency of distribution parameter measured in case of annular channel condition of LBE bubble column can be understood by assuming void fraction profile having maximum value near the wall surface.
5) Local liquid velocity profile measured in condition of forced convection cannot be predicted by using mixing length model for single phase flow. Assuming bubble induced turbulence, good agreement was obtained between experimental and predicted velocity profiles by assuming slip velocity on the wall surface. In case of poor wettability condition, there might be repetition of dry and wet due to bubble on the wall surface. Therefore, macroscopic point of view, such slip conditions should be assumed to predict the velocity profiles for poor wettability conditions.

As mentioned above, the interfacial drag, surface wettability and slip conditions in the LBE two-phase flow should be well investigated to clarify the flow characteristics. In present experimental condition, predicted cross sectional averaged void fraction along flow direction can be improved by taking more precise interfacial drag force into account to the two-fluid model. The cross sectional averaged void fraction is affected by wall wettability. The radial distribution of local liquid velocity is also affected by such wettability effect. In case of predicting such liquid velocity distribution, the assumed slip velocity on the wall surface was almost same value as the superficial liquid velocity. The slip velocity might be affected by the void fraction on the wall surface, however, the prediction of velocity field in the LBE two-phase flow with poor wettability system can be strongly improved by introducing the macroscopic slip velocity assumption.

For further understanding of the LBE two-phase flow, the void fraction and liquid velocity distributions in the near wall region should be precisely measured by changing the wall

wettability, which could contribute to the further improvement of prediction method of the LBE two-phase flow.

List of publications

Journals

[1] G. Ariyoshi, Y. Asai, D. Ito, Y. Saito, K. Mishima, Measurements of turbulence in a liquid-metal two-phase flow by using a miniature electro-magnetic probe. Japanese Journal of Multiphase Flow; Vol. 27, 615-622 (2014) [和文].

[2] G. Ariyoshi, R. Inatomi, D. Ito, Y. Saito, Effect of wall wettability condition on drift-flux parameters in lead-bismuth two-phase flow in circular and annular bubble columns. J. Nucl. Sci.Technol.; Vol.55, 239-253 (2017).

[3] G. Ariyoshi, D. Ito, K Ito, Y. Saito, Radial momentum transfer mechanism of lead-bismuth-nitrogen gas-liquid two-phase flow. J. Nucl. Sci.Technol.;
（投稿準備中）.

Book

[1] G. Ariyoshi, D. Ito, Y. Saito, Experimental study of flow structure and turbulent characteristics in lead-bismuth two-phase flow. Nuclear Back-end and Transmutation Technology for Waste Disposal Beyond the Fukushima Accident 2015 (K. Nakajima Ed.). Springer, 107-115 (2015).

Proceedings

[1] G. Ariyoshi, D. Ito, Y. Saito, K. Mishima. Flow characteristics of lead-bismuth flows at low liquid velocity conditions. Proc. The Fifteenth Kyoto – Tsinghua – Seoul National University Thermal Engineering Conference; 2015 Dec 12-13; Kyoto, Japan.

[2] G. Ariyoshi, D. Ito, Y. Saito, K. Mishima. Turbulent structures in lead-bismuth flows measured by using intrusive probe methods. Proc. ICMF – 2016 – 9th International Conference on Multiphase Flow; 2016 May 22nd – 27th; Firenze, Italy.

[3] G. Ariyoshi, D. Ito, Y. Saito, K. Mishima. Turbulent characteristics in lead-bismuth flows flowing in poor and good wettability pipes. Proc. 24th International Conference on Nuclear Engineering (ICONE24); 2016 Jun 26 – 30; Charlotte NC, USA.

International Conferences

[1] G. Ariyoshi, D. Ito, Y. Saito, Experimental study of flow structure and turbulent characteristics in lead-bismuth two-phase flow. Nuclear Back-end and Transmutation Technology for Waste Disposal Beyond the Fukushima Accident. (2013).

[2] G. Ariyoshi, D. Ito, Y. Saito, K. Mishima, Measurements of turbulence in a liquid lead-bismuth flow. The 12th International Workshop on Asian Network for Accelerator-Driven System (ADS) and Nuclear Transmutation Technology (NTT); (2014).

[3] G. Ariyoshi, D. Ito, Y. Saito, K. Mishima, Effect of wall surface condition on flow structure in a LBE two-phase flow. The First Topical Meeting on Asian Network for Accelerator-Driven System (ADS) and Nuclear Transmutation Technology (NTT); (2015).

[4] G. Ariyoshi, D. Ito, Y. Saito, K. Mishima, Flow characteristics of lead-bismuth flows at low liquid velocity conditions. The Fifteenth Kyoto – Tsinghua – Seoul National University Thermal Engineering Conference; (2015).

[5] G. Ariyoshi, D. Ito, Y. Saito, K. Mishima, Turbulent structures in lead-bismuth flows measured by using intrusive probe methods. ICMF – 2016 – 9th International Conference on Multiphase Flow; (2016).

[6] Y. Saito, G. Ariyoshi, D. Ito, Development of measurement technique for bubble velocity vector in gas-liquid two-phase flow by using 4-sensor probe. ICMF – 2016 – 9th International Conference on Multiphase Flow; (2016).

[7] G. Ariyoshi, D. Ito, Y. Saito, K. Mishima, Turbulent characteristics in lead-bismuth flows flowing in poor and good wettability pipes. 24th International Conference on Nuclear Engineering (ICONE24); (2016).

[8] G. Ariyoshi, D. Ito, Y. Saito, K. Mishima, Turbulent LBE flow in vertical circular pipes with different wall surface condition. NTHAS10 The tenth Korea-Japan Symposium on Nuclear Thermal Hydraulics and Safety; (2016).

[9] R. Inatomi, G. Ariyoshi, Y. Saito, D. Ito, Effect of wall surface wettability on two-phase flow characteristics in a lead-bismuth bubble column. NTHAS10 The tenth Korea-Japan Symposium on Nuclear Thermal Hydraulics and Safety; (2016).

[10] G. Ariyoshi, R. Inatomi, D. Ito, Y. Saito, K. Mishima, Turbulent LBE flow in vertical circular pipes with different wall surface condition. 6th Japan-Korea Joint Seminar on Nuclear Thermal Hydraulics and Safety for Students and Young Researchers; (2016).

[11] R. Inatomi, G. Ariyoshi, Y. Saito, D. Ito, Effect of wall surface wettability on two-phase flow characteristics in a lead-bismuth bubble column. 6th Japan-Korea Joint Seminar on Nuclear Thermal Hydraulics and Safety for Students and Young Researchers; (2016).

[12] G. Ariyoshi, D. Ito, K. Ito, Y. Saito, Measurement of liquid velocity and void fraction in vertical upward LBE two-phase flow under poor wettability conditions. NTHAS11 The eleventh Korea-Japan Symposium on Nuclear Thermal Hydraulics and Safety; (2018).

[13] G. Ariyoshi, D. Ito, K. Ito, Y. Saito, Measurement of liquid velocity and void fraction in vertical upward LBE two-phase flow under poor wettability conditions. 7th Japan-Korea Joint Seminar on Nuclear Thermal Hydraulics and Safety for Students and Young Researchers; (2018).

National Conference

[1] 有吉 玄、浅井 勇吾、伊藤 大介、齊藤 泰司、三島 嘉一郎、小型電磁流速計を用いた液体金属二相流の乱流計測、日本混相流学会 混相流シンポジウム2013, (2013).

[2] 有吉 玄、浅井 勇吾、伊藤 大介、齊藤 泰司、三島 嘉一郎、鉛ビスマス二相流乱流の詳細構造に関する研究　京都大学原子炉実験所 第48回学術講演会, (2014).

[3] 有吉 玄、伊藤 大介、齊藤 泰司、三島 嘉一郎、低ボイド率条件下における液体金属二相流の乱流計測　日本混相流学会 混相流シンポジウム2014, (2014).

[4] 有吉 玄、伊藤 大介、齊藤 泰司、三島 嘉一郎、低ボイド率領域における鉛ビスマス気液二相流の乱流計測　日本原子力学会 秋の大会, (2014).

[5] 有吉 玄、鉛ビスマス気液二相流の乱流計測に関する研究　日本原子力学会 秋の大会 熱流動部会 若手交流フォーラム, (2014).

[6] 有吉 玄、伊藤 大介、齊藤 泰司、三島 嘉一郎、鉛ビスマス気液二相流の乱流計測　第63回 理論応用力学講演会, (2014).

[7] 有吉 玄、伊藤 大介、齊藤 泰司、三島 嘉一郎、液体鉛ビスマスの単相および気液二相流れの乱流計測　京都大学原子炉実験所 第49回学術講演会, (2015).

[8] 有吉 玄、伊藤 大介、齊藤 泰司、三島 嘉一郎、鉛ビスマス気液二相流の相分布および液相速度計測　日本混相流学会 混相流シンポジウム2015, (2015).

[9] 有吉 玄、伊藤 大介、齊藤 泰司、三島 嘉一郎、鉛ビスマス気液二相流の相分布および液相速度計測　日本混相流学会 混相流シンポジウム2015 ベストプレゼンテーションアワード, (2015).

[10] 有吉 玄、伊藤 大介、齊藤 泰司、三島 嘉一郎、鉛ビスマス気液二相流の流動構造におよぼす流路表面性状の影響　日本原子力学会 秋の大会, (2015).

[11] 有吉 玄、鉛ビスマス気液二相流の流動構造におよぼす流路表面性状の影響　日本原子力学会 秋の大会 熱流動部会 若手交流フォーラム, (2015).

[12] 有吉 玄、伊藤 大介、齊藤 泰司、三島 嘉一郎、鉛ビスマスの流動構造におよぼす流路表面性状の影響　第3回 原子力関係科学技術の基礎的研究の動向調査委員会, (2016).

[13] 有吉 玄、伊藤 大介、齊藤 泰司、三島 嘉一郎、鉛ビスマス流れの乱流構造に対する流路表面性状の影響　京都大学原子炉実験所 第50回学術講演会, (2016).

[14] 有吉 玄、稲富 良太、伊藤 大介、齊藤 泰司、三島 嘉一郎、鉛ビスマス流れにおよぼす壁面濡れ性の影響 – 接触式プローブ法を用いた局所速度変動および相分布計測 –　日本混相流学会 混相流シンポジウム2016, (2016).

[15] 稲富 良太、有吉 玄、齊藤 泰司、伊藤 大介、鉛ビスマス流れにおよぼす壁面濡れ性の影響 – プール体系におけるボイド率計測 –　日本混相流学会 混相流シンポジウム2016, (2016).

[16] 有吉 玄、稲富 良太、伊藤 大介、齊藤 泰司、三島 嘉一郎、鉛ビスマス流れにおよぼす壁面濡れ性の影響 – 接触式プローブ法を用いた局所速度変動および相分布計測 – 日本混相流学会 混相流シンポジウム2016 ベストプレゼンテーションアワード, (2016).

[17] 稲富 良太、有吉 玄、齊藤 泰司、伊藤 大介、鉛ビスマス流れにおよぼす壁面濡れ性の影響 – プール体系におけるボイド率計測 – 日本混相流学会 混相流シンポジウム2016 ベストプレゼンテーションアワード, (2016).

[18] 有吉 玄、稲富 良太、伊藤 大介、齊藤 泰司、三島 嘉一郎、鉛ビスマス気液二相流におよぼす壁面濡れ性の影響 – 強制対流体系におけるボイド率計測 – 京都大学原子炉実験所 第51回学術講演会, (2017).

[19] 稲富 良太、有吉 玄、伊藤 大介、齊藤 泰司、鉛ビスマス気液二相流におよぼす壁面濡れ性の影響 – プール体系におけるボイド率計測 – 京都大学原子炉実験所 第51回学術講演会, (2017).

[20] 有吉 玄、伊藤 大介、齊藤 泰司、三島 嘉一郎、鉛ビスマス気泡塔内流動におよぼす流路壁面濡れ性の影響 日本原子力学会 春の大会 熱流動部会 若手交流フォーラム, (2017).

[21] 有吉 玄、稲富 良太、伊藤 大介、齊藤 泰司、鉛ビスマス気泡塔内流動のボイド率計測（壁面濡れ性の影響）日本混相流学会 混相流シンポジウム2017, (2017).

[22] 前田 啓介、有吉 玄、伊藤 大介、齊藤 泰司、一次元二流体モデルを用いた鉛ビスマス気液二相流の流動特性の予測 日本混相流学会 混相流シンポジウム2017, (2017).

[23] 有吉 玄、鉛ビスマス気泡塔内流動のボイド率計測（壁面濡れ性の影響）日本混相流学会 混相流シンポジウム2017 ベストプレゼンテーションアワード, (2017).

[24] 前田 啓介、有吉 玄、伊藤 大介、齊藤 泰司、一次元二流体モデルを用いた鉛ビスマス気液二相流の流動特性の予測 日本混相流学会 混相流シンポジウム2017 ベストプレゼンテーションアワード, (2017).

[25] 有吉 玄、稲富 良太、伊藤 大介、齊藤 泰司、鉛ビスマス気泡塔内のボイド率計測および乱流モデルを用いた数値解析に関する研究　京都大学原子炉実験所 第52回学術講演会, (2018).

[26] 前田啓介、有吉 玄、伊藤 大介、伊藤 啓、齊藤 泰司、二流体モデルによる鉛ビスマス気液二相流動特性の予測　京都大学原子炉実験所 第52回学術講演会, (2018).

Summer School

[1] G. Ariyoshi, D. Ito, Y. Saito, K. Mishima, Measurement of phase distributions and liquid velocity in a lead-bismuth gas-liquid two-phase flow. SCK/CEN ACADEMY Heavy Metal Summer School; (2015).

Awards

[1] SCK/CEN ACADEMY Heavy Metal Summer School, Best poster award. (2015).

[2] 24th International Conference on Nuclear Engineering (ICONE24), ICONE-24 Student Best Paper Competition – Asia/Japan. (2016).

[3] 6th Japan-Korea Joint Seminar on Nuclear Thermal Hydraulics and Safety for Students and Young Researchers, Best poster award. (2016).